Computational investigation of intense short-wavelength laser interaction with rare gas clusters

Nicolas Bigaouette

Thesis submitted to the
Faculty of Graduate and Postdoctoral Studies
In partial fulfillment of the requirements
For the Ph.D. degree in Physics

Ottawa-Carleton Institute of Physics
Department of Physics
Faculty of Science
University of Ottawa
Ottawa, Canada

Lay down, your sweet and weary head
Night's falling, you've come to journeys end

Sleep now, and dream of the ones who came before
They are calling from across a distant shore

Why do you weep?
What are these tears upon your face?
Soon you will see all of your fears will pass away
Safe in my arms, you're only sleeping

What can you see on the horizon?
Why do the white gulls call?
Across the sea a pale moon rises
The ships have come to carry you home

And all will turn to silver glass
A light on the water, all souls pass

Hope fades, into the world of night
Through shadows falling out of memory and time

Don't say, we have come now to the end
White shores are calling
You and I will meet again
And you'll be here in my arms, just sleeping

What can you see on the horizon?
Why do the white gulls call?
Across the sea a pale moon rises
The ships have come to carry you home

And all will turn to silver glass
A light on the water, gray ships pass into the west

Fran Walsh, Howard Shore, and Annie Lennox.
The Lord Of The Rings: The Return Of The King

Summary

Clusters of atoms have remarkable optical properties that were exploited since the antiquity. It was only during the late 20^{th} century though that their production was better controlled and opened the door to a better understanding of matter. Lasers are the tool of choice to study these nanoscopic objects so scientists have been blowing clusters with high intensities and short duration laser pulses to gain insights on the dynamics at the nanoscale. Clusters of atoms are an excellent first step in the study of bio-molecules imaging. New advancements in laser technology in the shape of Free Electron Lasers (FEL) made shorter and shorter wavelengths accessible from the infrared (IR) to the vacuum and extreme ultra-violet (VUV and XUV) to even X-rays . Experiments in these short wavelengths regimes revealed surprisingly high energy absorption that are yet to be fully explained.

This thesis tries to increase the global knowledge of clusters of rare-gas atoms interacting with short duration and high intensity lasers in the VUV and XUV regime. Theoretical and numerical tools were developed and a novel model of energy transfer based on excited states will be presented.

The first part describes the current knowledge of laser-cluster interaction in the short wavelength regime followed by the description of the new model. In the second part of the thesis the different tools and implementations used throughout this work are presented. Third, a series of journal articles (of which four are published and one to be submitted) are included where our models and tools were successfully used to explain experimental results.

Statement of Originality

I hereby certify that the work of the present thesis, to the best of my knowledge, is original and my own. All codes used for the numerical studies and their analysis were written by me, except some contributions from Edward Ackad (a postdoctoral fellow in the group for two years) who contributed (in terms of lines of code) around 15 % of the MD package and 20 % of the ionization library. Transitions cross-sections (ground to excited states and excited states to continuum) used in the ACI model were obtained by him using the Cowan code, the only external package used throughout this work. A smaller contribution was done by two summer students, Julien Roy and Stan Hatko, who helped in some technical aspect of the code development. My huge work on the simulation packages allowed Edward Ackad to generate generous amount of data that was used for the publications; he still uses it today after departing Ottawa for an Assistant Professor position at Southern Illinois University at Edwardsville.

Acknowledgements

Graduate studies is a gargantuan challenge full of difficulties, disappointment and discouragement. It is also greatly enriching, satisfying and something to be proud of. Even though I present here my own thesis, many great people were behind me and helping me surpass myself.

I would like to first thank my supervisor, professor Lora Ramunno, for allowing me to pursue my graduate studies under her umbrella. I am glad she trusted me as her first PhD student and I hope to have come up to her expectations. Even though difficulties sometimes emerged, I am greatly thankful of the trust she had in me. She gave me the freedom and the tools I needed to fulfill my goals and ideas. She gave me the responsibility of both the purchase and maintenance of her two clusters, an invaluable experience. She advised me wisely during the years. I hope the end of my studies will not mean the end of some collaboration.

I would also like to thank Edward "Eddie" Ackad for the numerous and deep discussions on both professional and personal matter. He never refused to answer my questions, even pushing me to answer them myself instead of blindly answering. You are a good friend that I'm already missing.

Moving to a different city, in a different culture and language can be challenging, but the many friends I've made in Ottawa supported me without question. I must name Charles Varin and Martin Bertrand who became true friends that I will hopefully keep after my move back to Montreal.

I am grateful to my family who encouraged me before and during those years, supporting me into never giving up – *encore un p'tit coup de coeur!* My parents, brother, sisters who helped me move in during this emotional time. I want to show gratitude to my in-laws for supporting me without question and understanding my countless absences; the question *tonton travail?* will simply be a memory from now on.

I cannot thank enough my beautiful and sweet Christine that supported me during all these long years, remotely at first and more closely during the last one. You've been so supportive, patient and understanding with me, at all times, the best as the worst. I know it's been hard for you and I deeply apologize for everything I made you go through; listening to my grumbles, seeing me leave every Sunday night. You never

stopped believing in me. I deeply thank you for always being there for me. You said I was your pillar during your own PhD. I'm saying you are my keystone, keeping me in balance, preventing me from falling, strengthening me. You've been a saint to endure my countless absent hours. I sincerely cannot wait to be back in your arms and enjoy our time together – as a family of soon three. I cannot wait to see our *petit poulet* and show him the world.

I love you, and always will.

Table of contents

List of Figures

List of Publications

1

Laser-Cluster interaction

1.1 Clusters of atoms and strong laser fields

Clusters of atoms have been in use for a longer time than we might normally think. Gold clusters were used in ancient Rome for their optical properties; their size could be controlled to produce different glass colours. Gustav Mie was the first to theoretically describe the interaction of light with (gold) spheres in 1908, explaining the light absorption dependence on cluster size. During the last part of the twentieth century, the discovery of C_{60} fullerenes marked the real beginning of cluster studies [1].

As the Romans discovered, the size of these nanoparticles is a key property. Techniques to fully control the size of produced clusters allowed a wide range of studies and applications. Three main classes of cluster creation techniques exist [2, 1]. First, supersonic jet methods force high pressure gas through a small nozzle into a vacuum chamber where atoms condensate into clusters. Second, gas aggregation methods similarly condensate atoms after their injection into a gas chamber. Lastly, clusters can be created by breaking up a material surface by either particle collision, laser ablation or high electric field. These techniques provide great control over the created cluster size.

Along with the recent developments and advances in nanosciences, the advance of

high-power and short duration lasers opened the door for ground breaking ultra-fast studies. With femtosecond (1 fs = 10^{-15} s) lasers it became possible to study atomic motion, similar to a camera flash capturing a moving object.

The study of rare gas cluster interaction with femtosecond lasers represents a merging of nano and ultrafast science. Many femtosecond lasers have a wavelength of 800 nm in the infrared (IR) and clusters have been studied thoroughly with this "long" wavelength. Investigation of energetic electrons (keV) or highly charged ion (MeV) emission, X-ray production or even table-top neutron sources [3] were performed since the 1990s [4, 5].

The IR regime sparked a new field of ultrafast physics. By stripping electrons from their parent ion through tunnel ionization and accelerating them in the laser's strong electric field, a train of pulses of high harmonics can be created, a process called High Harmonic Generation (HHG). Created during a single femtosecond pulse, this train of shorter pulses can reach attosecond (1 as = 10^{-18} s) duration, an exciting developing field [6].

Clusters are invaluable tools because they bridge the gap between single atoms and solids. Their high density allows them to exhibit collective effects similar to bulk materials, while their small size increases their surface to volume ratio. At the smallest range, clusters can be used as models for small molecules and at the opposite they still present interesting optical properties even at 10,000 atoms [1].

In addition to their great size scalability, cluster explosion by-products after interaction with a strong laser field are accessible, revealing detailed information about the internal dynamics. For example, time-of-flight (TOF) mass spectrometry can reveal the ion charge state spectrum, which is a signature of the amount of energy absorbed from the laser pulse. This type of data is not accessible in laser-bulk interaction, since most matter remains in a solid state.

Clusters of atoms can be composed of different elements. Rare gas atoms have closed outer electronic shells, making them less prone to chemical reactions and as a result do not interact much with each other. Rare-gas clusters are thus weakly bound by Van der Waals forces and generally form an icosahedral structure [7]. The electronic wavefunctions are more localized around the nucleus than in metal clusters, which simplifies the cluster environment treatment.

A critical characteristic of laser-cluster interaction for the present work is the fact that clusters can be studied numerically. Full quantum resolution is not possible even for clusters consisting of a couple of atoms, while on the other range of the methods spectrum

rate equations and (nano)plasma models are too macroscopic to reflect the large field gradient present during cluster dynamics [8]. The tool of choice for this problem is Molecular Dynamics (MD) where trajectories are treated classically; Newton's equations of motion are solved at each time step and quantum effects are included using specific rates.

The importance of laser-cluster interaction as an investigative tool is illustrated by the vast amount of work on the subject, mainly in the IR regime [8]. Varin *et al.* [9] recently developed an electrodynamic particle-in-cell (PIC) code for IR studies on pre-ionized clusters. PIC methods have a better scaling than MD in terms of number of particles simulated, and since they treat the electromagnetic field dynamically (through Maxwell's equations) field retardation effects are taken into account, which can be important for large clusters. On the downside PIC methods do not have the precision of MD for close range interactions and collisions. A novel addition by Varin *et al.* is to add microscopic corrections to PIC for more realistic close range interactions [10]. Since the grid must resolve the electromagnetic wave, PIC simulations can thus be a challenge when the wavelength is small but this opens the door to a new frontier of modelling.

The interest of this thesis is in modelling short wavelength interaction with clusters. In recent years, laser light sources have been moving to shorter wavelengths due to groundbreaking new Free Electron Laser (FEL) facilities; Vacuum Ultra-Violet (VUV), Extreme Ultra-Violet (XUV), soft X-rays and even hard X-rays are now accessible. In FELs, relativistic electrons are sent through an undulator in which they emit a coherent pulse, tunable in wavelength (by changing the electron initial energy) from microwaves to X-rays [5, 11, 12] at unprecedented intensities. A single 10 to 100 fs FEL pulse can contain 10^{13} photons, the same amount produced by the best synchrotrons during *one second* [13]. Even though FEL installations require large facilities, some researchers are working on a smaller version, as "short" as 55 meters [14].

At shorter wavelengths, treating the laser as simply an electromagnetic field during ionization is no longer valid and photons must be considered. The Keldysh parameter γ dictates which ionization regime must be considered. In cases where $\gamma \ll 1$ the electric field of the laser is strong enough that the ion's Coulomb potential is distorted to such an extent that electrons can tunnel out. However, when $\gamma \gg 1$ the laser frequency is too large compared to the field's strength. Ionization is then dominated by single (or a few) photon absorption. Experiments in 2002 [15, 13] at DESY's FLASH (**F**ree-electron-**Las**er in **H**amburg) on xenon clusters in the VUV regime (98 nm wavelength, 12.65 eV

photon energy) had γ values between 8 and 100, putting it in the regime dominated by photon processes. During these experiments, unexpected high charge states were seen that could not be explained by traditional energy transfer mechanisms. Theoretical work was then performed to explain these high charge states; these models will be covered in chapter 1.2.

At shorter wavelengths, argon clusters were studied in the XUV regime [16]. The 32.8 nm (37.8 eV) photons are 22 eV above argon's first ionization potential and 10.2 eV above the second. It was found that ionization is a multistep process of photo-electrons emission and because of the subsequent charge buildup in the cluster, the electron energy distribution is non-thermal.

In 2006, a proof-of-principle experiment showed that it is possible to do (soft) X-ray diffraction imaging using FLASH pulses [17]: Chapman *et al.* were able to image a micrometer-wide stick-figure pattern engraved on a 20 nm thin film. Imaging was possible even though the sample was eventually destroyed by the high intensity X-ray laser pulse. Similar studies on xenon clusters were performed in 2010 [18] where diffraction patterns were obtained for clusters in single laser shots at 13 nm (95.37 eV).

More multiphoton ionization experiments on nitrogen, argon, neon and helium were performed at FLASH. For the even shorter wavelength of 13.7 nm (90.5 eV), xenon clusters irradiated at 7.5×10^{15} W/cm^2 produced charged states of up to 21+ [19, 20], meaning 60 XUV photons had to be absorbed per atom. Xenon's giant 4d resonance is suspected to be the cause of these high charge states.

The Linac Coherent Light Source (LCLS) at SLAC, Stanford, is another important FEL facility where the first FEL hard X-rays lasing was performed in 2010 [21, 22]. Single Neon atoms were studied with this hard X-ray source [23] showing fully stripped neon nucleus. Later, protein nanocrystallography was performed on photosystem I in 2011 [24] and on photosystem II in 2013 [25]. These two large cell membrane proteins are implicated in photosynthesis of algae, plants, and some bacteria. By using pulses shorter than the explosion time scale, the protein's structure could be reconstructed, opening the door for determination of the biomolecular structure that does not crystallize correctly for use in traditional crystallography studies. In the same Nature issue, mimivirus, the second largest known virus at 450 nm of diameter, was imaged using single shot hard X-ray pulse (0.69 nm, 1.8 keV) [26]. LCLS pulses have a duration of 70 to 500 fs at wavelengths of 0.15 nm to 2.2 nm [27].

Cluster studies continue to this day in regimes such as VUV [28], XUV [29, 30, 31]

and X-rays [32, 33, 34] and there is much theoretical work to be done as new phenomena are uncovered.

1.2 Microscopic mechanisms underlying cluster dynamics

Interaction of light with single rare gas atoms is a well studied problem but the collective effects of the high density of atoms in a cluster gives rise to many mechanisms of energy absorption and redistribution throughout the cluster. This chapter will cover the different mechanisms by going over the different wavelength regimes, from the long wavelength (IR) to the shorter XUV.

The different mechanisms described in this chapter can be sorted into two main families. First, the laser-driven, or laser-particles, mechanisms are the simplest as they are the result of the direct interaction between laser and particles. They are normally described using isolated atoms but can be adapted to take into consideration the cluster environment; see chapter 2.4.2 for details. For example, single-photon ionization where one photon is absorbed by a bound electron and gets promoted to the continuum is a direct interaction between laser and atom.

The second family consists of indirect mechanisms where particle-particle interaction is vital. These indirect mechanisms do not necessarily transfer energy from the laser to the cluster but are still an important aspect of cluster dynamics as they can affect energy absorption and charge state spectra. For example, impact ionization where an electron hits an atom and promotes a bound electron to the continuum by sharing some of its kinetic energy is independent of the presence of a laser (but obviously still requires free electrons). As will be described later, indirect mechanisms are still important for the cluster dynamics and can also help energy transfer from the laser to the cluster.

The cluster environment, due to the large particle density, has an important influence on both the laser-driven and particle-particle interaction, and on aspects of incorporating its effect on laser-cluster interaction. It is a substantial aspect of the current work.

Most studies on clusters are performed on femtosecond IR laser pulses that span a large range of intensity. This type of laser is widespread and dominated by Ti:sapphire lasers, which are pumped with another laser. Pump lasers include Na:YVO_4 or Nd:YAG, the latter which lases at 1064 nm and is frequency-doubled to 534 nm in a nonlinear crystal. The Ti:sapphire then emits 800 nm light with a wide range of intensity.

The advance of Free-Electron Lasers (FEL) allowed high intensity of VUV, XUV and even X-ray laser source. As described previously, FEL require large facilities, mainly

due to the linear particle accelerator required to seed the undulator with relativistic electrons and as such are scarce. Nevertheless their tunable wavelength allows them to access different interesting regimes.

The different regimes are shown in figure 1. The vertical axis shows the different regimes as function of wavelengths. They will be presented, in the following subsection, in order of wavelength, from longest to shortest. At each regime, dominant processes will be presented.

As can be seen in figure 1, the laser's intensity also dictates the regime. The Keldysh adiabatic parameter γ separates regimes where ionization processes are dominated by either photons or field [35] and reads

$$\gamma = \sqrt{\frac{\mathrm{Ip}}{2U_p}} = \frac{\omega}{\omega_t}, \tag{1}$$

where Ip is the atom's ionization potential, U_p is the ponderomotive energy

$$U_p = \frac{e^2 E^2}{4m\omega^2}, \tag{2}$$

e and m the electron's charge and mass, E the laser's electric field strength, ω its angular frequency and ω_t the tunnelling frequency:

$$\omega_t = \frac{eE}{\sqrt{2m\mathrm{Ip}}}. \tag{3}$$

When $\gamma \ll 1$, the laser field strength is large compared to the ionization potential. In that case, a bound electron will experience a significant bending of the atomic potential and will thus have a significant probability of tunnelling out. For this to happen, the ionization potential Ip must be smaller than the ponderomotive energy U_p. Figure 1 shows, as dashed lines, constant values of the ponderomotive energy. The plain line shows a ponderomotive energy value equal to the (first) ionization potential of xenon. The field dominated regime lies under this line.

Otherwise, when $\gamma \gg 1$, the laser field strength is weak compared to the ionization potential and the latter is not as important as before in the subsequent dynamics. The amplitude of the electron's quiver motion in the laser field is given by

$$x_q = \frac{F}{\omega^2}, \tag{4}$$

where F is the force of the laser field and ω its angular frequency. When $\gamma \gg 1$, the quiver amplitude x_q is minimum; the electric field oscillates too rapidly for the electrons to perceive it and photon interaction with the cluster is thus dominant.

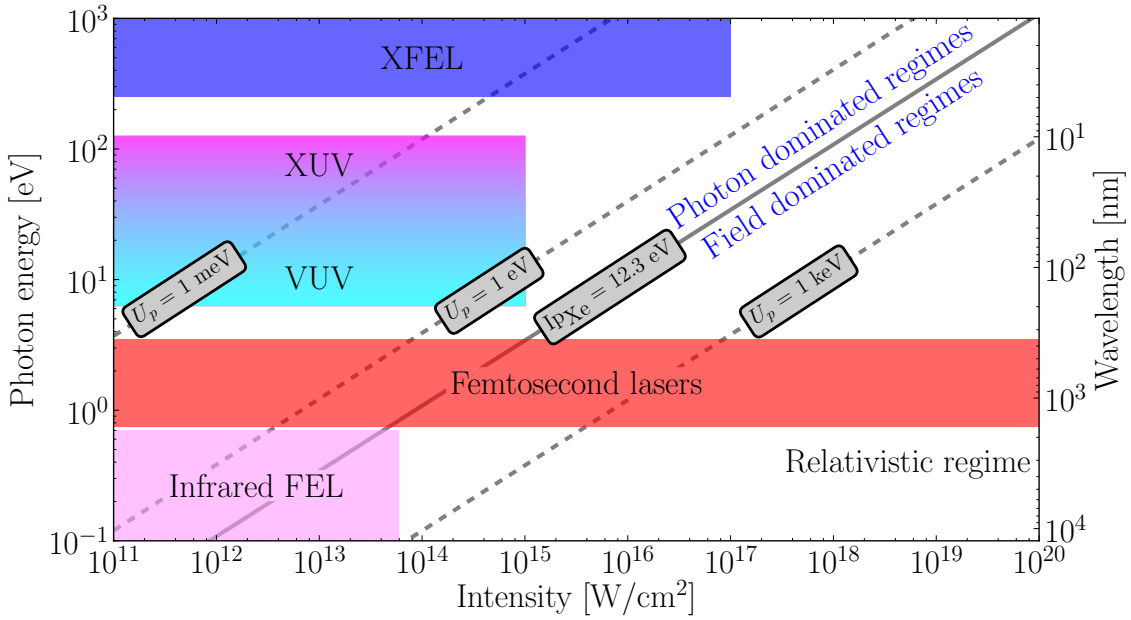

Figure 1: Wavelength and intensity regimes. For xenon, the lower right half is dominated by field processes and the upper left half by photon processes. Diagonal lines represent constant ponderomotive potential U_p. The demarcation between the two halves occurs when the ponderomotive potential equals the ionization potential ($U_p = Ip$). Note that the present work concentrates on the VUV and XUV regimes where photon processes dominate (at the studied intensities).

Note that the two regimes are not clearly segregated; Keldysh parameter predicts which process will dominate – photon or field processes – but both can occur. Photon processes could happen in the field-dominated regime and the laser field can still move electrons around in the photon-dominated regime.

In table 1 the first ionization energies of the different rare gas elements used in this thesis (argon and xenon) are shown. As can be seen from table 1 and figure 1, xenon and argon can be single-photon ionized in the VUV regime where photons of 15.76 (for argon) and 12.13 eV (for xenon) are possible. While xenon's 5p states have the smallest Ip's, the cross-section for photoionization of the 4d shell is approximately ten times larger at 13.7 nm (90.5 eV) – the so called xenon giant 4d resonance [36] – making ionization of these inner-shells possible [37, 38].

Let us now turn to a more detailed examination of the different mechanisms present in the different regimes, as well as some regime-independent processes.

	Argon			Xenon		
Z	Configuration	Ip [eV]	λ [nm]	Configuration	Ip [eV]	λ [nm]
0	$3p^5$	15.7596109	78.6721	$5p^6$	12.129843	102.214
1	$3p^4$	27.62967	44.8736	$5p^5$	20.975	56.4
2	$3p^3$	40.735	30.4368	$5p^4$	31.05	39.9305
3	$3p^2$	59.58	20.8097	$5p^3$	42.20	29.3801
4	$3p^1$	74.84	16.5666	$5p^2$	54.1	22.9176
5	$3s^2$	91.290	13.5814	$5p^1$	66.703	18.5875
6	$3s^1$	124.41	9.96577	$5s^2$	91.6	13.5354
7				$4d^{10}$	105.978	11.699
8				$4d^9$	179.84	6.89414
9				$4d^8$	202.0	6.13783
10				$4d^7$	229.02	5.41368
11				$4d^6$	255.0	4.86213
12				$4d^5$	280.9	4.41382
13				$4d^4$	314.1	3.94728
14				$4d^3$	342.9	3.61575
15				$4d^2$	374.1	3.3142
16				$4d^1$	403.9	3.06968

Table 1: First few ionization potentials for (atomic) rare gas elements. Source: NIST [39]

1.2.1 Long wavelength: The IR regime

Most femtosecond lasers are Ti:sapphire lasers that have a wavelength centred around 800 nm. This type of laser sparked cluster research. They cover a wide range of intensity and as such can touch different regimes, from the photon-dominated at low intensities to the field-dominated at higher intensities, even going up to levels where relativistic effects cannot be neglected.

Much work was done in the field-dominated (IR) regime over the years as evidenced by the wide literature on the subject, see for example reference [8] or [40]. The VUV and XUV regime – the photon-dominated one – is much less explored and is thus the main aspect of the present work. Some effects in the IR are still presented here for clarity. These processes are dominant in the field-dominated regime (see figure 1).

Above Threshold Ionization (ATI)

Above Threshold Ionization (ATI) was one of the first observed effects of intense laser-matter interaction in 1979 [41]. In ATI, more photons are absorbed by atoms than are normally required to ionize it. This results in photoelectron spectra showing peaks at energies much larger than expected separated by the photon energy. Being a multiphoton process, ATI requires large intensities ($\gamma \ll 1$) [42, 43].

Tunnel ionization

The most striking effect in the IR regime is tunnel ionization [44]. The Coulomb potential of an atom can be bent enough by the (oscillating) laser field and the probability of a bound electron tunnelling out becomes significant, as shown in figure 2. Tunnel ionization is also sometimes called optical field ionization (OFI), or more simply field ionization, since one can describe the process as the laser field being the source of the potential bending and ionization.

Tunnel ionization is at the heart of High Harmonic Generation (HHG) and attosecond science [8]. A laser pulse, normally in the IR regime, bends the atomic potential felt by bound electrons, allowing them to tunnel out. They are then accelerated in the laser field where they gain energy. As the laser field changes direction within a laser cycle, electrons are forced back onto their parent ion where they can recombine and emit high energy photons. The emission spectra, containing only odd harmonics, shows an intensity

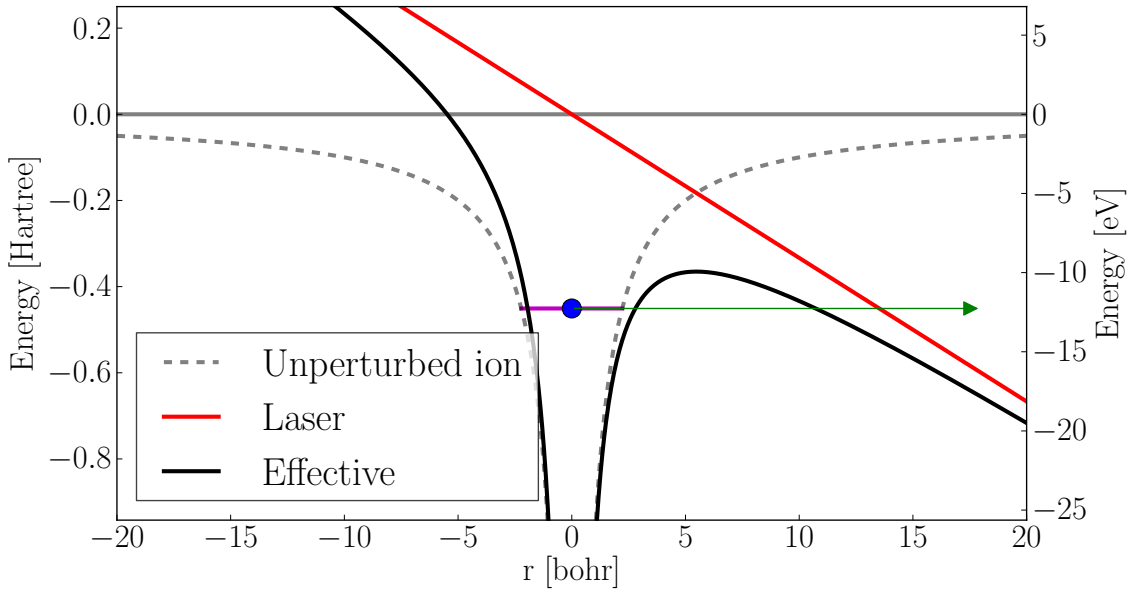

Figure 2: Tunnel ionization. The potential due to the laser (red) bends the unperturbed ion potential (grey dashed). The electron (blue dot) sitting at the unperturbed eigenvalue (magenta) now has a probability to tunnel through the total potential barrier (black line). The laser frequency must be small enough for the probability to be non-negligible (large wavelength) and intensity large enough ($\gamma \ll 1$).

decrease as a function of harmonic number, followed by a plateau and a cutoff. Since the description of the phenomena in 1993 [45], HHG studies expanded into its own sub-field. For example, Murphy *et al.* used the 21st harmonic of a 800 nm Ti:sapphire to ionize xenon clusters [29, 30] with these new 32.6 eV (38 nm) photons. For more details on HHG see references [6] and [43].

Inverse Bremsstrahlung Heating

Once electrons are created in the IR regime they can continue to absorb energy from the laser. Inverse Bremsstrahlung Heating (IBH) is the inverse process of Bremsstrahlung where an electron emits a photon when deflected, either by a heavier ion in the case of plasma, or by magnetic fields in the case of synchrotrons. IBH is thus the absorption of photons accelerating the electrons [46].

For large frequencies, the quiver amplitude of equation (4) is small; the electric field oscillates too rapidly for the electrons to gain significant acceleration. But for smaller frequencies (larger wavelengths), the quiver amplitude can be significant. In the case of IR, electrons can be pushed outside the cluster and back in; at 3×10^{16} W/cm^2 and 800 nm, the quiver amplitude is $x_q \approx 500 a_0$, where a_0 is the Bohr radius [47], while a $Xe_{1,415}$ cluster is 115 a_0.

The linear momentum gained by electrons in the laser field is then redistributed as thermal energy by collisions and scattering on heavier ions. IBH plays an important role in the IR regime where the laser field easily drives the electrons through the cluster [8].

The rate of change of energy E over time due to IBH (per electron) is given [8] by:

$$\left\langle \frac{\mathrm{d}E}{\mathrm{d}t} \right\rangle = 2U_p \frac{\tau\omega^2}{\tau^2\omega^2 + 1}, \tag{5}$$

where τ is the inverse of the electron-ion collision frequency, ω the angular frequency of the laser and U_p the ponderomotive potential.

1.2.2 Shorter wavelengths: Into the VUV and XUV regime

With new FEL facilities, high laser intensities can be reached at lower wavelength (and thus larger photon energy) than traditional femtosecond lasers. *Vacuum ultra-violet* (VUV) radiation, ranging from 200 to 10 nm (6.2 to 124 eV), is normally absorbed by the atmosphere. Its study requires vacuum chambers (hence the name) or a pure nitrogen propagation medium. At short wavelengths, the photons can start to ionize

inner shell electrons. In that case, the term *extreme ultraviolet* (XUV, or EUV) is used. XUV wavelengths range from 121 nm (hydrogen's Lyman alpha line, 10.25 eV) to 10 nm (124 eV). As the two regimes have overlapping wavelengths, they are often used interchangeably but XUV is generally used with wavelengths where no material is known to be transparent [48]. Note that in other fields, XUV can be used to describe soft X-rays [49, 50]

At relatively low intensity (less than 10^{14} W/cm^2 [40]), in the photon-dominated regime, atoms and ions can be ionized by photon absorption. If the photon energy is superior to the electron's binding energy (see table 1 for numerical values) single photon ionization will be the dominant energy transfer mechanism.

While not as strong as in the IR regime, IBH is still important in the VUV [51] up to 62 nm [47].

Photon absorption

Initially described by Einstein as the photoelectric effect, a bound electron absorbs a photon from the laser and is promoted to the continuum where it is free to leave its parent ion. Figure 3 shows a schematic of the mechanism. For example, the first energy level of atomic xenon is at -12.27 eV, requiring a photon wavelength equal or shorter than 101.1 nm for ionization.

If the photon energy exceeds the electron's binding energy, the difference in energy will be transferred as extra kinetic energy in the resulting photoelectron. Thus, it can be used to sample the states in the target by measuring the photoelectron energy spectrum [8].

However, if the photon energy is less than the binding energy, then a single photon cannot ionize an atom. But if the intensity is large enough, the photon density will be sufficient that many photons can be absorbed during a small time interval. This effect is called multiple-photon ionization (MPI, not to be confused with the Message Passing Interface used in parallel programming) and is a non-linear process. The ionization rate of ν-photon MPI is given by [8]:

$$\Gamma_\nu = \sigma_\nu I^\nu. \tag{6}$$

Being a nonlinear process, multi photon ionization becomes significant at higher intensities than single photon ionization. But being photon processes, both are superseded by tunnel ionization at even higher intensities (or when $\gamma \gg 1$).

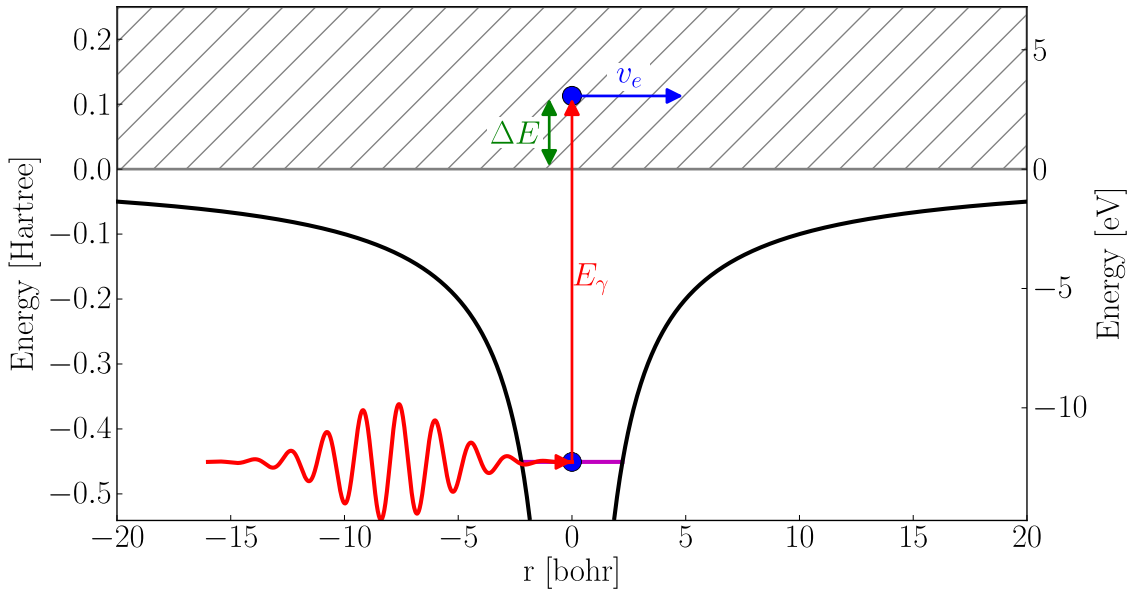

Figure 3: Single photon ionization for the atomic, isolated model. A photon (red) is absorbed by a bound electron (blue) which is promoted to the continuum. The remaining energy ΔE between the photon's and the Ip results in electron's kinetic energy K_e. Chapter 2 describes the cluster environment influence.

Auger effect

At even shorter wavelength, the photon energy might be large enough to not only ionize the highest energy electron but also some inner-shell electrons. When such an inner shell electron gets ionized, it leaves a hole; the atom is thus in an excited state. An outer shell electron will then transition by *Auger decay* to the hole. The transition energy is used by a third electron (the Auger electron) to leave the ion, leaving the latter doubly-ionized. Figure 4 shows a diagram of the process.

To access core electrons, photons must be highly energetic, as usually found in X-rays. While not the focus of the present work, an interesting aspect is that xenon atoms have a giant resonance of the (inner-shell) 4d state; the cross-section of photoionization of the 4d electron is ten times larger than the one of valence electrons at 13.7 nm wavelength (90.5 eV) [36]. This process was included in the model for a comparison with a 2009 experiment by Thomas *et al.* [37] on xenon clusters at FLASH-DESY. The German group saw clusters becoming nanoplasmas from which the outer shell ions undergo Coulomb explosion while the relatively neutral core expands hydrodynamically. These results could be reproduced by our model as shown in a recently published article entitled

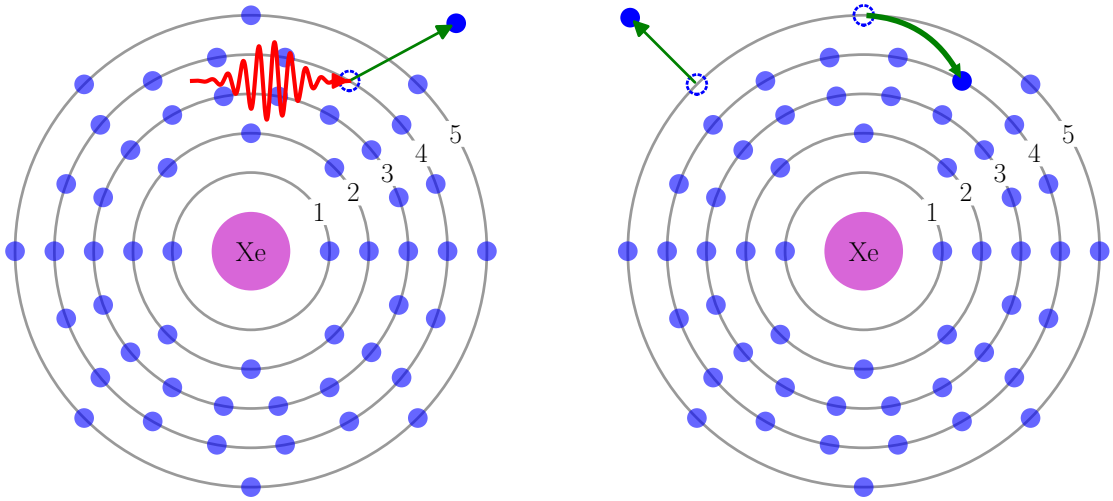

(a) Step 1: An xenon 4d inner shell electron absorbs a high energetic photon and leaves the atom.

(b) Step 2: An outer shell electron decays into the created hole, transferring the energy difference between the two states to a third electron which is ejected (the Auger electron).

Figure 4: Auger ionization of a xenon 4d electron by a high energetic X-ray photon. Xenon's 54 electrons are shown as blue dots with the distance to the core representing their principal quantum numbers n.

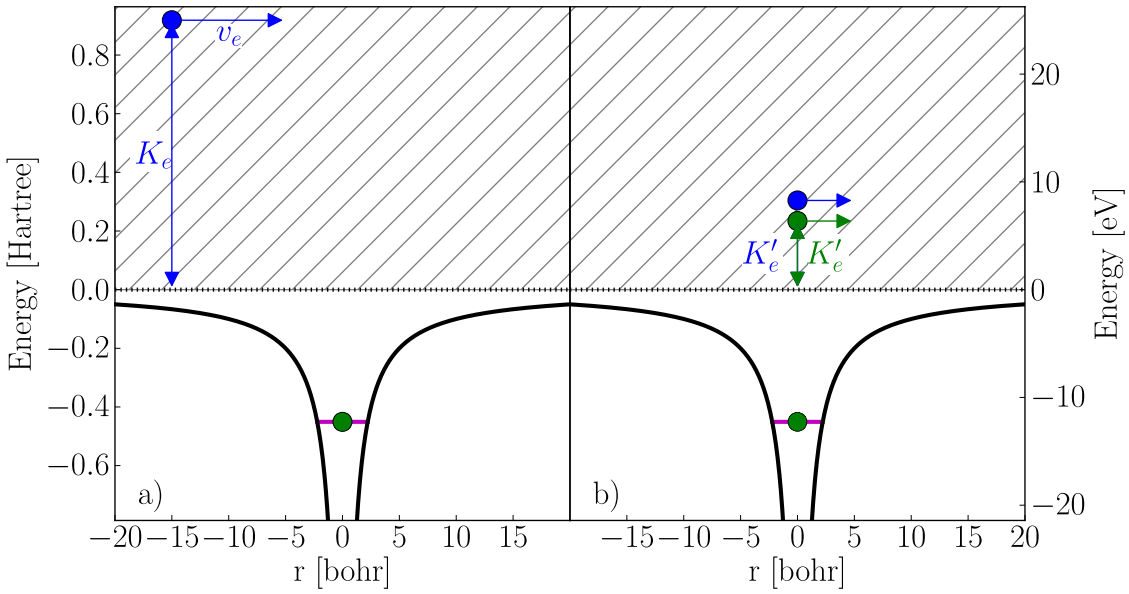

Figure 5: Impact ionization. The colliding electron (blue dot) gives a portion of its energy to a bound electron (green dot), promoting it to the continuum.

"Recombination effects in soft-X-ray cluster interactions at the xenon giant resonance", published in May 2013 in *New Journal of Physics* [38] and included in chapter 6.

1.2.3 Regime independent processes

Once electrons are created in the cluster, other mechanisms appear. During impact ionization a first electron collides with an atom and, if it has enough kinetic energy, will transfer a portion of it to a bound electron, promoting it to the continuum. Figure 5 shows the energy diagram of the process.

Impact ionization can be modelled through cross-sections. These cross-sections are normally obtained from the semi-empirical Lotz formula [52]:

$$\sigma = \sum_i^N a_i q_i \frac{\ln\left(E/\mathrm{Ip}_i\right)}{E\mathrm{Ip}_i}\left(1 - b_i \exp\left\{-c_i\left(E/\mathrm{Ip}_i - 1\right)\right\}\right), \tag{7}$$

where Ip_i is the ionization potential of the i^{th} shell and E the impacting electron's kinetic energy *at infinity* (or above threshold).

1.2.4 New regime, new processes

By going to shorter wavelengths, FEL installations allowed experiments at high intensities in the VUV and XUV regime. These experiments saw surprisingly high charge states

resulting from the cluster explosion [15, 18]. For example, Wabnitz *et al.* saw, at FEL-DESY, Xe^{4+} when Xe_{80} clusters were irradiated with 98 nm, 100 fs FEL pulses of, what was thought at the time, 2×10^{13} W/cm^2 intensity. For larger clusters ($Xe_{30,000}$), xenon ions up to Xe^{8+} were observed. This was surprising as the 98 nm photons (12.7 eV) could only ionize neutral xenon to Xe^{1+} by themselves; data showed that up to 30 photons were absorbed per atom for the largest clusters. Using a different source of photons and at a different wavelength (21st harmonic of an 800 nm Ti:sapphire, XUV: 32.6 eV, 38 nm), Murphy *et al.* observed the same pattern of high charge states in xenon clusters [29, 30].

Such high charge states could not be explained by the previous processes only. New mechanisms were thus proposed to explain these surprising results. The four main models proposed throughout the years are covered next.

Atomic potentials

First, Santra & Greene proposed using *atomic potentials* instead of the Coulomb potential in a rate equation model (with infinite spatial extension and constant density) as seen in figure 6a. The atomic nucleus is normally shielded by bound electrons but inside the electronic cloud the shielding disappears and the nucleus potential is more important. If an impacting electron can get close enough to the core, it will feel the unshielded potential. In reference [53], Santra & Greene used an approximated form for the atomic potential, fitting one parameter with the first ionization potential. A later [54] publication used a potential shape generated by the code written by Herman and Skillman [55] (HS) to describe a more realistic potential, based on a Hartree-Fock formulation. Using these atomic potentials, they saw Xe^{3+}, Xe^{5+} and Xe^{7+} for intensities of 1.4×10^{12}, 1.4×10^{13} and 7.3×10^{13} W/cm^2 respectively for $Xe_{1,500}$ clusters, similarly to what was seen in at FEL-DESY.

Barrier suppression

Another model proposed by Siedschlag and Rost [56] in 2004 was the barrier suppression in single photon absorption which is shown in figure 6c. Due to the proximity of neighbours, the potential barrier between them is lowered and a photo-transition to the continuum becomes possible, even with a single photon.

Many-Body Recombination

Many-Body Recombination (MBR) was proposed in 2005 [57] as a simple mechanism to explain the high charge states seen in the experiments at FEL-DESY. In a strongly coupled plasma, electrons can recombine easily to a high excited state after collisions with numerous bodies. Later, these newly bound electrons can absorb a new photon from the laser field for another transition to the continuum – see figure 6b. Because MBR is much more efficient than three-body recombination (due to the large density of charged particles), much more photons are absorbed this way. It was also shown that MBR deposited more energy in the clusters than traditional IBH. The method's simplicity lies in the fact that in a classical MD simulation, MBR is automatically included without extra implementation as the high excited states have energies which are close to each other and can thus be treated classically. Jungreuthmayer *et al.* were able to see Xe^{3+}, Xe^{5+} and Xe^{7+} for intensities of 1.5×10^{12}, 1.5×10^{13} and 7×10^{13} W/cm^2 respectively when simulating $Xe_{1,000}$ clusters.

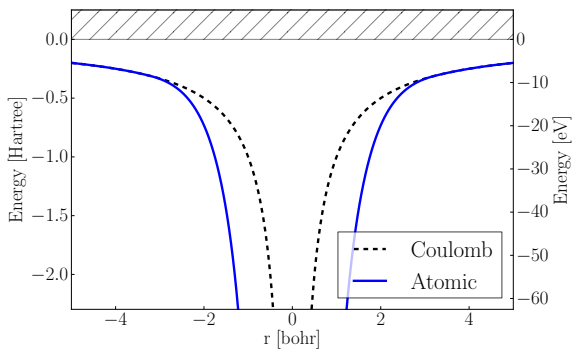

(a) Atomic potential (blue line) drops faster than Coulomb one (black dashed line), allowing more energy absorption through IBH.

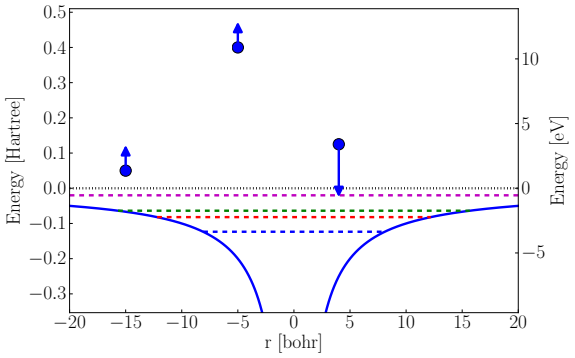

(b) MBR: energy exchange between free electrons during collisions makes one recombine to a highly excited state where it can reabsorb a new photon from the laser field.

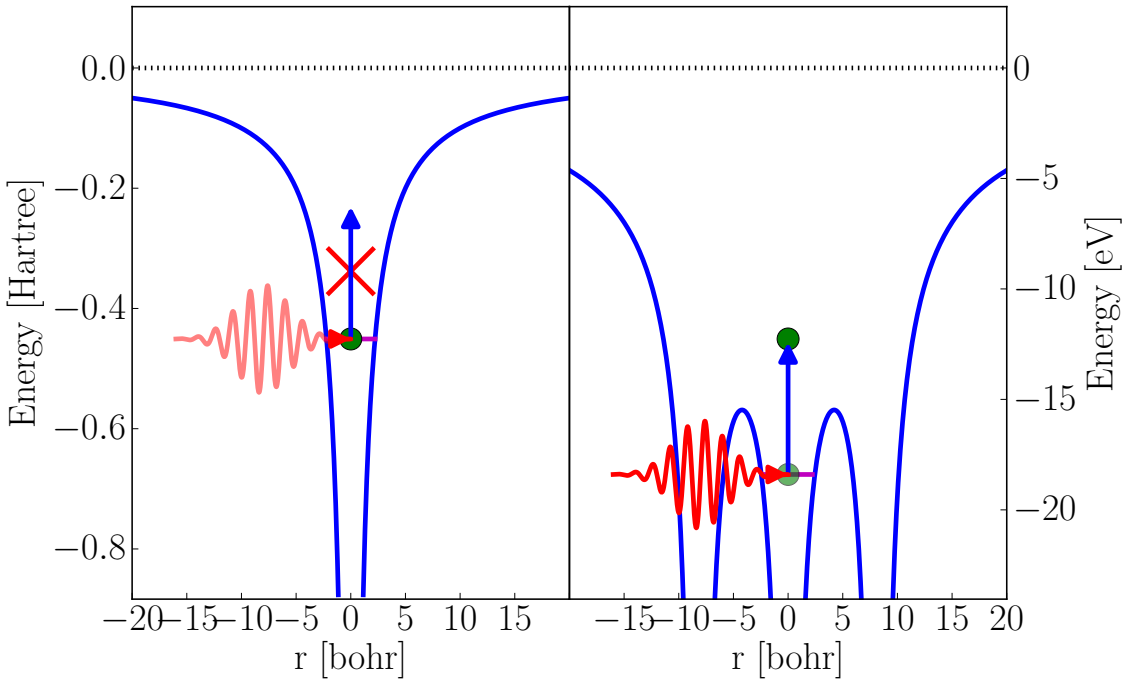

(c) Barrier suppression between ions in a cluster environment allows a single photon to ionize deeper levels (right), not accessible with a single atom (left).

Figure 6: More heating mechanisms

1.3 Contributions of thesis

This thesis' goal is better understanding of laser-matter interaction. More specifically, the question of *how* the energy is deposited in a nanoscale object –a rare gas cluster– by an ultra-short and ultra-intense laser pulse will be studied. This interaction largely depends on the specific target material and on the pulse's wavelength and duration, both defining the interaction regime. A specific regime will thus be targeted; mainly short wavelengths, from VUV to XUV, as many questions raising from recent experiments are still debated.

While many tools exist to study laser-matter interaction, only classical approaches can be considered since a full quantum calculation, even with some degree of approximations, is not possible. Clusters become nanoplasmas quite rapidly and have large charge and field fluctuations inside them. This and their finite nature makes it hard to use tools such as rate equations to model them. Pure classical simulations allow for relatively large systems to be simulated and are thus the tool of choice.

1.3.1 Tools

Chapter 2 describes the different tools and models that were developed and implemented to answer our questions. While chapter 2.1 concentrates on the classical aspect of the problem, chapter 2.5 describes in detail use of a quantum approach named QFDTD for Quantum Finite-Difference Time-Domain. Note that all implementations used are original work; all code packages were developed from scratch by me or under my direction and no external packages were used. The MD package described in chapter 2.1 ($\sim$16k lines of code) contains 86 % of code written by me, 12 % by Edward Ackad (postdoctoral fellow) and smaller contributions from Julien Roy (undergraduate student) during his summer 2012 internship. Furthermore, the QFDTD package ($\sim$16k lines of code) contains 3 % of code written by Stan Hatko (undergraduate student) while the rest is my original work. Most tools were written in C++ with Python being used for analysis and plotting.

For libraries described in chapter 2.7, 79 % of the ionization library was written by me, 20 % by Edward Ackad with smaller contributions from Stan Hatko during his summer 2012 internship. All other libraries described in chapter 2.7 were fully written and developed by me.

These powerful tools were extremely useful and will allow the group to continue its investigation of laser-clusters interaction after my departure.

In addition to the models described in chapter 1.2, a notable new one was developed that revealed itself to be of great importance in the description of laser-clusters

interaction. This new model is discussed next.

1.3.2 Augmented Collisional Ionization (ACI)

Wabnitz's *et al.* experiments at FLASH-DESY in 2002 revealed the interestingly high charge states in xenon clusters. Since then, different groups proposed models to explain these results as described in chapter 1.2.4. Then, in 2010, Bosted *et al.* re-calibrated the intensity used during the 2002 experiments. Instead of the previously thought 2×10^{13} W/cm^2, the intensity was re-calibrated to 8×10^{12} W/cm^2, less than half of the initial value. Additionally, the largest clusters were tripled in size, from $Xe_{30,000}$ to $Xe_{90,000}$. Could the different models still produce the same amount of high charge states at the new, lower intensities?

Additionally, in 2008, experiments [16, 30] were performed in the XUV regime near 30 nm (41 eV). At this wavelength, the photon energy is too small for inner shell ionization of rare gas atoms, yet too large (at reported intensities) for any appreciable laser-field-driven processes, such as collisional heating, that dominate intense laser-cluster interactions at longer wavelengths. This presents the opportunity to isolate the influence of the internal electronic structure from the laser-cluster interaction.

Our group thus proposed a new mechanism for energy transfer from the laser field to the cluster via two-step collisional ionization. With this two-step model, an electron might not have enough kinetic energy to directly collisionally ionize an atom (or ion), but it could still transfer some of its energy to promote a bound electron to an excited state. Once an atom is excited, it is easier to ionize, due to the large cross-sections of excited atoms and ions, by subsequent impact from a low energy electron. This provides the opportunity for low energy electrons to still participate in the cluster ionization, giving the name *augmented collisional ionization* (ACI) to the process.

Figure 7 shows an energy diagram of ACI and the different transitions possible. This two-step model is implemented using cross-sections for collisional transition (ground state to excited state and excited state to continuum), similarly to traditional impact ionization. See chapter 2.4.4 for more details on cross-sections.

The ACI model revealed to be an important contribution to the field. As will be seen from the publications, experimental results can be reproduced with this model.

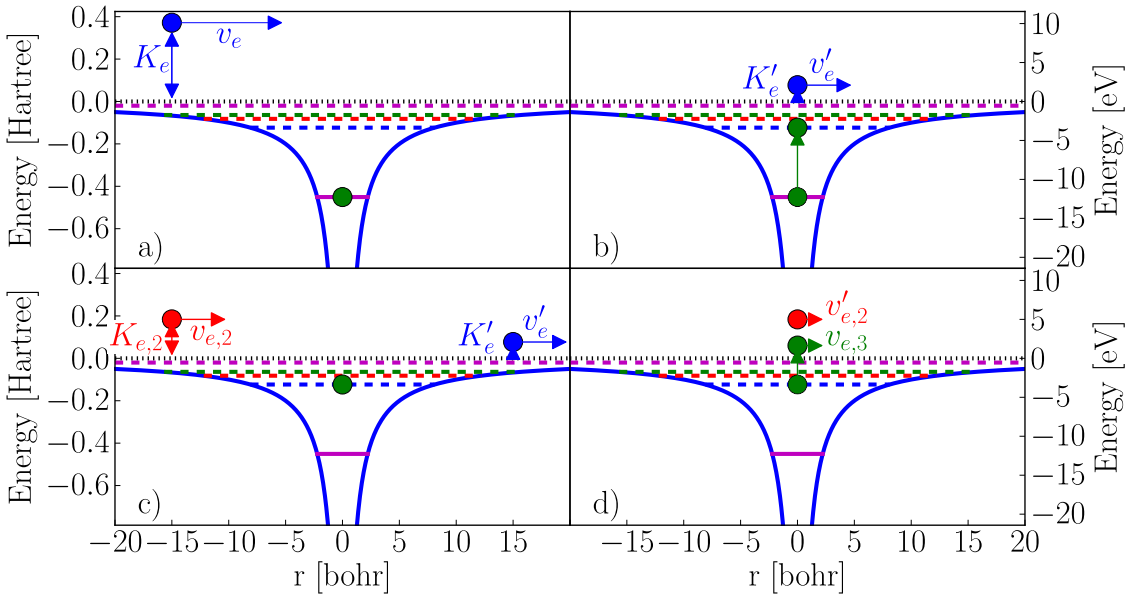

Figure 7: ACI. First electron (in blue) collides with ion in a) and gives $K_e - K'_e$ of energy for the transition of a bound electron (in green) from the ground state in a) to an excited state in b). That first electron is thus slowed from v_e in a) to v'_e in b). A third electron (in red) collides with the ion in c) and gives the remaining kinetic energy required for the transition to continuum in d). The first step is a) to b) and the second step is from c) to d).

1.3.3 Publications

After the tools are presented in chapter 2, the present thesis consists of a series of four published articles and one article in preparation where the models and tools are tested and used.

ACI introduction paper

The work on excited states and ACI in clusters was first published in "Augmented collisional ionization via excited states in XUV cluster interactions" published in 2011 in *Journal of Physics B: Atomic, Molecular and Optical Physics* [58] and can be found in chapter 3 (page 62). Argon clusters (Ar_{80} and Ar_{147}) were simulated with parameters used in experiments at FLASH-DESY in 2008 by Bosted *et al.* [16]. (32.8 nm – 37.8 eV, 25 fs and intensities from 5×10^{13} to 10^{14} W/cm^{-2}). It was found that not only could ACI explain the Ar^{4+} seen at FLASH but that it was also a dominant process, happening more often than traditional impact ionization. Due to the efficiency of ACI, high charge states can be reached in shorter time than previously thought which can have a significant impact on biomolecules imaging. This first ACI article was a stepping stone in the current work as it showed the validity of the model, as simple as it could be.

Cluster size influence

Chapter 4 presents the article "Clusters in intense XUV pulses: Effects of cluster size on expansion dynamics and ionization". Also published in 2011 (*Physical Review A* [59]), argon clusters were simulated in the XUV regime (32.8 nm, I = 5×10^{13} W/cm^2, 25 fs) with cluster sizes from Ar_{55} to $Ar_{2,057}$. It was found that the dynamics are highly collisional and larger clusters even more so. By rapidly ionizing the lower charge states, collisional processes will prevent photo-ionization even before the laser pulse ended. This mechanism was called *collisionally reduced photoabsorption*. The amount of energy absorbed through photo-ionization by Ar_{55} clusters was reduced by 30 % and 45 % by $Ar_{2,057}$ clusters when collisional processes are included. Higher charge states are more abundant and also appear sooner during the dynamics in large clusters compared to smaller ones. ACI is vital for the description; 20 % of ions are in an excited state after the laser peak. During the laser pulse, the distribution of charge inside clusters is relatively isotropic but as the simulation evolves, the clusters' outer shells tend to lose electrons more than the

core and eventually disintegrate through Coulomb explosion. The core stays relatively neutral and expends thermodynamically.

The ion kinetic energy distribution revealed that Ar^{2+} provided most of the high energy tail. Additionally, the highest charge states had the least energy. The highest charges states being created in the (neutral) core, the electrons shield these high charge states, preventing them from accelerating as much as the outer shells ions.

Electrons thermalize rapidly to a Maxwellian distribution. The larger clusters' distribution are isotropic due to the high collisional rates while smaller clusters keep the anisotropy coming from photoionization.

Revisiting the 100 nm experiment

Chapter 5 contains the draft of the article "Augmented Collisional Ionization in the VUV regime; a theoretical study". After Wabnitz *et al.*'s 2002 DESY-FEL experiment's intensity was re-calibrated in 2010, we hypothesized that our ACI model could still explain the high charge states seen in xenon clusters, even with the lower intensities. Since the VUV (98 nm, 12.65 eV) photons cannot ionize a Xe^{1+} to Xe^{2+} (see table 1 for xenon ionization potentials), all charge states higher than Xe^{1+} must be created with other processes. We included single photon ionization, impact ionization, ACI and recombination in simulations of Xe_{80} to $Xe_{5,083}$ interacting with DESY's 100 fs laser pulse at different intensities. We compared our model with previous work with ACI disabled and found good agreement. The high performance of my code implementation (see chapter 2.6 on GP-GPU) allowed running thousands of MD simulations. The chaotic nature of the many-body problem requires acquiring vast amount of data for valid statistics, giving more weight to our results. On average, it was found that two more charge states are accessible when ACI is enabled, a clear indication that ACI has a central role amongst the ionization channels.

Due to the spatial intensity profile of the laser pulse, simulations were run at different intensities to simulate the effect of experimental data acquired from clusters dispersed in the laser's spatial profile. This improves the validity of simulation data when comparing with experiments. Our data was in good agreement with the 2002 experiment. Both the dominant charge states and the highest charge states matched the experiment data. This was not the case of other models which used the old intensity.

The last part of the article discusses the influence of the potential depth of equation (22). By allowing deeper potentials in our simulations, it was hypothesized that

larger charge states could be obtained. The influence of the potential depth used in simulations is often neglected in the literature. That article section sheds some light on the topic. Since electrons are now allowed to go deeper in the ions potential well, recombination must be used to prevent them from having a total energy less than the ion's eigenvalues which would not be allowed according to quantum mechanics.

Recombination

Finally, chapter 6 presents the article "Recombination effects in soft-X-ray cluster interactions at the xenon giant resonance" published in May 2013 in New Journal of Physics.

Xenon atoms, centred at around 13 nm (95.4 eV), have a photoabsorption cross-section approximately ten times larger for the 4d electrons than for the outer-most shell 5p electrons; inner shell ionization is thus possible and Auger processes create highly charged ions, even in the case of xenon gas [60].

In experiments at 13.7 nm (90.5 eV) by Thomas *et al.* in 2009 [37], the amount of Xe^{1+} observed in clusters was significantly more than in xenon gas, indicating that recombination effects were important. At the time, it was clear that photoabsorption and recombination alone could not explain by themselves these results.

Thomas *et al.*'s experiment was described using our models. Xenon clusters of sizes 147, 1,415 and 5,083 were simulated under a 13.7 nm (90.5 eV) laser at different intensities from 1×10^{11} to 5.8×10^{14} W/cm^2. Time-of-flight spectra were in good agreement with the experiment. We also saw that the higher charge states came from the clusters' outer-shells while the lower charged ions came from the clusters' core. Even though ions in the neutral core can reach high charge states, they recombine quickly to lower charge states. The expansion of ionized clusters is best described by a Coulomb explosion of the outer-shells and a hydrodynamically expending neutral core.

A quantum approach

Going further, interesting questions came up. For example, how is a bound electron's wavefunction affected by a neighbouring ion or the cluster potential? From my background in electromagnetic simulations, I was surprised to read an article using the FDTD method – normally used in electrodynamic simulations – for quantum calculations. I was curious how far could the FDTD method be applied to quantum problems and if it could

answer some of our questions. A QFDTD simulation package was thus developed, again from scratch, implementing two kinds of time evolution; real and imaginary. The model and its implementation details are discussed in chapter 2.5.

The work developed in chapter 2.5 was published in the article "Nonlinear grid mapping applied to an FDTD-based, multi-center 3D Schrödinger equation solver" presented in chapter 7. Published in 2012 in *Computer Physics Communications* [61], it explains the QFDTD method and its implementation, with emphasis on the new nonlinear mapping introduced for faster calculation. The QFDTD package is the first to use both the real and imaginary time evolution, opening the door to easier calculation of eigenvalues, eigenstates and their time evolution in a time-dependent and arbitrary spatial shape potential. The method was first validated by comparing with the analytic solutions of the hydrogen atom and then applied to solve the H_2^+ molecule. Comparison with experimental data was in good agreement for the eigenvalues while the eigenstates could be visualized easily. A new method to calculate eigenstates is also presented in the article. The publication also describes in detail the nonlinear mapping that allows reducing both the memory usage required to store the grid and the time required to calculate the time evolution. The method is a generic way to obtain a nonuniform grid with cells concentrated around multi-centres of interest for use in any (finite difference based) partial differential equation solvers.

The different methodology and tools used and developed throughout the years will be presented and discussed before referring to the publications stemming from this thesis' work.

2

Methodology and Tools

A large selection of methods exists to study laser-cluster interaction, differentiated by their amount of approximation.

An exact solution of the quantum mechanical system is generally intractable. Theoretical investigations thus require some degree of approximation, a compromise between feasibility and exactitude. On one end of the spectrum, the most general methods involve solving the Time-Dependent Schrödinger Equation (TDSE) directly and Quantum Monte-Carlo (QMC) methods [62]. Unfortunately, these methods can only be applied to the simplest systems of small numbers of electrons; clusters cannot be studied by these methods.

Larger systems can be studied using *ab initio* methods ("from first principles") which cover a wide range of techniques. This class of methods includes *Hartree-Fock* (HF) methods which consist of approximating the ground state wavefunction by a single Slater determinant [63, 64]. In HF methods, instantaneous electron-electron Coulomb repulsion is not included directly in the system's Hamiltonian. Instead, only the average field resulting from other electrons is used, giving the often used name of *self-consistent field* methods. Other *ab initio* methods are the *Post Hartree-Fock* methods where electron correlation is added [65]. An example is the *Configuration Interaction* (CI) method.

Because of their great accuracy, these methods are restricted to relatively small systems, generally less than 10 atoms. Full *ab initio* treatment of clusters is also not possible.

Larger systems require more approximations. *Density Functional Theory* (DFT) is an often used method for cluster studies requiring quantum aspects, with either quantum or semiclassical propagation [64, 8]. It begins by formulating an expression for the total energy of electrons and ions and derives static and dynamic equations from it. All approximations are done in the selection of this (energy) functional. The upper limit on these methods is of practical restrictions, mainly computational power available. Furthermore, because the chosen functional approximate the underlying quantum system, specific quantum effects might not be included; for example shell effects or tunnelling are neglected.

Because DFT methods are mean field in nature, they cannot account for the large field fluctuations seen in strong field cluster dynamics.

Continuing on the spectrum of methods, classical methods like Molecular Dynamics (MD) solve Newton equations of motion with any type of forces between particles [66]. When used in laser-cluster simulations, MD generally uses the instantaneous electrostatic (Coulomb) force between charged particles. MD codes have the advantage of being straightforward to implement and use, give macroscopic properties easily and allow a relatively large amount of particles to be simulated, while still allowing specific quantum treatment when necessary (for ionization events for example). For these reasons it is the method of choice for use in the present work.

A limitation of MD is that it cannot account for field propagation effects. For large clusters of more than tens of thousands of atoms, these effects can be significant. Particle-in-cell (PIC) methods, where particles interact with a grid propagating the electromagnetic field (through Maxwell's equations), is able to describe these retardation effects. PIC can be successful in modelling large clusters, but they tend to be more complex and lack the simplicity of MD. Additionally, because they model particles as having the same size as the underlying grid, they do not describe close range interactions. Nevertheless, Varin *et al.* developed a new method that adds microscopic corrections to PIC close range interactions [9]. With these microscopic corrections, collisions between particles are described similarly to MD, ensuring a better description of the dynamics. This MPIC method has great prospects as not only can it describe what MD does but can go further by including the electromagnetic field propagation and its effects. Additionally, its scaling allows it to describe larger clusters and it can be parallelized more easily than MD.

For smaller systems though, the complexity of PIC and MPIC and their grid's overhead give MD a clear advantage.

Some refinements to the MD algorithm allow it to be used for larger systems while still keeping the same underlying code structure. For example, organizing particles in a hierarchical tree [67, 68] can speed up the force calculation from a $O(N^2)$ scaling to $O(N \log N)$. More details on the tree algorithm is presented in chapter 2.3 (page 38).

On the end of the methods spectrum are rate equation methods. In these, an expression for the time dependence of some parameters is written down and solved, analytically or numerically. Too many approximations are made by rate equations for use in the current work. For example, they often assume an infinite bulk. They also cannot describe the large variation in field and charge present in the clusters.

For a detailed review of the different methods, see reference [8].

In the following chapter, the tools and their implementation applied in this thesis will be presented. Unless stated otherwise, all implementations are original and were done from scratch, except the Hartree-Fock-based Cowan code [69] used in the calculation of various required cross-sections.

2.1 Molecular Dynamics (MD)

Due to the high charge states seen in experiments with clusters the most practical method to microscopically study the ionization dynamics is *Molecular Dynamics* (MD) where ions and electrons are treated classically.

In MD, bodies interact directly through classical instantaneous forces. Even though the method's name contains the term "molecular", these forces can be of any nature; gravitational, van der Waals, Lennard-Jones, electrostatic, etc. The method numerically integrates Newton's equations of motion, resulting in a time evolution of the system.

The total force (from two-body interactions) acting on particle i of mass m_i from all other N particles in the system is:

$$m_i \mathbf{a}_i = \mathbf{F}_i = \sum_{j \neq i} \mathbf{F}_{j \to i}. \tag{8}$$

In the present work, the force between charged particles is the instantaneous electrostatic Coulomb force:

$$\mathbf{F}_{C,j \to i}(\mathbf{r}) = \frac{k q_i q_j}{r_{ji}^2} \hat{\mathbf{r}}_{ji}. \tag{9}$$

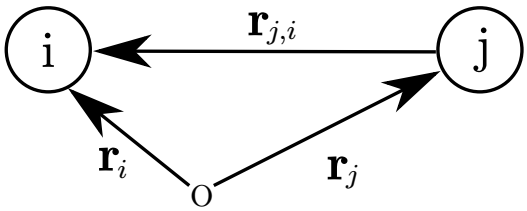

Figure 8: Vectors definition between particles i and j

which only depends on the distance $\mathbf{r}_{ji}$ between particles and the charge states Z_i of these particles $q_i = Z_i e_0$ (q_i is particle i's charge and e_0 is the elementary charge). In the case of electrons, the charge state is simply -1.

Calculating $\mathbf{F}_i$ from (8) and (9) requires one operation per particle present in the system; updating the force on one particle is an $O(N)$ operation (doubling the number of particles will double the required calculation time). Since there are N particles, calculating the force for all particles has a scaling of $O(N^2)$ (doubling the number of particles will quadruple the required calculation time). Some forces used in different research areas are short range and can then be cut off at a certain distance. This effectively reduces the scaling from $O(N^2)$ to $O(N)$ but the Coulomb potential, being long range, cannot be artificially cut off. Chapter 2.3 discusses a different algorithm that allows a reduction to $O(N \log N)$.

Figure 8 shows the vector definitions used throughout this work. We define particle i as the particle we are interested in (for example, the particle we are calculating the force on), and particle j the particle that is generating the field or potential that is measured at location of particle i. We thus have:

$$\mathbf{r}_j + \mathbf{r}_{j,i} = \mathbf{r}_i, \tag{10}$$

$$\mathbf{r}_{j,i} = \mathbf{r}_i - \mathbf{r}_j, \tag{11}$$

$$\hat{\mathbf{r}}_{j,i} = \frac{\mathbf{r}_{j,i}}{|\mathbf{r}_{j,i}|}. \tag{12}$$

Equation (8) can be time integrated for every particle i using the Velocity-Verlet (VV) scheme:

$$\mathbf{x}_i^{(n+1)} = \mathbf{x}_i^{(n)} + \mathbf{v}_i^{(n)}\Delta t + \frac{\mathbf{a}_i^{(n)}}{2}\Delta t^2, \tag{13a}$$

$$\mathbf{a}_i^{(n+1)} = \frac{\mathbf{F}^{(n)}}{m_i}, \tag{13b}$$

$$\mathbf{v}_i^{(n+1)} = \mathbf{v}_i^{(n)} + \frac{\mathbf{a}_i^{(n)} + \mathbf{a}_i^{(n+1)}}{2}\Delta t, \tag{13c}$$

where Δt is the integration time step, $\mathbf{x}_i$ the position vector, $\mathbf{v}_i$ the velocity vector and $\mathbf{a}_i$ the acceleration vector, all evaluated for particle i at either the time step n or the next one $n+1$. Equations (13), when applied to every particle i of the system, can thus be used to propagate in time the whole cluster.

Every particle in the system stores its position $\mathbf{x}^{(n)}$, its velocity $\mathbf{v}^{(n)}$ and also the total force acting on it $\mathbf{F}^{(n)}$. This total force is the sum of all contribution of equation (9) from all other particles in the system.

The MD algorithm basically calculates the force between every pair of particles in the system. Since there are N total particles, there are $O\left(N^2\right)$ interactions to calculate. Doubling the number of particles will quadruple the computational burden, effectively putting an upper limit on the number of particles that can be simulated to tens of thousands.

A cluster example can be seen in figure 9. This cluster is composed of 147 xenon atoms (large blue spheres) and absorbs some photons (red wave-packets) from the laser field. Atoms are ionized; electron are created (small grey spheres) which move through the cluster. Ions are represented by colours from blue for neutral to red for Xe^{5+}. The figure was generated using PyMOL[1] on actual simulation-created data.

2.2 Short range potential shapes

2.2.1 Potential linearity

In the present work, the potential (and field) is assumed to be linear in charge state. For example, the potential and field created by a 3+ ion will be three times larger than the one created by a 1+ ion, for short range as for long range. The following close range potential derivations rely on this property.

Additionally, the potential created by an electron is assumed to be equal in strength but of opposite sign from the one created by a 1+ ion.

These properties greatly simplify the case of ionization, described in chapter 1.2 (page 5), when a new electron is created in the code. Indeed, when an electron is located exactly on top of an ion, right after an ionization event for example, the resulting potential on the other particles will have not changed.

[1] *The PyMOL Molecular Graphics System*, Version 1.5.0.4, Schrödinger, LLC. http://pymol.org/

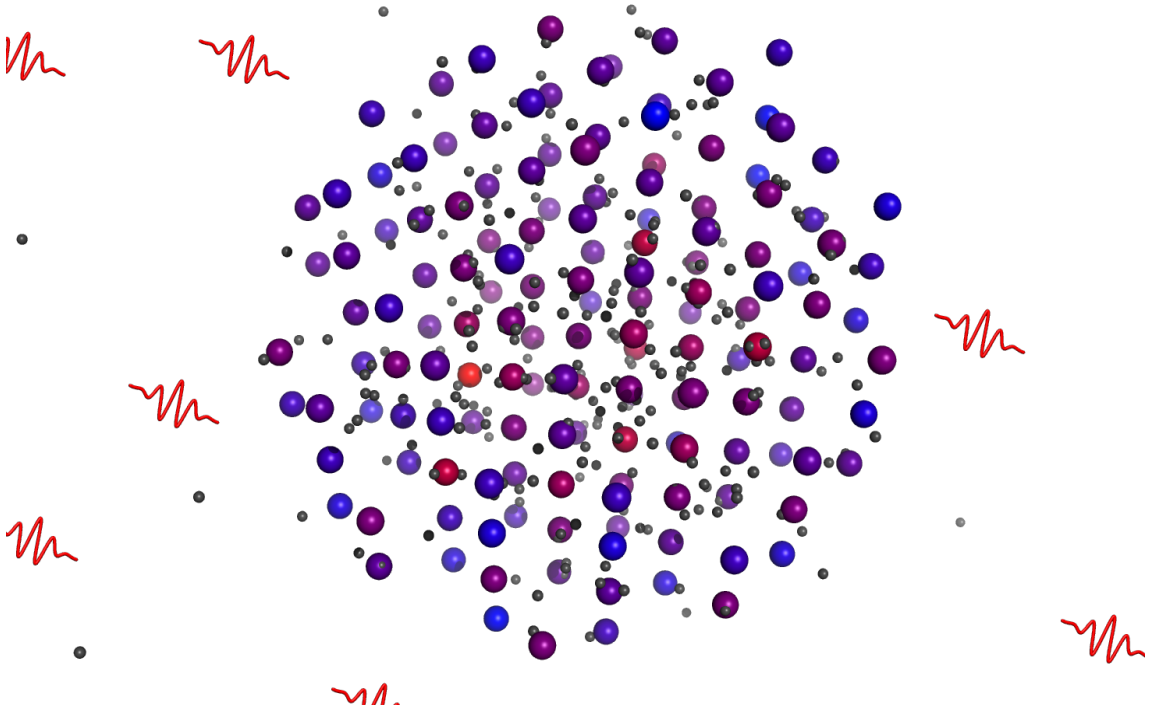

Figure 9: Example ionized Xe_{147} cluster; xenon as large spheres with colours from blue for neutral to full red for Xe^{5+}, electrons in small grey spheres. Photons from the laser field are displayed as red wave-packets.

2.2.2 Coulomb potential singularity

An important problem to consider is the close range behaviour of the Coulomb force in equation (9) which diverges. The problem is resolved by changing the shape of equation (9) at close range. Different *smoothing potentials* can be used to prevent the discontinuity of the Coulomb potential (or force).

Additionally, from a quantum mechanical point-of-view, electrons should not be able to classically recombine to an ion below the ground state energy. A softened potential also prevents the electron from falling too deep within the potential well of an ion. If this were to happen, the cluster as a whole would become artificially heated. However, as we will see in chapter 5 (page 81), it can be important to account for the effect of a deeper potential on a hot electron. To account for this, and still prevent artificial cluster heating, we have implemented electron recombination to the ground state, as described in chapter 1.2 (page 5).

Different potential shapes were investigated for the close range potential. Figure 10 plots the different shapes of potentials and their respective electrostatic field. These shapes are obtained by simply finding the location R where the value and the slope of the close-range shape ϕ_{cr} fits with the Coulomb potential ϕ_C:

$$\phi_C|_R = \phi_{cr}|_R \,, \tag{14a}$$

$$\left.\frac{\partial \phi_C}{\partial r}\right|_R = \left.\frac{\partial \phi_{cr}}{\partial r}\right|_R . \tag{14b}$$

These locations R are the cutoff radius of these shapes and mark the switch between the long range Coulomb potential and the short range potential.

2.2.3 Harmonic

For the harmonic potential, we have:

$$\phi_{j,H} = -Ar^2 + \phi_0. \tag{15}$$

We note that at $r_{j,i} = 0$, the potential value is the "potential depth" ϕ_0. Matching equations (14) at R gives:

$$\phi_{j,H}(\mathbf{r}_i) = \frac{-4\phi_0^3}{27(kq_j)^2} r_{j,i}^2 + \phi_0, \tag{16a}$$

$$R = \frac{3kq_j}{2\phi_0}, \tag{16b}$$

$$\mathbf{E}_{j,H}(\mathbf{r}_i) = \frac{kq_j}{R^3}\mathbf{r}_{j,i}. \tag{16c}$$

2.2.4 Super-Gaussian

The super-gaussian potential is given by:

$$\phi_{j,SG}(\mathbf{r}_i) = \phi_0 \exp\left\{-\frac{1}{2}\left(\frac{r_{j,i}}{\sigma}\right)^{2m}\right\}. \tag{17}$$

In the case where $m = 1$, equation (17) is simply a gaussian shape. Matching equations (14) at R gives values for σ and R:

$$\sigma = \frac{kq_j m^{1/2m}}{\phi_0} \exp\left\{\frac{1}{2m}\right\}, \tag{18a}$$

$$R = \frac{kq_j}{\phi_0} \exp\left\{\frac{1}{2m}\right\}, \tag{18b}$$

$$\mathbf{E}_{j,SG} = \frac{\phi_0 m}{r_{j,i}} \exp\left\{-\frac{1}{2}\left(\frac{r_{j,i}}{\sigma}\right)^{2m}\right\}\left(\frac{r_{j,i}}{\sigma}\right)^{2m}\hat{\mathbf{r}}_{j,i}. \tag{18c}$$

2.2.5 Gaussian distribution

An efficient way to correct the close range problem is to treat electrons as charge distributions instead of point particles. There is thus no discontinuity when the two charged distribution (particles) overlap. As such, the electrostatic potential due to a charged particle j (of gaussian shape of width σ) at location $\mathbf{r} = r\hat{\mathbf{r}}$ is

$$\phi_j(\mathbf{r}) = \frac{kq_j}{r}\ \mathrm{erf}\left\{\frac{r}{\sigma\sqrt{2}}\right\}, \tag{19}$$

where $\mathrm{erf}\{\}$ is the error function. The associated electrostatic field is thus

$$\mathbf{E}_j(\mathbf{r}) = -\boldsymbol{\nabla}\phi_j(\mathbf{r}) = kq_j\left(\frac{\mathrm{erf}\left\{\frac{r}{\sigma\sqrt{2}}\right\}}{r^2} - \sqrt{\frac{2}{\pi}}\frac{\exp\left\{-\frac{r^2}{2\sigma^2}\right\}}{\sigma r}\right)\hat{\mathbf{r}}. \tag{20}$$

When the distance r is large compared to σ, the error function tends towards 1 and the exponential tends towards 0 (since it's a gaussian shape). The potential (19) and electric field (20) thus tend towards Coulombic for large distances.

The value of σ is arbitrary: the smaller it is, the closer the potential will be from the pure Coulomb one. We can set a value for σ from the extremum value of the potential which occurs at $\mathbf{r} = 0$. At $\mathbf{r} = 0$, an indetermination $\frac{0}{0}$ occurs. Using l'Hospital rule, we get the limit of ϕ as $\mathbf{r}$ reaches 0:

$$\lim_{\mathbf{r}\to 0} \phi_j(\mathbf{r}) \equiv \phi_j(0) = \frac{kq_j}{\sigma}\sqrt{\frac{2}{\pi}}, \tag{21}$$

from which we get the particle width:

$$\sigma = \frac{kq_j}{\phi_j(0)}\sqrt{\frac{2}{\pi}}. \tag{22}$$

The free parameter is thus the "potential depth" $\phi_j(0)$. Even though $\phi_j(0) > 0$ we call this parameter "depth" since the potential energy of an electron on top of an ion would be minimal, similar to the gravitational potential energy of a ball is minimal at the bottom of a well.

Another problem that the smoothing of equations (19) and (20) solves is the one of *numerical heating* which occurs when particles artificially gain (or lose) energy during the calculation of equations (13). This absence of conservation of energy is due to a too large time step Δt. Indeed, the discretization of equations (13), and most importantly of subequation (13b), assumes the force on each particle to have a linear variation between time steps. If the time step is too large and the curvature of equation (20) cannot be sampled by the moving particle between each time steps, then the energy will not be conserved.

Figure 10 shows the different potential shapes and their respective electrostatic field.

It was found that the potential given by the charge distribution of equation (19) and the associated electrostatic field of (20) give the least numerical heating. As explained previously, the time discretization used to integrate the equations of motion assumes that the change in force between two time steps is linear. As can be seen in figure 10, the electric field curve from the charge distribution (magenta) does not have a discontinuity (in its first derivative) and is therefore the preferred one.

To validate the selection of the smoothing curve, photo-ionization was forced on a single atom and the total energy calculated. In this ionization case, the electron comes out of the ion with a maximum of kinetic energy so that its total energy is the difference

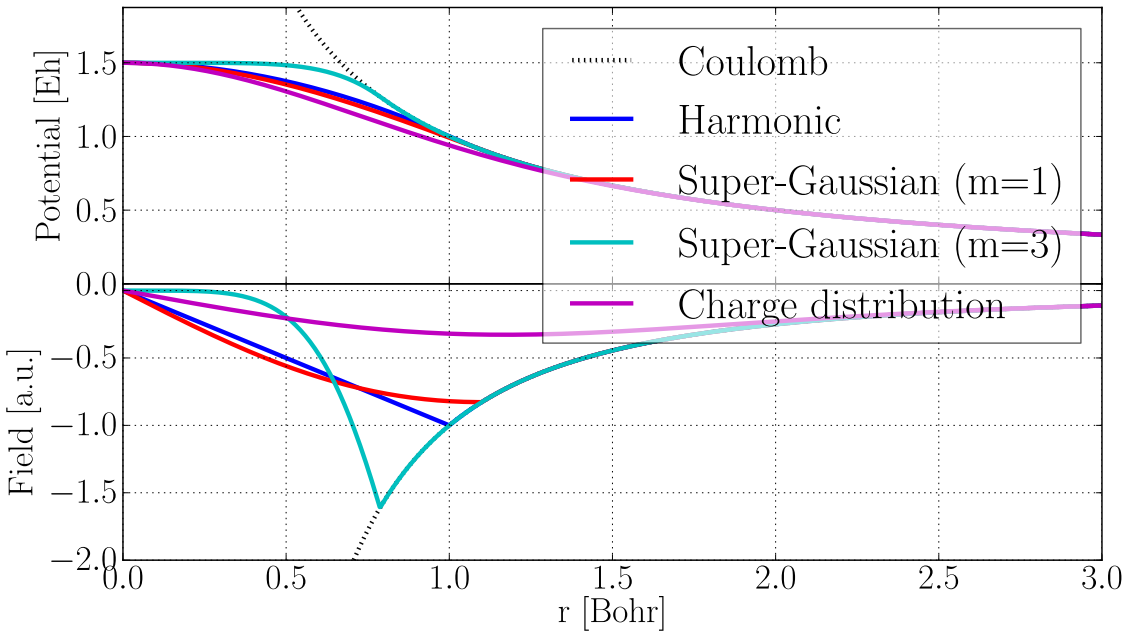

Figure 10: Potential shapes and their respective electric field. Note the use of atomic units and the potential depth $\phi_0 = 1.5$ Hartree $= 40.8$ eV.

between the photon energy and the ionization potential. It is thus a good candidate for a quantitative measurement of numerical heating. If the total energy is conserved, then the selected parameters (potential depth, smoothing curve and time step) can be used with good confidence. Figures 11 and 12 show the energy variation of the process as a function of time step (for different potential depths) and as a function of potential depth (for different time steps). A time step of 0.5 attosecond (as) is often taken as it minimizes the energy variation for a large range of potential depths, as can be seen in figure 12. It is important to note that a greater precision is not obtained by going under $\Delta\, t \approx 0.05$ as as can be seen in figure 11. This is caused by the precision of the computer. While it is normal that such a limit exist, it is relatively high due to the actual code implementation. Indeed, the dynamical aspect of the code is implemented in SI units when large differences between numbers can be easily obtained. When these numbers are combined in the algorithm's implementation, the computer floating point precision is insufficient. Nevertheless, a time-step of 0.05 as is sufficient for the work. The specific parameters (time step and potential depth) are specified in the different studies in later chapters.

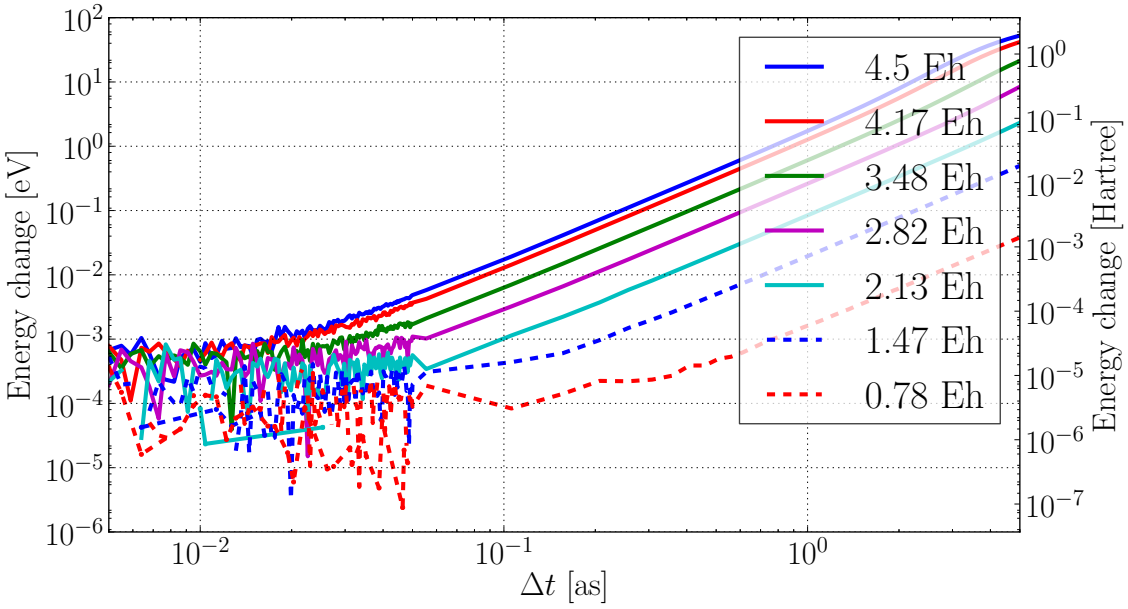

Figure 11: Energy variation after single photon ionization as a function of the time step size Δt.

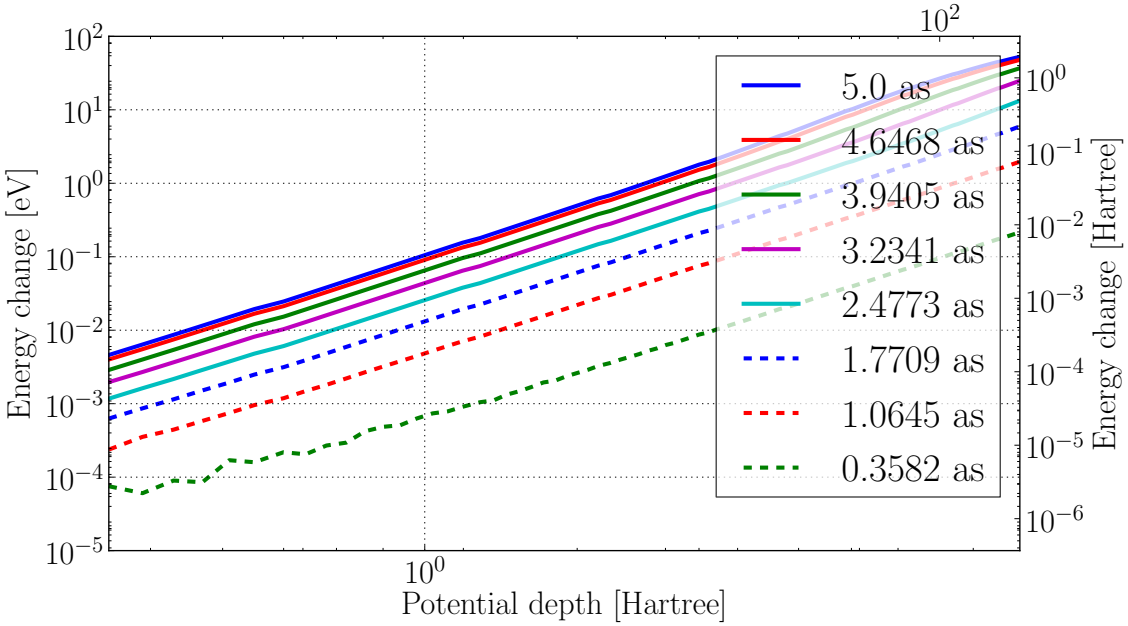

Figure 12: Energy variation after single photon ionization as a function of the potential depth.

2.2.6 Look-up tables

The preferred potential shape, the Gaussian distribution described previously, uses the error function which raises a major computational issue: it is slow, or at least too slow to be called at each interaction pair calculation. I decided to implement a look-up table instead. The potential and field functions are pre-calculated for a charge state of 1+. Since both potential and field are linear in charge (the potential caused by a 2+ ion is twice the one of a 1+), their value for any particle is simply scaled by its charge state.

Once the potential and field curves are calculated, they are approximated using

$$x_{\text{norm}} = \frac{x}{\Delta x}, \tag{23}$$

$$i = \text{int}\left(x_{\text{norm}}\right), \tag{24}$$

$$A = lut\left[i\right] + \left(lut\left[i+1\right] - lut\left[i\right]\right)\left(x_{\text{norm}} - \text{double}\left(i\right)\right), \tag{25}$$

where x is the distance between the two particles, lut is the array containing the look-up table, i the index of the look-up table and A the value to approximate using the look-up table.

The OpenCL implementation is different. The look-up tables are first transferred to the OpenCL device where they will be indexed using:

$$x_{\text{norm}} = \frac{x}{\Delta x}, \tag{26}$$

$$i = \text{convert\_int\_sat\_rtz}\left(\text{floor}\left(x_{\text{norm}}\right)\right), \tag{27}$$

$$A = lut\left[i\right] + \left(lut\left[i+1\right] - lut\left[i\right]\right)\left(x_{\text{norm}} - \text{convert\_float}\left(i\right)\right). \tag{28}$$

The OpenCL function convert_float() converts an integer to a floating point value and convert_int_sat_rtz() converts a floating point to an integer, rounding towards zero (_rtz) and saturating (_sat) the conversion in case of out-of-range [2] (if the floating point value exceeds the range of the integer type, the maximum value for the integer is used instead of a dangerous undefined behaviour).

This effectively produces a linear interpolation between the look-up table values. In the present work, 10,000 points are used for the table with a maximum value for x at the potential shape cutoff distance. In the case of the gaussian distribution shape, four times the particle width σ is used as the cutoff distance.

[2] https://www.khronos.org/registry/cl/sdk/1.2/docs/man/xhtml/convert_T.html

2.3 Long range potential: Hierarchical Tree algorithms

The $O(N^2)$ scaling of the MD algorithm for long-range forces can be problematic when the number of particles simulated is more than many thousands, which is a potential target for laser-cluster interaction. Some interesting variations of the MD algorithm exist to reduce the computational burden. One class of methods uses *hierarchical tree* algorithms as introduced by Barnes and Hut in 1986 [67]. To reduce the computational burden, particles are grouped in a hierarchical tree (quadtree in two dimensions, octree in three). While Barnes used his *treecode* to solve the N-body problem in the context of gravitational interactions, it can also be applied in the electrostatic case.

The main issue with the direct calculation of forces in MD is the lack of distinction between the close and distant particles. While the resulting potential of a distant particle is small, the computational cost required to calculate it is the same as in the case of a nearby particle. Some MD calculations use an artificial cutoff: particles farther than this cutoff will be ignored. This is acceptable when the force acting on particles is of short range, either due to screening or to the nature of the force (Lennard-Jones for example). In the present work, the dominant force is the Coulomb force and is long range by nature; it thus cannot be artificially cut off as in the case of close range forces used in other fields.

Could distant particles be grouped together, with their contribution to the force (or potential) being calculated only once (per "group")? Because individual particles which are part of a distant group will have a similar contribution to the potential at the location of particle i, the interaction with this group can instead be approximated through the multipole expansion [68] of the group of particles, or cell in terms of the tree algorithm:

$$\phi_i = \sum_{j \text{ cell}} \phi_{j \to i} = \sum_{j \text{ cell}} \frac{k q_j}{r_{ji}}, \tag{29}$$

$$\approx \frac{M_c}{R} + \sum_{\alpha} \frac{r_\alpha D_{c,\alpha}}{R^3} + \frac{1}{2} \sum_{\alpha,\beta} \frac{Q_{c,\alpha,\beta} r_\alpha r_\beta}{R^5}, \tag{30}$$

where M_c, $D_{c,\alpha}$ and $Q_{c,\alpha,\beta}$ are the monopole, dipole and quadrupole moments of the cell defined as:

$$M_c = \sum_{j \text{ cell}} q_j, \tag{31a}$$

$$D_{c,\alpha} = \sum_{j \text{ cell}} q_j r_{j,\alpha}, \tag{31b}$$

$$Q_{c,\alpha,\beta} = \sum_{j \text{ cell}} q_j \left(3 r_{j,\alpha} r_{j,\beta} - r_j^2\right) \delta_{\alpha,\beta}, \tag{31c}$$

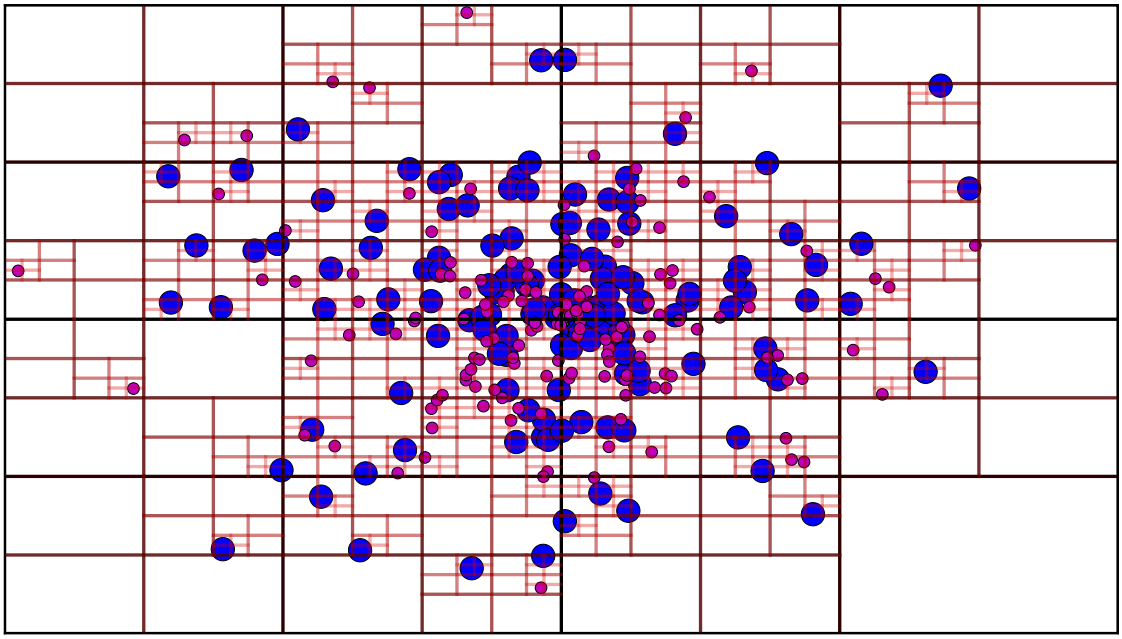

Figure 13: Quadtree: 2D's equivalent of the 3D octree. 300 particles (half ions in blue, half electrons in magenta) represent an exploding cluster. Cells' moments are propagated up the tree to the root cell. Particles distant from a cell can interact directly with it instead of resolving all particles contained in it, thus reducing the computational burden.

and R is the distance between the cell's centre-of-charge and the particle of interest i.

The tree algorithm first split the computational domain into an octree (in three dimensions) or quadtree (in two dimensions) until only a maximum of one particle is present per cell as can be seen figure 13. The deepest cells of the tree, containing only one particle, are called leaves. Once every particle in the system is inserted in the tree, the electrostatic moments are propagated from the leaves up to the root cell, the top cell enclosing the whole domain.

Then, instead of iterating through all particles for the calculation of the force on the particle of interest i, the tree is traversed. If the cell is "far enough" (with a given definition of far enough, discussed next) it can be added to the cell interaction list for later processing through the cell's moments. In the case of the cell being too close, it must be resolved into its eight *daughter* cells (or four in 2D). The daughter cells containing particles are visited, while the empty ones are ignored. Leaf cells can be reached using this process; in this case, the particles in the leaves are considered close enough to the particle of interest i and a direct interaction is wanted. Leaf particles will thus be added to a second interaction list containing particle-particle direct interactions. The process

is recursively repeated until all particles are added to an interaction list, either directly or through a parent cell. Note that an optimization done in the implementation allows many particles per leaves and automatically adds them to the particles interaction list when traversing the tree, preventing trees which are overly unbalanced.

Different selection rules exist for the criteria of "far enough". These rules are called *Multipole Acceptance Criteria* or MAC [70]. Barnes' original rule simply referred to as "s/d" compares an input parameter θ with the cell's size s divided by the distance between the cell's center-of-charge and particle of interest i (see figure 14a). If the ratio s/d is smaller than the parameter θ, the group of particles contained inside the cell is approximated through the cell's moments and the cell is added to the cells interaction list. At the opposite, if the ratio is larger than θ, the cell will be resolved into its daughters. In the limit where θ reaches zero, no more cells are added to the cells interaction list (they are all resolved) and the MD algorithm emerges, though with a large overhead due to the tree construction and traversal.

Unfortunately, this MAC can cause huge errors when a large amount of charge is present in a corner of a cell [70]. In this case, a cell could be added to the cell interaction list even though the error introduced by the multipole expansion is significant. Different MAC have thus been proposed to mitigate this problem. The *minimum distance* MAC replaces the distance d in the MAC with the minimum distance to one of the cell's edge (figure 14b). The *B-max* MAC instead replaces the size of the cell with the largest distance between one of the cell's corner to the center-of-charge (figure 14c). Another MAC was proposed by Bédorf *et. al.* [71] and is a mix of the two previous. The MAC reads:

$$d > \frac{s}{\theta} + \delta, \tag{32}$$

where δ is the distance between the cell's geometric center and its center-of-charge (figure 14d). If the previous equation holds (d is large enough) then the multipole expansion is used and the cell is added to the interaction list.

Because not all interaction pairs are considered in the calculation of the force and potential in this tree algorithm, a significant speedup is obtained. Due to the tree traversal algorithm, the scaling improves from $O\left(N^2\right)$ to $O\left(N \log N\right)$ [67, 68, 70].

A variation of the hierarchical treecode is obtained when a sufficiently large θ is used. In this case, the root cell (the largest one) is never resolved into its daughters. By adding more moments to the approximation then the first three of equations (31) and removing contributions of nearby particles, the *Fast Multipole Method* (FMM) is obtained [70].

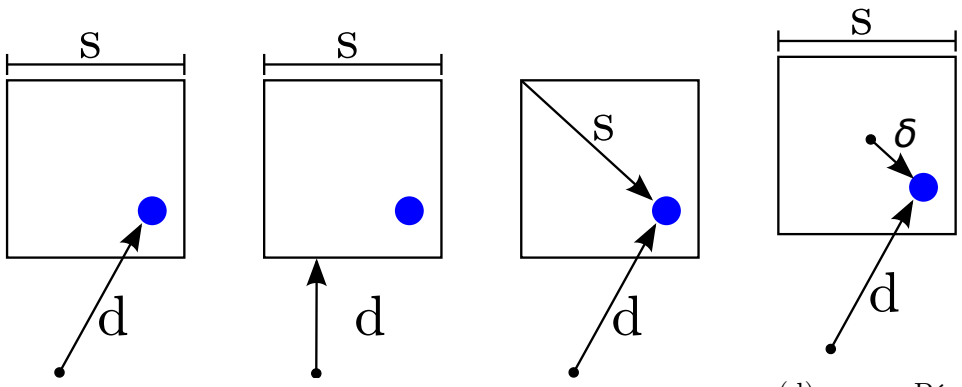

(a) s/d (b) min. d (c) B-max (d) Bédorf [71]

Figure 14: Different Multipole Acceptance Criteria (MAC). See text for descriptions.

FMM was developed by Greegard in 1988 [72] independently of Barnes' hierarchical tree method. While conceptually similar, its implementation details are quite different and it has not been implemented in the current work while the hierarchical tree algorithm was.

2.4 Implementation details

The following will go over some specific details of the code implementation. An explanation as to why a new MD code was written is first presented. The model approximating the cluster environment for atomic processes is then presented, followed by specific details to photon and impact ionization. Next, the use of cross-sections for ionization events is explained and finally recombination as implemented in the code is presented.

2.4.1 MD code

Our group previously used Barnes and Hut's treecode implementation, freely available [73] (through the GPL version 2 license). The code was adapted to simulate charged particles (Coulomb force) instead of masses (gravitational force) with some ionization routines added (see for example reference [57]). While reducing development time by re-using already written code, the maintenance burden introduced by many factors (initial implementation written in the C language, usage of global variables throughout the code, multiple coding styles from different people throughout the years, lack of revision control system giving freedom of deleting code from the active version without losing the ability to roll back, many subtle and important bugs, stability issues, etc.) convinced me to start from scratch. This allowed modern development techniques to be used. For

example, all development was done through a revision control system (subversion [74] at first, then switched to git [75]) in the C++ language instead of C. The object oriented nature of C++ allowed encapsulation of different parts of the code which could then be tested and validated individually through unit testing. This gave much better flexibility to the code, a required asset to push further the development of features.

A substantial number of MD packages are freely available and their use was considered instead of re-implementing a new one from scratch. Examples are GROMACS[3], NAMD[4] and LAMMPS[5]. A major issue with these pre-existing MD packages is their target audience; they aim to simulate large bio-molecules with mostly short range interactions. Another important problem is the number of particles throughout the simulations. While many packages assume a constant number of particles, the present work required creating (ionization) and annihilating (recombination) particles during simulations. Controlling the MD part of the code allowed better integration of the ionization aspects.

Additionally, other MD packages were not mature enough or simply non-existent at the time. For example the largely used HOOMD-blue[6] which uses extensively Nvidia GPUs released its first version (v0.6.0) in February 2008. The knowledge and experience gained by writing from scratch such a package is also invaluable.

2.4.2 Potential threshold V_b

Many ionization processes described in the introduction consider an isolated atom but clusters have close to solid density (10^{22} – 10^{23} cm^{-3}); the cluster environment cannot be ignored.

This environment can be approximated by a constant value that shifts the potential [76]. The shift is $U_b = -e_0 V_b$ where V_b is the potential due to the cluster at the ion's location (ignoring nearby electrons) and U_b is the potential energy a test particle of charge state -1 (an electron) would have if it were placed right on top of the ion. This can be justified by the fact that bound states of rare gas atoms are localized close to the nucleus and the cluster potential spatial variation around atoms is small.

To illustrate this shifting, figure 15 shows the potential energy landscape of an example "cluster" of two ions. Plotted on this figure is the potential energy of a test particle of charge state -1 (an electron) in the cluster environment. The contribution from the ion is

[3]GROMACS: http://www.gromacs.org/
[4]NAMD: http://www.ks.uiuc.edu/Research/namd/
[5]LAMMPS: http://lammps.sandia.gov/
[6]HOOMD-blue: http://codeblue.umich.edu/hoomd-blue/

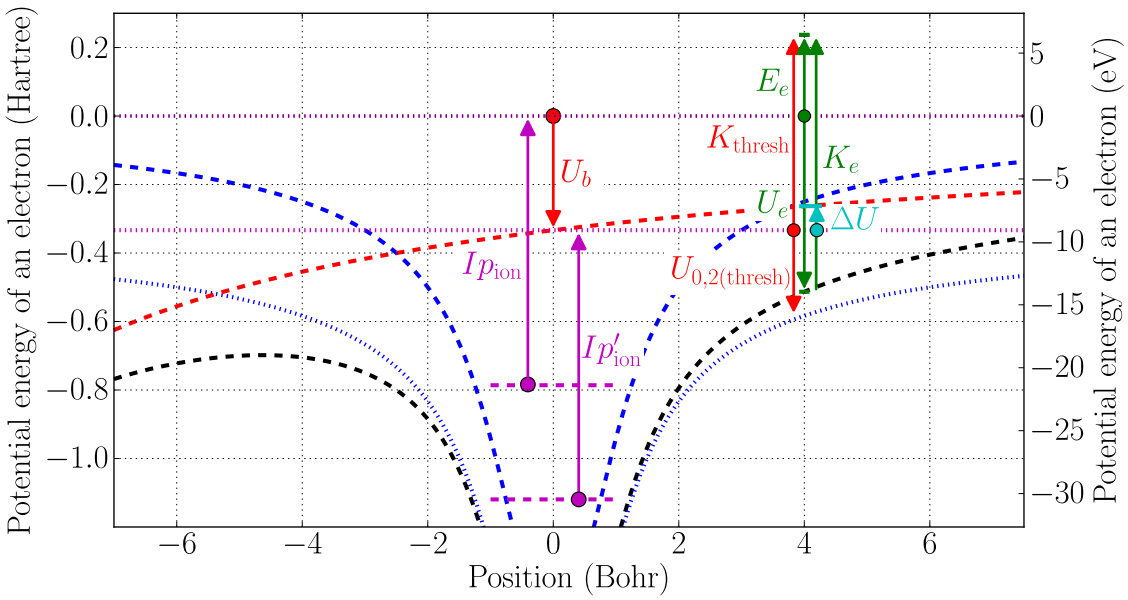

Figure 15: Cluster environment potential energy landscape and the U_b approximation. A 1+ ion at $r = 0$ and a 5+ at $r = -15$ Bohr. The potential energy curves are those of a test particle of charge state -1 (electron). The first ion's contribution is in blue-dashed line. The second ion's contribution is in red-dashed line and represents the cluster environment. The black-dashed line represents the total from the two ions. The blue-dotted line is the first ion's potential shifted by U_b. The upper horizontal magenta-dotted line is the isolated atom threshold, while the lower one is the shifted one due to the cluster environment.

the blue dashed line on the figure. Note the distinction between potential and potential energy. A positive charge (an ion) creates a positive potential but the potential *energy* of the test particle (of charge state -1) in that positive potential is negative, hence the negative curves in figure 15.

Continuing in the example case of figure 15, we introduce a second ion as an example of the simplest cluster environment. This second ion, of charge state 5+ in this example and located at r = -15 Bohr, is creating a potential that is not constant around the first ion (red-dashed line). The potential energy of the test particle in this potential is plotted as the red dashed line. The total potential energy of the test particle due to the two ions is plotted as a black dashed line.

The first ion's threshold is thus influenced by the second ion. The continuum, instead of being at zero, is shifted by U_b. This approximates the influence of the second ion as

being constant in the first ion's vicinity. This threshold shift is shown in figure 15 as the red arrow U_b.

The effect of U_b is to shift the ion's states to lower energies. This is shown on the figure as Ip_{ion}, the energy required for a bound electron to be promoted to the isolated ion's continuum, being shifted downward to Ip'_{ion}. The effective ion's potential energy curve, also shifted by U_b, is shown as the dotted blue line.

This cluster potential U_b is then treated as the atom's threshold to continuum. By using U_b as the threshold, atomic properties such as impact ionization cross-sections can be used, even in the cluster environment.

2.4.3 Notes on ionization definition

Special care needs to be taken when calculating particle energies during ionization processes. In this work, an ionization event is defined as one electron that leaves its isolated parent ion, reaching infinity with a final kinetic energy of zero.

As described in the previous chapter 2.4.2 (page 42), the cluster influence on ionization is approximated as a new threshold, which we call V_b.

The following paragraphs will discuss specific details concerning single photon ionization and impact ionization, both in the special case of an isolated atom or ion. The generalization to the cluster environment is done through the updated threshold, as discussed in chapter 2.4.2 (page 42).

Single photon ionization

In the case of single photon ionization, a new electron is created right on top of the ion with an updated charge state. At this point, all other particles in the cluster will not see a difference; the potential $\phi'(\mathbf{r})$ created by this new particles pair

$$\phi'(\mathbf{r}) = \phi_j(\mathbf{r}; Z+1) + \phi_k(\mathbf{r}; -1), \tag{33}$$

is the same as the previous ion's $\phi_j(\mathbf{r}; Z)$ (see equation (19) for the potential shape mainly used).

For the new electron to reach infinity with a null kinetic energy, it must have, at its creation time, enough kinetic energy to leave the ion. This kinetic energy must thus match the potential energy between the ion (with an updated charge state) and the electron so the total energy of the electron with respect to the ion is zero.

Additionally, the electron will contain in its kinetic energy the difference between the absorbed photon and the ionization potential of the ion.

Impact ionization

For impact ionization (still in the case of an isolated atom), the impacting electron's kinetic energy used in equation (7) is the kinetic energy the electron has *at infinity*, meaning that the impacting electron and the isolated atom (or ion) are separated in an unbound system.

At infinity, the electron's total energy only contains kinetic energy. We call this kinetic energy K_{thresh} for "kinetic energy above the threshold". This K_{thresh} can simply be calculated as $K_{\text{thresh}} = \max(0, K_e + U_e)$ where K_e is the electron's kinetic energy and U_e its potential energy with respect to the ion. K_{thresh} is thus the electron's total energy *with respect to the ion*. In the case of a classically bound electron, the total energy is less than zero: the max() enforces a positive kinetic energy.

When a cluster environment is present, a similar approach is taken to obtain K_{thresh}. Instead of taking the extra energy above zero for K_{thresh}, the extra energy above the new threshold U_b is used. This value can easily be obtained from the actual electron's kinetic energy K_e, it's *total* potential energy in the cluster environment and the threshold U_b by:

$$K_{\text{thresh}} = \max(0, K_e + U_e - U_b) \tag{34}$$

and is shown in figure 15 as a red arrow with its base at U_b.

K_{thresh} is the kinetic energy that must be used in Lotz formula (7). Cross-sections are discussed in the next section.

When an impact ionization event occurs and if the impacting electron has more kinetic energy, it can either keep the extra, give all the extra, or give a fraction of the extra to the new electron. We split the extra kinetic energy between the two electrons to assure that they do not fall back into the ion.

2.4.4 Cross-sections

Implementing any kind of ionization in the model is done through cross-sections. Because cross-sections can be obtained from experiments for any kind of target, it is easily integrated into the model.

Single photon ionization

For single-photon ionization, experimental cross-sections $\sigma(\omega)$ for xenon were obtained from reference [77] and from reference [78] for argon.

Once cross-sections are obtained, they are converted to a rate of ionization using

$$\Gamma(\omega) = \sigma(\omega) I(t). \tag{35}$$

which is equivalent to equation (6) with $\nu = 1$.

Then, this rate is weighted [79] by the time step size and compared to a random number r between 0 and 1:

$$1 - \mathrm{e}^{-\Gamma \Delta t} > r. \tag{36}$$

When the previous test succeeds, ionization takes place and a new electron is created in the code. Then, the intensity profile of the laser $I(t)$ is decreased by one photon to incorporate laser depletion. This is especially important for a more accurate description of cluster interaction with low fluence pulses.

Collisional processes

For impact ionization cross-sections, Lotz formula of equation (7) is used with experimental parameters obtained from reference [80] (for neutral xenon) and [81] (for higher charge states). For argon, data from [52] and [82] is used. When $K_{\mathrm{thresh}} \leq 0$, a null cross-section is simply used.

As for ACI, numerical cross-sections from ground state to excited state and from excited state to continuum were calculated by Edward Ackad using a Hartree-Fock code from Cowan [83, 69]. Only the first eight excited states were considered (with $l < 4$) for charge states up to 17+ for both xenon and argon.

The impact parameter of the impacting electron is calculated by:

$$b = \frac{|\mathbf{v} \times \mathbf{r}|}{|\mathbf{v}|}, \tag{37}$$

where $\mathbf{v}$ is the impacting electron's velocity vector and $\mathbf{r}$ the vector from the impacting electron to the target. If the impacting parameter lies inside the calculated cross-section, excitation or ionization takes place. In the case of excitation, the total cross-section of all excited states are used and a final state randomly selected from all those accessible, weighted by their cross-sections relative to the total one.

2.4.5 Recombination

In a classical simulation electrons might cool down into the ions' infinite Coulomb potential where they would have a total energy less than what is allowed in quantum mechanics. This would lead to artificial cluster heating, as this electron surrenders its energy to the cluster as it cools. Using a smoothing potential as in equation (19) will prevent the singularity. Additionally, if the potential depth $\phi(0)$ used (see equation (21)) is deep enough, the total energy of an electron might fall below the energy of the state. Recombination to the ground state is thus used to prevent such non physical events. When an electron's total energy (with respect to the ion) falls below the energy of the lowest unoccupied state, recombination is forced: the electron disappears from the simulation and the ion charge state is decreased by one.

Additionally, recombination plays an important role in the dynamics of the exploding cluster. Experiments at FLASH in 2009 on xenon clusters in the XUV regime [37] could be reproduced by our models when recombination was enabled; we found that the lower charge states detected would come from the cluster core where recombination is important. This study was published in May 2013's edition of *New Journal of Physics* [38] and is included in this thesis in chapter 6 (page 89).

Recombination was also required for the work in chapter 5 (page 81), as it allowed us to lower the potential depth of the ions for more physical simulations.

2.5 Quantum FDTD (QFDTD)

One model proposed to explain the high charge states seen in some experiments is the lowering of the ionization barrier, used in conjunction with classical MD simulations. This model assumes that an electron can be ionized when the potential of a neighbouring ion lowers the potential of the electron's parent ion - this is called "Barrier Lowering" [47, 8]. An open question is how close this model, used with a classical MD, is to reality. Special care needs to be taken when a particle, evolving in a quantum world, is to be treated classically. How does the bound electron's wavefunction react to the presence of a second ion perturbing the potential? How can the U_b approximation to the cluster environment, described in chapter 2.4.2, be tested? Is the wavefunction really evolving into a state where we can say the electron is shared by the two ions? If the electron is really shared by the two ions, can we classically let it evolve inside the cluster environment?

These questions pushed us to look at the quantum aspects in more detail. Many tools exist to calculate the ground state of a system, even with multiple electrons (with

different levels of approximations), as described previously. Additionally, excited states are capital in ACI and as such we needed a tool that could give us information not only on the ground state but also on excited states.

After stumbling on an interesting article that used the Finite-Difference Time-Domain (FDTD) algorithm to solve Schrödinger equation [84] it was decided to explore this idea since not much work could be found on this *Quantum FDTD* (QFDTD) method and beceause of previous experiences implementing electrodynamics FDTD.

FDTD is an established algorithm developed in 1966 by Yee [85] to solve Maxwell's equation on a grid using leap-frog integration. It is actually the method used in PIC simulations to propagate the electromagnetic field through the grid. The number of scientific articles using FDTD has exponentially increased since the '80s largely due to the increase in computational resources. Indeed, a three dimensional grid with the three vector components of both the electric and magnetic fields requires huge amount of memory that was definitely not present in the late '60s. The reader is invited to read the excellent book on FDTD by Allen Taflove and Susan Hagness [86] covering 40 years of FDTD development in electrodynamics simulations.

Other simulation techniques like Finite-Element Methods (FEM) or Finite-Volume Methods (FVM) can be seen as more complex than Finite-Differences Methods (FDM). This gives some elegance and simplicity to the FDM algorithms. Additionally, since FDTD is an explicit algorithm, implementations are generally easy and efficient and the local nature of the algorithm makes it easily parallelizable on distributed memory systems.

Sullivan was the first to apply the FDTD method to solve the Schrödinger equation in his 2000 book [87] where he obtains the wavefunction of an electron hitting a potential barrier in one dimension. Later, in 2001, he used the FDTD method to simulate one and two electrons in a quantum dot [88]. The Hartree-Fock approximation was used to describe the two electrons problem and thus required the use of Fourier transforms to calculate the Coulomb and exchange terms. Due to this additional calculation, the problem was restricted to two dimensions only. The following year, he introduced a method to calculate the eigenstates of an arbitrary system using FDTD [89]. This method requires two distinct simulations: the first one finds the eigenvalues and the second one stores the states corresponding to these eigenvalues, doubling the simulation time required. The interaction with a magnetic field was included through the vector potential and later [90, 91] used to calculate spin interaction. Only in 2005 were the first three

dimensional simulations [92] performed as proof of concept; only a single electron was simulated. Eigenstates and eigenvalues were obtained for a simple quantum well in addition as a two ions system. A more complicated three dimensional system was later simulated in [93], still with a single electron.

Later Sudiarta suggested [84] a new way to use the FDTD method to solve the Schrödinger equation for a single electron system. By switching to *imaginary time*, Schrödinger equation can be solved more easily and more efficiently to get the eigenvalues and eigenstates of the system. It was later shown that the interaction with a magnetic field could also be added to the imaginary-time method [94] and that FDTD could be used to construct the thermal density matrix of a single particle [95]. Strickland *et al.* parallelized the method [96] and even released its code through the GPL v2 license[7].

Both real-time and imaginary-time methods were implemented for this thesis. The two algorithms are described as follows.

2.5.1 Real time

First, let's define the time dependent Schrödinger equation describing a wavefunction ψ inside a potential V:

$$\mathrm{i}\hbar\frac{\partial}{\partial t}\left|\psi\left(\mathbf{r},t\right)\right\rangle = \left(-\frac{\hbar^2}{2m}\boldsymbol{\nabla}^2 + V\left(\mathbf{r},t\right)\right)\left|\psi\left(\mathbf{r},t\right)\right\rangle. \tag{38}$$

To ease the calculation, let's switch to atomic units where $\hbar = 1$, $m = 1$ and $e_0 = 1$:

$$\mathrm{i}\frac{\partial}{\partial t}\left|\psi\left(\mathbf{r},t\right)\right\rangle = \left(-\frac{1}{2}\boldsymbol{\nabla}^2 + V\left(\mathbf{r},t\right)\right)\left|\psi\left(\mathbf{r},t\right)\right\rangle. \tag{39}$$

At initial time $t = 0$, the wavefunction $\left|\psi\left(\mathbf{r},t\right)\right\rangle$ is decomposed into its eigenstates basis:

$$\left|\psi\left(\mathbf{r},t=0\right)\right\rangle = \sum_{n=0}^{\infty} c_n \left|\phi_n\left(\mathbf{r}\right)\right\rangle. \tag{40}$$

The time-evolution operator (or propagator) $\hat{U}\left(t\right)$ is, in atomic units:

$$\hat{U}\left(t\right) = \exp\left\{-\mathrm{i}t\hat{H}\right\}, \tag{41}$$

and when applied to the initial state (40) gives the time evolution of the wavefunction:

$$\hat{U}\left(t\right)\left|\psi\left(\mathbf{r},t=0\right)\right\rangle = \left|\psi\left(\mathbf{r},t\right)\right\rangle = \mathrm{e}^{-\mathrm{i}t\hat{H}}\sum_{n=0}^{\infty} c_n \left|\phi_n\left(\mathbf{r}\right)\right\rangle. \tag{42}$$

[7] http://sourceforge.net/projects/quantumfdtd

Since the operator $\hat{H}$ applied to the eigenstates $|\phi_n(\mathbf{r})\rangle$ gives the eigenvalues E_n, the previous equation becomes:

$$|\psi(\mathbf{r},t)\rangle = \sum_{n=0}^{\infty} \mathrm{e}^{-\mathrm{i}tE_n} c_n |\phi_n(\mathbf{r})\rangle . \tag{43}$$

The time evolution of each eigenstates is thus an oscillation between their real and imaginary parts of which the frequency is given by the eigenvalue E_n.

Equation (39) can now be solved either in real-time or imaginary-time, the former being explained first.

Let's separate the real and imaginary components of equation (39) (and simplifying the notation):

$$\mathrm{i}\frac{\partial}{\partial t}(\psi_R + \mathrm{i}\psi_I) = \left(-\frac{1}{2}\boldsymbol{\nabla}^2 + V\right)(\psi_R + \mathrm{i}\psi_I), \tag{44}$$

giving two equations describing the time evolution of two effective fields:

$$\frac{\partial}{\partial t}\psi_R = \left(-\frac{1}{2}\boldsymbol{\nabla}^2 + V\right)\psi_I, \tag{45a}$$

$$\frac{\partial}{\partial t}\psi_I = -\left(-\frac{1}{2}\boldsymbol{\nabla}^2 + V\right)\psi_R. \tag{45b}$$

The real and imaginary parts in equation (45) can be compared to the electric and magnetic fields in the traditional electrodynamics FDTD method. The integration is performed using a leap-frog scheme. We first define $\psi^n_{i,j,k}$ the wavefunction located at the grid cell (i,j,k) and at time step n. Then equation (45b) is evaluated at time step n and, using (second order) central-differences, we get:

$$\left.\frac{\partial}{\partial t}\psi_I\right|_n = -\left.\left(-\frac{1}{2}\boldsymbol{\nabla}^2 + V^n\right)\psi_R\right|_n, \tag{46}$$

$$\frac{\psi_I^{n+1/2} - \psi_I^{n-1/2}}{\Delta t} = -\left(-\frac{1}{2}\boldsymbol{\nabla}^2 + V^n\right)\psi_R^n, \tag{47}$$

$$\psi_I^{n+1/2} = \psi_I^{n-1/2} - \Delta t\left(-\frac{1}{2}\boldsymbol{\nabla}^2 + V^n\right)\psi_R^n. \tag{48}$$

Similarly, defining the time derivative in (45a) at time step n and again using (second order) central-differences:

$$\left.\frac{\partial}{\partial t}\psi_R\right|_{n+1/2} = \left.\left(-\frac{1}{2}\boldsymbol{\nabla}^2 + V^n\right)\psi_I\right|_{n+1/2}, \tag{49}$$

$$\frac{\psi_R^{n+1} - \psi_R^n}{\Delta t} = \left(-\frac{1}{2}\boldsymbol{\nabla}^2 + V^n\right)\psi_I^{n+1/2}. \tag{50}$$

$$\psi_R^{n+1} = \psi_R^n + \Delta t\left(-\frac{1}{2}\boldsymbol{\nabla}^2 + V^n\right)\psi_I^{n+1/2}, \tag{51}$$

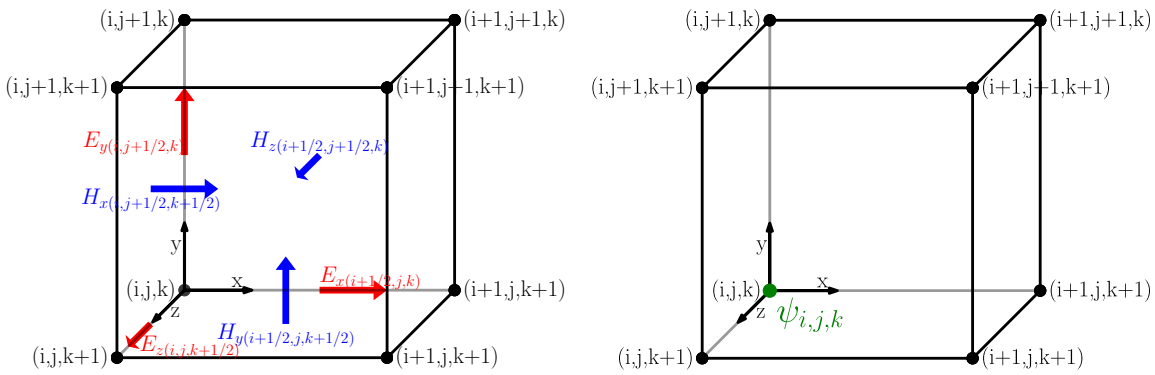

(a) Yee cell

(b) QFDTD cell

Figure 16: Yee cell used in electrodynamic FDTD vs QFDTD cell with id (i, j, k). Other vertices represent neighbouring cells. The QFDTD cell is simpler as ψ is scalar (as opposed to vectorial electric $\mathbf{E}$ and magnetic $\mathbf{H}$ fields) and defined at the grid cell location (i, j, k) (compared with half-indexes shifted electromagnetic fields).

Lastly, the Laplacian is discretized on a grid using (second order) central-differences:

$$\boldsymbol{\nabla}^2 \psi^n_{i,j,k} \approx \frac{\psi^n_{i+1,j,k} - \psi^n_{i-1,j,k}}{2\Delta x} + \frac{\psi^n_{i,j+1,k} - \psi^n_{i,j-1,k}}{2\Delta y} + \frac{\psi^n_{i,j,k+1} - \psi^n_{i,j,k-1}}{2\Delta z}. \tag{52}$$

Equations (48), (51) and (52) are then used to propagate in time the real and imaginary components of the electronic wavefunction. Note that, contrary to the Yee cell in the electrodynamics FDTD, the two components of the wavefunction do not have to be defined at different location inside the grid cell; they are defined at the same locations as shown in figure 16.

Equations (48) and (51) by themselves only describe the time evolution of a wavefunction inside a potential; it does not give a direct way to obtain the eigenstates of an Hamiltonian. Different approaches exist to obtain these; Sullivan describes some of them. Eigenvalues though are relatively easy to obtain.

By numerically propagating in time a wavefunction ψ using equations (48) and (51) the system's eigenstates will evolve according to equation (43). This evolution is an oscillation between the real and imaginary part at a specific frequency; the states' eigenvalue. By taking a Fourier transform of the time evolution, eigenvalues can be identified on a power spectrum. The published article of chapter 7 describes a novel method of extracting the eigenvalues of all eigenstates present in the simulated wavefunction ψ.

2.5.2 Imaginary time

The second QFDTD method, called the *imaginary-time* method, differs in that it first requires that the potential be constant in time ($V(\mathbf{r},t) \rightarrow V(\mathbf{r})$). Further, a Wick rotation is performed in time ($\mathrm{i}t \rightarrow \tau$) and the Schrödinger equation in imaginary time is obtained:

$$-\frac{\partial}{\partial\tau}\left|\psi(\mathbf{r},\tau)\right\rangle = \left(-\frac{1}{2}\boldsymbol{\nabla}^2 + V(\mathbf{r})\right)\left|\psi(\mathbf{r},\tau)\right\rangle. \tag{53}$$

Note that equation (53) is not complex and is similar to the heat equation.

Contrary to the real-time method, the "time" evolution of the imaginary method is not oscillatory. Indeed, the propagator of equation (41) becomes, in imaginary time:

$$\hat{U}(\tau) = \exp\left\{-\tau\hat{H}\right\}, \tag{54}$$

and the wavefunctions evolution becomes:

$$\left|\psi(\mathbf{r},\tau)\right\rangle = \sum_{n=0}^{\infty} c_n \mathrm{e}^{-\tau E_n}\left|\phi_n(\mathbf{r})\right\rangle. \tag{55}$$

The imaginary time evolution is thus an exponential growth with the different eigenstates having different growth rates. It thus becomes possible to isolate the different eigenstates from each other. Previous work used to isolate eigenstates once and continue, or restart, the simulation. This was not working well as the floating point error made by the computer during calculation let the ground state reappear shortly. I developed a novel method to isolate these states, as described in the published article of chapter 7 (page 106).

Because equation (53) is real, only a single scalar field needs to be discretized on the grid. The discretization is similar to the real-time method: equation (53) is evaluated at time step n and the time derivative is discretized, in this case using (first order) forward-differences (and again simplifying the notation):

$$-\left.\frac{\partial}{\partial\tau}\psi\right|_n = \left[\left(-\frac{1}{2}\boldsymbol{\nabla}^2 + V\right)\psi\right]_n, \tag{56}$$

$$\frac{\psi^{n+1}-\psi^n}{\Delta\tau} = \left(\frac{1}{2}\boldsymbol{\nabla}^2 - V\right)\psi_n, \tag{57}$$

$$\psi^{n+1} = \left[1 + \Delta\tau\left(\frac{1}{2}\boldsymbol{\nabla}^2 - V\right)\right]\psi^n. \tag{58}$$

The Laplacian is discretized with equation (52). Since a single scalar field is used to describe ψ, special care needs to be taken in the code implementation. Indeed, equation

(58) uses the Laplacian of the wavefunction at the previous time step n to update the wavefunction to time step $n+1$. For example, calculating $\psi^{n+1}_{i,j,k}$ requires $\psi^{n}_{i-1,j,k}$ and $\psi^{n}_{i+1,j,k}$ (for the x derivative in the Laplacian) but when calculating the next value in x ($\psi^{n+1}_{i+1,j,k}$) the required values are now $\psi^{n}_{i,j,k}$ and $\psi^{n}_{i+2,j,k}$, the former being already updated. The easiest and simplest way to solve this dependency problem is to store two grids; one for ψ^n and another for ψ^{n+1}, alternating between them when calculating equations (58).

2.5.3 Stability criteria

Due to the explicit nature of the FDTD algorithm (values can be obtained at the next time step from values at the current time step only) the method is conditionally stable; an upper bound on the time step size must be taken. The Courant-Friedrichs-Lewy (CFL) condition gives the upper bound. Dai *et al.* derive [97] the stability condition for a constant in time potential:

$$\Delta t < \frac{2}{\frac{2\hbar}{m}\left(\frac{1}{\Delta x}+\frac{1}{\Delta y}+\frac{1}{\Delta z}\right)+\max\left|V\left(\mathbf{r}\right)\right|/\hbar}. \tag{59}$$

2.5.4 Nonlinear mapping

While being simple and powerful, the QFDTD method (both real-time and imaginary-time) suffer from a major flaw; its memory usage. Since a three dimensional grid scales as $O\left(N_x \cdot N_y \cdot N_z\right)$ where N_i is the number of grid cells in one dimension, many gigabytes of memory are often required. Specifically in the case of QFDTD is the fact that the electronic wavefunction must span an infinite space, or at least be truncated where the wavefunction can be safely assumed always close to zero. Additionally, the Coulomb potential vary drastically close to the nucleus which requires a small grid cell size to efficiently sample, uselessly increasing the resolution far from the singularity and multiplying the memory requirement.

In this thesis I developed a method to concentrate three dimensional grid cells close to centres of interest and thus reduce significantly the amount of memory required for a given precision. Dubbed *nonlinear mapping*, it maps the discrete, integer based, space of a computer memory to the continuous regular space. Many interesting features of this mapping make it applicable to other type of solvers in the most generic way.

The reader will find the full details of this work in the article published in 2011 and included in chapter 7.

2.6 Acceleration through video cards and OpenCL

A new trend in High Performance Computing (HPC) is code acceleration through graphics cards. Similar to the ubiquitous Moore's Law in the CPU world, video cards power evolved exponentially during the last twenty years, pushed by the never ending need of more realistic video games. From "dumb" devices drawing primitive shapes on a display, they evolved to extremely powerful devices and started to act more like CPUs by being programmable (shaders) during the first half decade of 2000. The term *Graphical Processing Unit* (GPU) was coined in 1999 by Nvidia, the biggest vendor of video cards, as a selling point for their product and to emphasize the fact that their chips were becoming more and more like CPUs.

2.6.1 General-Programming GPU (GP-GPU)

Due to this increase in power, attempts were made to use these video cards as accelerators for computations other than real video operations. Because GPUs have intrinsically high parallelism (for example the same operation is performed on all pixels of an image in parallel) HPC users and developers became interested. In his 2005 book, Taflove described a way to use a video card's GPU to accelerate his electrodynamics FDTD solver [86]. At that time no General-Programming GPU (GP-GPU) framework existed so Taflove (and anyone interested in using GPUs at that time) had to "translate" the FDTD algorithm into one that could be understood by a video card. This process was extremely difficult as it required using low level graphic primitives; in his case, OpenGL calls. Normally OpenGL, the Open Graphics Library, is used to draw animated scenes on the user's screen; it must not be confused with OpenCL described later. A notable example of OpenGL usage is video games where the user is immersed in a virtual three dimensional space. The process of re-writing an algorithm into OpenGL calls is one that only a few highly skilled and knowledgeable people can tackle.

In 2007, Nvidia saw an opportunity for market expansion. Why not let the non-videogames programmer use the powerful GPUs for something other than video operations? For this to happen, a programming framework had to be released; the number of programmers and scientists able to exploit OpenGL to their advantage was limited. They thus released their *Compute Unified Device Architecture*, later renamed CUDA. CUDA allows writing normal C or C++ programs with some extensions, called *kernels*, that can be run on the GPU. These kernels have the same structure as C functions but

are executed concurrently by every core on the GPU[8]. The number of cores on a recent consumer grade video card is now of the order of many hundreds; a 50$ Nvidia GT 620 has 96 CUDA cores and 1 GB of RAM, while the GTX TITAN has 2688 CUDA cores and 6 GB but costs more than 1,000 $. Even though the highest priced GPU can be more expensive than complete workstations, no CPUs can offer close to three thousand cores for a still affordable price.

A year after CUDA was released, Apple wanted a framework that would allow programs to be accelerated on their top-of-the-line product's GPU while still being able to run on their lower-end range of products (which did not have a discrete video card). Additionally, some Apple products were released with ATI video cards (Nvidia's main competitor) which, understandably, never supported CUDA. They thus released a framework called *OpenCL* (standing for Open Compute Language) in 2008 with the help of many partners (IBM, ATI, Intel and even Nvidia). While conceptually similar to CUDA (smaller routines are written in a kernel function and launched individually on the GPUs by the main program) OpenCL has the advantage of targeting heterogeneous platforms consisting of (possibly and not limited to) many CPUs, many cores and GPUs. The main advantage of OpenCL is its portability; a program written in OpenCL can not only run on GPUs from ATI and Nvidia but also on traditional CPUs, exploiting all cores available on the CPUs transparently.

It was thus decided to port the two codes (MD and QFDTD) to OpenCL to take advantage of the GPU power while retaining portability.

2.6.2 GPU programming challenges

Porting a code to run on GPUs is not as simple as recompiling for the new architecture. While being portable, OpenCL does require, unfortunately, rewriting many parts of the code.

Refactoring

Certain factors must be considered when porting codes to GPU frameworks. First, because GPU cores are much slower than a core on a CPU, parallelisms must be extracted from algorithms. The code must thus be completely refactored to exploit the parallelism. For example, a CPU implementation of the MD algorithm can be implemented by looping

[8]Technically, GPUs don't have "cores" *per se* like CPUs but the comparison can still be made.

over particles and calculating all properties at once, for every particle. On the contrary, due to the high vectorized nature of GPUs, it makes more sense to calculate only one particle property but for all particles before switching to the next property.

Second, the main drawback of GP-GPU programming is the fact that GPUs have their own memory, independent of the system's memory; kernels will only have access to the device's memory. Data required for kernel calculation must thus be first transferred to the device's memory and similarly the resulting data must be transferred back to the host memory where it can be further processed by the rest of the main program. Video cards today are connected to a computer through PCI-Express (PCIe) connections. While fast, there can still be a bottleneck if data is to be transferred back and forth similarly to main memory. It is thus necessary to reduce to a minimum the data transfer between the host and the device, similarly to communications in a distributed memory parallel programming paradigm.

In the case of the MD algorithm, every interaction pair is independent of all others and can thus be calculated concurrently; this is the basis of the OpenCL implementation. The main loop that calculates the electrostatic field and potential at every particle's position is implemented as an OpenCL kernel. Each thread on the GPU will thus calculate the interaction between one particle and all others. Once the MD kernels are launched on the GPU; they are only halted when either the ionization routines have to be called (every femtosecond) or when data needs to be saved (to take a snapshot of the simulation for example). This prevents the GPU from being interrupted too often and reduces the amount of data transfers. Using this OpenCL implementation, MD simulations could be run 80 times faster on GPUs than on conventional CPUs.

As for the QFDTD, only the real time algorithm was implemented as OpenCL kernels since the imaginary time method did not require long simulation times. As in the case of the MD, the real time algorithm is left running on the GPU until data needs to be saved to a snapshot or post-processed to reduce transfers.

Debugging

One of the most problematic aspects of GPU programming is the lack of debugging tools. Many tools and techniques exist to detect and fix problems in normal CPU codes. The following describes them and their counterpart, when present, on GPUs.

Printing

The simplest method of debugging is printing the variables' values to the screen and inspecting them for erroneous values. While not really efficient, it is sometimes useful, quick and simple "hack" to get an insight of how the code is working. Unfortunately, such printing function (such as C or C++'s *printf()*) cannot be used at all on a GPU! The reason is that the main processor must be able to *read* the variable from memory to be able to print it to screen and yet the variable's content is *not* in main memory, only the video card's memory. It must be noted though that some OpenCL drivers (for example AMD's APP SDK[9] or Intel's SDK for OpenCL Applications 2013[10]) have specific extensions that allow using *printf()*-like functions inside OpenCL kernels. These extensions must explicitly be enabled in kernel files using

```
#pragma OPENCL EXTENSION cl_amd_printf : enable
```

for the Intel SDK, or

```
#pragma OPENCL EXTENSION cl_intel_printf : enable
```

for the AMD SDK. These extensions are possible since these drivers support running the kernels directly on the CPU. In the case of AMD, the extension only works when the kernels are executed on the CPU (not on an AMD video card). Nvidia does not have a similar extension for their OpenCL driver. Debugging using printf() is thus easier when running on a CPU with either Intel's or AMD SDK.

Valgrind

Another useful bug squashing weapon used in debugging on Linux is called *valgrind*[11]. This extremely useful tool verifies memory access and can thus report on out-of-bound accesses (accessing memory locations which are out of range of an array), a major type of error in programming that one *has* to expect will happen. Valgrind can also detect uses of uninitialized variables, a dangerous type of error that can be hard to detect otherwise.

Since valgrind was specifically designed to intercept main memory access it cannot be used when the program is running of a GPU. Alternatively, when the program is running

[9] http://developer.amd.com/tools-and-sdks/heterogeneous-computing/amd-accelerated-parallel-processing-app-sdk/

[10] http://software.intel.com/en-us/vcsource/tools/opencl-sdk

[11] http://www.valgrind.org/

on the CPU through the use of the Intel or AMD SDKs, valgrind detects a huge amount of errors, probably due to errors *inside* these SDKs, rendering the analysis useless.

One of the best tool in debugging code cannot, unfortunately, be used to debug codes running on GPUs.

Debuggers

The last tool used in debugging is an actual debugger. A normal debugger will take control of the program, allowing the developer to pause the execution at any time, inspect variables' values or even change them. A popular debugger on Linux is the free and open-source *gdb*, the GNU Project debugger[12]. Many more proprietary debuggers exist, some of them free and others expensive. Traditional debuggers work by taking control of the program and accessing directly their memory content. It is not possible for them to access GPU memory or control functions inside the different SDKs. Some debuggers, like the pricey but powerful DDT[13] allow some form of debugging capabilities on video cards. A free one called gDEBugger[14] supported debugging OpenCL kernels. It was acquired by AMD which released an updated version[15] in April 2012 but discontinued it. It was superseded by CodeXL[16] released in February 2013. As can be seen, at the time the code was developed the different debuggers available were scarce, limited or expensive but are now maturing.

HPC Facilities

While high performance computing (HPC) are relatively widespread and accessible, GPU clusters are harder to find. SHARCNET[17], a large HPC consortium, has two clusters containing GPUs (Angel and Monk) but they are obviously submerged by user demand.

Prof. Thomas Brabec and my supervisor Prof. Lora Ramunno were able to purchase a GPU cluster, spurring the development of the GPU codes described above.

Due to my experience with GPUs, I was placed in charge of the purchase process

[12] https://www.gnu.org/software/gdb/
[13] http://www.allinea.com/products/ddt/
[14] http://www.gremedy.com/
[15] http://developer.amd.com/tools-and-sdks/heterogeneous-computing/amd-gdebugger/
[16] http://developer.amd.com/tools-and-sdks/heterogeneous-computing/codexl/
[17] https://www.sharcnet.ca/

which consisted in building a solution that would maximize performance while staying under-budget, communicating with multiple vendors to validate the solution, writing a Request for Proposals (RFP) and transparently evaluating vendors offering. Additionally, I (remotely) installed and configured the operating system (Gentoo Linux[18]) before the equipment was shipped in August 2012 and also configured the queuing system (Slurm[19]) to maximize the cluster's resources and even submitting new features[20].

This HPC cluster (Primus), containing 20 Nvidia Tesla M2075 video cards, is an important lab component that will allow the research group to continue its high profile research.

2.7 Libraries

Additionally to the MD and QFDTD packages, eight libraries were developed to support some generic features shared between the two.

2.7.1 timing.git

This library includes timing routines used to measure running time, estimated time of arrival (ETA), code profiling, etc. It consists of 1,300 lines of C++ code and can be found here: https://gitlab.cphoton.science.uottawa.ca/nbigaouette/timing.

2.7.2 stdcout.git

Add logging features allowing saving the output of any code execution to a (compressed or not) log file consisting of 500 lines of C++ code. Can be found here: https://gitlab.cphoton.science.uottawa.ca/nbigaouette/stdcout.

2.7.3 prng.git

A pseudo-random number generator (PRNG) library. Wrapper around dSFMT [98], a SIMD-oriented Fast Mersenne Twister implementation. Defines easy to use PRNG functions, distributions, seed, etc. Keeps track of the seed and how many times pseudo-random numbers were generated, allowing to replay the series in case of simulation reloading. 500 lines of C++ code (not counting dSFMT) and found here: https://gitlab.cphoton.science.uottawa.ca/nbigaouette/prng

[18] http://www.gentoo.org/
[19] http://www.schedmd.com
[20] http://slurm.schedmd.com/team.html

2.7.4 memory.git

Some wrappers around malloc() and calloc() that will automatically check that memory allocation succeeded. Will also keep track of the amount of memory allocated and allow setting a maximum value, preventing over-allocation due to bugs or user errors. Can also return the binary representation of a number as a string for easier debugging. 1,200 lines of C++ code. Available here:
https://gitlab.cphoton.science.uottawa.ca/nbigaouette/memory

2.7.5 io.git

Input and Output library. Includes wrappers around TinyXML library [99] for reading simulation input files in XML format, wrappers around NetCDF [100] for self-contained output files, used for both post-processing and simulation snapshots. 2,950 lines of C++ code (not counting TinyXML). Available here:
https://gitlab.cphoton.science.uottawa.ca/nbigaouette/io

2.7.6 libpotentials.git

Functions implementing and abstracting different potential shapes as described in chapter 2.2. 4,300 lines of C++ code. Available here:
https://gitlab.cphoton.science.uottawa.ca/nbigaouette/libpotentials

2.7.7 oclutils.git

Library to ease the use of OpenCL devices. Allows listing and selecting the best GPU available on a workstation and locking it to prevent other simulations from using it. Contains an array abstraction to ease the transfer of data from the host (main memory) to device (GPU memory) and vice-versa. Also includes a SHA512 checksum check to validate memory and detect any issue during transfers. 3,300 lines of C++ code. Available here: https://gitlab.cphoton.science.uottawa.ca/nbigaouette/oclutils

2.7.8 get_libraries.git

Simple script that will download all the required libraries or update them to the lasted version from git, compile them and install them in the user's directory. 240 lines of bash code. Available here:
https://gitlab.cphoton.science.uottawa.ca/nbigaouette/get_libraries

2.7.9 Ionization library

All ionization processes described in chapter 1.2 and consisting of 18,000 lines of C++ code. The library is available here:
https://gitlab.cphoton.science.uottawa.ca/nbigaouette/ionization

The ionization library is a large part of the work as can be seen by the amount of line of code. Each ionization processes of chapter 1.2 have a function that, when called, will iterate over the list of ions and calculate if the ionization takes place or not. In the case of collisional processes (impact ionization and ACI), the iteration is over electrons instead. The MD stores each electrons' nearest neighbour in a flag, allowing the ionization library to calculate the required values for ionization.

To keep the library generic (so it can be used with other simulation packages, not just the MD developed here), the library does not explicitly create electrons (or recombine them). It instead calls functions that *must* be defined in the simulation package for the exact values to set.

3

Augmented collisional ionization via excited states in XUV cluster interactions

Edward Ackad, Nicolas Bigaouette, Lora Ramunno
Journal of Physics B: Atomic, Molecular and Optical Physics
44(16), August 2011, 165102
doi:10.1088/0953-4075/44/16/165102

Author contributions

The MD package was mostly written by N. B. The post processing scripts used to analyze data and generate figures were entirely written by N. B. Generated figures were then tweaked by E. A. for inclusion. Cross-sections for ACI were calculated by E. A. who wrote a large part of the article text. All authors contributed to the discussion.

J. Phys. B: At. Mol. Opt. Phys. **44** (2011) 165102 (5pp) doi:10.1088/0953-4075/44/16/165102

Augmented collisional ionization via excited states in XUV cluster interactions

Edward Ackad, Nicolas Bigaouette and Lora Ramunno

Department of Physics, University of Ottawa, Ottawa, Ontario K1N 6N5, Canada

Received 9 March 2011, in final form 25 May 2011
Published 25 July 2011
Online at stacks.iop.org/JPhysB/44/165102

Abstract
The impact of atomic excited states is investigated via a detailed model of laser–cluster interactions, which is applied to rare gas clusters in intense femtosecond pulses in the extreme ultraviolet (XUV). We investigate a two-step ionization process via excited atomic states, which allows the creation of high charge states and rapid dissemination of laser energy. Through simulations corresponding to recent argon cluster–XUV experiments, this two-step process is shown to play a primary role; this is consistent with our hypothesis that XUV–cluster interactions provide a unique window into the role of excited states due to the relative lack of photoionization and laser field-driven phenomena. Our analysis suggests that excited states may be important for material interactions with intense radiation in a variety of wavelength regimes, including potential implications for proposed studies of single-molecule imaging with intense x-rays.

(Some figures in this article are in colour only in the electronic version)

Over the last decade, coherent radiation sources have been developed that can probe light–matter interactions at ever smaller wavelengths and unprecedented intensities [1, 2]. Recent experiments have moved into the extreme ultraviolet (XUV), including several that have explored intense XUV interactions with rare gas clusters [3, 4]. The XUV regime near 30 nm is unique because the photon energy is too small for inner shell ionization of rare gas atoms [5], yet too large (at reported intensities) for any appreciable laser-field-driven processes that dominate intense laser–cluster interactions at longer wavelengths, such as collisional heating. We therefore propose that this regime presents a unique opportunity to isolate the influence of the internal electronic structure of atoms within clusters on intense radiation–cluster interactions.

To date, microscopic models of cluster interactions with intense radiation in the near IR [6] or vacuum ultraviolet (VUV) [7–10] have not incorporated effects of excited electronic states of constituent atoms and ions. As a result, its influence in such interactions is unknown over a broad wavelength range, including the XUV.

In this paper, we introduce a general model that explicitly incorporates the effect of atomic and ionic excited states on collisional ionization, and apply it to a molecular dynamics code for rare gas cluster interactions with intense radiation. By including the process whereby a ground-state electron of any charge species can be internally promoted to an excited state by a colliding electron, ionization is allowed to occur through a two-step process: excitation followed by ionization from the excited state. This requires two sequential collisions, each of less energy than is required by single-step collisional ionization from the ground state. This generally applicable two-step process, which we call 'augmented collisional ionization' (ACI), is applied to the 32 nm experiment with argon clusters [3]. ACI is found to dominate, allowing the system to access higher charge states than the single-step collisional ionization process alone.

The incorporation of ACI into our laser–cluster interaction model provides the first explanation of the observation of high charge states (Ar^{4+}) in the 32 nm system. Further, we find that cluster atoms quickly become excited and then ionized through ACI, demonstrating that the pulse energy is spread rapidly through the cluster. This work therefore provides a fundamental insight into the dynamics of XUV–cluster interactions, an area that has, to date, been the subject of only a small number of theoretical investigations [3, 4, 11, 12], none of which accounted for the experimentally observed high charge state. A multistep ionization model was proposed that explained the electron spectra for all but the highest pulse intensities [3]. Other theoretical investigations of the electron emission spectra using a kinetic Boltzmann

model including non-equilibrium and equilibrium dynamics [11] and using both Monte Carlo and molecular dynamics simulations [12] give possible accounts of the significant low-energy electron yield.

We find that excited states in collisional systems play a crucial role in understanding both the charge state spectrum and how quickly charge states are produced due to increased energy transfer between electrons and ions. Although the XUV provides a unique regime in which to study these effects, our results are more generally applicable. This work thus opens the door to the study of the importance of excited states in other material systems and in wavelength regimes ranging from the infrared to x-rays. Further, the more rapid energy transfer to ions through the ACI process could also affect explosion dynamics, which may be an important consideration in proposed single-molecule imaging studies with intense x-rays [13].

1. Method

The motion of the ions and electrons is calculated via classical molecular dynamics. Quantum effects are included by determining transition cross-sections and using a Monte Carlo scheme to determine when excitation or ionization occurs. In the case of ionization, a free electron is added to the dynamics simulation. The new electron's total energy with respect to the outer ionization threshold is dependent on the local field and thus its radial position in the cluster. In the case of excitation, no new electron is added, but the parent atom/ion is set to be in an excited state, which determines its future ionization potential and cross-section.

The photoionization probability is calculated at each time-iteration for every atom and singly charged ion, and this is used to determine if a photoionization event is to occur. The photon flux is determined via the intensity, which is modulated by the pulse time profile and photon absorption. Since we are interested primarily in the generation of the high charge state, we do not average over the spatial profile of the pulse when determining charge state populations, but rather consider only the peak intensity.

The cross-section for the photoionization of neutral argon was obtained from [14], while those of ionic argon were obtained using Los Alamos atomic physics codes [15].

The atom–electron collision in the cluster environment is modelled as an isolated atom–electron collision in a background cluster potential. This allows the collisional cross-sections for both the ionization and excitation to be calculated using an isolated atom–electron model; we include these cross-sections for up to Ar^{6+}.

Single-step collisional ionization cross-sections were calculated using the Lotz formula [16]. The Born plane-wave approximation [17] was used for both excitation and ionization from an excited state, similar to [18]. Computed collisional excitation cross-sections were compared to experimentally measurable excitations to metastable states; our results for neutral argon closely match the experimental results for the metastable part of the $3p^6 \rightarrow 3p^5 4s$ excitation ($^3P_0$ and $^3P_2$) [19].

The subset of excited states used consist of single-electron states with $l < 4$, which are the lowest energy states and thus the most important. Including more excited states adds to the total collisional cross-section, although states near the threshold require almost as much energy as ionization and are thus almost as infrequent. The energy of the excited states and the cross-sections were obtained using the Hartree–Fock implementation of the Cowan code [17]. We found that there is some distortion of these excited states for neutrals next to bare Ar^{4+} ions; however, its effect is negligible since this situation does not occur within the simulations.

The inclusion of excited states does not alter photonionization. This is because photoexcitation away from a resonance is rare as only states of $|\Delta l| = 1$ are accessible. The photon wavelength must also be approximately equal to the transition energy. In electron–atom collisions, in contrast, the electron can transfer any amount of its orbital angular momentum and available kinetic energy.

The influence of the cluster is accounted for by determining the potential V_p at the atom due to all particles farther than the nearest neighbour distance, R (>6.4 Bohr for argon), and approximating it as a constant external potential in the vicinity of the atom. The potential at the atom is reinterpreted as the cluster-free threshold of the atom, similar to [9].

This approximation is justified by considering an atom at $\vec{r} = 0$ that is surrounded by two neighbouring ions on the z-axis at $\pm\vec{R}$, representing the nearest neighbours in one orthogonal direction with arbitrary charge states Z_1 and Z_2; this is easily generalized to include neighbours in other directions. Both neighbours contribute a constant term, Z/R, to the Hamiltonian of the atom which merely shifts the threshold. Using first-order perturbation theory, the lowest order correction to the eigenvalue is

$$\Delta E = -\frac{Z_1 + Z_2}{R^3} \langle \phi_0 | \hat{q} | \phi_0 \rangle , \qquad (1)$$

where $\hat{q}$ is the quadrupole operator. The state ϕ_0 is an eigenstate of the atomic Hamiltonian, and therefore the angular momentum operator, making the dipole term zero. The potential of the electrons within $R/2$ of the atom is also removed from V_p. The collisional system therefore closely approximates an isolated system as the error is primarily quadrupole.

The screening effects of the electrons within $R/2$ on the ionization potential are not easily modelled microscopically due to the highly collisional nature of the system. Screening effects, if present, would only alter the relative energy of the steps for excitation and ionization, but the energy steps for ACI would still be significantly smaller than those for single-step ionization. Thus this would not change the relative importance of ACI over single-step ionization.

During a collision, the energetically accessible states are determined by the kinetic energy of the impacting electron relative to the target atom's cluster-free threshold. This includes ionization if energetically permissible. The total cross-section for all of the possible final states is used to determine if any excitation or ionization event will occur. If the electron's impact parameter, $b = |\vec{v} \times \vec{r}|/|\vec{v}|$, is within this

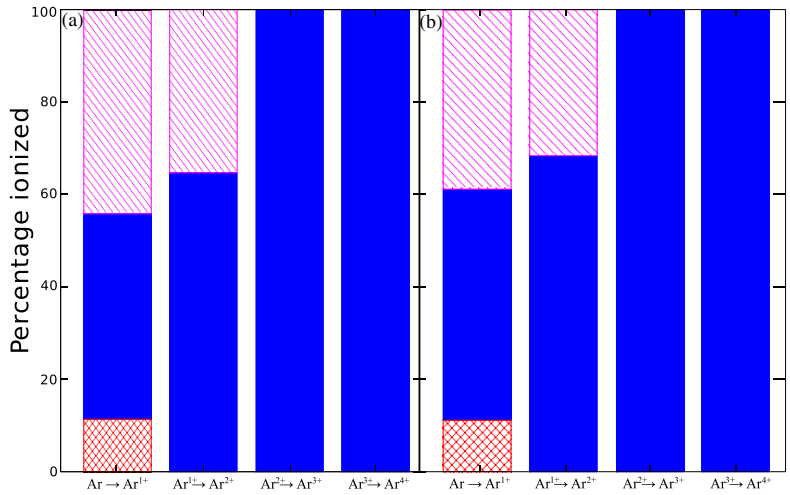

Figure 1. The relative contributions of photoionization (diagonal lines), single-step ionization (cross-hatching) and ACI (solid) in the creation of each ion species of argon by the interaction of (a) Ar_{80} and (b) Ar_{147} with 32.8 nm radiation at 5×10^{13} W cm^{-2}.

total cross-section, then a state is chosen at random, weighted by its cross-section relative to the total cross-section.

We have not included mechanisms for excited state decay. While it is possible for the excited states to decay radiatively, the shortest lived states will be the states of $|\Delta l| = 1$. These decays are on the nanosecond scale [20, 21], thus unlikely to affect our results.

Collisional de-excitation, which entails an impact electron gaining energy by de-exciting the atom, is more probable though still unlikely to play a role. This is because the cross-section for ionization from an excited state is much larger than the de-excitation cross-section, favouring ionization provided the impact electron has the small amount of energy needed to ionize. Further, even if we were to allow collisional de-excitation to occur, it would be unlikely to significantly alter our results, since any impact electron that would gain energy would more than likely use that extra energy to excite or ionize another atom, leading to the same results, on average.

2. Results

We simulated the interaction of argon clusters exposed to 32.8 nm radiation both with and without the ACI mechanism included. Conventional collisional ionization was included in all simulations. We used a pulse width of 25 fs and varied the intensity from 5×10^{13} to 10^{14} W cm^{-2}. Although the average cluster size in [3] was 80 atoms, a population of larger clusters is possible in the cluster jet. Thus we considered two sizes: Ar_{80} and the closed-shell icosahedral structure Ar_{147}. The smaller closed-shell icosahedral Ar_{55} may also be present but would likely have a much smaller contribution to the Ar^{4+} signal. For each parameter set, we performed 10^4 simulations. We ran each Ar_{80} simulation to 800 fs and each Ar_{147} simulation to 1 ps.

In table 1, we list the average yield of Ar^{4+} per cluster for each set of simulations. It shows that Ar^{4+} emerges at the intensity quoted in [3] only when ACI is included. Without ACI, Ar^{4+} do occur at higher intensities, though the yield is orders of magnitude less than when ACI is included. While we see an increase in the number of Ar^{4+} in the larger versus smaller clusters, the influence of cluster size is still smaller than the increase from the ACI ionization channel. Thus we find that, at all intensities, ACI is the single largest effect.

Table 1. Average yield of Ar^{4+} at different intensities for argon cluster sizes of 80 and 147, with (third column) and without (second column) ACI included.

	ACI	
Intensity (W cm^{-2})	No	Yes
Ar_{80}		
5×10^{13}	0	0.0114
7.5×10^{13}	0.0002	0.0601
10×10^{13}	0.0008	0.1490
Ar_{147}		
5×10^{13}	0	0.0338
7.5×10^{13}	0.0008	0.1510
10×10^{13}	0.0037	0.4183

To further illustrate the dominance of ACI, figure 1 plots that fraction of each ionization channel that led to the creation of the various charge states: photoionization is represented by diagonal line fill, ACI by solid fill and single-step collisional ionization by cross-hatch fill. The left histogram is for Ar_{80}, and the right for Ar_{147}. Photoionization contributes only to the creation of Ar^{1+} and Ar^{2+}, as expected. Since the percentage of photoionization is lower in the larger cluster, we see that clusters become more collisional as their size increases. Single-step collisional ionization contributes significantly only to the creation of Ar^{1+}. ACI, however, dominates the creation of Ar^{2+} to Ar^{4+}, and is the exclusive mechanism for the creation of Ar^{4+}.

Next, we examine the dynamics of the interaction to further explore the role of ACI and the prevalence of the excited

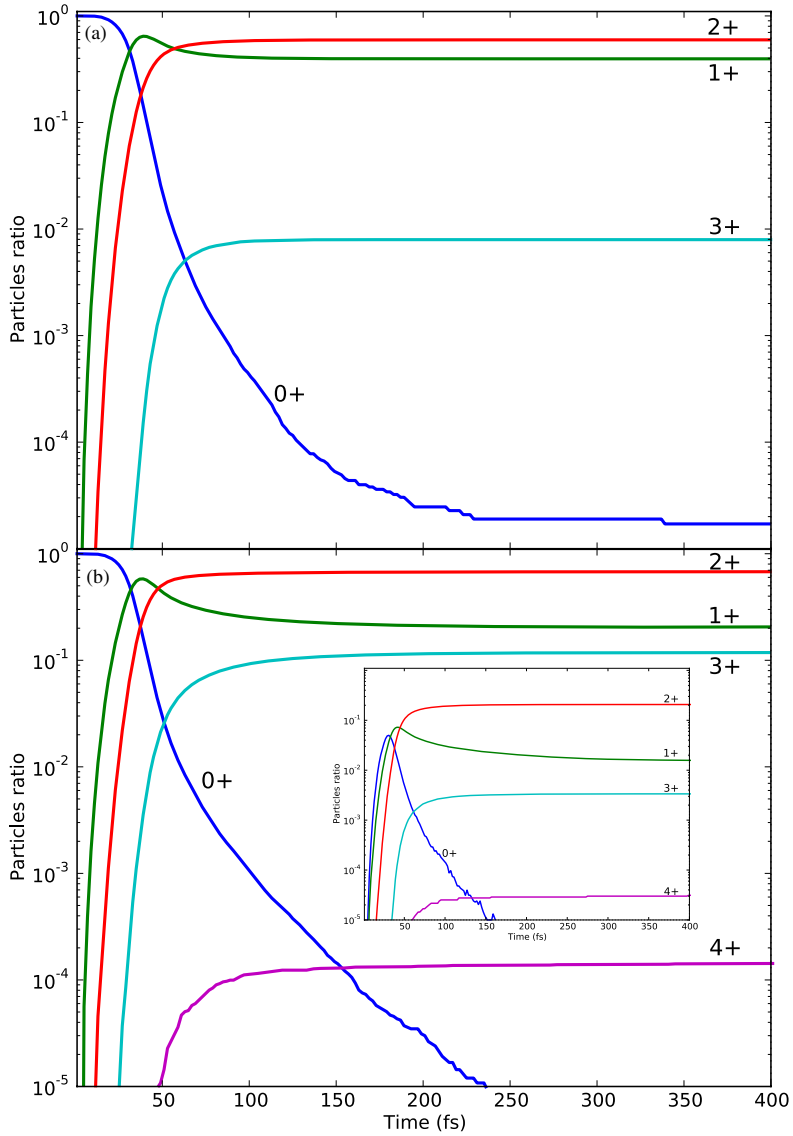

Figure 2. The (normalized) charge species populations versus time for Ar_{80} interaction with 32.8 nm radiation, without (a) and with (b) ACI. The inset in (b) gives the relative excited charge species population versus time.

states. Figure 2 plots the relative (inner ionized) charge state population versus time for Ar_{80} both without (top) and with (bottom) ACI included for a 25 fs laser pulse which starts at the origin and peaks at around 34 fs. With ACI, the higher charge states appear earlier and in greater abundance. The peak in Ar^{1+} happens roughly 2 fs earlier with ACI, the Ar^{2+} surpasses Ar^{1+} 10 fs earlier and a sizable Ar^{3+} population emerges 7 fs earlier and surpasses the atomic population around 12 fs earlier than without ACI. The final abundance of Ar^{3+} is more than an order of magnitude larger when ACI is present. In both cases, the Ar^{2+} is the most abundant species at the end, but the ratios between species populations are very different. With ACI we also see the emergence of Ar^{4+}, which appears at the tail of the laser pulse but reaches a plateau around 100 fs later, at which time it surpasses the abundance of atoms.

The shapes of the curves in figure 2 can be understood by regarding the ensemble results in terms of a rate equation model in which population flows from neutral atoms to the higher charge states by ionization couplings. We find that the neutral population decreases rapidly only once the laser has approached its peak. Afterwards population largely flows to the ion charge states by a mix of further photoionization (minor) and collisional ionization (dominant). The earlier crossings mentioned above and the larger populations of Ar^{2+}, Ar^{3+} and Ar^{4+} obtained in figure 2(b) are due to the increased coupling of the different ion charge states by allowing for the collisional excitation step and ACI. In both cases there continues to be a decrease in the Ar^{1+} population after the laser pulse due to collisions, although the decrease is much larger when ACI is included.

The inset in figure 2 displays the fraction of each charge species that is in excited states as a function of time. The abundance of excited states (after the pulse peak) closely follows that of the internal charge states; a sizable fraction of each charge species is excited. Most ions remain excited for less than a few femtoseconds due to being ionized via collisions with previously ionized cluster-bound electrons.

Figure 1 shows that virtually all Ar^{3+} and Ar^{4+} are ionized by ACI. Figure 2 shows that these populations grow significantly once the laser pulse is finished (as they are due to ACI) and that these collisional processes are still frequent after the laser.

ACI thus allows the cluster to reach high charges and to do so earlier than otherwise possible. This is a result of having a significant proportion of each charge species excited. Consequently, impact electrons do not require as much kinetic energy to ionize the excited electrons as single-step ionization or as the excitation step itself. The final charge state spectra indicated in figure 2 were generated by runs at a single intensity, which would represent only the peak region of the laser pulse.

3. Conclusion

In summary, we found that the detection of Ar^{4+} in [3] can be explained by augmented collisional ionization (ACI), a two-step process wherein collisional ionization occurs via intermediate excited states. ACI was found to dominate; it occurs much more frequently than single-step collisional ionization from the ground state which alone cannot reproduce the high charge state. While we applied our model to cluster–XUV interactions, ACI will likely play a role in any highly collisional system, including in a variety of finite condensed systems interacting with intense radiation in a wide range of wavelength regimes.

We have also shown that ACI provides a route to high charge states in a shorter time, due to the efficacy of the energy transfer afforded by the lower energy gaps of excitation compared to direct ionization. The energy imparted to a small finite system will thus be highly sensitive to the ramp up of the pulse, which may have consequences for the direct imaging of single biomolecules with short, intense x-ray pulses. Thus a good understanding of the excited states of the photo-sensitive parts of the biomolecule (i.e. atoms and molecules that have largest photoionization cross-sections) and a sharp ramp up of the imaging pulse will be crucial.

Acknowledgments

The authors would like to thank Thomas Brabec, Paul Corkum and Jean-Paul Britcha for many fruitful discussions. This work is supported by NSERC, MRI and CFI.

References

[1] Wabnitz H *et al* 2002 Multiple ionization of atom clusters by intense soft x-rays from a free-electron laser *Nature* **420** 482
[2] Young L *et al* 2010 Femtosecond electronic response of atoms to ultra-intense x-rays *Nature* **466** 56
[3] Bostedt C *et al* 2008 Multistep ionization of argon clusters in intense femtosecond extreme ultraviolet pulses *Phys. Rev. Lett.* **100** 133401
[4] Murphy B F, Hoffmann K, Belolipetski A, Keto J and Ditmire T 2008 Explosion of xenon clusters driven by intense femtosecond pulses of extreme ultraviolet light *Phys. Rev. Lett.* **101** 203401
[5] Gnodtke C, Saalmann U and Rost J M 2009 Ionization and charge migration through strong internal fields in clusters exposed to intense x-ray pulses *Phys. Rev.* A **79** 041201
[6] Fennel Th *et al* 2010 Laser-driven nonlinear cluster dynamics *Rev. Mod. Phys.* **82** 1793–842
[7] Siedschlag C and Rost J-M 2004 Small rare-gas clusters in soft x-ray pulses *Phys. Rev. Lett.* **93** 043402
[8] Santra R and Greene C H 2003 Xenon clusters in intense VUV laser fields *Phys. Rev. Lett.* **91** 233401
[9] Fennel T, Ramunno L and Brabec T 2007 Highly charged ions from laser–cluster interactions: local-field-enhanced impact ionization and frustrated electron-ion recombination *Phys. Rev. Lett.* **99** 233401
[10] Jungreuthmayer C, Ramunno L, Zanghellini J and Brabec T 2005 Intense VUV laser cluster interaction in the strong coupling regime *J. Phys. B: At. Mol. Opt. Phys.* **38** 3029–36
[11] Ziaja B, Wabnitz H, Weckert E and Möller T 2008 Femtosecond non-equilibrium dynamics of clusters irradiated with short intense VUV pulses *New J. Phys.* **10** 043003
[12] Arbeiter M and Fennel T 2010 Ionization heating in rare-gas clusters under intense XUV laser pulses *Phys. Rev.* A **82** 013201
[13] Chapman H N 2009 X-ray imaging beyond the limits *Nat. Mater.* **8** 299
[14] Marr G V and West J B 1976 Absolute photoionization cross-section tables for helium, neon, argon, and krypton in the VUV spectral regions *Atomic Data Nucl. Data Tables* **18** 497
[15] Archer B J, Clark R E H, Fontes C J and Zhang H 2000 Gipper user manual *LA-UR-00-5693*
[16] Lotz W 1967 An empirical formula for the electron-impact ionization cross-section *Z. Phys.* A **206** 205
[17] Cowan R D 1981 *The Theory of Atomic Structure and Spectra* (Berkeley, CA: University of California Press)
[18] Micheau S, Bonte C, Dorchies F, Fourment C, Harmand M, Jouin H, Peyrusse O, Pons B and Santos J 2007 Dynamics of rare gas nanoclusters irradiated by short and intense laser pulses *High Energy Density Phys.* **3** 191–7
[19] Borst W L 1974 Excitation of metastable argon and helium atoms by electron impact *Phys. Rev.* A **9** 1195–200
[20] Bruce M R, Layne W B, Whitehead C A and Keto J W 1990 Radiative lifetimes and collisional deactivation of two-photon excited xenon in argon and xenon *J. Chem. Phys.* **92** 2917–26
[21] Eichhorn C, Fritzsche S, Löhle S, Knapp A and Auweter-Kurtz M 2009 Time-resolved fluorescence spectroscopy of two-photon laser-excited 8p, 9p, 5f, and 6f levels in neutral xenon *Phys. Rev.* E **80** 026401

4

Clusters in intense XUV pulses: Effects of cluster size on expansion dynamics and ionization

Edward Ackad, Nicolas Bigaouette, Kyle Briggs and Lora Ramunno
Physical Review A 83(6), June 2011, 063201
doi:10.1103/PhysRevA.83.063201

Author contributions

The MD package was mostly written by N. B. Most post processing scripts used to analyze data and generate figures were written by N. B. and tweaked by E. A. The article text was written by E. A. with some corrections by N. B. Data acquisition was done by both N. B. and E. A. All authors contributed to the discussion.

Clusters in intense XUV pulses: Effects of cluster size on expansion dynamics and ionization

Edward Ackad, Nicolas Bigaouette, Kyle Briggs, and Lora Ramunno
Department of Physics, University of Ottawa, Ottawa, Ontario K1N 6N5, Canada
(Received 1 November 2010; published 27 June 2011)

We examine the effect of cluster size on the interaction of Ar_{55}-Ar_{2057} with intense extreme ultraviolet (XUV) pulses, using a model we developed earlier that includes ionization via collisional excitation as an intermediate step. We find that the dynamics of these irradiated clusters is dominated by collisions. Larger clusters are more highly collisional, produce higher charge states, and do so more rapidly than smaller clusters. Higher charge states produced via collisions are found to reduce the overall photon absorption, since charge states of Ar^{2+} and higher are no longer photoaccessible. We call this mechanism *collisionally reduced photoabsorption*, and it decreases the effective cluster photoabsorption cross section by more than 30% for Ar_{55} and 45% for Ar_{2057}. The time evolution of the electron kinetic energy distribution begins as a (mostly) Maxwellian distribution. Further, the electron velocity distribution of large clusters quickly become isotropic while smaller clusters retain the inherent anisotropy created by photoionization. Last, the total electron kinetic-energy distribution is integrated over the spatial profile of the laser and the log-normal distribution of cluster size for comparison with a recent experiment [C. Bostedt *et al.*, Phys. Rev. Lett. **100**, 133401 (2008)], and good agreement is found.

DOI: 10.1103/PhysRevA.83.063201 PACS number(s): 36.40.Wa, 34.80.Dp, 52.65.−y

I. INTRODUCTION

The interaction of atomic clusters with intense ultrafast laser pulses has been investigated over a range of wavelengths in recent years. Most of this work has been in the infrared (IR) regime [2], but as new very intense shorter wavelength sources have come online, this interaction has been investigated up to the soft-x-ray [3–10].

Cluster interaction with intense laser pulses is highly wavelength dependent. In the IR, tunnel ionization and electron heating processes dominate and the subsequent plasma dynamics are driven by the laser field itself [2,11]. This is not true at shorter wavelengths. Experiments on clusters in the vacuum ultraviolet (VUV) regime near 100 nm [12] observed unexpectedly high ionic charge states and a much larger energy absorption than predicted by existing models [7]. This sparked a concerted theoretical effort over the last eight years. Santra *et al.* proposed an enhancement to inverse bremsstrahlung heating (IBH) due mainly to using self-consistent potentials for ions [13] and later plasma screening effects [14]. Jungreuthmayer *et al.* proposed a many-body dielectric recombination scheme for the strongly coupled plasma electrons in the cluster whereby the electrons could then be driven by the laser field to reionize [15]. Siedschlag *et al.* proposed allowing photoionization to occur above the classical potential barrier of the neighboring ion [16]. Ziaja *et al.* incorporated many of these and found they all played various roles depending on the intensity [17]. It is clear from these works that clusters irradiated by short laser pulses with wavelengths in regime of single photon ionization represent a new and theoretically challenging area of physics.

Recent experiments around 40 nm have begun to probe the regime in which the photoelectron has a significant amount of kinetic energy and ions are photoaccessible [1,18]. Contrary to the longer wavelength regimes, the laser field coupled very weakly to the cluster electrons, producing a photoelectron spectrum with almost no signal above the atomic photoelectron energy in gas. The lower energy region showed that the cluster was charging and cooling subsequent photoelectrons down to lower energy. The clusters also produced high charge states well above what was detected in gas. This interaction was also found to depend on cluster size [1,18]. Further, it was found that even small clusters emitted ions with very little kinetic energy (less than 30 eV) [1]. An attempt to address the charge transfer and explore the explosion dynamics was done using heterogeneous clusters [9,19] at 13 nm. Other work at 13 nm examined the disintegration of the cluster [6] through the electron spectrum [20]. Many aspects of these 13-nm experiments are not well understood even in gases [21].

The extreme ultraviolet (XUV) regime offers unique opportunities in the study of the dynamics of finite systems such as clusters [22,23]. Single photon ionization from the ground state of rare-gas atoms is accessible, though inner-shell ionization is not. In addition, unlike in the IR and VUV, the IBH of freed electrons is negligible, due to the very low quiver energy, decoupling cluster plasma dynamics from the laser field [24,25]. However, electrons ionized from atoms have a significant amount of kinetic energy, enough to collisionally ionize neutral argon. Thus the XUV regime is special owing to the lack of mechanisms found in the IR [2], VUV [25], and soft-x-ray [26]; see Ref. [27] for a review of these.

To date, there have only few theoretical works in this regime, however. Bostedt *et al.* proposed a multistep model to explain the photoelectron spectrum of their experiment on small argon clusters exposed to intense 32-nm laser pulses [1]. Single-photon ionization events were determined based on a Monte Carlo model, and after each ionization step an electron is emitted from the cluster with an energy that depended upon building positive space charge of the cluster. Ziaja *et al.* also examined the photoelectron emission spectrum, but used a kinetic Boltzmann equation technique that was then compared to molecular-dynamics simulations results [24]. They found good agreement with the measured electron emission spectrum and showed that IBH was insignificant at 32 nm. Arbiter *et al.* used a molecular-dynamics and Monte Carlo technique to look at the electron emission spectrum at different intensities finding that at high intensity there are a significant number of thermal electrons emitted from the cluster [28].

Most recently, we showed the importance of two-step collisional ionization via an intermediate excited state in a microscopic model [29]. This model allowed atom and ions to first be excited by an impact electron, which requires much less energy than ionization, and then ionized from the excited state. We called this model augmented collisional ionization (ACI) and were able to reproduce the highest charge state seen in Ref. [1]. This paper gives a detailed analysis of argon cluster interaction with intense 32-nm laser pulses, including examining the cluster explosion dynamics and how these depend upon cluster size, and how collisional processes lead to a reduction of photoabsorption by the cluster, which we call collisionally reduced photoabsorption (CRP). Understanding cluster dynamics in the XUV regime, while interesting in its own right, may also inform planned single shot large molecule imaging experiments at even shorter wavelengths [30,31].

The paper is organized as follows. In Sec. II we describe the model and including details of how photoionization, collisional ionization, and augmented collisional ionization (ACI) are implemented. Section III presents the results for argon clusters of size 55, 147, 561, and 2057 atoms, with Sec. III A concentrating on ions and Sec. III B on electrons. In Sec. III B 3 we obtain the calculated photoelectron spectrum corresponding to the experimental results of Ref. [1], and find good agreement. Finally, Sec. IV gives a summary of all the results. Atomic units ($\hbar = e = \mathrm{m}_e = 1$) are used throughout unless otherwise specified.

II. THEORY

In this work we use hybrid approach to simulate the time evolution of argon clusters in an XUV radiation field, where classical molecular dynamics is used for ion and electron motion and a Monte Carlo scheme is used to determine ionization events. Ionization rates are determined by the quantum-mechanical transition cross section for the various processes. The simulation begins with a neutral cluster of atoms. Ionization events result in electrons being created within the code, and in an increment in the charge state of the the parent neutral or ion. Collisional excitation events are also permitted, whereby a neutral or ion may become excited; in this case no new electron is added to the simulation but the parent neutral or ion is set to be in an excited state, which determines its future ionization potential and ionization cross section.

In order to mitigate numerical heating, the classical motion of particles was calculated assuming the particles were Gaussian distributions, instead of point particles, via the following smoothed potential:

$$\phi = \begin{cases} Q/r & r \geqslant \sigma, \\ QB \exp\left[-\frac{1}{2}\left(\frac{r}{\sigma}\right)^2\right] & r < \sigma, \end{cases} \tag{1}$$

where r is the radial distance, B is the maximum potential depth for a singly charged ion, Q is the charge, and σ is an effective smoothing radius given by

$$\sigma = \frac{Q}{B} \exp\left(\frac{1}{2}\right). \tag{2}$$

Note that ϕ is continuously differentiable at the transition point $r = \sigma$. To ensure energy conservation, the potential of an electron and a singly charged ion are set to be equal in magnitude, and the potential depth of the multiply charged ions are integer multiples of that of the singly charged ion's potential depth. Newly ionized electrons are created at the same location as their parent ion to avoid dipole heating. This allowed for the use of a constant 5-as time step which produced negligible heating ($< 0.1\%$ increase in the total energy).

Ionization in the cluster environment is modeled as an isolated system within a background cluster potential. We take the cluster potential as constant over the outermost electron's wave function. Thus the cluster potential at the location of an ion or neutral is taken as the threshold for ionization for that ion or neutral. All ionization processes are then calculated with respect to this threshold. This allows for the use of atomic photoionization and collisional excitation and ionization cross sections with only a small error due to the approximation [29].

In the XUV, direct photoionization is the only way for the radiation field to deposit energy into the cluster. The single-photon ionization probability is determined at each time iteration for every neutral and ion, depending on its charge state and the photon flux. The photon flux is determined via the intensity, which is modulated both by the time profile of the pulse and by photon absorption. After each photoionization event the intensity of the pulse is decreased by one photon. This more accurately models low fluence pulses. The cross section for the photoionization of neutral argon was obtained from Ref. [32]. Those of ionic argon were obtained using Los Alamos Atomic Physics Codes [33]. Multiphoton ionization is negligible at this photon fluence [1].

Two channels are available for collisional ionization: a single-step transition from the ground state and a two-step transition through an intermediate excited state called augmented collisional ionization (ACI) [29]. Testing for collisional ionization was done once the projectile electron, going toward the target atom or ion, was within a 4-Bohr radius. The cross section of all energetically accessible states (excitation and ionization) are combined to give the total cross section for the occurrence of an event (whether excitation or ionization). If the impacting electron's trajectory is within this cross section an event will take place. A Monte Carlo scheme is used to determine which type of event takes place based on the relative weights of the cross section for each transition. Single-step collisional ionization cross sections were calculated using the semiempirical Lotz formula and coefficients found in Ref. [34].

The Born plane-wave approximation [35] was used for both excitation and ionization from an excited state, similar to Ref. [36]. Photoionization from excitation states is negligible due to the smaller cross section and photon flux in the XUV compared with the VUV [15].

The excited states considered consist of a subset of all possible excited states. Only single electron excited states were used and of those, only the lowest eight states with $l < 3$ were implemented. This subset is the most important as it contains the lowest energy states. Including more single electron excited states adds to the total collisional cross section, although states near the threshold require almost as much energy as ionization and are thus almost as infrequent. The

energies of the excited states and the cross sections were obtained using the Hartree-Fock implementation of the Cowan code [35] summing up to $l = 6$ and with a continuum spacing for ionization of 0.1 Rydberg. A linear interpolation was then used for cross sections between these values.

III. RESULTS

In this section we illuminate the details of the laser cluster interaction and determine the effects of cluster size on key measures of the cluster dynamics. These include ion charge state evolution and distribution, excited-state evolution, the relative importance of the relevant ionization channels, and electron energies and charge transfer. Generally, the interaction dynamics proceeds as follows. After the first few direct photoionizations, the cluster builds up a positive space charge such that at some point subsequent photoelectrons are prevented from escaping the cluster; this is described Ref. [1] via their multistep ionization model. Our model further allows the cluster-bound photoelectrons to either release further electrons via collisional ionization or cause collisional excitation of neutrals or ions in the cluster during and after the laser pulse.

The parameters of the radiation field for each data set were $\lambda = 32.8$ nm, $I = 5 \times 10^{13}$ W/cm^2, and a full width at half maximum of 25 fs. Closed-shell icosahedral argon clusters of 55 (two shells), 147 (three shells), 561 (five shells), and 2057 (eight shells) were used. These clusters were relaxed according to a Lennard-Jones potential for neutral argon. The results presented are for clusters assumed to be in the laser focus, and each plot is an ensemble average over many simulations, the number of which was chosen to ensure that more than 4×10^4 atoms are included in the average.

A. Ions

The charge states of the ions are a signature of the dynamics of intense laser cluster interaction. Charge states higher than what is accessible through photoionization is an indication that there are cluster-driven processes that are not present in intense laser interaction with the gas phase of the material. This occurs in clusters when the photon fluence is high enough to have at least a modest amount of photoionization within a single cluster, so that collisional processes become relevant. The parameter range of this work is such that the interaction is well above the collisional threshold.

1. Charge state

In argon gas targets, only the Ar^{2+} is accessible via direct photoionization. However, experiments with clusters have detected higher charge states indicating the importance of cluster-driven processes such as collisions [29]. Figure 1 plots our calculated charge state distribution for argon clusters of sizes (a) 2057, (b) 561, (c) 147, and (d) 55, for the laser parameters listed above. Though photoionization stops after the laser pulse has passed, collisional ionization and excitation can still occur. Thus these snapshots were taken after these processes also stopped, at 1 ps after the pulse. The bare charge states are reported.

We see that the average charge state increases with cluster size. This is despite the fact that larger clusters have fewer

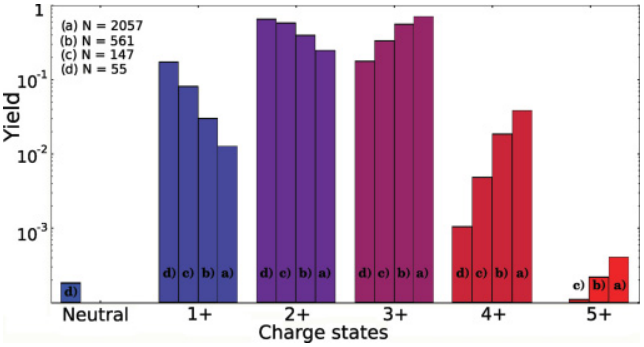

FIG. 1. (Color online) The charge species yield per atom for (a) Ar_{2057}, (b) Ar_{561}, (c) Ar_{147}, and (d) Ar_{55} clusters interacting with a 25-fs, 32-nm laser pulse of 5×10^{13} W/cm^2. These snapshots were taken 1 ps after the pulse, after collisional events were no longer occurring.

photons per atom compared with smaller clusters. However, larger clusters develop a larger space charge, and thus there are a greater number of photoelectrons that become bound to the cluster. These can then precipitate a collisional ionization or excitation event. Further, in a larger cluster there are more available collisional ionization or excitation targets. As we will see later in Sec. IVA4, collisional processes dominate over direct photoionization in charge state creation above Ar^{1+}.

Figure 2 gives the ratio of the Ar^{3+} to Ar^{4+} yields per atom of as a function of cluster size. Simulation results for additional cluster sizes were included in this graph. The yields of both the Ar^{3+} and Ar^{4+} increase with cluster size, and moreover, the Ar^{4+} yield increases more rapidly than the Ar^{3+} decreasing the ratio. This rapid increase of the Ar^{4+} seen in Fig. 1 is thus not explained simply as an increase in Ar^{3+}, but indicates that collisional processes become more important for larger clusters. This is because it is only through collisional processes that charge states above Ar^{2+} can be created.

2. Charge state evolution

Our model also allows for the detailed tracking of each ion species during the interaction. The normalized population

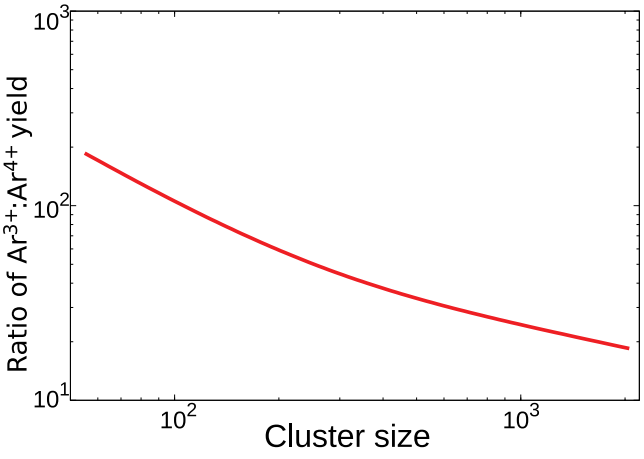

FIG. 2. (Color online) The ratio of the Ar^{3+} to Ar^{4+} yields per atom as a function of cluster size.

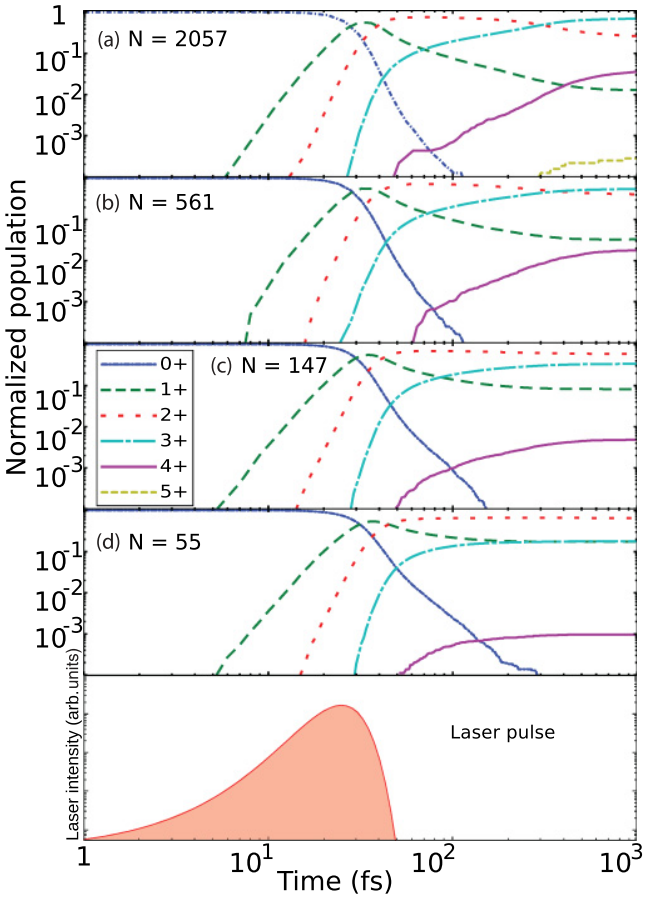

FIG. 3. (Color online) The charge species yield per atom as a function of time for (a) Ar_{2057}, (b) Ar_{561}, (c) Ar_{147} and, (d) Ar_{55} clusters interacting with a 25-fs laser pulse of 5×10^{13} W/cm^2. The bottom plot is the temporal profile of the 25-fs laser pulse.

of each charge state as a function of time is shown in Fig. 3 for different sized clusters. Each plot shows the fraction of atoms that are neutral (blue dashed-dotted lines), Ar^{1+} (green medium-dashed lines), Ar^{2+}(red sparsely dashed lines), Ar^{3+} (cyan long- and short-dashed lines), Ar^{4+} (magenta solid lines), and Ar^{5+} (yellow short-dashed line). At the bottom of the figure, we include a plot of the temporal profile of the Gaussian laser pulse. Note that a logarithmic scale is used for the time axis.

All clusters begin neutral and are initially ionized primarily by photoionization. The behavior of the low charge species early on is qualitatively similar for all cluster sizes. The population of neutrals decreases rapidly and is surpassed by the Ar^{1+} followed by the Ar^{2+}. The Ar^{2+} remains the most abundant charge state for the two smaller clusters. The larger clusters continue to have ionization well past 100 fs, and at around 300 fs the Ar^{3+} becomes (and remains) the most abundant. After 1 ps, almost no further collisional ionization occurs.

The abundance of the higher charge states is quite small during the actual laser pulse. Contrary to longer wavelength regimes, which are dominated by IBH, here photoionization is the only direct contribution of the laser pulse to charge state creation. The absorption of the XUV photons starts the ionization process, but the higher charge states appear in significant numbers only after the cluster has absorbed a sufficient amount of energy (as is further demonstrated in Sec. III B 1). At the intensity we consider, this begins only near the tail end of the laser pulse and continues for several hundred fs.

The crossings of the curves in Fig. 3 occur earlier for larger clusters. Given that there are fewer photons per atom for the larger clusters, this cannot be due to increased photoionization, and thus indicates that larger clusters are more efficient at dispersing the energy from the laser through increased collisions.

The location of the low charge state crossings all occur about 7 fs earlier for the Ar_{2057} compared with the Ar_{55}. This is almost 30% of the full width at half maximum of the laser pulse, and results in a significant decrease in how much energy the larger cluster can absorb from the laser. This is because more ions become transparent to the laser earlier due to collisions in the larger cluster, and thus do not absorb as many photons. If photoionization were the dominant process, the low charge state crossings for larger clusters would occur later, not earlier, than for the smaller clusters, due to the larger number of photons per atom for the smaller clusters.

The fact that the neutrals decrease in population faster in larger clusters due to increased collisional ionization processes has other consequences. Neutrals have the largest photoionization cross section. As their population decreases the overall photoionization cross section of the cluster as a whole will also decrease, further decreasing the importance of photoionization in the larger clusters. Further, photoionization increases the overall temperature of cluster-bound electrons, while it is decreased by collisional ionization. Thus the electron temperature would be smaller when collisional ionization of neutrals is included because cluster-bound photoelectrons ionized from the neutrals contribute more energy than those photoionized from the Ar^{1+}. Thus a decrease in the number of photoelectrons released from the neutrals would result in a decrease of the electron temperature. Thus if these effects are neglected, this could overestimate energy absorption of the cluster.

We quantify the reduction of total cross section and electron temperature due to collisions by performing our simulations with and without collisional processes included. Without collisional processes, we find Ar_{2057} absorbs 1840 photons on average, 1401 by neutrals and 439 by Ar^{1+}. With collisional processes included, Ar_{2057} absorbs 1151 photons, 618 by neutrals and 533 by Ar^{1+}. Thus the total number of photons absorbed is decreased by 37%, resulting in a 46% reduction in the amount of energy the electrons obtain from the laser. We call this *collisionally reduced photoabsorbtion* (CRP).

The effect is smaller in the less collisional smaller clusters. Without any collisional processes Ar_{55} absorbs 50 photons on average, 38 by neutrals and 12 by Ar^{1+}. With all collisional processes included Ar_{55} absorbs 38 photons, 23 by neutrals and 15 by Ar^{1+}. Thus the total number of photons absorbed is decreased by 24% in Ar_{55} clusters. This still results in a 31% reduction in the amount of energy the electrons obtain from the laser. While smaller than for the Ar_{2057} clusters it is not a negligible effect.

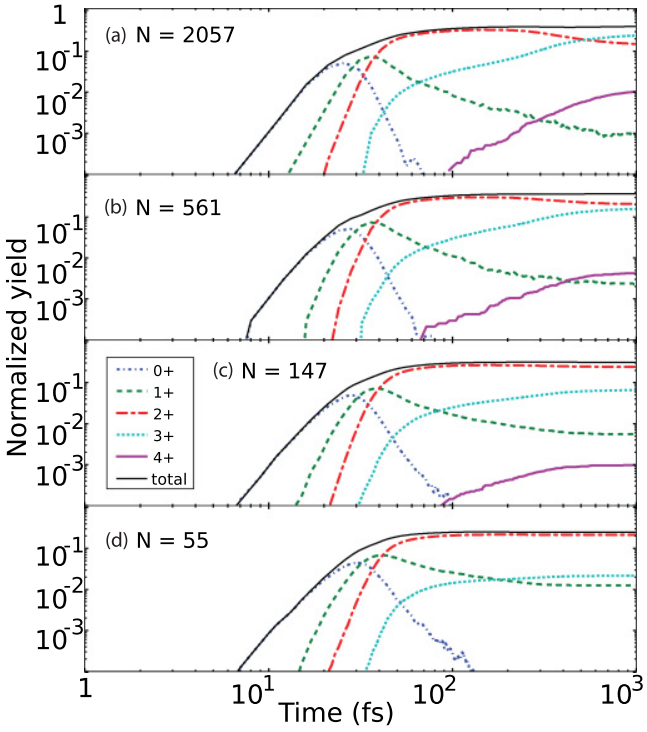

FIG. 4. (Color online) Number of excited neutrals and ions, normalized to the total number of atoms, as a function of time for (a) Ar_{2057}, (b) Ar_{561}, (c) Ar_{147}, and (d) Ar_{55} clusters interacting with a 25-fs laser pulse of 5×10^{13} W/cm^2. The solid (black) line is the total number of excited neutrals and ions.

3. *Excited states evolution*

The efficacy of collisional ionization is driven largely by the access to excited intermediate states. Figure 4 gives the excited state yield per atom of all neutrals and ions corresponding to the simulations of Fig. 3. Also shown is the total number of excited ions as the solid (black) line. The curves are very similar in shape to Fig. 3. Close to 20% of all neutrals and ions for each charge species is excited at any given time. The proportion of excited species, for the most part, increases with the charge state. This is because the energy gap from an excited state to the threshold is larger for higher charge states. For lower charge states this energy gap is smaller, meaning that these excited species are comparatively shorter lived. The lower energy electrons are more abundant than higher energy ones, and thus excited states with a smaller gap to threshold are more frequently ionized. The proportion of excited ions is higher at later times because collisions are much less frequent.

The evolution of the ionic and excited-state populations show that the laser cluster interaction in the XUV is a process begun by photoionization but where collisional and photoionization processes occur in tandem, significantly affecting each other as quantified in Fig. 3. The large amount of Ar^{3+} in Fig. 3 and excited neutrals and ions shown in Fig. 4, where both snapshots are during the laser pulse, indicate that a significant amount of collisional ionization is occurring as these species can only be created via collisional processes. Further, the collisional processes modify the photoabsorbtion rate of the cluster. More excited neutrals (as found in the larger clusters in particular) indicate that more neutrals could eventually be collisionally ionized via augmented collisional ionization (ACI), which is the dominant cause of CRP as will be shown in the next section.

Once sufficient energy has been deposited into the system by the laser, collisional processes (most notably ACI) disperse the energy throughout the cluster. The larger the cluster the more rapidly the cluster becomes dominated by collisional processes and thus reaches higher charge states.

4. *Mechanisms of ionization*

In order to examine the influence of each ionization mechanism directly, we plot for each charge state in Fig. 5 the percentage of that charge state population that was ionized by the various available ionization mechanisms. The

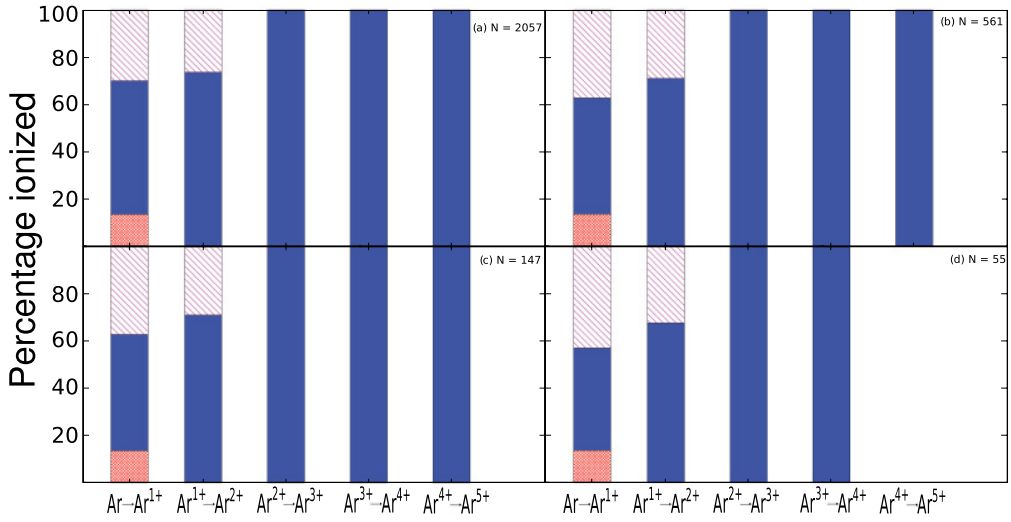

FIG. 5. (Color online) Percentage of events that led to the ionization of the indicated charge state, for all the relevant mechanisms, for (a) Ar_{2057}, (b) Ar_{561}, (c) Ar_{147}, and (d) Ar_{55}. The ionization mechanisms are photoionization, single-step impact ionization, and augmented collisional ionization shown by (magenta) diagonal lines, (red) diamonds, and solid (blue) fills, respectively.

diagonal-lined boxes (magenta) give the percentage ionized by photoionization. The diamond-filled boxes (red) give the percentage ionized by standard one-step collisional ionization. The filled boxes (blue) give the percentage ionized via ACI.

For 32-nm radiation, only the neutral and Ar^{1+} ions can be photoionized. For all cluster sizes, photoionization of neutrals is proportionally larger than for the Ar^{1+}, though it decreases for larger clusters, from 44% for Ar_{55} to 30% to Ar_{2057}. The photoionization of the Ar^{1+} decreases from 36% for Ar_{55} to 28% for Ar_{2057}.

The photoionization cross section of Ar^{1+} is close to half that of the neutral [1], though this ratio is not born out in Fig. 5. This is further evidence of how collisional processes affect the dynamics. We find that a significant number of neutrals are being ionized by collisional processes, predominantly ACI, before photoionization can occur. There is thus a change due to CRP in the expected photoionization yield for the cluster compared with what is expected for the same number of atoms in gas for the same photon fluence.

The proportion of neutrals ionized by single step collisional ionization is very similar for all cluster sizes at around 17%. While it does in fact occur for higher charge states, it is below the 1% range (thus not visible in the graph) demonstrating that ACI dominates. The proportion of neutrals and Ar^{1+} ionized by ACI is larger for larger clusters. This accounts for the relative drop in the photoionization since the single-step collisional ionization remains roughly constant. This is due to the system becoming more collisional at earlier times for larger clusters increasing the effect of CRP.

The roles of photoionization and collisional processes are thus very clear. In this regime of intensity and wavelength, the system is initially driven by photoionization but its evolution is shaped by collisional processes. The higher charge states appear in large numbers well after the pulse is over, created by collisional processes, which become more important for larger clusters.

5. *Charged shell structure*

We now consider the spatial distribution of the charge states within the clusters. The initial icosahedral structure has closed shells which remain largely intact due to the force on the ions being primarily from their mutual repulsion [6]. Thus to understand the charge state distribution, we consider the net charge per atom as a function of shell index. The net charge within a shell is the total charge of all particles in that shell including ions and electrons classically bound to the ions; this is then divided by the number of atoms in the shell to obtain the net charge per atom. This is plotted versus shell index in Fig. 6 for Ar_{2057}, Ar_{561}, Ar_{147}, and Ar_{55} clusters at the end of the simulation, i.e., after ionization processes have ceased.

The average over all shells of the net charge per atom is shown in Fig. 6 as the horizontal blue solid line, and it gives a measure of how the cluster as a whole is charged. It decreases with the increasing cluster size, indicating that while larger clusters access higher charge states the electrons remain bound to the cluster. Consistent with previous work [9], the net charge per atom of the outer shells is found for all cluster sizes to be much higher than that of inner shells. Moreover, only the outermost shell is above the average. Therefore in all cases

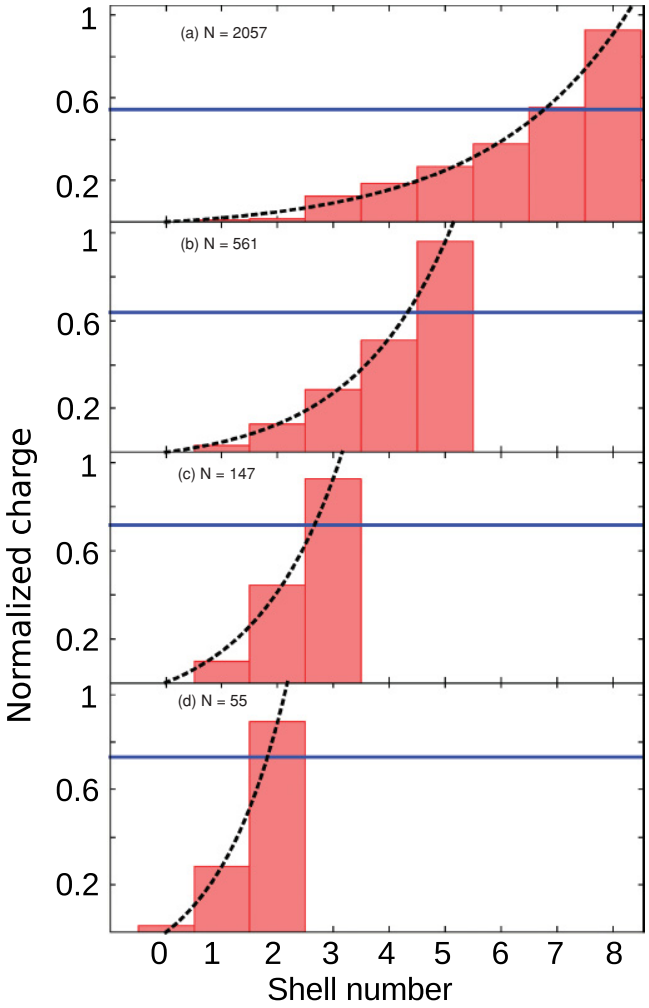

FIG. 6. (Color online) Net charge per atom versus shell index for (a) Ar_{2057}, (b) Ar_{561}, (c) Ar_{147}, and (d) Ar_{55} as determined at the end of the simulations. The solid (blue) line is the average of the net charge per atom over all the shells.

most of the charge resides on the outermost layer(s) of the cluster. Taking the quasineutral core to consist of those shells which are below the mean, we find that the core size generally increases with increasing cluster size, leaving the outermost shell to explode fastest.

We can fit the net charge per atom versus shell number by an exponential function,

$$f(s) = a\,\{\exp[b(s-2)] - 1\}, \tag{3}$$

where s is the shell number and a and b are fit parameters; b quantifies the disparity in mean charge state across the shells. We plot these fits as black lines in Fig. 6, and list the fitting parameters in Table I. The value of b increases with decreasing cluster size, showing that smaller clusters have a larger disparity in the net charge per atom between shells, particularly between the outermost and next outermost shells. Larger clusters have a smaller disparity, since the larger space charge retains more electrons overall.

In Fig. 7 we plot a snapshot of the net charge per atom versus shell index shortly after the laser pulse (at 60 fs). The

TABLE I. Fitting parameters for the net charge per atom versus shell index, according to the function given by Eq. (3).

Cluster size	*a*	*b*
2057	0.041	0.394
561	0.062	0.562
147	0.157	0.646
55	0.230	0.789

result is quite different from Fig. 6, which gives a snapshot long after the laser pulse when all collisional ionization processes have ceased. In Fig. 7 the net charge per atom is more evenly distributed over the shells. This implies that the shell structure is a consequence of charge migration through collisional ionization, which is effectuated by the electrons. For larger clusters, however, charged outer shells are already emerging, whereas for the Ar_{55} and Ar_{147} clusters they are still quite homogeneous. This, along with Fig. 3, suggests that the smaller clusters take longer to become collisional. The formation of charged outer shells early on in the larger clusters is another indication of a significant overlap of the photoionization and collisional ionization dominated regimes as was found in Sec. III A 3.

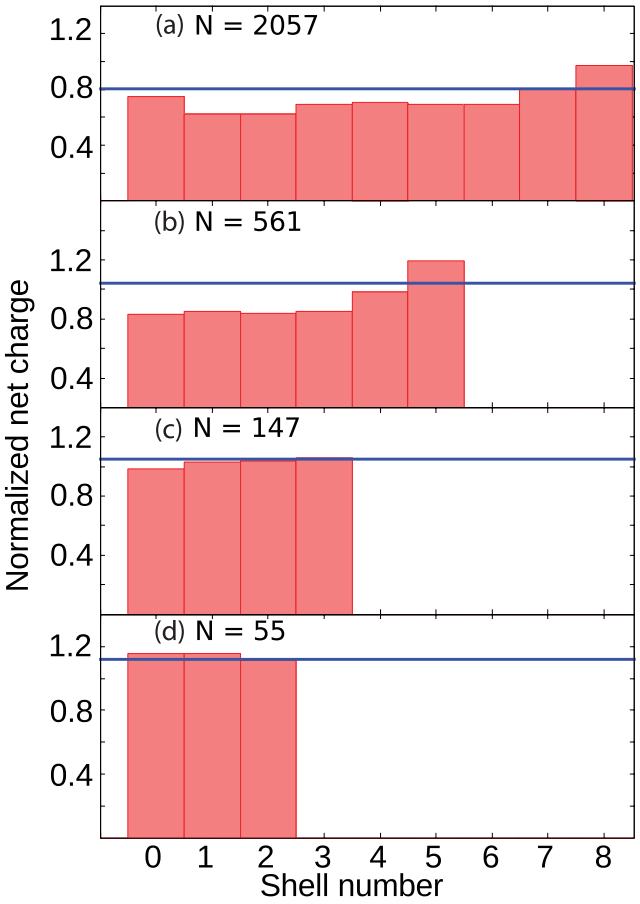

FIG. 7. (Color online) Net charge per atom versus shell index for (a) Ar_{2057}, (b) Ar_{561}, (c) Ar_{147}, and (d) Ar_{55} clusters after the laser pulse. The solid (blue) line is the average over all shells.

Figures 6 and 7 lead to the following explanation of the sequence of events. During the laser pulse the cluster charges up and some outer ionization takes place. After the laser pulse collisional ionization causes charge migration from the outer shells to the core as electrons lose their energy by collisionally ionizing targets and falling deeper into the cluster's potential. The outer shells then explode faster than the inner shells, which contain these cooled electrons.

6. Kinetic energy

The final kinetic-energy distribution of the ions provides information about how the cluster has evolved after the laser pulse and is measurable in experiments. In Fig. 8 we plot the ion kinetic-energy distribution (red solid line) for Ar_{2057}, Ar_{561}, Ar_{147}, and Ar_{55} clusters at the end of the simulations. To gain further insight into how the cluster disintegrates, we also plot the kinetic-energy distributions for each charge state individually: (green) long dashes for Ar^{1+}, (blue) medium dashes for Ar^{2+}, (magenta) short dashes for Ar^{3+}, and (black) dash dots for Ar^{4+}.

The largest clusters produce the most energetic ions. For all cluster sizes the Ar^{2+} is the most energetic and dominates the

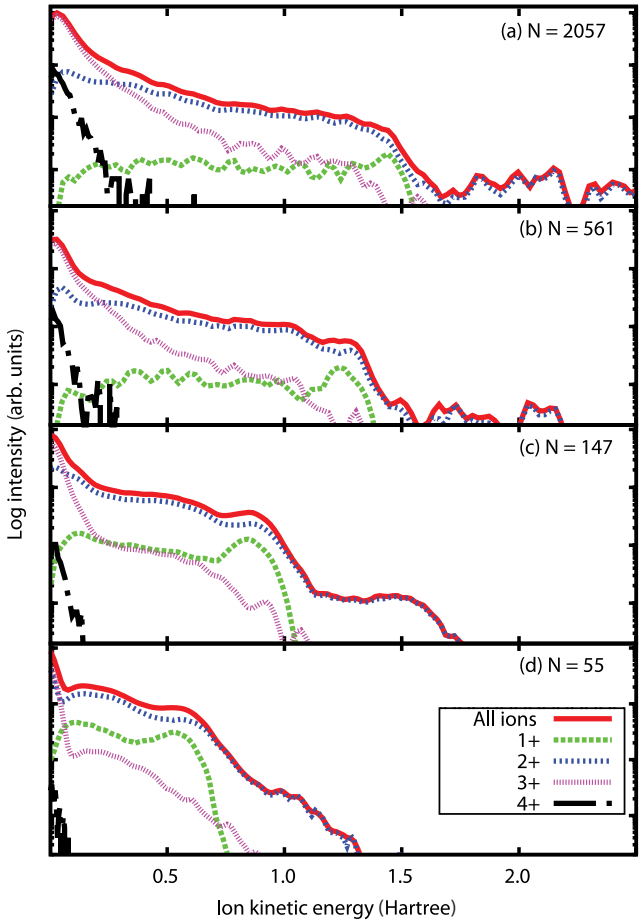

FIG. 8. (Color online) Ion kinetic-energy distributions of (a) Ar_{2057}, (b) Ar_{561}, (c) Ar_{147}, and (d) Ar_{55} clusters at the end of the simulations for each charge state. The solid (red) lines represent the total ion spectrum.

high-energy end of the spectrum. For each cluster size, there is an obvious "knee" in the total spectrum that clearly follows the Ar^{2+} spectrum. This is because the Ar^{2+} is the most populous ion in all but the innermost shells. Note that the shell location of the ions was determined by detailed positional analysis (not shown here) and is not evident from Fig. 8. The Ar^{2+} ions on the high-energy side of the knee are from the exploding outermost shell and acquire a large amount of kinetic energy because there is a relatively low amount of electron screening. The Ar^{2+} on the low-energy side of the knee are from the other shells.

Ar^{4+} appear as the least energetic ions. This is due to most of the Ar^{4+} being produced in the core where collisions are more frequent. Since the core is more shielded than the outer shells, these Ar^{4+} are effectively screened and thus gain less kinetic energy.

The Ar^{3+} populations decrease smoothly as a function of kinetic energy for the larger clusters, and dominate the total spectrum at low energies (below around 0.2 Hartree). There is a knee in the Ar^{3+} spectrum for the smaller clusters, at 0.2 and 0.1 hartree for Ar_{147} and Ar_{55}, respectively, though the knee is somewhat washed out for the larger clusters. The ions with kinetic energy preceding the knee are in the core and expand slowly due to electron screening. The Ar^{3+} dominates at low energy because it is the most populous ion in the core.

The Ar^{1+} ions are distributed almost evenly over the range of energy for the larger clusters with only a small peak at the high-energy end. In the smaller clusters, this peak is more pronounced. In all cases, this peak arises from ions on the outermost shell of the clusters, with energies about half of the energy of the most energetic Ar^{2+}, indicating that the highest energy Ar^{2+} and Ar^{1+} are not screened. These high kinetic energy Ar^{1+} (those at the peak) and Ar^{2+} (those after the knee) primarily reside on the outermost shell and were ionized in the laser pulse solely by photoionization. They were thus not exposed to nor screened by low-energy electrons. This explains why there is no similar phenomenon of a large knee or peak for Ar^{3+} as they must be created by collisional processes.

In Fig. 8(c) a significant decrease in the Ar^{1+} spectrum is evident around 1 hartree. This is consistent with the experimental observations in Ref. [1] for similarly sized clusters, which stated that Ar^{1+} fragments were measured only up to 30 eV (1.1 hartree). The largest contribution of high-energy ions will come from the intensity peak of the laser pulse and from the largest clusters in the log-normal size distribution. The Ar_{147} are thus the most likely origin of these fragments and our model agrees well with the experimental ion kinetic energy observed.

B. Electrons

In the XUV, the laser interacts with the cluster through photoionization. The electrons are ejected from their parent ion or atom largely parallel to the laser polarization, but its subsequent motion is almost completely independent of the laser field due to the very small quiver energy at short wavelengths, even at these high intensities. Thus electron motion is determined entirely by the Coulomb fields of the other charged particles in the cluster. After photonionization, electrons that do not have enough energy to escape the cluster space charge will disperse its energy throughout the cluster via collisions. The following sections provide details of how the energy is transferred, which requires a microscopic model of the relevant process to provide an accurate analysis of electron energy distribution.

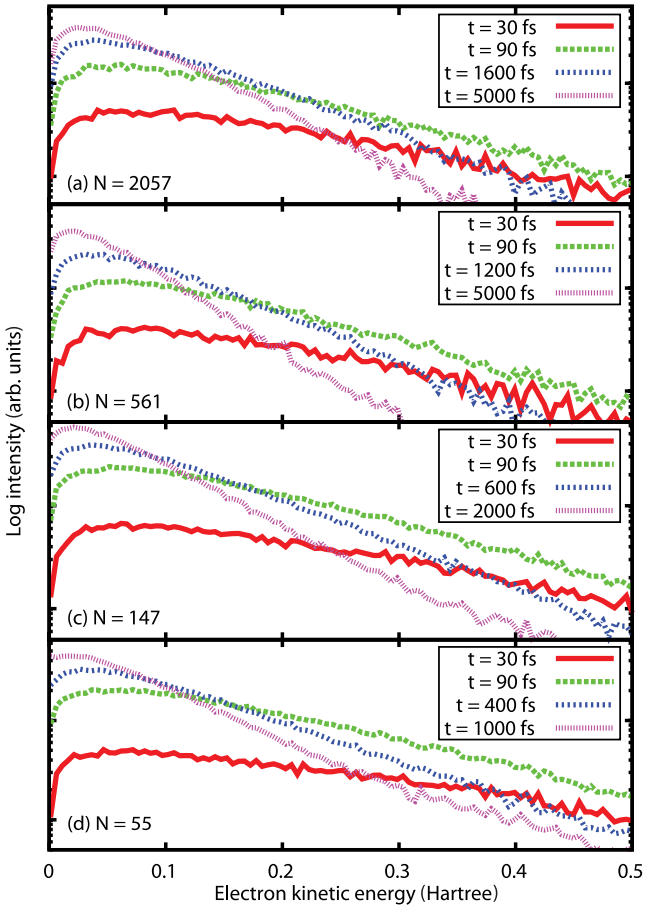

FIG. 9. (Color online) Electron kinetic-energy distribution for (a) Ar_{2057}, (b) Ar_{561}, (c) Ar_{147}, and (d) Ar_{55}. The time at which each distribution was calculated is indicated in the legends.

1. *Kinetic-energy distribution*

The electron kinetic-energy distribution for clusters of different sizes at different times is shown in Fig. 9. These times are as follows: near the peak of the laser pulse at 30 fs (red solid line), shortly after the laser pulse at 90 fs (green large-dashed line), after a significant decrease in the intensity of the high-energy tail at times indicated in the legends (blue medium-dashed line), and at the end of the simulation when the electron distribution no longer changes, again at times indicated in the legends (magenta short-dashed lines).

The plots show that distributions at 30 fs are the only ones that deviate significantly from a single temperature Maxwellian distribution since the tails are not linear on the log plot. By 90 fs, they have become Maxwellian as indicated by the linear tails and this is verified by a quantitative analysis. Though not shown, the distributions of each cluster size remain the same for at least another 60 fs, before the clusters begin exploding. Thus the electrons thermalize quickly, indicating

a high degree of collisions. Once the clusters start to explode at longer times, the distributions become less energetic, as evident from the graphs.

At 90 fs, there are proportionally more low-energy electrons in larger clusters compared with smaller clusters, which have a proportionally larger number of high-energy electrons; the differences are about ∼10% between the Ar_{55} and Ar_{2057}, so they may be difficult to see directly from the graph. This indicates that in larger clusters, fast electrons generally lose their kinetic energy more readily than in small clusters. This is consistent with the finding of Sec. IV2 that the larger clusters disperse the laser energy more quickly than small clusters. As there are more collisions in larger clusters, there will be faster thermalization and more collisional ionization, the latter of which actually removes energy from the ionized electron population.

The aforementioned changes as the clusters evolve. At ∼150 fs (not shown) the distributions for all sizes are very similar, and at later times smaller clusters will have more lower energy electrons due to more rapid cluster explosion. Larger clusters have a larger quasineutral core and thus disintegrate more slowly; this allows for the preservation of more energetic electrons thus the distributions for the larger clusters take a longer time to become less energetic. Note that the (blue) medium-dashed line plots look very similar for each of the cluster sizes, but they were all calculated at different times, the latest time being for the largest cluster.

2. *Velocity distribution*

The laser polarization direction sets the axis along which most photoionization occurs. Anisotropic photoelectron emission was observed in low intensity synchrotron experiments, though emission from clusters was less anisotropic than from atoms [37]. Only collisional processes can destroy the anisotropy inherent to photoionization. Since we have seen that clusters in intense laser pulses are highly collisional systems, which become more collisional as the size of the cluster is increased, we might expect that the effect of collisional processes would cause reduced anisotropy of the electron emission.

Figure 10 shows the electron velocity distribution at different times for Ar_{2057}, Ar_{561}, Ar_{147}, and Ar_{55} clusters. The times chosen are the same as in the previous section, and are also listed in the legends of the figures. The distributions parallel (lines) and perpendicular (symbols) to the laser polarization are shown for each cluster size and for each time. Though not shown explicitly, each distribution is symmetric about its respective axis. Data for both perpendicular directions are also included, though they are plotted with similar symbols of the same color for a given time. The degree of anisotropy is evident by the difference between the line and the points.

At 30 fs, near the peak of the laser pulse, the low velocity electrons are increasingly isotropic as cluster size increases. This indicates that larger clusters thermalize more rapidly than the smaller clusters, and are thus more collisional.

There is increasing isotropy at high velocity as cluster size increases at all times. The high velocity electrons are those which have escaped the cluster and are no longer subject to collisions. In the small clusters, they thus form a peak centered at 1.27 hartree, the $3p$ photoelectron velocity.

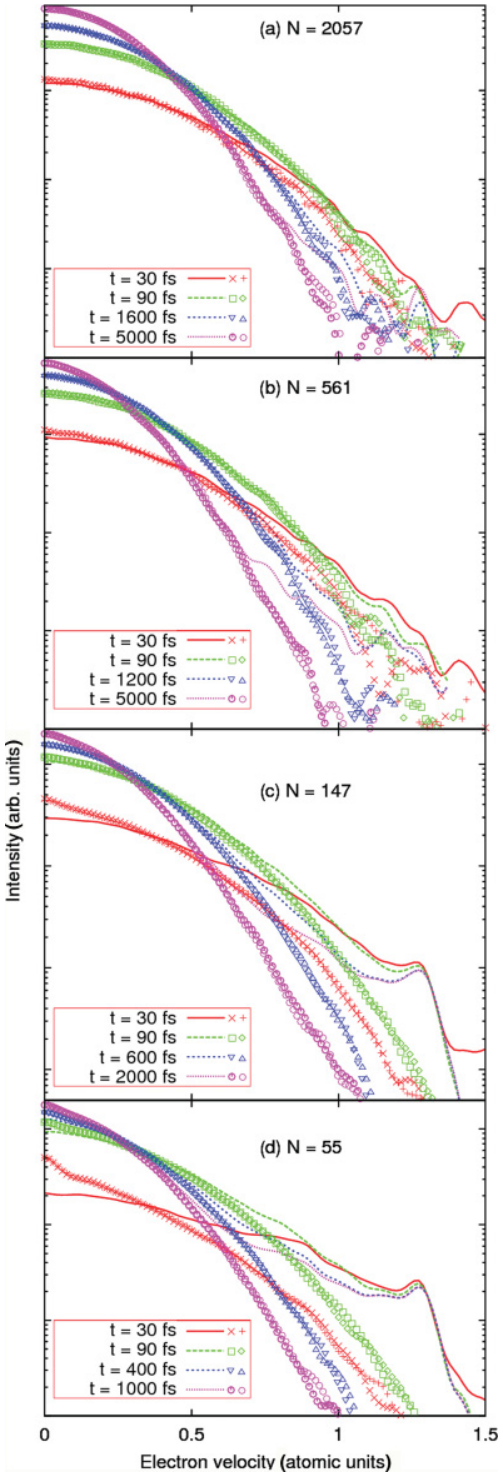

FIG. 10. (Color online) Electron velocity distribution parallel (lines) and perpendicular (symbols) to the laser polarization for clusters of size (a) Ar_{2057}, (b) Ar_{561}, (c) Ar_{147}, and (d) Ar_{55}. The time at which each distribution was calculated is indicated in the key. Note that both perpendicular directions are considered, and these are both plotted for each time with similar symbols of the same color, as indicated in the key.

It can also be seen that in Ar_{147} clusters there is a larger decrease in intensity along the polarization axis from 30 fs to the final time at a velocity just below the peak, near 1 hartree, than in Ar_{55}. This is due to the Ar_{147} clusters having a larger space charge and being more collisional. This results in a decrease of the velocity of the later photoelectrons. The same is true in the larger clusters, which are even more collisional and also have a larger space charge. Thus the Ar_{2057} clusters have the largest difference, as seen in Fig. 10(a). This trend explains the lack of a clear $3p$ peak in the Ar_{561} and Ar_{2057} clusters.

The trend toward isotropy for larger clusters continues to increase for the highest velocities shown. The Ar_{2057} clusters show the same amount of anisotropy at 30 fs as at the end of the simulation, indicating that many of the early photoelectrons have undergone some collisions before exiting the cluster. In smaller clusters, even more electrons leave the cluster unabated. In the Ar_{561} cluster this causes a larger anisotropy gap between 30 fs and the end of the simulation than in Ar_{2057}. In the smallest clusters, this leads to the formation of the distinct photoelectron peaks.

The anisotropy at early times observed in the small clusters for low velocity electrons has similar origin. There is a significant proportion of electrons which exit the cluster unabated. This leaves only a few remaining electrons to collisionally ionize or excite neutrals or ions, which lose some of their kinetic energy and thus velocity. In larger clusters there are many more targets and a larger space charge at 30 fs which increases the number of collisions and removes the anisotropy at low velocity.

The electron velocity distribution shows that larger clusters are more collisional and become so earlier. This leads to an increase in the isotropy of the emitted electrons.

3. *Connection with experiment*

Finally, we compare our simulations with experimental data of Ref. [1] by calculating the electron energy spectrum over the intensity profile of the pulse. The spatial profile of the pulse was assumed to be Gaussian with a focus of 50 μm [1], and the cluster jet size was taken to be 100 μm, the same size as the nozzle. The cluster size distribution was assumed to be log normal with $\langle N \rangle = 80$ and $\Delta N = 80$, which was estimated via simulations with Ar_{80} as well as the two nearest closed-shell icosahedral clusters, i.e., Ar_{55} and Ar_{147}.

We calculated the electron energy spectrum by integrating over cluster size and laser intensity profile, for intensities from 5×10^{13} to 1×10^{12} W/cm^2. Figure 11 shows our result (blue dashed line) compared with the experimental result (red solid line) for a peak intensity of 5×10^{13} W/cm^2 [1]. Our data were normalized to the peak of the experimental signal and folded with an energy window of 0.25 eV as in the experimental paper [1].

The agreement between the curves for the 22-eV peak is best on the high-energy side. The dip in the experimental curve near 17 eV is partially reproduced. The low-energy tail increases as in the experimental results due to electrons being ejected from the cluster in the presence of the growing cluster potential. Thus we found reasonable agreement, given our lack of knowledge of the laser profile and the precise experimental setup.

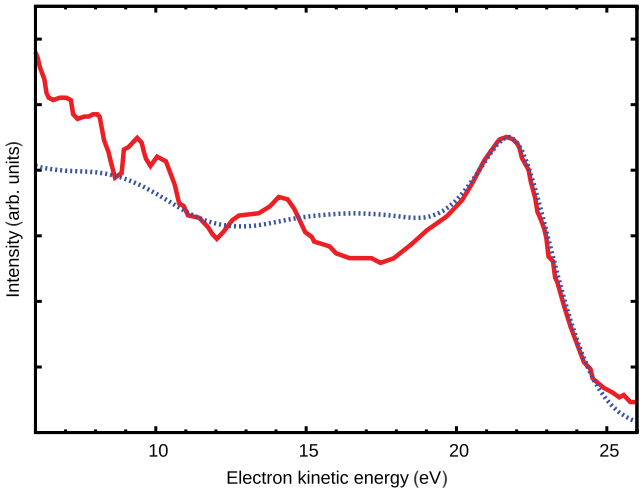

FIG. 11. (Color online) The electron kinetic energy distribution integrated over the spacial profile of a Gaussian pulse with a peak intensity of 5×10^{13} W/cm^2 a focus of 50 μm and integrated over a log normal distribution of cluster sizes with $\langle N \rangle = 80$ and $\Delta N = 80$ is shown as the (blue) dashed line. The experimental data (red solid line) is taken from Ref. [1].

In Ref. [29] the role of augmented collisional ionization was shown to be necessary in order to obtain the highest charge states seen in Ref. [1], Ar^{4+}. Figure 11 shows that the model is also capable of explaining the dominant features in the electron spectrum seen in the experiment. The success of this model is due to the more accurate treatment ionization processes.

IV. SUMMARY

We have shown the effect of cluster size on many aspects of intense XUV-cluster interaction. Our model is verified by reasonable agreement with experimental observations in Ref. [1]. This includes reproducing the electron emission spectrum, obtaining the highest observed charge state, and obtaining a close match of the maximum kinetic energy of the Ar^{1+} species for Ar_{147} clusters.

We find that, for all measures and aspects of the cluster, collisional processes contribute significantly. Further, the size of the cluster increases the importance of the collisional processes. Larger clusters proceed from predominantly photoionization driven to collisional ionization driven more rapidly than smaller clusters. This causes a significant modification in the total cluster photoionization cross section versus what would be expected from a gas, since fewer neutrals are photoionized when collisional processes are included. This results in a decrease in the deposition of energy by the laser. Even for a small cluster with 55 atoms, neglecting collisional processes will overestimate the amount of energy absorbed from the laser by over 30%. We term this process *collisionally reduced photoabsorbtion* (CRP).

The charge states were shown to be in greater abundance, proportionally, in the larger clusters. The highest charge states appear earlier in larger clusters and their appearance happens

well into the disintegration of the cluster. At the photon fluence considered, almost no charge states above Ar^{3+} were observed during the laser pulse. Those that were created almost exclusively by a two-step collisional ionization process, wherein an ion is first collisionally excited, then ionized from the excited state, are termed augmented collisional ionization (ACI). ACI was shown to be the dominant collisional channel in general. At any given time, around 20% of neutrals and ions are in an excited state.

An examination of the charge of the cluster shells as a function of time show evidence of charge migration from the outer to inner shells. Immediately following the laser pulse, the shells are almost uniformly charged, with the notable exception of the more highly charged outer shell in the larger clusters. However, as the system further evolves, collisions cause an increased charging of the outer shell of all cluster sizes, resulting in the explosion of the outer shell and slow expansion of the inner shells, a process observed experimentally in mixed clusters [9].

An analysis of the ion kinetic-energy distribution of each charge state species found that the high-energy tail was almost entirely due to Ar^{2+}. Most of the highest charge states were found to have very little kinetic energy. This because they are created in the core of the cluster where they are shielded by electrons during the cluster disintegration.

The electron kinetic-energy distribution was found to be close Maxwellian, except for very early times, indicating rapid electron thermalization. The electron velocity distribution was found to be largely isotropic for large clusters, but highly anisotropic for small clusters. This is due to the high velocity electrons in the small clusters originating from photoionization events. The isotropy in the large clusters is evidence of high velocity electrons undergoing multiple collisions before escaping the cluster.

Our findings may have implications for the direct single-shot imaging of large molecules with high intensity x rays [38]. These systems will be highly collisional, which may, for example, lead to a rapid change in the photoabsorbtion cross section of the molecule via CRP. Models of this interaction will need to account for this effect.

ACKNOWLEDGMENTS

The authors would like to thank Thomas Brabec, Paul Corkum, Konstantin Popov, and Jean-Paul Britcha for many fruitful discussions. This work was supported by the National Sciences and Engineering Research Council of Canada, the Ministry of Research and Innovation of Ontario, the Canada Research Chairs program, and the Canadian Foundation for Innovation.

[1] C. Bostedt *et al.*, Phys. Rev. Lett. **100**, 133401 (2008).
[2] T. Fennel, K.-H. Meiwes-Broer, J. Tiggesbäumker, P.-G. Reinhard, P. M. Dinh, and E. Suraud, Rev. Mod. Phys. **82**, 1793 (2010).
[3] H. Wabnitz, A. R. B. de Castro, P. Gürtler, T. Laarmann, W. Laasch, J. Schulz, and T. Möller, Phys. Rev. Lett. **94**, 023001 (2005).
[4] A. A. Sorokin, S. V. Bobashev, T. Feigl, K. Tiedtke, H. Wabnitz, and M. Richter, Phys. Rev. Lett. **99**, 213002 (2007).
[5] T. Laarmann, M. Rusek, H. Wabnitz, J. Schulz, A. R. B. de Castro, P. Gürtler, W. Laasch, and T. Möller, Phys. Rev. Lett. **95**, 063402 (2005).
[6] H. Thomas, C. Bostedt, M. Hoener, E. Eremina, H. Wabnitz, T. Laarmann, E. Plönjes, R. Treusch, A. R. B. de Castro, and T. Möller, J. Phys. B **42**, 134018 (2009).
[7] T. Laarmann, A. R. B. de Castro, P. Gürtler, W. Laasch, J. Schulz, H. Wabnitz, and T. Möller, Phys. Rev. Lett. **92**, 143401 (2004).
[8] H. Iwayama *et al.*, J. Phys. B **42**, 134019 (2009).
[9] H. Thomas, C. Bostedt, M. Hoener, E. Eremina, H. Wabnitz, T. Laarmann, E. Plönjes, R. Treusch, A. R. B. D. Castro, and T. Möller, J. Phys. B **42**, 134018 (2009).
[10] L. Fang *et al.*, Phys. Rev. Lett. **105**, 083005 (2010).
[11] *Strong Field Laser Physics* (Springer, 2008).
[12] H. Wabnitz *et al.*, Nature (London) **420**, 482 (2002).
[13] R. Santra and C. H. Greene, Phys. Rev. Lett. **91**, 233401 (2003).
[14] Z. B. Walters, R. Santra, and C. H. Greene, Phys. Rev. A **74**, 043204 (2006).
[15] C. Jungreuthmayer, L. Ramunno, J. Zanghellini, and T. Brabec, J. Phys. B **38**, 3029 (2005).
[16] C. Siedschlag and J.-M. Rost, Phys. Rev. Lett. **93**, 043402 (2004).
[17] B. Ziaja, H. Wabnitz, F. Wang, E. Weckert, and T. Moller, Phys. Rev. Lett. **102**, 205002 (2009).
[18] B. F. Murphy, K. Hoffmann, A. Belolipetski, J. Keto, and T. Ditmire, Phys. Rev. Lett. **101**, 203401 (2008).
[19] C. Bostedt, M. Adolph, E. Eremina, M. Hoener, D. Rupp, S. Schorb, H. Thomas, A. R. B. de Castro, and T. Möller, J. Phys. B **43**, 194011 (2010).
[20] C. Bostedt, H. Thomas, M. Hoener, T. Möller, U. Saalmann, I. Georgescu, C. Gnodtke, and J.-M. Rost, New J. Phys. **12**, 083004 (2010).
[21] M. Richter, S. V. Bobashev, A. A. Sorokin, and K. Tiedtke, J. Phys. B **43**, 194005 (2010).
[22] I. Georgescu, U. Saalmann, and J. M. Rost, Phys. Rev. Lett. **99**, 183002 (2007).
[23] U. Saalmann, I. Georgescu, and J. M. Rost, New J. Phys. **10**, 025014 (2008).
[24] B. Ziaja, H. Wabnitz, E. Weckert, and T. Möller, New J. Phys. **10**, 043003 (2008).
[25] I. Georgescu, U. Saalmann, and J. M. Rost, Phys. Rev. A **76**, 043203 (2007).
[26] C. Gnodtke, U. Saalmann, and J. M. Rost, Phys. Rev. A **79**, 041201 (2009).
[27] U. Saalmann, C. Siedschlag, and J. M. Rost, J. Phys. B **39**, R39 (2006).
[28] M. Arbeiter and T. Fennel, Phys. Rev. A **82**, 013201 (2010).
[29] E. Ackad, N. Bigaouette, and L. Ramunno e-print arXiv:1011.5216v1 [physics.atom-ph].
[30] F. Légaré *et al.*, Phys. Rev. A **71**, 013415 (2005).

[31] M. M. Seibert *et al.*, J. Phys. B **43**, 194015 (2010).
[32] G. V. Marr and J. B. West, At. Data Nucl. Data Tables **18**, 497 (1976).
[33] B. J. Archer, R. E. H. Clark, C. J. Fontes, and H. Zhang, LA-UR-00-5693 (2000).
[34] W. Lotz, Zeitschrift für Physik A Hadrons and Nuclei **206**, 205 (1967).
[35] *The Theory of Atomic Structure and Spectra* (University of California Press, Berkeley, 1981).
[36] S. Micheau, C. Bonte, F. Dorchies, C. Fourment, M. Harmand, H. Jouin, O. Peyrusse, B. Pons, and J. Santos, High Energy Density Phys. **3**, 191 (2007).
[37] D. Rolles *et al.*, Phys. Rev. A **75**, 031201 (2007).
[38] L. Young *et al.*, Nature (London) **466**, 56 (2010).

5

Effect of Augmented Collisional Ionization and potential depth in the VUV regime; a theoretical study

Nicolas Bigaouette, Edward Ackad, Lora Ramunno

To be submitted

Author contributions

The MD package was mostly written by N. B., as was the text. The ACI cross-sections were calculated by E. A. All post processing scripts used to analyze data and generate figures were written by N. B. Data generation and analysis was performed by N. B. All authors contributed to the discussion.

Effect of Augmented Collisional Ionization and potential depth in the VUV regime; a theoretical study

Nicolas Bigaouette* and Lora Ramunno†
Department of Physics, University of Ottawa, 150 Louis Pasteur, Ottawa ON, K1N 6N5, Canada

Edward Ackad‡
Department of Physics, Southern Illinois University Edwardsville, State Route 157 Edwardsville, IL 62026, United States
(Dated: August 26, 2013)

We revisit the 2002 experiment at FLASH-DESY FEL facilities on Xenon clusters interacting with VUV (98 nm, 12.65 eV) 100 fs laser pulses, in light of a re-calibration of the intensity to 40% of its originally quoted value. We found that augmented collisional ionization, a mechanism we recently investigated for XUV-cluster interactions, increases the maximum charge state by two, and gives a maximum charge state and most abundant charge state compatible with experimental observations. Further, we found a significant effect of potential depth, which further increases agreement with experiment.

I. INTRODUCTION

The advance of Free Electrons Lasers (FEL) around the world gave access to unprecedented intensity at wide range of wavelengths, including from the VUV to X-ray. Recent experiments have studied the interaction of such laser pulses with clusters of atoms. These clusters are nanoscopic objects at solid density. Additionally, their finite size makes them easier to study, both theoretically and experimentally.

Many studies of the interaction of laser-matter have been done at wavelengths ranging from the IR to X-ray regimes. Experiments in 2002 by Wabnitz *et al.*[1] at FLASH-DESY FEL facilities on clusters of Xenon and VUV radiation saw surprisingly high charge states (Xe^{8+}) using 98 nm (12.7 eV). The heating and ionization mechanisms known at that time could not explain the high charge states; more work was required. Three major models emerged to explain these high ionization levels.

First, the lowering of the potential barrier was suggested for photo-ionization [3–6] where a neighbouring ion lowers the barrier, making the absorption of a single photon by the electron energetically possible.

Second, Santra and Green suggested using atomic potential instead of the Coulomb potential. They used a simple screening potential [7] and later a more realistic one [8] based on a Hartree-Fock-Slater code written by F. Herman and S. Skillman [9] and saw 30 times more VUV photons absorbed by a cluster environment compared with using a Coulomb potential. Charge states up to Xe^{6+} for Xe_{1500} clusters were obtained with simulations using the atomic potentials.

Jungreuthmayer *et al.*[2] identified an additional mechanism dubbed "Multi-Body Recombination" (MBR) heating. Through laser-cluster simulations based on classical dynamics, they showed that the created plasma is cold and dense enough to fall within the strongly coupled plasma regime. As such, the plasma is highly collisional and via multiple collisions electrons can recombine to a highly excited state with high probability. This newly recombined electron can then reabsorb a new photon from the laser, effectively increasing the system's energy absorption from the laser.

In 2010, the intensity of the DESY-FEL pulses[1] was re-calibrated to be 40% of the originally quoted value [10]. The question now arises: given that the previous models showed good agreement with experimental result at the originally quoted intensity, is there something potentially missing from the previous models in light of this intensity adjustment? In this paper, we investigate two possible effects that might contribute.

First, our group recently investigated the involvement of atomic excited states in collisional ionization in laser-cluster interaction experiments in the XUV[11–13]. We presented a model wherein collisional ionization is allowed to occur in two steps. First, a colliding electron may promote a bound electron to an excited state. Then another colliding electron may promote this excited one into the conduction band. This allows lower-energy electrons to ionize an atom/ion, where such ionization would not be possible via the usual single-step collisional ionization models. We called this process "Augmented Collisional Ionization" (ACI), and we now seek to investigate its role in the VUV laser-cluster regime. We do this via a classical model similar to that employed by Jungreuthmayer *et al.*

Second, we investigate the effect of the electron-ion potential in classical simulations, given the large effect of potential shape on VUV-cluster interaction found by Santra and Green. Though in this work we only use the Coulomb potential, we investigate how the potential

depth of the softened version affects simulation outcomes. This provides some hints as to how a different potential shape may interact with classical simulations.

In the first part of this paper, we will describe our classical approach to the clusters' dynamics followed by the different ionization processes which are treated quantum mechanically. Results are then presented by first showing the influence ACI has on the maximum charge states seen in simulations. Then, the cluster size influence is studied and compared to experiments by averaging over the spatial distribution of the laser pulse. Last, we investigate the influence of the potential depth used in our simulations on the maximum charge state seen.

II. MODEL

Clusters are nanoscopic systems and as such are hard to model using statistical approaches which often assume infinite systems. Our model thus tracks every particle present using a classical molecular dynamics (MD) code. Such MD codes are excellent tools for the simulation of a low number of particles since no approximation is used (apart from the classical instantaneous electrostatic interactions). Unfortunately, the N-body problem has no analytic solutions and is chaotic, requiring large amount of data for valid statistics. Furthermore, the MD interaction calculation has an $O(N^2)$ scaling which renders simulations of tens of thousands of particles using long range interactions virtually impossible. Approximations to the N-body problem are possible; hierarchical tree code [14] and fast-multipole methods [15] can reduce the burden to an $O(N \log(N))$ problem.

These algorithms have overheads which makes them slower for a lower number of particles. They can also introduce some errors in the force and potential calculations. While these errors are not significant for the dynamics aspect of the simulation, they can influence the calculated rates of quantum transitions. We instead decided to port the classical dynamics aspect of the simulation to the OpenCL framework. This allows us to accelerate calculation on general-purpose graphical processing units (GP-GPU), bringing a speed up of between 40 and 80 times.

The Coulomb interaction between particles is softened at small distances to avoid numerical errors due to the singularity. Particles are treated as Gaussian charge densities where the potential is given by (in atomic units):

$$\phi(r) = \frac{Z}{r}\mathrm{erf}\left\{\frac{r}{\sigma\sqrt{2}}\right\} \tag{1}$$

with erf the error function, Z the charge state of the particle and σ the width of the charge density given by:

$$\sigma = \frac{Z}{D}\sqrt{\frac{2}{\pi}} \tag{2}$$

The maximum depth of the potential of a $Z = 1$ ion is given by the parameter D. At large distances ($r >> \sigma$), this smoothed potential converges to the Coulomb potential.

Initially, the simulated cluster is a collection of neutral atoms. As time passes, the laser is modelled as both an oscillating electric field with a carrier envelope and a flux of photons. Electrons and ions are created in the code by ionization events modelled via quantum rates. These are now described in the following section.

A. Single photon ionization

The first step in the interaction is single photon ionization of the neutral atoms. As such ionization events occur, the laser amplitude is depleted. Experimental cross sections for Xenon in the VUV regime were taken from experimental data [16]. These cross-sections are converted to rates and a Monte-Carlo test evaluates the ionization probability.

At the studied intensities (10^{12} to 10^{13} W/cm^2) and wavelength (98 nm, 12.65 eV), tunnel ionization is negligible, as is multi-photon absorption. In addition, ions cannot be further ionized via single photon ionization.

B. Threshold V_p

Many processes are modelled using quantum rates known for isolated atoms. For example, the semi-empirical Lotz cross-sections for impact ionization assumes the impacting electron comes from infinity where its potential energy is null. However the cluster environment must be taken into account. We model these interactions as those of an isolated system residing in a constant potential created by the cluster environment. This potential V_p is the contribution of all particles outside the nearest neighbour distance in the pre-ionized cluster.

C. Impact ionization

Impact ionization is implemented using the semi-empirical Lotz cross-sections[17] with parameters taken from references [18] for the neutral and [19] for ionized Xenon. The impact parameter b of the impacting electron is calculated through $b = |\mathbf{v} \times \mathbf{r}| / |\mathbf{v}|$ where $\mathbf{v}$ is the impacting electron's velocity vector and $\mathbf{r}$ the vector from the impacting electron to the target. If the impact parameter lies inside the calculated cross section, ionization takes place. We take the impacting electron's total energy with respect to the threshold V_b as its effective kinetic energy.

D. Augmented Collisional Ionization (ACI)

In recent work, we introduced a model [12] which we dubbed "Augmented Collisional Ionization" (ACI) that

we applied to Argon experiments at 32.8 nm [20] and Xenon clusters in soft X-rays (13.7 nm, 90.5 eV)[13, 21]. We now port that model over to the VUV regime.

In the ACI model, electrons are created in a two step process. After an electron collides with an atom or ion, we allow for the final state to be an excited atom or ion plus a reduced-energy impact electron. Once excited, an atom or ion can be impact-ionized more easily by a second, lower energy, impacting electron. ACI thus allows electrons in the lower energy tail of the kinetic energy spectrum to contribute to the cluster ionization. Additionally, more ionization paths are present in the model.

ACI is modelled similarly to impact ionization. Cross sections for the different transitions are taken from a Hartree-Fock implementation of the Cowan code[22]. For this work on Xenon clusters, eight excited states ($l < 4$) per charge state are used, for ionization levels up to Xe^{17+}.

E. Ground state recombination

We include in our model recombination to the ground state as described in detail in our previous work [13]. If an electron's total energy with respect to the V_p threshold becomes lower than the ground state energy, this electron is recombined with the parent ion and disappears from the simulation. The ion's charge state is updated to reflect the process.

This allows having a potential that is as close as Coulombic as possible (except at really close range where the potential converges to $\phi = ZD$) without having electrons with classical energy below the ground state. Interestingly, it also accelerates the $O(N^2)$ force calculation by reducing the number of particles in the system.

F. Many Body Recombination

MBR is automatically included in a classical MD simulation and is thus included in our results.

An important distinction between MBR and ACI is the direction in which the electronic transition takes place. In the case of ACI, the transition is going "up the energy ladder": a bound electron first in the ground state will receive energy from an impacting electron. Afterwards, the excited atom is ionized more easily by other impacting electrons due to, firstly, the cross-section of the excited state to continuum state being larger than the cross-section from the ground state to continuum. Secondly, the energy required for the excited state to continuum transition is less than that of the ground state to continuum transition and as such more free electrons have a chance to ionize the excited atom. On the other hand, MBR is a transition from the continuum to a highly excited state. While the later is treated purely classically, the former is implemented using cross-sections taken from a Hartree-Fock calculation. The lower excited states used in ACI are distant from each other and must be treated discretely while the higher states in MBR are so dense that their classical treatment does not result in much error.

III. RESULTS

A. Effect of Augmented Collisional Ionization

We examine the effect of ACI by performing VUV-cluster interaction simulations for a range of VUV intensities, and a range of cluster sizes, both with and without the ACI mechanism enabled in our code. The small nature of these clusters, the random process of the Monte-Carlo ionization procedures and the chaotic nature of the many-body problem requires acquiring a large sample for valid statistics; 5,000 simulations were run for small clusters, and 100 for larger clusters. The Coulomb potential depth is limited at close range to prevent the large field close to the discontinuity from cause numerical heating. In this subsection, equation (1) is used with $D = 12$ eV. Cross-sections were taken from experimental data from reference [16] for single photon ionization. For impact ionization, experimental cross-sections from references [18] and [19] rather than Lotz [17] were used.

When irradiated with a 98 nm (12.95 eV) laser pulse, all atoms in the cluster become rapidly ionized to $Z = +1$. This is due to the fact that single photon ionization cross-section is largest (68 Mb) at this longer wavelength for neutral Xenon. Since the photon energy is not sufficient to ionize an isolated Xe^{1+} to Xe^{2+}, only the first charge state is accessible through single photon ionization in our model. Larger charge states are caused by other mechanisms as is evidenced by experiments with gas targets.

The cluster dynamics after the laser pulse is mainly an expansion; no significant ionization has been observed during that time. As such, simulations were run up to 400 fs which is approximately 150 fs after the end of the laser pulse. We have not seen any major changes when continuing the simulations for longer times.

We first compare the highest charge states seen in both our simulations and the 2002 experiment at DESY with the re-calibrated intensity values [10]. We do this by running simulations close to experimental parameters at the peak laser intensity only.

We ran simulations with Xe_{90} clusters to compare with Figure 1 of Wabnitz *et al.* at the revised intensity of 8×10^{12} W/cm^2. Figure 1 shows the resulting charge state spectrum. The left subplot shows data when ACI is not enabled, while the right subplot shows the spectrum when ACI is enabled, with the ratio of excited states in hatched regions. As we can see, ACI increases by two the maximum charge state from Xe^{3+} to Xe^{5+}. The 2002 experiment showed a clear signal for at least Xe^{4+} for Xe_{80} clusters. Without ACI, there is only a very small, almost negligible, fraction of Xe^{3+} while there is signifi-

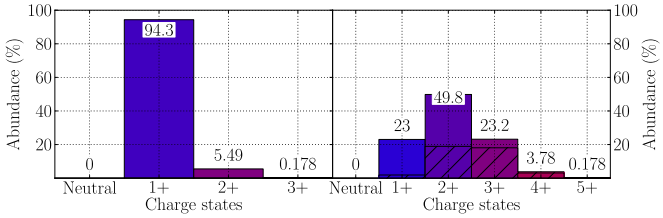

FIG. 1: Charge states spectra of Xe_{90} clusters at $8{\times}10^{12}$ W/cm^2 with ACI disabled (left) and enabled (right)

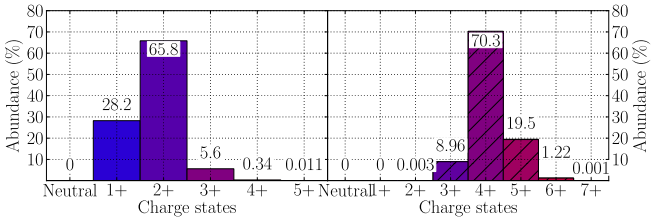

FIG. 2: Charge states spectra of Xe_{1000} clusters at $1.5{\times}10^{13}$ W/cm^2 with ACI disabled (left) and enabled (right)

cant abundance of Xe^{4+} when ACI is enabled; this corresponds more closely to the highest charge state seen in the experimental data. Further, we see by the hatched areas on the right graph, that at the end of the simulation with ACI enabled, there are a large percentage of ions that are in an excited state, that is, that have gone through one step of the two step ACI process.

We also ran simulations of $Xe_{1,000}$ clusters at 1.5×10^{13} W/cm^2, which is close to the experimental parameters of the largest intensity plot of Figure 1 of Wabnitz *et al.*, assuming a similar recalibration. We plot the charge spectra with and without ACI in Figure 2. When ACI is disabled, the maximum (significant) charge state seen is Xe^{4+}, whereas the maximum (significant) charge state of Xe^{6+} if found when ACI is enabled. We note however that our simulated intensity value is somewhat lower than the expected re-calibrated experimental value, so this is a lower bound. Nevertheless, this is an indication that ACI may play a vital role in the dynamics.

To compare to the previous theoretical work of Jungreuthmayer *et al.* [2], we also measured the number of electrons which are in a many-body recombined (MBR) state. We found that around 18 % of the total number of electrons are in an MBR state starting from around the peak of the laser pulse through the end of the simulations, close to the previous value found of around 25 %. This is an indication that MBR is still important in the description of the dynamics.

The previous results can only predict the highest charge state seen because only the intensity at the peak was considered in our simulations. As such, the charge state distributions we observed in figures 1 and 2 have a much higher most abundant charge state than seen in experiment. Thus, we next consider the effect of the spatial profile of the laser pulse.

Distance to focus	Normalized height	Intensity ($\times 10^{12}$ W/cm^2)
0	1	8.000
$\sqrt{-2\sigma^2 \ln\left(\frac{1+e^{-1/2}}{2}\right)}$	$\frac{1+e^{-1/2}}{2}$	6.424
σ	$e^{-1/2}$	4.852
$\sigma\sqrt{2\ln(2)}$	1/2	4.000
$\sqrt{2}\sigma$	e^{-1}	2.943
2σ	e^{-2}	1.083

TABLE I: Intensity of laser pulse at different distances of the focus assuming a gaussian spatial profile with a standard deviation σ.

We take the density of clusters coming out of the nozzle to be constant in space over the laser focal volume. As such, the clusters distributed across focal volume will sample a different laser intensity depending on their location. For a given peak intensity value and cluster size, we then run a series of simulations at different intensities. The resulting spectra are then weighted accordingly.

We perform simulations with spatial averaging for the re-calibrated peak intensity 8×10^{12} W/cm^2, corresponding to Figure 1 of Wabnitz *et al.*. Similarly to that figure, we also study the effect of cluster size. However, due to computational resources limits, the largest clusters we simulated were $Xe_{5,083}$, whereas in the experiment it was $Xe_{30,000}$ (revised in 2010 to $Xe_{90,000}$). Our spatial averaging was done with weight values presented in Table I. Considering a focus diameter (FWHM) of $\tau = 20\mu$m we have $\sigma = \tau\left(2\sqrt{2\ln(2)}\right)^{-1} = 11.77\mu$m.

For this set of simulations, we forcibly recombine, at the end of every simulation, electrons that are closer than 4 Bohr to an ion and have a negative energy. This energy is calculated as the electron's kinetic energy plus the potential energy between this electron and the nearby ion. This is the most conservative estimate of what would be detected in an actual experiment

Figure 3a shows the charge state distribution for Xe_{90} clusters and figures 3b, 3c and 3d show the distribution of icosahedral clusters with their 7^{th}, 8^{th} and 11^{th} closed shells ($Xe_{1,415}$, $Xe_{2,057}$ and $Xe_{5,083}$, respectively). All icosahedral configurations were relaxed using a Lennard-Jones potential for neutral xenon.

For each cluster size, we see spatial averaging gives most abundant charge states that are more in-line with experimental observations, as expected. Enabling ACI increases the highest charge states (with significant abundance) in each case by one or two, with the largest change seen for the largest cluster size. Additionally, the most abundant charge state is shifted from Xe^{1+} to Xe^{2+} when ACI is enabled for large clusters, while staying at Xe^{1+} for the smallest (Xe_{90}) clusters. Similar to experiment, we see the general trend that the highest charge states

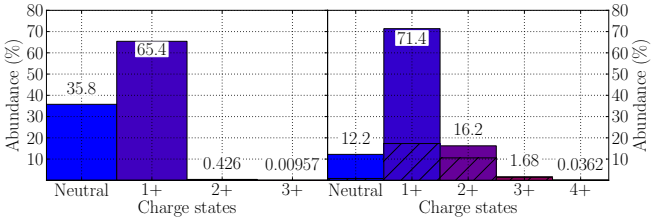

(a) Xe_{90}

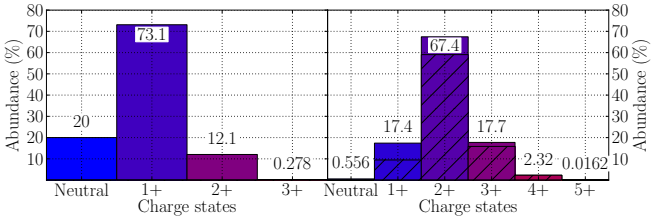

(b) $Xe_{1,415}$

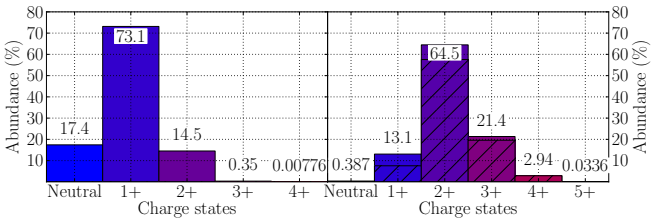

(c) $Xe_{2,057}$

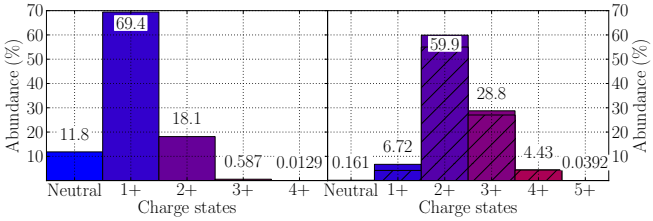

(d) $Xe_{5,083}$

FIG. 3: Charge states spectra of different cluster sizes using intensities of table I. ACI disabled (left) and enabled (right)

and the distributions in general are shifting to larger values as the cluster size increases.

It is interesting to note that the Xe^{3+} population doubles between the $Xe_{1,415}$ and $Xe_{5,083}$ clusters. Though $Xe_{5,083}$ clusters are less than four times larger than $Xe_{1,415}$, they have 4 more closed shells. The doubling of the Xe^{3+} is likely caused by the number of ions on the cluster surface increasing more slowly than the number of ions in the cluster volume. For example, the $Xe_{1,415}$ clusters have 35 % of atoms inside their volume, while this proportion drops to 24 % for $Xe_{5,083}$. Since we have seen that the higher charge states reside on the cluster boundaries in XUV-cluster interaction, as reported in [11], we expect to see a slower increase of the yield of the highest charge states compared to the cluster size increase.

B. Effect of potential depth

In previous studies[7, 8] the shape and depth of the ion potential was found to have a large influence through increased inverse Bremsstrahlung heating (IBH). The potential depth parameter of 12 eV used above prevents electrons from falling too deep within an ion's potential well. Using deeper potentials would allow the possibility for larger angle scattering and possibly increased IBH, even within the Coulomb potential used in this paper. To explore this avenue, however, we need to prevent electrons from acquiring too low an energy. We do this by employing ground state recombination model developed in our previous work[13]. This allows us to use a deeper potential while preventing numerical heating.

As the potential gets deeper, the field close to the ion increases and a smaller time step must be used for simulations, significantly increasing the computational resources required. We used a very small time step of 0.15 as which minimizes the calculation error while still providing reasonable simulation duration. We compared the results that follow with simulations run with a smaller time step of 0.1 as and found only negligible differences in the charge states distribution. Additionally, since recombination will change the charge state distribution even after the laser has passed by redistributing energy throughout the cluster, simulations must be run for a longer time. In this case, simulations went up to 1 ps where the cluster is fully exploded. Because of this increase computational load, we did not perform spatial averaging for the results that follow. Also, due to the smaller time step used in this section not as many runs could be performed as was done in the previous section; 60 runs were used to generate every charge state spectrum shown on figures 4

We find that the depth of the potential does have an influence on the cluster dynamics. Figures 4a and 4b show the results for Xe_{80} clusters under a 8×10^{12} W/cm^2 laser pulse for a potential depth parameter D of 27.2 eV (1 Eh) and 81.63 eV (3 Eh) – see equation (2). Refer to figure 1 for the corresponding simulation done at D =12 eV (0.441 Eh).

We clearly see an increase in both the maximum and dominant charge state seen as the potential depth parameter increases. While the shallow potential depth of 12 eV gives interesting results, we see that a deeper potential is required to obtain higher charge states, most notably, a sizable Xe^{4+} population. This is relevant because when forcible recombination was applied to the comparable Xe_{90} simulations with spatial averaging (see Figure 3a), there was not a significant Xe^{4+} population that remained.

We see that for D = 3 Eh, the distribution is similar to that with D = 1 Eh. This is very interesting, and indicates the saturation of the energy absorption. This suggests that large-angle scattering also saturates.

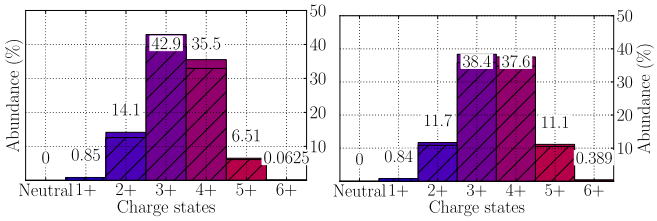

(a) $D = 27.2$ eV (1 Eh) (b) $D = 81.63$ eV (3 Eh)

FIG. 4: Charge state spectra after 1 ps of Xe_{80} using an intensity of 8×10^{12} W/cm^2 and different potential depths D (see equation (2)). ACI is enabled for both figures.

IV. CONCLUSION

We revisited the 2002 VUV-Xenon cluster experiment at DESY, in light of the recent recalibration of the VUV laser intensity to a much lower value. We applied a classical dynamics model to study the influence of augmented collisional ionization and potential depth and found that ACI does influence both the maximum charge state and distributions. For Xe_{80} clusters at 8×10^{12} W/cm^2 and Xe_{1000} clusters at $1.5{\times}10^{13}$ W/cm^2, the maximum charge state seen was increased by two when ACI was enabled, giving results that are more compatible with the 2002 DESY experiment than when ACI was not included. This give an indication that ACI may plays an important role in the cluster dynamics. We also performed spatial averaging over the laser pulse, and found a most-abundant charge state that was compatible with experiment when ACI was enabled, for a range of cluster sizes. Finally, we looked at the potential depth influence on charge state spectra. We applied a model that allows recombination to the ground state to prevent artificial electrons heating. We found that using a deeper potential in our classical code does result in higher charge states, though the effect of this saturates at a depth of around 1 Hartree. Implementing a more realistic atomic potential rather than a Coulomb potential would be an interesting further extension of this work.

[1] H. Wabnitz, L. Bittner, A. R. B. de Castro, R. Dhrmann, P. Grtler, T. Laarmann, W. Laasch, J. Schulz, A. Swiderski, K. von Haeften, T. Mller, B. Faatz, A. Fateev, J. Feldhaus, C. Gerth, U. Hahn, E. Saldin, E. Schneidmiller, K. Sytchev, K. Tiedtke, R. Treusch, and M. Yurkov, Nature **420**, 4825 (2002).

[2] C. Jungreuthmayer, L. Ramunno, J. Zanghellini, and T. Brabec, Journal of Physics B: Atomic, Molecular and Optical Physics **38**, 30293036 (2005).

[3] C. Siedschlag and J.-M. Rost, Physical Review Letters **93**, 43402 (2004).

[4] U. Saalmann and J.-M. Rost, Physical Review Letters **91** (2003), 10.1103/PhysRevLett.91.223401.

[5] U. Saalmann, C. Siedschlag, and J.-M. Rost, Journal of Physics B: Atomic, Molecular and Optical Physics **39**, R39R77 (2006).

[6] I. Georgescu, U. Saalmann, and J.-M. Rost, Physical Review A **76**, 18 (2007).

[7] C. Greene and R. Santra, Physical Review Letters **91**, 14 (2003).

[8] R. Santra and C. Greene, Physical Review A **70** (2004), 10.1103/PhysRevA.70.053401.

[9] F. Herman and S. Skillman, *LANL* (Prentice-Hall, 1963).

[10] C. Bostedt, M. Adolph, E. Eremina, M. Hoener, D. Rupp, S. Schorb, H. Thomas, A. R. B. de Castro, and T. Mller, Journal of Physics B: Atomic, Molecular and Optical Physics **43**, 194011 (2010).

[11] E. Ackad, N. Bigaouette, K. Briggs, and L. Ramunno, Physical Review A **83**, 063201 (2011).

[12] E. Ackad, N. Bigaouette, and L. Ramunno, Journal of Physics B: Atomic, Molecular and Optical Physics **44**, 165102 (2011), arXiv:1011.5216.

[13] E. Ackad, N. Bigaouette, S. Mack, K. Popov, and L. Ramunno, New Journal of Physics **15**, 053047 (2013).

[14] J. E. Barnes and P. Hut, Nature **324**, 446449 (1986).

[15] P. Gibbon and G. Sutmann, in *Quantum Simulations of Complex Many-Body Systems: From Theory to Algorithms*, NIC Series, Vol. 10 (2002) p. 467506.

[16] J. B. West and J. Morton, Atomic Data and Nuclear Data Tables **22**, 103107 (1978).

[17] W. Lotz, Zeitschrift fur Physik **206**, 205211 (1967).

[18] H. Tawara and T. Kato, Atomic Data and Nuclear Data Tables **36**, 167353 (1987).

[19] A. Heidenreich, I. Last, and J. Jortner, The European Physical Journal D **35**, 567577 (2005).

[20] C. Bostedt, H. Thomas, M. Hoener, E. Eremina, T. Fennel, K.-H. Meiwes-Broer, H. Wabnitz, M. Kuhlmann, E. Plonjes, K. Tiedtke, R. Treusch, J. Feldhaus, A. R. B. de Castro, and T. Moller, Physical Review Letters **100**, 133401 (2008).

[21] H. Thomas, C. Bostedt, M. Hoener, E. Eremina, H. Wabnitz, T. Laarmann, E. Plnjes, R. Treusch, A. R. B. de Castro, and T. Mller, Journal of Physics B: Atomic, Molecular and Optical Physics **42**, 134018 (2009).

[22] R. D. Cowan, *Nature*, Los Alamos Series in Basic and Applied Sciences, Vol. 140 (University of California Press, 1981) Chap. 8 and 16, p. 626627.

[23] M. Y. Amusia, *Atomic Photoeffect* (Springer, 1990).

[24] J. E. Barnes, Journal of Computational Physics **87** (1990), 10.1016/0021-9991(90)90232-P.

[25] C. Bostedt, H. Thomas, M. Hoener, T. Mller, U. Saalmann, I. Georgescu, C. Gnodtke, and J.-M. Rost, New Journal of Physics **12** (2010), 10.1088/1367-2630/12/8/083004.

[26] T. Fennel, K.-H. Meiwes-Broer, J. Tiggesbumker, P. M. Dinh, and E. Suraud, Reviews of Modern Physics **82**, 17931842 (2010).

[27] M. Hoener, C. Bostedt, H. Thomas, L. Landt, E. Eremina, H. Wabnitz, T. Laarmann, R. Treusch, A. R. B. de Castro, and T. Mller, Journal of Physics B: Atomic, Molecular and Optical Physics **41**, 181001 (2008).

[28] B. Iwan, J. Andreasson, M. Bergh, S. Schorb, H. Thomas, D. Rupp, T. Gorkhover, M. Adolph, T. Mller, C. Bostedt, J. Hajdu, and N. Tmneanu, Physical Review A **86** (2012), 10.1103/PhysRevA.86.033201.

[29] H. Iwayama, A. Sugishima, K. Nagaya, M. Yao, H. Fukuzawa, K. Motomura, X.-J. Liu, A. Yamada, C. Wang, K. Ueda, N. Saito, M. Nagasono, K. Tono, M. Yabashi, T. Ishikawa, H. Ohashi, H. Kimura, and T. Togashi, Journal of Physics B: Atomic, Molecular and Optical Physics **43**, 161001 (2010).

[30] M. Krikunova, M. Adolph, T. Gorkhover, D. Rupp, S. Schorb, C. Bostedt, S. Roling, B. Siemer, R. Mitzner, H. Zacharias, and T. Mller, Journal of Physics B: Atomic, Molecular and Optical Physics **45**, 105101 (2012).

[31] T. Laarmann, A. de Castro, P. Grtler, W. Laasch, J. Schulz, H. Wabnitz, and T. Mller, Physical Review Letters **92** (2004), 10.1103/PhysRevLett.92.143401.

[32] T. Laarmann, M. Rusek, H. Wabnitz, J. Schulz, A. de Castro, P. Grtler, W. Laasch, and T. Mller, Physical Review Letters **95** (2005), 10.1103/PhysRevLett.95.063402.

[33] R. Moshammer, Y. Jiang, L. Foucar, A. Rudenko, T. Ergler, C. Schrter, S. Ldemann, K. Zrost, D. Fischer, J. Titze, T. Jahnke, M. Schffler, T. Weber, R. Drner, T. Zouros, A. Dorn, T. Ferger, K. Khnel, S. Dsterer, R. Treusch, P. Radcliffe, E. Plnjes, and J. Ullrich, Physical Review Letters **98** (2007), 10.1103/PhysRevLett.98.203001.

[34] D. Rupp, M. Adolph, T. Gorkhover, S. Schorb, D. Wolter, R. Hartmann, N. Kimmel, C. Reich, T. Feigl, A. R. B. de Castro, R. Treusch, L. Strder, T. Mller, and C. Bostedt, New Journal of Physics **14**, 055016 (2012).

[35] U. Saalmann, Journal of Physics B: Atomic, Molecular and Optical Physics **43**, 194012 (2010).

[36] M. Schffler, K. Kreidi, D. Akoury, T. Jahnke, A. Staudte, N. Neumann, J. Titze, L. Schmidt, A. Czasch, O. Jagutzki, R. Costa Fraga, R. Grisenti, M. Smolarski, P. Ranitovic, C. Cocke, T. Osipov, H. Adaniya, S. Lee, J. Thompson, M. Prior, A. Belkacem, T. Weber, A. Landers, H. Schmidt-Bcking, and R. Drner, Physical Review A **78**, 013414 (2008).

[37] Z. B. Walters, R. Santra, and C. H. Greene, Physical Review A **74**, 43204 (2006), arXiv:0510187v3 [arXiv:physics].

[38] B. Ziaja, H. Wabnitz, F. Wang, E. Weckert, and T. Mller, Physical Review Letters **102** (2009), 10.1103/PhysRevLett.102.205002.

[39] B. Ziaja, H. Wabnitz, E. Weckert, and T. Mller, New Journal of Physics **10**, 043003 (2008).

[40] J. Zweiback, T. Ditmire, and M. Perry, Physical Review A **59**, R3166R3169 (1999).

[41] M. Arbeiter and T. Fennel, New Journal of Physics **13**, 053022 (2011).

[42] D. Bauer, Journal of Physics B: Atomic, Molecular and Optical Physics **37**, 30853101 (2004).

[43] C. Deiss, N. Rohringer, J. Burgdrfer, E. Lamour, C. Prigent, J.-P. Rozet, and D. Vernhet, Physical Review Letters **96** (2006), 10.1103/PhysRevLett.96.013203.

[44] F. Dorchies, T. Caillaud, F. Blasco, C. Bont, H. Jouin, S. Micheau, B. Pons, and J. Stevefelt, Physical Review E **71** (2005), 10.1103/PhysRevE.71.066410.

[45] R. von Pietrowski, K. von Haeften, T. Laarmann, T. Mller, L. Museur, and A. V. Kanaev, The European Physical Journal D **38**, 323336 (2006).

[46] A. Kramida, Y. Ralchenko, J. Reader, and N. A. Team, "NIST Atomic Spectra Database (ver. 5.0)," (2012).

6

Recombination effects in soft-x-ray cluster interactions at the xenon giant resonance

Edward Ackad, Nicolas Bigaouette, Stephanie Mack,
Konstatin Popov and Lora Ramunno *New Journal of Physics* 15(5), May 2013, 053047
doi:10.1088/1367-2630/15/5/053047

Author contributions

The MD package was mostly written by N. B. as was the recombination routines. The ACI cross-sections were calculated by E. A., who also derived the recombination rates equations. Original text by E. A. Figures were generated by E. A. with scripts originally written by N. B. but heavily modified. All authors contributed to the discussion.

New Journal of Physics
The open access journal for physics

Recombination effects in soft-x-ray cluster interactions at the xenon giant resonance

Edward Ackad[1,3], **Nicolas Bigaouette**[2], **Stephanie Mack**[2], **Konstatin Popov**[2] **and Lora Ramunno**[2]

[1] Department of Physics, Southern Illinois University Edwardsville, Edwardsville, IL 62026, USA
[2] Department of Physics, University of Ottawa, Ottawa, ON K1N 6N5, Canada

New Journal of Physics **15** (2013) 053047 (16pp)
Received 19 November 2012
Published 29 May 2013
Online at http://www.njp.org/
doi:10.1088/1367-2630/15/5/053047

Abstract. Xenon clusters in an intense soft-x-ray pulse are examined in detail and compared with recent experimental results by reproducing the experimental signals (Thomas *et al* 2009 *J. Phys. B: At. Mol. Opt. Phys.* **42** 134018). Good agreement is found between our theoretical model and the experimental results. A detailed analysis of the experimental signals and their constituents is performed. We find that, unlike large clusters, the smaller $N = 147$ have a saturated electron kinetic energy distribution (Bostedt *et al* 2010 *New J. Phys.* **12** 083004). We also find the highest charge states which are detected were initially on the outer shell of the cluster whereas the core ions recombine significantly and are detected as only moderately or singly charged (Hoener *et al* 2008 *J. Phys. B: At. Mol. Opt. Phys.* **41** 181001). Further, we find it is the outer shell ions which obtain the highest kinetic energy upon disintegration (Trost *et al* 2012 *Frontiers in Optics Conf.* (Optical Society of America) p FW5G.5).

[3] Author to whom any correspondence should be addressed.

Contents

1. Introduction

The x-ray regime has previously been the purview of synchrotrons which are only capable of reaching the linear, single-photon regime. Recent experimental advances now allow for ultra-intense x-ray sources opening a whole new regime of physics [5–7]. This regime is crucial for the development of several areas within nanoscience and its applications, and thus a detailed understanding of this new regime where nonlinear x-ray phenomena may occur is necessary [8–13].

Clusters irradiated with intense, short laser pulses has been a field of continued interest for the past two decades. Many new phenomena have been shown to occur in these systems which bridge the gap between solid and gas phases of matter. Comprehensive reviews on theoretical and experimental methods and results in laser–cluster interactions may be found in [14–16].

Increasingly, laser–cluster interactions are studied in a wavelength regime where single-photon effects are more important than laser-field effects [17–20]. Recently Thomas *et al* [1] explored the interaction in a particularly interesting regime. They examined xenon clusters in the soft-x-ray regime at the giant resonance of atomic xenon. This allowed for a probing of a mechanism fraught with difficulty in measuring: many-body recombination. This built on previous work which showed the importance of recombination in the charge transfer of layered heterogeneous clusters [3]. In all previous (longer wavelength) regimes and with most elements, higher charge states are observed in clusters compared with the gas phase. Xenon has a well known inner-shell resonance [21] centered at around 13 nm, the Auger decay of which leads to multiply charged xenon ions. Thus even in a low intensity beam the singly charged ion signal from a gas is much smaller than the doubly or triply charged signal [22].

In their experiment, Thomas *et al* observed an increase in the singly charged ion signal for clusters, compared with an almost negligible signal in gas. It was clear that some electron–ion recombination was taking place but the details of the experiment, as noted by Thomas *et al*, required further mechanisms beyond photoionization and recombination to completely understand the details of the laser–cluster interaction and subsequent expansion of the cluster [1].

In this work we describe Thomas *et al*'s experiment using our theoretical model. Our microscopic model replicates all the measured signals from the experiment and allows us to

tease out details which are not experimentally accessible. Previous work in this area has focused on explaining the thermal emission of electrons far above the dominant atomic emission line despite the large cluster potential in clusters of $\langle N \rangle = 2000$. It was found to be due to the supra-dense plasma created by the ultra-short, ultra-intense pulse [2].

We find that at the reported intensities, the small clusters are saturated in their thermal emission of electrons at intensities above $2.5 \times 10^{13}\,\mathrm{W\,cm^{-2}}$. We find good agreement with the experimental time-of-flight spectra and our model's results. Our results show that the nanoplasma does not span the entire cluster and the highly charged ions detected come from the outer shell of the cluster. The lower charged states, including the singly charged ion and high velocity atoms, come from the nanoplasma core. They are initially highly charged but recombine with the available plasma electrons and are detected as much lower charged states. The ion kinetic energy was found not to be saturated and the very high energy tail comes entirely from clusters at the peak of the laser pulse. Lastly, we find the expansion of the cluster is best described as a mix of an exploding outer shell and a hydrodynamically expanding core where recombination significantly reduces the charge state of the inner ions.

2. Method

We have significantly extended our previous model [23] in order to incorporate new features relevant for the soft-x-ray regime. The model remains fully microscopic and incorporates photoionization, single-step collisional ionization, collisional excitation and ionization from these excited states in what we term augmented collisional ionization [23]. Further, we have included many-body recombination, Auger decay and multiphoton ionization.

When an inner shell electron is ionized it leaves the atom or ion in an excited state. This state may decay by Auger decay. This occurs when an outer electron decays to the lower, empty, inner state and transfers the energy to other outer electrons which may then ionize or become excited. In the present work, as with Thomas *et al*'s experiment [1], xenon is irradiated with photons of energy matching the center of the giant 4d resonance [21]. The cross-section for photoionization from the inner 4d shell is around ten times larger than from the outer 5p shell [21]. The Auger decay occurs with different decay times depending on the different decay channels. Our model randomly selects a decay channel by taking into account the relative weights of all the possible decay channels. Experimental cross-sections and decay times [22] were used where available and Hartree–Fock calculations were used otherwise [24].

The experimental conditions under consideration also allow for multiphoton ionization, which we implemented similarly to the single-photoionization case [23], but where the laser depletion is by more than one photon. The cross-sections were taken from [25] with some modifications. The four-photon cross-section for the Xe^{13+} and Xe^{14+} was changed to $1 \times 10^{-114}\,\mathrm{cm^8\,s^3}$ to match the Xe^{12+}, and the Xe^{15+} to Xe^{18+} were set to be five-photon processes with a cross-section of $1 \times 10^{-149}\,\mathrm{cm^{10}\,s^4}$. These are underestimates of the multiphoton cross-section in all cases.

Finally, many-body recombination to the ground state was incorporated into our model. Once electrons are ionized from an atom, they are allowed to classically propagate within the cluster. Through collisions, it is possible that an electron may lose enough energy to become classically bound to a single ion. If the energy of an electron is equal to or below the lowest lying empty state of this ion, the electron is considered to have recombined to that ion. It is removed from the code and the ion charge state is decreased by one. To reduce dipole heating,

only electrons less than 1 bohr from an ion are tested for recombination. Recombination not to the ground state but to an excited state is treated classically.

The particles interact at close range as Gaussian charge distributions [23] and at long range using the Coulomb potential. The depth of the potential well of an ion of charge state Z is Z times that of a singly charged ion. Since ionization potentials (Ip) are not strictly linear with Z, the depth of the singly charged ion must be chosen such that all charge states have a potential at $r = 0$ deep enough for recombination to be possible (i.e. potential depth $<$ Ip). Furthermore, the time-step must be small enough not only to prevent accumulating errors during the integration of the equations of motion, but also to prevent electrons from falling too deep into an ion's potential—a situation allowed classically but not quantum mechanically. For the present work a depth of 1 hartree and a time-step of 500 zs are used.

2.1. Propagation to the detector

A full comparison with experimental results ideally requires the propagation of the particles to the detector. This is a challenging endeavor as electrons' motion is on the attosecond time scale while the particles reach the detector on a microsecond time scale. We have thus devised a three-phase strategy to accomplish this with only small approximations.

In the first phase, the cluster interacts with the laser pulse and collisional ionization and recombination both continue for some time afterward. This simulation is run using the shortest time step, and includes all microscopic interactions. Eventually (after about 2 ps for small clusters) ionization becomes infrequent as the cluster disintegrates [26]. Once this happens, phase two is initiated. The ionization routines are switched off in the code, but many-body recombination is still allowed. To increase the efficiency of the calculation, a dynamic time-step is used based on the closest distance between any two particles ($\mathrm{d}t \approx R_{\min}/c$ where c is the speed of light). This stage is performed with the time-of-flight field set to the same value as in the experiment of interest. Once the cluster is sufficiently sparse, Rydberg systems are forcibly recombined. This recombination results in a very small underestimate in most cases but makes the long-time propagation feasible by reducing the number of particles. The propagation times for this second phase are around 10 ps.

Once the particles are far enough away from each other, the dominant force they feel is the time-of-flight detector field. The final phase is then initiated. The particles' position and velocity are used as initial conditions to solve Newton's equations of motion for the constant time-of-flight field in a single integration to the field-free region. Then they are propagated in the field-free region to the detector, again with only a single integration step, thereby simulating the whole process of the experiment.

Experimental signals which do not have time-of-flight fields, such as kinetic energy measurements, are performed in the same manner, albeit without the time-of-flight field.

Finally, we incorporate the spatial profile of the laser pulse in our calculations, which is assumed to be Gaussian. We simulate laser–cluster interactions at different intensities, but also consider that clusters at different locations within the laser spatial profile will be at different distances from the detector. Clusters which interact with the wings of the pulse are closer to and farther from the detector than the clusters which interact with the peak of the pulse. This has the effect of broadening the time-of-flight peaks a non-negligible amount as clusters further away will have more kinetic energy (due to more time in the time-of-flight field) while the opposite is true for clusters initially closer to the detector. This was observed virtually as the time-of-flight signals were built up.

3. Recombination in nanoplasmas

Electron–ion recombination is crucial to understanding the results of Thomas *et al*'s experiment. To ensure we have a suitable model for recombination to the ground state, we compare the results of our code to a well-known plasma model for three-body recombination [27]. We compare with a more stringent system than xenon, i.e. argon, as it is three times lighter. The timescale for cluster disintegration is thus shorter for an argon cluster compared with a xenon cluster.

To calculate the recombination rate given by our code, we considered pre-ionized argon clusters of singly charged ions. By enabling our recombination routine (but not the ionization routines), we then can determine numerically the recombination rate as a function of time.

We compare our calculation with a standard three-body recombination model [27]

$$\frac{\mathrm{d}N_\mathrm{i}}{\mathrm{d}t} = \alpha_\mathrm{r} N_\mathrm{e}^2 N_\mathrm{i}, \tag{1}$$

where N_i is the ions density in cm^{-3}, N_e is the electron density in cm^{-3}, $\alpha_\mathrm{r} = 8.75 \times 10^{-27} T_\mathrm{e}^{-4.5}\,\mathrm{cm}^6\,\mathrm{s}^{-1}$ and T_e is the electron temperature in eV. For singly charged ions, $N_\mathrm{i} \approx N_\mathrm{e} \approx N$, then equation (1) becomes

$$\frac{\mathrm{d}N}{\mathrm{d}t} = \alpha_\mathrm{r} N^3. \tag{2}$$

Solving equation (2) yields

$$N(t) = \frac{N_0}{\sqrt{1 + 2N_0^2 \alpha_\mathrm{r} t}}, \tag{3}$$

where $N_0 (\approx 2.8 \times 10^{22}\,\mathrm{cm}^{-3})$ is the initial electron/ion density. Defining the number of recombinations as $N_\mathrm{R}(t) = N_0 - N(t)$ we obtain

$$N_\mathrm{R}(t) = N_0 \left(1 - \frac{1}{\sqrt{1 + t/\tau_\mathrm{r}}}\right), \tag{4}$$

where we defined the recombination time as $\tau_\mathrm{r} = \frac{1}{2\alpha_\mathrm{r} N_0^2}$.

Equation (1) is known to be valid for large systems but we found that it agrees with our simulations of recombination in nanoscopic systems as well. Figure 1 plots N_R as a function of time for our pre-ionized cluster simulations, along with the fits obtained from equation (4). In our simulations, we initialized our pre-ionized clusters with a Maxwell–Boltzmann electron temperature distribution of 13 eV, well within the range expected for laser–cluster nanoplasmas at current experimental conditions. We considered the following argon clusters which are common sizes in cluster experiments: Ar_{5083}, Ar_{1415} and Ar_{147}. We chose clusters of argon (rather than the three-times-heavier xenon) because we wanted to test our recombination model even in the regime where the cluster starts to expand. The points in figure 1 represent our numerically obtained simulation data. The solid lines are a least-squares fit to equation (4), where τ_r a fitting parameter. Since the cluster systems are finite and in motion, $N(t \to \infty) \neq 0$, i.e. not all electrons will recombine. Thus N_0 is also used as a fitting parameter. From the fits, we find that the recombination times for the Ar_{5083}, Ar_{1415} and Ar_{147} clusters are $\tau_\mathrm{r} = 14.0$, 17.8 and 13.4 fs, respectively. These values agree well (within 20%) when compared with the result of equation (4): 15 fs. This good agreement suggests that our recombination model is sufficiently accurate to replicate the dominant features of three-body recombination, even for cluster disintegration.

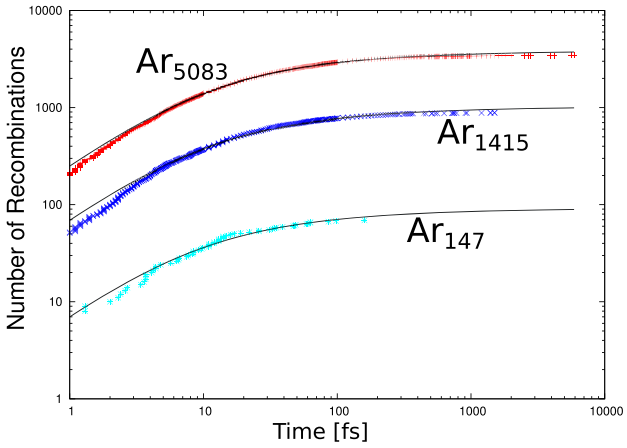

Figure 1. The number of recombinations as a function of time as calculated from singly charged cluster simulations (points). The lines represent fits of these data to the well-known three-body recombination model from [27].

4. Results

A detailed comparison with the experiment described in [1] was performed for xenon clusters with 147 atoms interacting with a $\lambda = 13.7$ nm laser pulse. This was done using the three-phase simulation described in section 2.1, which propagates the particles all the way to the detector. The spatial and time profile of the laser are assumed to be Gaussian. To model the laser–cluster interaction over the laser spatial profile, we simulated 12 intensities ranging from 1×10^{11} W cm^{-2} to 5.8×10^{14} W cm^{-2} m. Clusters away from the laser focus contribute significantly to the final signal since they are in much larger number than clusters irradiated near the peak intensity. To ensure meaningful statistics, more than three dozen simulations were performed at each intensity. These were integrated to generate results directly comparable to experimental signals.

It is worth noting that a key difference between the experimental signal and the results presented in this work is the influence of uncondensed gas. In most cluster experiments the ion signal from the uncondensed gas is small, if not negligible, especially for high charge states. The current regime differs significantly from this as the laser wavelength is in the middle of xenon's giant resonance. Thus the uncondensed gas produces highly charged ions as is common in x-ray experiments. Nevertheless, good agreement with the experiment is found.

4.1. Electrons

The total kinetic energy spectrum of the electrons is calculated assuming a field-free propagation to the detector. The results are plotted as the blue (upper) line in figure 2 for the complete experimental signal (i.e. all calculated laser intensities are included). An illustration of the pulses intensity is shown in the inset. The kinetic energy distribution decreases close to monotonically until $E \approx 3.5$ hartree. Beyond this a plateau is formed extending to 20 hartree (≈ 544 eV).

The low energy part of the signal lacks clear atomic peaks as no uncondensed gas was included in the simulation. The spectrum matches qualitatively with the results from [2] despite the difference in cluster size.

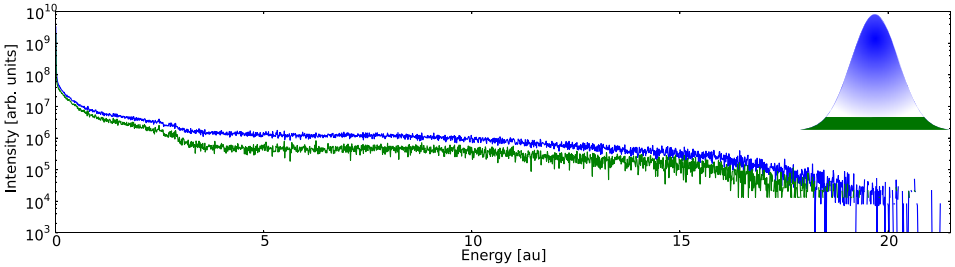

Figure 2. The blue curve is the total electron kinetic energy distribution. The green curve is the normalized total electron kinetic energy distribution without the peak intensities of the laser pulse, $I \geqslant 5 \times 10^{13}\,\mathrm{W\,cm^{-2}}$. Due to the renormalization of the green curve, both have the same number of electrons in the signal. The inset is an illustration of the intensity of the laser pulse for each curve: the blue curve is the entire pulse and the green curve is the pulse when only intensities less than $5 \times 10^{13}\,\mathrm{W\,cm^{-2}}$ are included given the green (lower) shape in the illustration.

To explore the origin of the high energy electron plateau, we replot the curve after removing the contributions of the higher intensities and renormalizing the signal. This is plotted as the green (lower) line in figure 2, which shows the (renormalized) electron kinetic energy distribution excluding contributions from the portions of the laser spatial profile with intensities $\geqslant 5 \times 10^{13}\,\mathrm{W\,cm^{-2}}$. Thus the green (lower) curve shows the electron kinetic distribution from clusters not irradiated by the most intense part of the pulse. Instead it is the clusters irradiated by the green (lower) part of the pulse illustration in the inset. The two distributions are very similar, indicating that the high energy kinetic energy signal is saturated. Removing intensities below $5 \times 10^{13}\,\mathrm{W\,cm^{-2}}$ has a much more dramatic change on the distribution (not shown). The highest energy electrons do not exclusively come from the peak of the laser pulse. Clusters irradiated with the spatial wings of the laser pulse, even at ten times less intensity than the peak, still generate electrons at the highest end of the distribution.

At intensities $\geqslant 5 \times 10^{13}\,\mathrm{W\,cm^{-2}}$ electrons are not accelerated any more than at an intensity of $5 \times 10^{13}\,\mathrm{W\,cm^{-2}}$. The electrons from clusters irradiated at or near the spatial peak of the laser pulse ($\geqslant 5 \times 10^{13}\,\mathrm{W\,cm^{-2}}$) do not have a significantly different distribution of kinetic energy. However, the clusters irradiated at and near the spatial peak of the laser pulse ($\geqslant 5 \times 10^{13}\,\mathrm{W\,cm^{-2}}$) do produce higher charge states (see section 4.2.1) and thus more electrons. Since the clusters at and near the peak generate more electrons, but do not give these electrons more kinetic energy than clusters at outside the spatial peak, we draw the conclusion that the extra electrons quickly leave the cluster and do not increase the electron density of the cluster. Thus the electron kinetic energy distribution signal is saturated and cannot contain a hotter plasma unlike what was seen for larger clusters [2]. This saturation is cluster size dependent, as larger clusters would be able to support a higher electron density. The saturation intensity is thus higher for larger clusters.

4.2. Ions

The properties of the ions from the laser–cluster interaction are now examined. Comparison with experimental signals is shown followed by simplified plots to explain the full composition of the experimental signal.

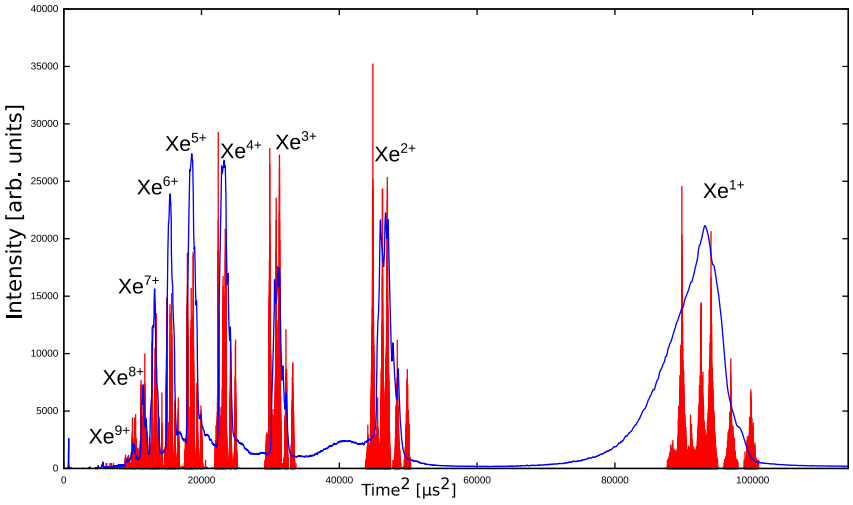

Figure 3. The full time-of-flight ion signal is shown in red including the xenon isotope distribution for xenon clusters of size $N = 147$ irradiated by a 10 fs pulse with $\lambda = 13.7$ eV and $I = 5.8 \times 10^{14}$ W cm^{-2}. The experimental results from [1] are shown as the solid blue line.

4.2.1. Time-of-flight signals. The full time-of-flight signal is shown in figure 3 which includes the mass isotope distribution of xenon. Good agreement is found when compared with the experimental results of [1] shown as the solid (blue) line. In particular, we find a large singly charged ion contribution which was observed experimentally to be dominant only in the cluster signal. As previously mentioned, our simulations do not include uncondensed gas, though it contributes non-negligibly to the experimental signals. This omission is the main contribution to the differences in the relative abundance of each charge state that exist between figure 3 and [1]. Differences in the width of the peaks are primarily caused by the exclusion of the log-normal cluster distribution. The experimental cluster jet contains a distribution of clusters of different sizes and is only peaked at $N = 147$. The other-sized clusters create ions with different kinetic energies. The experimental signal is a convolution of the signal from each size cluster causing much of the broadening [28].

Further analysis of full time-of-flight signal in figure 4(a) is now carried out without including the mass isotope distribution for clarity. Charge states up to Xe^{11+} are now visible as no foot is formed at the high charge states. Further, the width of the peaks may be seen to be decreasing for higher charge states. This will be further explored in section 4.2.3.

To further investigate the origin of the peaks in the time-of-flight signal the full signal is overlaid with partial signals with lower intensities removed. Figure 4(b) shows the full time-of-flight signal in red and the reduced signal from intensities $\geqslant 5 \times 10^{13}$ W cm^{-2} in green. In blue is the reduced signal from intensities $\geqslant 3 \times 10^{14}$ W cm^{-2}. The illustration in the singly charged box shows the portion of the pulse used to construct each of the distributions. The distributions in each box use different scales (both vertical and horizontal).

The high charge states (Xe^{7+} and above) emerge primarily from the very highest intensity spatial regions of the pulse. The Xe^{7+} charged states and above are almost exclusively created in intensities higher than $I \geqslant 5 \times 10^{13}$ W cm^{-2} (shown in green). The very highest intensities,

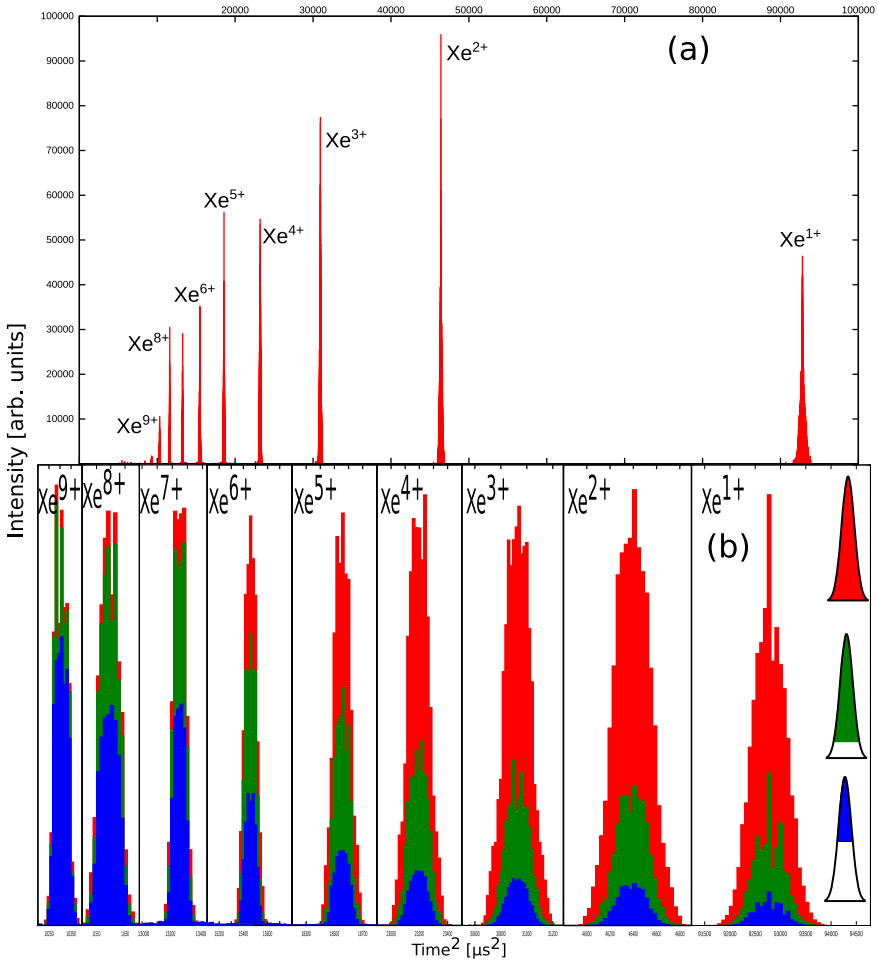

Figure 4. (a) The time-of-flight signal without mass isotopes. (b) Comparison of the full (single-isotope) time-of-flight signal in red with the time-of-flight signal from $I \geqslant 5 \times 10^{13}\,\mathrm{W\,cm^{-2}}$ only shown in green and $I \geqslant 3 \times 10^{14}\,\mathrm{W\,cm^{-2}}$ only shown in blue. Each charge state is on a different scale. The illustration on the right of the singly charged distribution shows the part of the pulse used to construct each distribution on a linear scale.

$I \geqslant 3 \times 10^{14}\,\mathrm{W\,cm^{-2}}$ (shown in blue) irradiate a smaller number of clusters but still generate more than 30% of the Xe^{7+} charged states and above. The higher charged states, Xe^{10+} and above, are almost exclusively created by the highest intensities, $I \geqslant 3 \times 10^{14}\,\mathrm{W\,cm^{-2}}$ (not shown).

The Xe^{1+} signal on the other hand emerges from the lower intensity regions. This remains true even when considering the relative number of clusters in the spatial region: the lower intensities will irradiate more clusters compared with the higher intensities and thus any signal from the lower intensities is amplified. Including this, the relative number of Xe^{1+} compared with the total number of atoms in the spatial region of the pulse, i.e. the fraction of Xe^{1+} per atom, the Xe^{1+} is still far more abundant in the low intensity region.

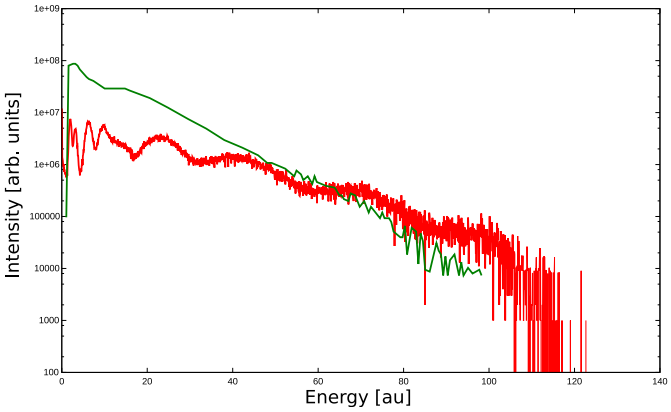

Figure 5. The IKED from [1] is shown as the solid (green) line and the results of this work are shown as the thick (red) line.

The widths of each reduced intensity peak in figure 4(b) give information about the contribution of different intensities to the high energy ions of a charge state. The highest energy ions of a charge state come from the highest intensity regions of the pulse. This is discernible from the asymmetry toward smaller times for the time-of-flight signals of the high intensity signal (blue and to a lesser extent green). However, for low charge states, the contribution from the very highest intensity is small. This is due to the proportionally smaller number of lower charge states and the smaller number of irradiated clusters, i.e. the high intensity part of the pulse irradiates few clusters and the intensity is so high that few Xe^{1+} are produced. Xe^{1+} are rarely produced by direct photoionization and are predominantly produced by three-body recombination.

4.2.2. Total kinetic energy distributions. The ion kinetic energy distribution (IKED) for $\langle N \rangle = 150$ was reported in [1] using a combination of the time-of-flight data and simulations. In figure 5 their results are shown as the (green) line to compare with our total IKED results shown as the thick (red) line. We find good agreement at the high energy region. Our results show a cut-off just above what the experimental detector found near 100 hartree ($\approx$2.7 keV).

There is, however, disagreement at lower energies. We find that this disagreement stems from a combination of uncondensed gas and clusters of different sizes which occur in the cluster's beam [28]. The smaller clusters ($N < 147$) and uncondensed gas create ions with significantly less kinetic energy and are included in the experimental signal but absent in this work. In [1], Thomas *et al* find that smaller clusters have a more rapidly decreasing high energy tail compared with larger clusters. Thus the experimental signal for $\langle N \rangle = 150$ will have a significant contribution from $\langle N \rangle = 55$ and produce a discrepancy at the low energy regime.

The solid (green) curve in figure 6(a) shows the reduced IKED signal when only intensities up to 2.5×10^{13} W cm^{-2} are included compared with the full signal in blue. This is illustrated in the spatial intensity profile in the inset for each curve. The low energy part of the IKED remains almost unchanged, except for the peak near 3.3 hartree which is absent. A sharp cut-off is seen in the reduced signal around 10 hartree ($\approx$270 eV). While the peak near 25 hartree is somewhat reproduced the very high energy ions are absent from the reduced signal.

The solid (green) curve in figure 6(b) shows the reduced signal when only intensities up to 5×10^{13} W cm^{-2} are included as illustrated in the inset by the green (lower) cut-off pulse shape.

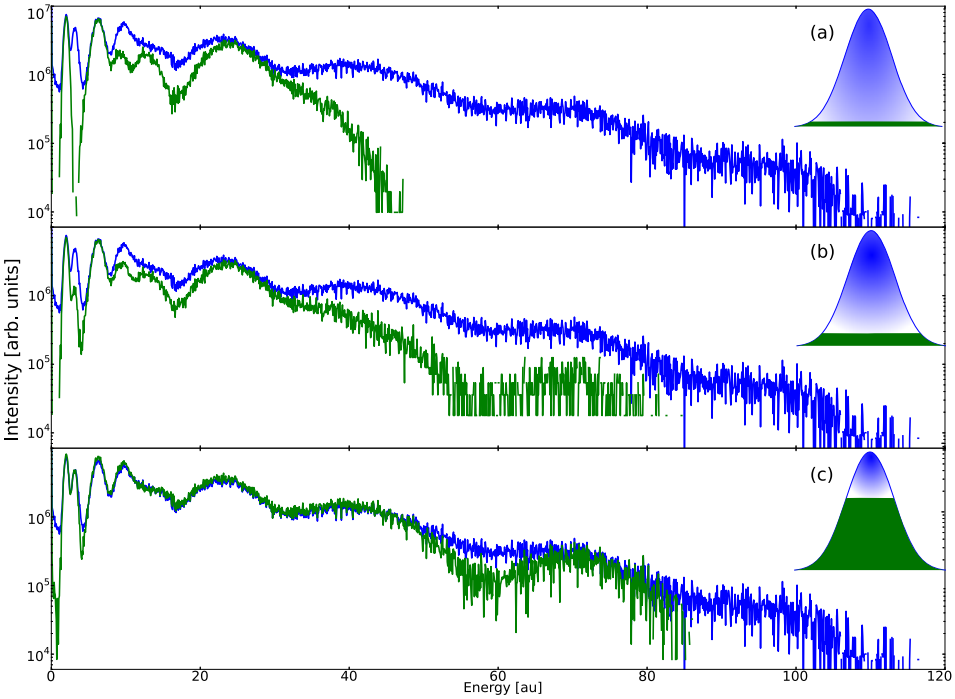

Figure 6. (a) The total ion kinetic energy in blue and the total ion kinetic energy excluding $I \geqslant 2.5 \times 10^{13}\,\mathrm{W\,cm^{-2}}$ in green. (b) The total ion kinetic energy in blue and the total ion kinetic energy excluding $I \geqslant 5 \times 10^{13}\,\mathrm{W\,cm^{-2}}$ in green. (c) The total ion kinetic energy in blue and the total ion kinetic energy excluding $I \geqslant 3 \times 10^{14}\,\mathrm{W\,cm^{-2}}$ in green. The insets are an illustration of the spatial intensity of the laser pulse for each curve: the blue curve is the entire intensity profile of the pulse and the green part is an illustration of the included intensities in the green curve.

Two new peaks now appear at 3.3 and 70 hartree. These peaks are thus largely the result of clusters irradiated at $\approx 2.5 \times 10^{13}\,\mathrm{W\,cm^{-2}}$.

The solid (green) curve in figure 6(c) shows the reduced signal when only intensities up to $3 \times 10^{14}\,\mathrm{W\,cm^{-2}}$ are included. The low energy region matches well with the full signal demonstrating that the clusters irradiated near the spatial peak of the laser pulse do not produce a significant amount of ions below 25 hartree. The high energy tail, however, is almost exclusively created by clusters near the spatial peak. Thus the high energy IKED is not saturated, unlike the high energy electron kinetic energy distribution, as discussed in section 4.1.

Different spatial regions of the pulse thus contribute differently to the IKED. As expected, the highest kinetic energy ions are produced by clusters irradiated by the spatial peak of the laser pulse. This is seen by examining the difference between the green and blue curves in figure 6(a) and noticing that the green curve ends near 85 hartree. Ions with kinetic energy above 85 hartree can only be produced when the cluster is irradiated with more than $3 \times 10^{14}\,\mathrm{W\,cm^{-2}}$. The low kinetic energy region is largely produced by clusters in the spatial wings of the pulse which are not irradiated with the peak intensity. The peak at 3.3 hartree, which is produced by the high intensity part of the pulse, is due to the disintegration of an inner shell of the cluster.

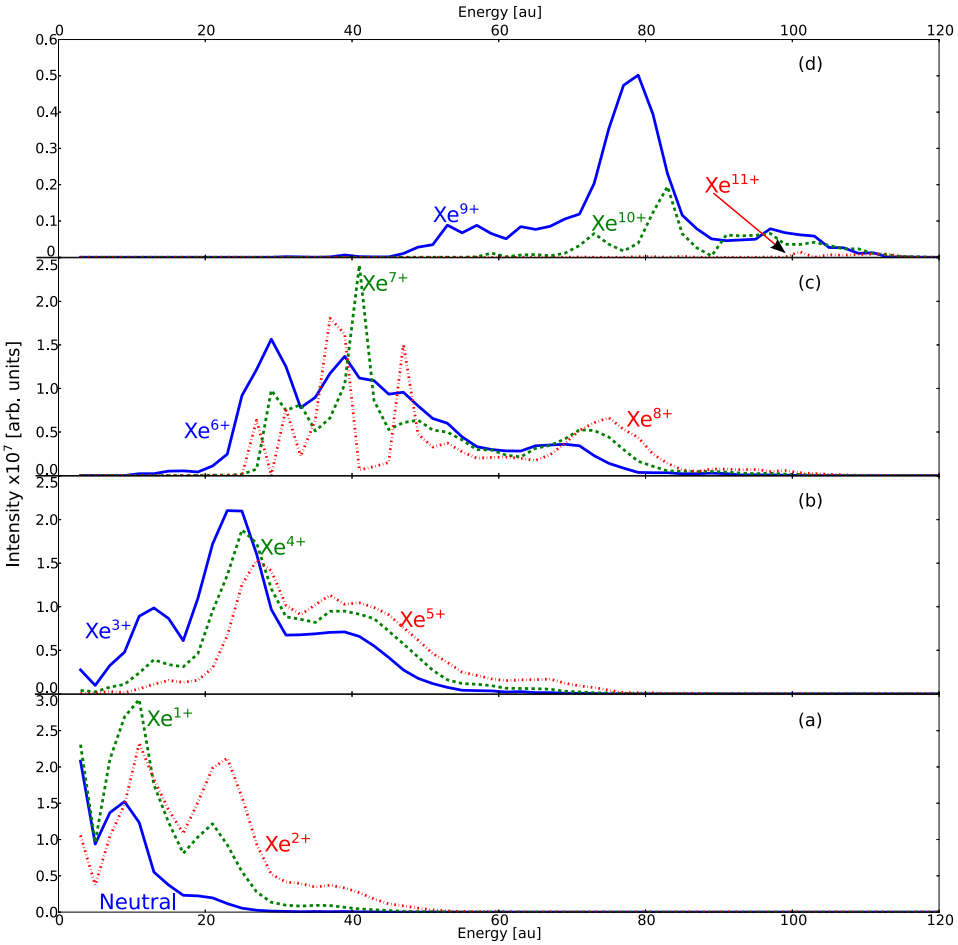

Figure 7. The kinetic energy distribution of the ionic states (a) 0–2, (b) 3–5, (c) 6–8 and (d) 9–11.

At the higher intensities there are more electrons which have escaped the cluster (see figure 2 and the explanation therein) leaving a larger charged core during the disintegration. The inner shell, more highly charged near the spatial peak of the pulse, gains more kinetic energy upon disintegration, forming the peak at 3.3 hartree.

4.2.3. Individual kinetic energy distributions. To further understand the expansion dynamics of the cluster, the IKED is now separated for each charge state. Figure 7(a) gives the IKED for the neutral (although undetectable in current experimental setups) as a solid (blue) line, the Xe^{1+} as a dashed (green) line and the Xe^{2+} as a dotted (red) line. Figures 7(b)–(d) give the IKED for the Xe^{3+} to Xe^{11+}, with the same respective curve styles as (a).

The plots in figure 7 are not normalized and thus show the relative abundance of each charge state as well. The IKED and abundance for the three charge states in figure 7(a) have peaks at the same energies except for the peak near 22 hartree which is largely suppressed in the neutrals. These curves resemble the Xe^{3+} curve in figure 7(b) for energies below around 35 hartree. Recombination thus significantly reduces the charge state of the low energy ions to predominantly less than Xe^{4+}.

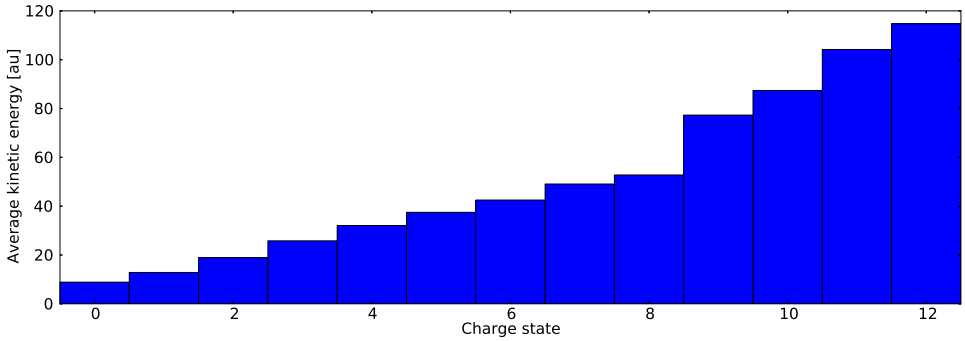

Figure 8. The average ion kinetic energy for each charge state.

The persistence of the peaks in figures 7(a) and (b) across multiple charge states suggest they are of a common origin. Higher charge states in the core of the cluster gain their kinetic energy during the initial disintegration of the core. During the disintegration some recombination occurs. This causes newly recombined ions to still have the same kinetic energy as their higher-charged brethren, thus giving the same peak across multiple charged states. This indicates that those ions were largely outside the cluster potential before the recombination occurred. The recombination thus mostly takes place after the disintegration of the cluster's core.

This must occur through recombination as high energy neutrals are also produced, with the same IKED peak locations as Xe^{1+} to Xe^{4+}. In fact there is a sizable peak around 9 hartree which corresponds to neutrals with a temperature of 2.8 million K. This peak is weakly present in the Xe^{5+} signal but increases significantly as the charge state is lowered peaking with Xe^{2+} but remaining large even for neutrals.

The differences between the low charge states ($<Xe^{4+}$) are predominantly at the high energy tail of the IKED due to the reduced probability of three-body recombination for fast moving ions. The lower charge states emerge from a common pool of ions and then recombine to lower charge states and thus produce IKED peaks in similar locations. The higher charged ions have IKED peaks at different energies showing that they are not part of the common pool of ions that will recombine to form the lower charge state ions. The higher charge states are in fact mainly from the outer shells of the clusters. The lower charge states are from the core of the cluster. The nanoplasma which formed in the core thus produces high charge states initially but upon disintegration most of these ions recombine to charge states below Xe^{5+}.

By integrating the curves in figure 7 for each charge state, we calculate the average ion kinetic energy for each charge state, shown in figure 8. A clear increase in the average kinetic energy of each charge state is found. The increase is gradual and does not have a unit linear slope in the charge state, i.e. the value for Xe^{4+} is not twice that of Xe^{2+}. The relationship between charge state and ejection energy is higher and closer to a linear relationship for charge states $Xe^{1}+$ to $Xe^{8}+$ compared with the quadratic relationship found in [1].

However, this is expected as only clusters of size $N = 147$ were included in our work. Smaller clusters, which are present in the experimental cluster beam, would significantly lower the average ejection energy.

The higher charge states, $>Xe^{9+}$, are infrequent, occurring more than four times fewer than even the Xe^{8+}. Because of this, we would need to do a larger number of simulations to determine

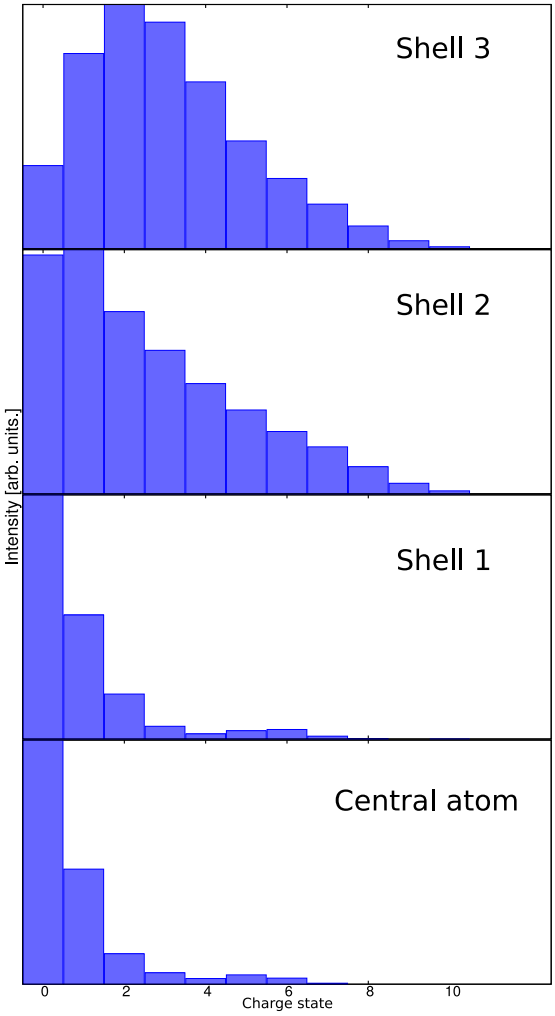

Figure 9. The charge state distributions for the central atom and the three shells of the 147 Xe clusters.

their properties more accurately. Nevertheless, our observation that they carry a considerable amount of kinetic energy upon disintegration is qualitatively correct, and borne out in both figures 7(d) and 8.

In conclusion, the highest charge states are thus found to be produced in the most intense spatial region of the laser pulse profile (cf figure 4(b)) and are the ions with the highest kinetic energy.

4.2.4. Relationship between the initial position of an atom and its final charge state. Having tracked the final detector states and obtained their kinetic energy, it is also possible to examine the relationship between the initial position of the atoms within the cluster, and their final charge state. Atomic clusters are roughly icosahedral shelled structures, and thus the position of an atom relative to its cluster center can be characterized by the shell from which it originated. There are three shells in a 147-atom cluster, plus a single central atom. The final charge state distributions

resulting from each shell (and the central atom), are plotted in figure 9 for the entire laser profile (all intensities integrated with their relative abundance).

We find that the highest charge states all originate from atoms in the outermost shell of the cluster (shell 3) [4]. While the physical center of the cluster produces higher charge states during the laser–cluster interaction [26], in the soft-x-ray regime, these recombine to much lower charge states (including neutral) prior to detection. Most of the neutrals from the outer shell are atoms that are simply never ionized due to being in the low intensity region of the laser's spatial profile.

The primary contribution to the Xe^{1+} signal comes from the inner shells of the cluster, and even more so from shell 1 than shell 2. This is due to the center of the cluster's nanoplasma being quasi-neutral and dense, allowing for efficient three-body recombination. Further from the center of the cluster the density decreases and thus the recombination rate also decreases. This makes the recombination to lower charge states less probable in the outer shell.

5. Conclusion

A detailed investigation into the results of Thomas *et al*'s xenon clusters in an ultra-intense resonant laser pulse has been performed. The time-of-flight signal was reproduced and analyzed to determine the role of the high and low intensity components of the laser pulse. The kinetic energy distribution of the electrons was found to be saturated at an intensity of 5×10^{13} W cm^{-2} while the ion's kinetic energy distribution was not. A detailed examination of the kinetic energy distribution of each charge state revealed that high energy neutrals are produced and that the lower charge states must come from a common pool of ions. Further, the highest charge states detected come from the outer shell of the cluster and these carry away the most amount of kinetic energy. Lower charge states were created via recombination and originated primarily from inner shells.

Acknowledgments

The authors thank Christoph Bostedt, Thomas Brabec and Jean-Paul Brichta for insightful conversations. This work was supported by SHARCNET, NSERC, Ontario's MRI, the Canada Research Chairs program, and the Canadian Foundation for Innovation.

References

[1] Thomas H, Bostedt C, Hoener M, Eremina E, Wabnitz H, Laarmann T, Plönjes E, Treusch R, de Castro A R B and Möller T 2009 Shell explosion and core expansion of xenon clusters irradiated with intense femtosecond soft x-ray pulses *J. Phys. B: At. Mol. Opt. Phys.* **42** 134018

[2] Bostedt C, Thomas H, Hoener M, Möller T, Saalmann U, Georgescu I, Gnodtke C and Rost J-M 2010 Fast electrons from multi-electron dynamics in xenon clusters induced by inner-shell ionization *New J. Phys.* **12** 083004

[3] Hoener M, Bostedt C, Thomas H, Landt L, Eremina E, Wabnitz H, Laarmann T, Treusch R, a De Castro R B and Möller T 2008 Charge recombination in soft x-ray laser produced nanoplasmas *J. Phys. B: At. Mol. Opt. Phys.* **41** 181001

[4] Trost J, Ackad E, Bigaouette N and Ramunno L 2012 Explosion of non-spherical clusters due to irradiation with intense femtosecond x-rays *Frontiers in Optics Conf.* (Optical Society of America) p FW5G.5

[5] Gorkhover T *et al* 2012 Nanoplasma dynamics of single large xenon clusters irradiated with superintense x-ray pulses from the linac coherent light source free-electron laser *Phys. Rev. Lett.* **108** 245005
[6] Thomas H 2012 Explosions of xenon clusters in ultraintense femtosecond x-ray pulses from the LCLS free electron laser *Phys. Rev. Lett.* **108** 133401
[7] Foucar L *et al* 2012 Ultra- atoms by intense x-ray free-electron laser pulses *Nature Photon.* **6** 858–65
[8] Doumy G *et al* 2011 Nonlinear atomic response to intense ultrashort x rays *Phys. Rev. Lett.* **106** 083002
[9] Richter M, Amusia M Ya, Bobashev S V, Feigl T, Juranić P N, Martins M, Sorokin A A and Tiedtke K 2009 Extreme ultraviolet laser excites atomic giant resonance *Phys. Rev. Lett.* **102** 163002
[10] Lambropoulos P, Nikolopoulos G M and Papamihail K G 2011 Route to direct multiphoton multiple ionization *Phys. Rev.* A **83** 021407
[11] Schorb S *et al* 2012 Size-dependent ultrafast ionization dynamics of nanoscale samples in intense femtosecond x-ray free-electron-laser pulses *Phys. Rev. Lett.* **108** 233401
[12] Rudek B *et al* 2013 Resonance-enhanced multiple ionization of krypton at an x-ray free-electron laser *Phys. Rev.* A **87** 023413
[13] Bostedt C *et al* 2012 Ultrafast x-ray scattering of xenon nanoparticles: imaging transient states of matter *Phys. Rev. Lett.* **108** 093401
[14] Saalmann U, Siedschlag Ch and Rost J M 2006 Mechanisms of cluster ionization in strong laser pulses *J. Phys. B: At. Mol. Opt. Phys.* **39** R39
[15] Bostedt C, Adolph M, Eremina E, Hoener M, Rupp D, Schorb S, Thomas H, de Castro A R B and Müller T 2010 Clusters in intense flash pulses: ultrafast ionization dynamics and electron emission studied with spectroscopic and scattering techniques *J. Phys. B: At. Mol. Opt. Phys.* **43** 194011
[16] Th. Fennel, Meiwes-Broer K-H, Tiggesbäumker J, Dinh P M and Suraud E 2010 Laser-driven nonlinear cluster dynamics *Rev. Mod. Phys.* **82** 1793–842
[17] Fennel T, Ramunno L and Brabec T 2007 Highly charged ions from laser–cluster interactions: local-field-enhanced impact ionization and frustrated electron–ion recombination *Phys. Rev. Lett.* **99** 233401
[18] Siedschlag C and Rost J-M 2004 Small rare-gas clusters in soft x-ray pulses *Phys. Rev. Lett.* **93** 043402
[19] Santra R and Greene C H 2003 Xenon clusters in intense VUV laser fields *Phys. Rev. Lett.* **91** 233401
[20] Ziaja B *et al* 2009 Energetics, ionization and expansion dynamics of atomic clusters irradiated with short intense vacuum-ultraviolet pulses *Phys. Rev. Lett.* **102** 205002
[21] Becker U, Prescher T, Schmidt E, Sonntag B and Wetzel H E 1986 Decay channels of the discrete and continuum xe 4d resonances *Phys. Rev.* A **33** 3891–9
[22] Uiberacker M *et al* 2007 Attosecond real-time observation of electron tunnelling in atoms *Nature* **446** 627–32
[23] Bigaouette N, Ackad E and Ramunno L 2011 Augmented collisional ionization via excited states in XUV cluster interaction *J. Phys. B: At. Mol. Opt. Phys.* **44** 165102
[24] Cowan R D 1981 *The Theory of Atomic Structure and Spectra* (Berkeley, CA: University of California Press)
[25] Makris M G, Lambropoulos P and Mihelič A 2009 Theory of multiphoton multielectron ionization of xenon under strong 93 eV radiation *Phys. Rev. Lett.* **102** 033002
[26] Ackad E, Bigaouette N, Briggs K and Ramunno L 2011 Clusters in intense XUV pulses: effects of cluster size on expansion dynamics and ionization *Phys. Rev.* A **83** 063201
[27] *Plasma NRL Formulary* 2009 Naval Research Laboratory, pp 54–5
[28] Arbeiter M and Fennel T 2010 Ionization heating in rare-gas clusters under intense XUV laser pulses *Phys. Rev.* A **82** 013201

7

Nonlinear grid mapping applied to an FDTD-based, multi-center 3D Schrödinger equation solver

Nicolas Bigaouette, Edward Ackad, Lora Ramunno
Computer Physics Communications 183(1), 2012, 38–45
doi:10.1016/j.cpc.2011.08.011

Author contributions

The whole QFDTD package was written by N. B. The post processing and analysis was performed entirely by N. B. The method developed to obtain eigenstates in imaginary time is original work by N. B. The nonlinear mapping is original work too but was inspired by conformal mapping as suggested by E. A. The whole text was written by N. B. with inputs from L. R. and E. A. All authors contributed to the discussion.

Computer Physics Communications 183 (2012) 38–45

Contents lists available at SciVerse ScienceDirect

Computer Physics Communications

www.elsevier.com/locate/cpc

Nonlinear grid mapping applied to an FDTD-based, multi-center 3D Schrödinger equation solver

Nicolas Bigaouette *, Edward Ackad, Lora Ramunno

Department of Physics, University of Ottawa, 150 Louis Pasteur, Ottawa ON, K1N 6N5, Canada

ARTICLE INFO

Article history:
Received 16 February 2011
Received in revised form 15 August 2011
Accepted 18 August 2011
Available online 26 August 2011

Keywords:
Quantum mechanics
Time-dependent Schrödinger equation
Nonlinear grid mapping
Finite-difference time domain
Coulomb potential

ABSTRACT

We developed a straightforward yet effective method of increasing the accuracy of grid-based partial differential equation (PDE) solvers by condensing computational grid points near centers of interest. We applied this "nonlinear mapping" of grid points to a finite-differenced explicit implementation of a time-dependent Schrödinger equation solver in three dimensions. A particular multi-center mapping was developed for systems with multiple Coulomb potentials, allowing the solver to be used in complex configurations where symmetry cannot be used for simplification. We verified our method by finding the eigenstates and eigenenergies of the hydrogen atom and the hydrogen molecular ion (H_2^+) and comparing them to known solutions. We demonstrated that our nonlinear mapping scheme – which can be readily added to existing PDE solvers – results in a marked increase in accuracy versus a linear mapping with the same number of (or even much fewer) grid points, thus reducing memory and computational requirements by orders of magnitude.

1. Introduction

There are many works devoted to solving the time-dependent Schrödinger equation [1,2]. Recently there have been several based on the finite-difference time domain (FDTD) technique [3–7], which is a standard algorithm in computational electrodynamics. In usual FDTD, Maxwell's equations are discretized on a grid and solved explicitly using leap-frog integration in time [8,9]. Since the FDTD algorithm is explicit and local, it is relatively straightforward to implement and parallelize.

Applying FDTD to solve the Schrödinger equation yields a method that is generally straightforward to implement and computationally efficient. This quantum mechanical version of FDTD has been developed by Sullivan et al., and later by Soriano et al., to study the eigenstates and dynamics of various quantum nanostructures [3], including two electrons in a quantum dot [4], quantum well wires [5] and spin evolution in a quantum dot [6]. In 2007, Sudiarta and Geldart proposed a modification for time-independent Hamiltonians which involved performing a Wick rotation of the time variable by $\pi/2$ in the complex plane [10]. The wavefunction evolves in imaginary time, and the eigenstates and eigenvalues are then extracted, even in the presence of a magnetic field [11].

In implementing either the "real time" or "imaginary time" method to solve the Schrödinger equation in three dimensions for a Coulomb potential, one quickly realizes the burden that the grid imposes. The Coulomb potential has an infinite range but is singular at the charge's location. The simulation domain must be large enough to fit all the eigenstates of interest (especially for the higher excited states), but the computational grid itself must be fine enough to resolve the potential and the states with reasonable accuracy. For the usual discretization scheme which uses a regularly spaced grid, this can lead to large memory requirements and correspondingly long computation times.

Nonuniform grids have been developed for the electrodynamics FDTD method [8], but they typically require a redefinition of the equations underlying the simulation. Thus they tend to be difficult to implement and prone to subtle errors. Curvilinear coordinates and unstructured grids have also been used in FDTD [12–16], but require revisiting the equations, for example taking Maxwell's equations in integral form instead of differential form. Gordon et al. [17] proposed a nonlinear discretization that can be applied to any explicit method of solving the Schrödinger equation with a Coulomb potential, taking into account prior knowledge of the asymptotic behavior of the wavefunction near the singularity. While this gives more accurate results (*e.g.*, a decrease of the relative error of eigenenergies), their nonlinear grid becomes linear away from the singularity, and thus would be susceptible to the same memory and computational restrictions of a purely linear grid.

A different approach to concentrate grid points near regions of interest uses a canonical coordinate transformation to map an infinite or semi-infinite domain onto a finite one [18–20]. Other groups used a variation of this method to concentrate points where the solution exhibits high gradients [21], in spectral methods to

0010-4655/$ – see front matter
doi:10.1016/j.cpc.2011.08.011

reduce the stiffness of a problem [22] or for a moving mesh in two-phase flows problem [23], finite differences [24] or matrix representations in 1D [25]. This technique (which we will refer to as "mapping") is also useful in the Fourier method since it provides an evenly spaced grid, which is necessary for the FFT algorithm [26,27]. Kokoouline et al. [28] developed a technique based on a Fourier grid method for solving the radial Schrödinger equation with a R^{-n} potential for $n = 3$ and $n = 6$. They construct a nonlinear mapping function from the shape of the potential. Similarly, others have used a nonlinear mapping to solve the (one-dimensional) radial Schrödinger equation using direct methods [29] or a plane-wave expansion in the transformed coordinate [30].

While mapping has been used extensively in spectral methods, there are only few works that combine it with FDTD. Xiaojun et al. [31] implemented a mapping in their 2D electrodynamics FDTD. Yang et al. [32] adapted a Crank–Nicolson (CN) electrodynamics FDTD on a mapped grid, but due to the implicit nature of the CN-FDTD, the grid cell sizes still appear in the equations, complicating the implementation. FDTD, to solve either Maxwell's or Schrödinger's equations, could be greatly enhanced with a robust mapping procedure.

In this paper, we propose a simple method of constructing an orthogonal, nonuniform grid via a nonlinear mapping of the spatial coordinates and apply it to an FDTD-based Schrödinger solver. Rather than using the mapping between space coordinates where the problem is more easily solved (for example to reduce the stiffness of the problem or to switch from an infinite to a finite domain), we perform a mapping to a discrete, integer space suitable for representing the index of an array in computer memory. Additionally, treating each dimension individually allows a straightforward implementation procedure. Furthermore, our approach is used to concentrate grid points in different regions of space and is not bound to a single center of interest as is the case generally in the literature. Grabowski et al. [33] did use three different subdomains, each with a different mapping function, to study a single center system (helium) using the pseudo-spectral method, but the three overlapping subdomains require special treatment, increasing the complexity of the implementation. While we apply our nonlinear mapping to the Schrö dinger equation with single and multiple Coulomb potentials, it is generally applicable to the discretization of any system of partial differential equations.

We organize our paper as follows. In Section 2, we introduce the Schrödinger solver, for both real and imaginary time evolution. We describe the general considerations of our nonlinear mapping scheme in Section 3.1, and provide details on obtaining a mapping function in Section 3.2. In Section 3.3 we describe the particular nonlinear mapping we have developed for one or multiple charge centers of interest within the Schrödinger solver. We validate our method for real and imaginary time evolution in Section 4, where we calculate the eigenenergies and eigenstates for two known systems: hydrogen and H_2^+. We compare our nonlinear mapping results to similar calculations that employ a linear grid, and find that the nonlinear mapping provides a much more efficient calculation for the same level of accuracy, or much higher accuracy for the same number of (or even much fewer) grid points.

2. Finite-differenced Schrödinger equation

The spinless one electron Schrödinger equation in a time-dependent potential $V(\mathbf{r}, t)$ is, in atomic units,

$$\mathrm{i}\frac{\partial}{\partial t}\left|\psi(\mathbf{r}, t)\right\rangle = \left(-\frac{1}{2}\nabla^2 + V(\mathbf{r}, t)\right)\left|\psi(\mathbf{r}, t)\right\rangle. \tag{1}$$

We solve Eq. (1) using an approach similar to the FDTD algorithm that is widely used in computational electrodynamics [8], where the electric and magnetic vector fields are solved on a computational grid. Since FDTD uses an explicit method for solving partial differential equations (*i.e.*, by using the current value of the fields to calculate the field values at a later time), they are generally easier to implement than implicit methods. In addition, FDTD algorithms can be efficiently parallelized due the local nature of the operators. This general approach can be adapted for a scalar field, such as the electron wavefunction [9]. We do this for both real time and imaginary time propagation, and describe the basic elements of each propagation scheme in the following subsections.

2.1. Real time

Here we describe the basic algorithm of real time propagation. First, the complex valued wavefunction is split into real and imaginary components [34]

$$\left|\psi(\mathbf{r}, t)\right\rangle = \left|\psi_R(\mathbf{r}, t)\right\rangle + \mathrm{i}\left|\psi_I(\mathbf{r}, t)\right\rangle. \tag{2}$$

The Schrödinger equation (1) then becomes

$$\frac{\partial}{\partial t}|\psi_R\rangle = -\frac{1}{2}\nabla^2\left|\psi_I(\mathbf{r}, t)\right\rangle + V(\mathbf{r}, t)\left|\psi_I(\mathbf{r}, t)\right\rangle, \tag{3a}$$

$$\frac{\partial}{\partial t}|\psi_I\rangle = \frac{1}{2}\nabla^2\left|\psi_R(\mathbf{r}, t)\right\rangle - V(\mathbf{r}, t)\left|\psi_R(\mathbf{r}, t)\right\rangle. \tag{3b}$$

Time derivatives can be approximated using central finite differences, as per the FDTD method, giving

$$|\psi_I\rangle_{ijk}^{n+1/2} = |\psi_I\rangle_{ijk}^{n-1/2} - \Delta t\left(V_{ijk}^n - \frac{1}{2}\nabla^2\right)|\psi_R\rangle_{ijk}^n, \tag{4a}$$

$$|\psi_R\rangle_{ijk}^{n+1} = |\psi_R\rangle_{ijk}^n + \Delta t\left(V_{ijk}^{n+1/2} - \frac{1}{2}\nabla^2\right)|\psi_I\rangle_{ijk}^{n+1/2}. \tag{4b}$$

The spatial derivatives are also discretized via central differences [3], which can be according to a linear grid (the usual case) or a nonlinear grid (the method we develop in this paper).

Due to the explicit discretization of the time derivative, there is an upper bound for the time step for stability to be ensured. The stability criterion for Δt was derived in Ref. [35], and depends on both the grid cell size and the maximum absolute value of the potential within the computational domain.

This explicit scheme lends itself to a leap-frog integration in time where the real and imaginary parts of the wavefunction are alternatively updated. Unlike in electrodynamics FDTD where there is a shifting in space of the vector components of the electric and magnetic fields according to the Yee cell, the real and imaginary parts of the electron wavefunction can both be defined at the same spatial position, (i, j, k).

The real time evolution method as described can be used to solve general time-dependent problems, including a time-dependent potential. In this paper, however, we apply the real time evolution to obtain the eigenenergies of a given (static) potential. This is analogous to techniques in electrodynamics where bound modes of an optical structure are obtained via FDTD. Here, we take the initial wavefunction to be white noise, *i.e.*, we choose a random value for the wavefunction at each spatial location in the grid. This samples all the available eigenmodes. We then allow this "noise" wavefunction to evolve in time. The eigenenergy spectrum is obtained by taking a Fourier transform of the resulting time domain signal. The accuracy of the spectrum will depend in part on the size of the computational domain and the spatial resolution of the grid, but also on the total time duration of the simulation, $t_{\max}$. To resolve two distinct neighboring eigenenergies E_m and E_{m+1}, where E_m is the eigenenergy of the mth state, we require

$$t_{\max} \gg \left| \frac{2\pi}{E_m - E_{m+1}} \right|, \tag{5}$$

since the frequency resolution of a discrete Fourier transform is $2\pi/t_{\max}$.

Previous work used a single spatial grid point to construct the time domain signal [34]. While a reasonable approach, there is some risk that some eigenenergies will be missed. This could happen, for example, if the chosen point in space happens to be close to a nodal point of the associated eigenstate. To remedy this problem, we construct a time domain signal that is based on a sum of the values of the wavefunction at each grid point, effectively using the whole simulation box as the source of the Fourier transform. But special care needs to be taken here too, as antisymmetric states can vanish if a simple sum is used. To avoid this, each value of the wavefunction to be summed is first multiplied by an arbitrary and unique weighting constant. The linearity property of the Fourier transform ensures the validity of this approach. In our code, the weight is taken as a random number between 0.5 and 1.5. The randomness assures a fair distribution of the weighting constants among the grid while the limited range of the random numbers prevent some cells to have significantly more weight than others. We are thus assured that all eigenstates present in the simulation box will be found.

Once the eigenenergy spectrum has been calculated, the associated eigenstates can be obtained as a function of space by re-running the same real time simulation and taking a running Fourier transform at each spatial location for the eigenenergy or eigenenergies of interest [34].

2.2. Imaginary time

Another approach for obtaining the eigenenergies and eigenstates of a time-independent potential $V(\mathbf{r})$ is to perform a Wick rotation of $\pi/2$ in the complex plane of the time variable [10]. Time becomes a purely imaginary quantity, and the Schrödinger equation (1) is transformed into the heat equation

$$-\frac{\partial}{\partial\tau}\left|\psi(\mathbf{r},\tau)\right\rangle = \left(-\frac{1}{2}\nabla^2 + V(\mathbf{r})\right)\left|\psi(\mathbf{r},\tau)\right\rangle. \tag{6}$$

To solve this equation numerically for a given initial wavefunction, we apply finite differencing to advance the system forward in imaginary time τ in an explicit scheme, similar to Section 2.1. The major difference is that Eq. (6) is real, thus the wavefunction can also be taken as real. Consequently, when using central finite differencing for the Laplace operator in Eq. (6), special care must be taken as the wavefunction update requires neighboring cells' values. This could cause an update operation to use an already updated value of its neighbor. A simple workaround is to store two grids instead of just one: one for the wavefunction at the current time step and one at the previous time step, using one to update the other.

Similar to the real time method, this imaginary time scheme is explicit, and thus still subject to an upper bound on the time step for stability [10].

The way in which the eigenstates emerge from imaginary time evolution can be understood by expanding the initial wavefunction, $|\psi(\mathbf{r},0)\rangle$, in the (yet unknown) eigenstate basis $|\phi_n(\mathbf{r})\rangle$

$$\left|\psi(\mathbf{r},\tau=0)\right\rangle = \sum_{n=0}^{\infty} c_n \left|\phi_n(\mathbf{r})\right\rangle. \tag{7}$$

Considering the time evolution of the wavefunction, we obtain

$$\left|\psi(\mathbf{r},\tau)\right\rangle = \sum_{n=0}^{\infty} \mathrm{e}^{-E_n\tau} c_n \left|\phi_n(\mathbf{r})\right\rangle, \tag{8}$$

where E_n are the eigenvalues of the respective eigenstates $|\phi_n\rangle$. The amplitude of these eigenstates evolve in imaginary time according to

$$c_n(\tau) = \mathrm{e}^{-E_n\tau} c_n. \tag{9}$$

Note that for bound states, the eigenvalues E_n are negative resulting in increasing exponentials. As the system evolves in imaginary time, the ground state quickly dominates because its amplitude grows exponentially faster than the amplitudes of the other states, given that its corresponding eigenenergy E_0 has a larger (negative) value than the other states.

Refs. [10,36] describe a method to obtain the eigenstates. However, due to the exponential increase of the eigenstates as seen in Eq. (9), we found that the ground state was growing to the point where the other states were buried in the floating point precision of the computer, limiting the duration of the simulation and the number of states found.

We propose a more robust and faster way of finding the excited states that is not limited by this problem. The (imaginary) time evolution of Eq. (6) is calculated until the ground state becomes dominant in Eq. (8), specifically when the amplitude increases from 1 initially to above 10,000. Then, the wavefunction is normalized, stored and labeled as the ground state $|\phi_0\rangle$. The simulation continues for a single time step and the projection of the ground state onto the wavefunction is removed to obtain a new wavefunction $|\psi(\tau_n)'\rangle$ that will be used to continue the simulation:

$$\left|\psi(\tau_n)'\right\rangle = \left|\psi(\tau_n)\right\rangle - |\phi_0\rangle\langle\phi_0|\psi(\tau_n)\rangle.$$

The new wavefunction $|\psi(\tau_n)'\rangle$ should now be free of the ground state and the simulation continues updating it. The dominant states should now be the first excited state $|\phi_1\rangle$. When the amplitude of $|\psi(\tau_n)'\rangle$ again reaches the maximum chosen, the wavefunction is once more normalized, stored and labeled as the first excited state $|\phi_1\rangle$. Another time step is performed and the projection of both the ground state and first excited state is removed from the wavefunction:

$$\left|\psi(\tau_n)''\right\rangle = \left|\psi(\tau_n)'\right\rangle - |\phi_0\rangle\langle\phi_0|\psi(\tau_n)'\rangle - |\phi_1\rangle\langle\phi_1|\psi(\tau_n)'\rangle.$$

The procedure continues until all wanted states are found. Since the wavefunction used in the calculation is free of all found lower states, they will never interfere with the current calculation: it could continue indefinitely.

Removing the states projection's completely is impossible as there will always be some rounding errors in the computer calculation. Moreover, the time evolution of Eq. (6), once discretized, will by itself introduce some rounding errors that will cause a certain overlap of the removed states into the wavefunction. Because of this, even though states projections are being removed, they will always reappear from the floating point noise. Anticipating this "rise from the ashes", the projections can be removed from the wavefunction at each time step, an unnecessary heavy burden. To prevent this overhead, one can easily calculate when the exponential growth of the ground state, the state with the fastest evolution, reaches from zero a certain value that is comparable to the main wavefunction. In our calculation, we remove the projections at periods of 3 atomic units of (imaginary) time, a conservative value when considering hydrogen and H_2^+. Note that the projections must be removed before a wavefunction is labeled as an eigenstate, insuring it does not contain any contribution from lower energy states.

3. Details of the nonlinear mapping

Spatial discretization is normally achieved using a regularly spaced grid. For some problems, however, it is advantageous to

use a nonuniform spatial grid; the Schrödinger equation with a Coulomb potential is a prime example. To get adequate resolution near the ion's location, the grid spacing must be small. The computational box, however, must remain relatively large to capture the infinite nature of the electronic wavefunction, a burdensome requirement even considering that this wavefunction is exponentially decreasing at large distances. For higher energy states, which extend over a larger volume with increasing energy, the computational box must be even larger. A regular, equally spaced grid would impose small grid spacing throughout the entire computational domain. We thus develop a scheme to increase the grid spacing at points far from the charge center to reduce the computational load, while keeping the grid spacing small near the charge center. In Section 3.1, we describe a general approach to a nonuniform grid that we call "nonlinear mapping" which can be readily incorporated into an existing PDE grid-based solver. We outline one general method for finding the mapping function in Section 3.2. We apply it in Section 3.3 to the Schrödinger equation for the special case of one or more Coulomb potentials, without requiring any symmetry properties thus ensuring generality of the solver.

3.1. General approach

Consider a one-dimensional problem where a function f depends on the position x. The generalization to three dimensions is straightforward in our case since all dimensions are independent of each other. We assume the position x to be a function of another variable i

$$x \to x(i). \tag{10}$$

Generally, the mapping transforms one spatial coordinate, in this case x, to another spatial coordinates x'. The transformed equation will then need to be discretized for a computer calculation. Instead of mapping onto a temporary transformed space which must then be discretized, we propose transforming directly to the discrete, integer space suitable for computer memory storage and calculation.

Typically, a grid is chosen such that the position of a grid cell would be linear in i, *i.e.*,

$$x(i) = i\Delta x, \tag{11}$$

where i is an integer; usually i is the index of the memory location where $x(i)$ and $f(x(i))$ are stored. This is a linear mapping between the index and the grid cell position, and gives a regular grid of spacing Δx.

We do not need to choose the mapping between x and i to be linear. For an arbitrary mapping $x(i)$, the spatial derivatives of $f(x(i))$ become

$$\frac{\partial f}{\partial x} = \frac{\partial i}{\partial x}\frac{\partial f}{\partial i} = \frac{1}{J_1}\frac{\partial f}{\partial i}, \tag{12a}$$

$$\frac{\partial^2 f}{\partial x^2} = \frac{1}{J_1^2}\frac{\partial^2 f}{\partial i^2} - \frac{J_2}{J_1^3}\frac{\partial f}{\partial i}, \tag{12b}$$

where we have defined

$$J_1 \equiv \frac{\partial x}{\partial i}, \qquad J_2 \equiv \frac{\partial^2 x}{\partial i^2}. \tag{13}$$

Because we consider each dimension independently, the Jacobian matrix describing the transformation is diagonal and J_1 represents the element of the corresponding dimension. Even though a transformation could be taken such that all dimensions are coupled as in Ref. [26], our decoupling greatly simplifies the implementation by dropping the Jacobian's matrix representation requirement. J_1 is thus associated with the grid points interdistance (a function of i for nonuniform grids) and J_2 is its rate of change. In the case of linear mapping, $J_2 = 0$, corresponding to a uniform grid cell interdistance $J_1 = \Delta x$.

The function f is discretized with respect to i, and these discrete values are used in the finite differencing. For example, forward difference discretization would give

$$\frac{\partial f}{\partial i} \approx \frac{f(i+\Delta i) - f(i)}{\Delta i} \equiv f_{i+1} - f_i. \tag{14}$$

Note that we have made the association between the variable i and the index in memory (the subscripts) where the corresponding value of f is stored. Since the indices i are integers, we have $\Delta i = 1$.

More complicated, nonlinear functions can thus be readily applied to PDEs in place of the linear mapping, Eq. (11). Required properties of a mapping functions are given by Andrae et al. [37]. First, the mapping and its inverse should exist (uniqueness or bijectivity). In other words, $x(i(x)) = x$. Second, the mapping function should be monotonic and third, it should be differentiable. Additionally, it should distribute the points in space in a sensible way, such that the spacing is smaller where more spatial resolution is required, and larger where it is not.

3.2. Details of the implementation

In this section we discuss a straightforward way of obtaining the mapping function $x(i)$ from an arbitrary source function $S(x)$. Consider first a single center of interest in one dimension located at $x = x_0$, around which greater resolution is required, down to a finite (minimum) cell size; this simplifies the derivation and can be easily generalized to many centers in three dimensions. The values of x will be between $x_{\min}$ and $x_{\max}$ and i between $i_{\min}$ and $i_{\max}$, usually 0 and $N-1$, N being the total number of cells.

Instead of finding a single strictly increasing monotonic function for $x(i)$, a difficult task, we will use three different functions that will describe three sections of the ideal monotonic function. Region 1 begins at the lower part of the subdomain and finishes at a distance d before the center's position x_0. Region 2 then covers from $x_0 - d$ to $x_0 + d$ and finally region 3 begins at $x_0 + d$ and finishes at the end of the subdomain. In regions 1 and 3, a nonlinear mapping is used while in region 2 (of width $2d$), a linear mapping is used. This linear part located on top of the center's location allows a free parameter in our mapping procedure: all grid points in that region will be equidistant of $\Delta x_{\min}$, the minimum that is required. The three regions are thus

$$\text{Region 1:} \quad x \in [x_{\min}, x_0 - d),$$

$$\text{Region 2:} \quad x \in [x_0 - d, x_0 + d),$$

$$\text{Region 3:} \quad x \in [x_0 + d, x_{\max}].$$

The parameter d depends on the subdomain's properties (size, number of cells, etc.) and also on the shape of the source function $S(x)$ which is described in the following part. Since the position of the center of interest is ill-defined in i-space even though in x-space it is well known (x_0), we will thus find an expression for $i(x)$, the *inverse* mapping, instead of the mapping $x(i)$.

The fundamental and novel step of our approach is to define the inverse mapping $i(x)$ as a cumulative sum of the absolute value of a "source" function $S(x)$:

$$i(x) = A \int_{x_{\min}}^{x} \left|S(x')\right| \mathrm{d}x' + i_{\min}, \tag{15}$$

where A is a normalization constant such that $i(x_{\max}) = i_{\max}$ is the highest cell index. This cumulative sum guarantees the monotonicity and uniqueness of the mapping which are essentials properties.

Any function can be used for $S(x)$, reducing the difficulty of finding a suitable mapping function.

For a position $x < x_0 - d$, the cumulative sum runs over only region 1. For a position $x_0 - d \leqslant x < x_0 + d$ the cumulative sum runs over regions 1 and 2 and for $x_0 + d \leqslant x$ the three regions are covered. When the integration is performed we have:

$$i(x) - i_{\min} = \begin{cases} i_1(x) & \text{in region 1,} \\ i_1(x_0 - d) + i_2(x) & \text{in region 2,} \\ i_1(x_0 - d) + i_2(x_0 + d) + i_3(x) & \text{in region 3,} \end{cases} \quad (16)$$

where $i_1(x)$, $i_2(x)$ and $i_3(x)$ are the individual functions of each region.

To find d, we use $i(x_{\max}) \equiv i_{\max}$ and isolate d from the expression:

$$i_{\max} = i_1(x_0 - d) + i_2(x_0 + d) + i_3(x_{\max}) + i_{\min}. \quad (17)$$

Depending upon the source function that generates i_1 and i_3, this may yield a transcendental equation for d, which may be solved using a root finding algorithm.

Having solved for d, we can now find the boundaries in i-space between the different regions. We call these j_1 and j_2:

$$i(x_0 - d) = i_1(x_0 - d) \equiv j_1, \quad (18a)$$

$$i(x_0 + d) = i_1(x_0 - d) + i_2(x_0 + d) \equiv j_2. \quad (18b)$$

This allows us to define the three regions in i-space as

Region 1: $i \in [i_{\min}, j_1)$,

Region 2: $i \in [j_1, j_2)$,

Region 3: $i \in [j_2, i_{\max}]$.

Once expressions for $i_1(x)$, $i_2(x)$ and $i_3(x)$ have been found, it is easy to invert each of them individually to get $x_1(i)$, $x_2(i)$ and $x_3(i)$. The full mapping is

$$x(i) = \begin{cases} x_1(i) & \text{in region 1,} \\ x_1(j_1) + x_2(i) & \text{in region 2,} \\ x_1(j_1) + x_2(j_2) + x_3(i) & \text{in region 3.} \end{cases} \quad (19)$$

Finally, we obtain the mapping's first and second derivatives J_1 and J_2 analytically from Eq. (19).

Generalization to multiple centers is straightforward. Since the previous derivation only requires $i_{\min}$, $i_{\max}$, $x_{\min}$ and $x_{\max}$, one can redefine these values for each center for each dimension, then apply the previous analysis. First, the main domain is separated into smaller subdomains at mid-points between centers, defining the x boundaries. Second, the cells also need to be distributed amongst the various centers. One can choose to distribute equally the cells to each subdomains, but in the case where the different subdomains vary greatly in size, the concentration of cells will be too high for smaller subdomains compared to bigger ones. A more careful approach is to give the same ratio of total cells to the ratio of space covered by the subdomains.

So far, we have outlined the general expressions of the mapping $x(i)$ and the procedure to analytically calculate the curve in the three regions without defining the source function $S(x')$ that is used in (15). This function can be user-defined depending on the problem to be solved. We explore in the next section a shape for $S(x')$ that can be used in our specific case of a Schrödinger solver.

3.3. Nonlinear mapping for the Coulomb potential

In this section we discuss a form of $x(i)$ which may be used to solve the Schrödinger equation with one or several Coulomb potentials. Near the singularity, the potential is deep and the electrostatic field is strong, requiring a finer grid to resolve the wavefunction. We have found that we can base our nonlinear mapping function on the electrostatic potential. Using

$$S(x') = \frac{-1}{|x' - x_0|} \quad (20)$$

in Eq. (15), the procedure in the previous section leads to the following inverse-mapping function:

$$i_1(x) = A \ln\left(\frac{x_0 - x_{\min}}{x_0 - x}\right) + i_{\min}, \quad (21a)$$

$$i_2(x) = (x - x_0 + d)/(\Delta x_{\min}) + i_{\min}, \quad (21b)$$

$$i_3(x) = A \ln\left(\frac{x - x_0}{d}\right) + i_{\min}. \quad (21c)$$

To obtain d, we substitute Eqs. (21) in Eq. (17) and isolate d. In this specific case, we obtain

$$\Delta x_{\min}(i_{\max} - i_{\min}) = d\left[\ln \frac{(x_0 - x_{\min})(x_{\max} - x_0)}{d^2} + 2\right] \quad (22)$$

which we solve using bisection method with an initial guess of $d = 0$ for a given minimum cell size $\Delta x_{\min}$. The following mapping is then obtained

$$x_1(i) = x_0 + (x_{\min} - x_0) \exp\left\{\frac{i_{\min} - i}{A}\right\}, \quad (23a)$$

$$x_2(i) = \Delta x(i - j_1) + x_{\min}, \quad (23b)$$

$$x_3(i) = d\left(\exp\left\{\frac{i - j_2}{A}\right\} - 1\right) + x_{\min}. \quad (23c)$$

This mapping can be applied to any number of centers by adjusting the $i_{\min}$, $i_{\max}$, $x_{\min}$ and $x_{\max}$ parameters accordingly for each dimension.

Kokoouline et al. [28] also proposed a mapping procedure based on the potential of the system, in their case for R^{-3} and R^{-6} potentials. Our main idea for the mapping, while similar, is more generic and can be applied to more problems. Indeed, the systems solved here are three-dimensional and are not restricted to one dimension. In addition, due to the Hamiltonian diagonalization required by the Fourier method, a second transformation is required in Ref. [28] to obtain an easier to diagonalize symmetrical matrix. Such a limitation is absent in the method proposed here since the Schrödinger equation is solved explicitly using the FDTD algorithm to obtain the actual wavefunction without the need to re-transform it.

As a simple example, Fig. 1 shows the mapping $x(i)$ for a domain $0 \leqslant x \leqslant 10$ Bohr where three centers are located at $x = 3$, 5 and 8 Bohr. The continuous blue curve shows the nonlinear mapping function obtained from Eqs. (23). The $N = 50$ integer values of i are indicated by red crosses. With a minimum cell size of $\Delta x_{\min} = 0.05$ Bohr, the linear regions have widths of $d_0 = 0.138$, $d_1 = 0.0853$ and $d_2 = 0.114$ Bohr. These widths are not identical since Eq. (22) depends on the different center positions and subdomain sizes. We see that the density of points is higher near the location of the charge centers, where the mapping is linear. As illustrated by our example, the nonlinear mapping procedure is insensitive to whether or not the centers are equally spaced.

The script used to generate Fig. 1 is available in Ref. [38] where the reader can see the details of the implementation.

Applying this one-dimensional method to three dimensions is straightforward. All ion locations are projected on the three spatial axes. The nonlinear mapping is then carried out along each axis separately. If two or more charge centers are located at nearly the same point along one of the axes, then the mapping is calculated such that these charge centers have "merged" and are located at the center of charge of the merged group.

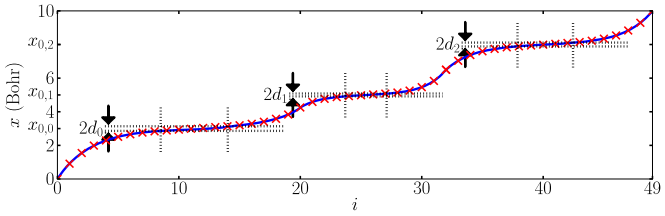

Fig. 1. (Color online.) Mapping $x(i)$ for three ions at $x_{0,0} = 3$, $x_{0,1} = 5$ and $x_{0,2} = 8$ Bohr for $N = 50$. The regions near the ion that employ a linear mapping ($\Delta x_{\min} = 0.05$ Bohr) are enclosed within the black dashed lines. Red crosses are located at integer values of i. See Ref. [38] for the implementation details.

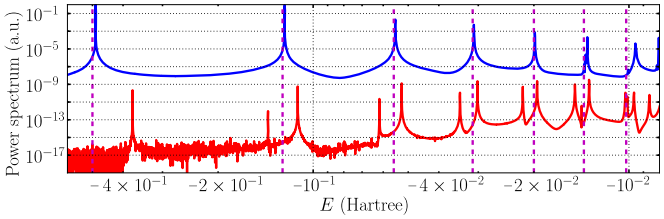

Fig. 2. (Color online.) Hydrogen spectrum calculated via the real time method of Section 2.1 using both linear mapping (red, lower curve, $\Delta x = 1.5$ Bohr) and nonlinear mapping (blue, upper curve, $\Delta x_{\min} = 0.25$ Bohr). Each method used a $150 \times 150 \times 150$ Bohr^3 domain and $100 \times 100 \times 100 = 10^6$ grid cells.

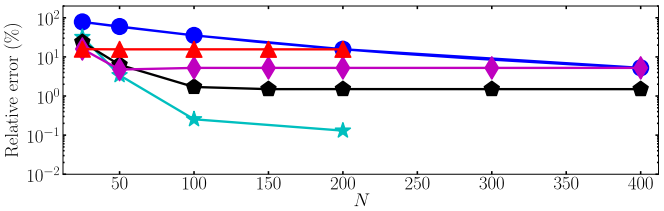

Fig. 3. (Color online.) Relative error in the ground state eigenenergy for a hydrogen atom as a function of the number of grid cells per dimension for the linear mapping method (blue circles), and the nonlinear mapping method with $\Delta x_{\min} = 0.01$ (cyan stars), 0.25 (black pentagons), 0.5 (magenta diamonds) and 1.0 (red triangles). The size of the simulation box was $200 \times 200 \times 200$ Bohr^3.

4. Validation and results

To validate our nonlinear mapping model, we consider a static potential $V(\mathbf{r})$ resulting from N_{ion} positive charges Z_n at positions $\mathbf{r}_n$,

$$V(\mathbf{r}) = -\sum_{n=0}^{N_{\text{ion}}} \frac{Z_n}{|\mathbf{r} - \mathbf{r}_n|}. \tag{24}$$

This is used with both the real and imaginary time evolution methods, even though the former can, in general, be applied to systems with a time-dependent V. Due to the varying cell sizes in the simulation domain, a different upper bound for the time step is required by each grid point. By taking the smallest value set by the smallest inter-grid-point distance, stability is ensured for the whole domain. We consider two cases below: the hydrogen atom and the hydrogen cation molecule H_2^+.

4.1. Hydrogen atom

As an initial test our nonlinear mapping, we apply it in this section to a single center system, the hydrogen atom. We use the real time method described in Section 2.1 to calculate the energy eigenvalue spectrum. Fig. 2 shows the calculated spectrum of hydrogen using both linear mapping (red, lower curve) and nonlinear mapping (blue, upper curve) for the same domain size and same number of grid points. The hydrogen ion has a charge state of $Z = +1$ and is located at the center of a box of size $150 \times 150 \times 150$ Bohr^3; for the computation, $100 \times 100 \times 100 = 10^6$ grid cells were used. The red spectrum was obtained with linear mapping, where $\Delta x = 1.5$ Bohr. The minimum cell size of the nonlinear mapping was $\Delta x_{\min} = 0.25$ Bohr. The dashed magenta vertical lines show the analytical eigenvalues $E_n = -0.5n^{-2}$ Hartree where n is the principal quantum number.

The results of Fig. 2 indicate that the nonlinear mapping gives much better results than the linear mapping, for the same box size and same number of cells. For the first six eigenvalues, the spectrum obtained via nonlinear mapping has a relative error 0.2–2% with respect to the expected analytical value. The relative error for the ground state energy obtained via the linear mapping is 26%. The other spectral peaks obtained via linear mapping have split as the grid is just too coarse to adequately sample the eigenstates. The splitting is probably due to a lifting of the degeneracy for the $n \geqslant 2$ states.

From Fig. 2, we can see that the nonlinear mapping did not adequately resolve the seventh state. This is due to the box size we have chosen. By plotting the analytical solution of the eigenstates associated with the seventh eigenvalue, we verified that there is significant amplitude outside of our chosen simulation box. We were restricted in the size of the chosen box by the linear mapping, since increasing the size while keeping the number of points constant would have reduced significantly the precision. With nonlinear mapping we could have easily extended the box size without sacrificing performance or accuracy.

We could improve upon the results of the linear mapping by choosing the grid cell size to be the same as the minimum cell size chosen for the nonlinear mapping. This would give us the same resolution near the ion as that given by the nonlinear mapping. However, for our example, we would then need to increase the number of cells in each dimension by a factor of 6, or the total number of cells by a factor of 216. This would increase the memory requirement from 64 MB to 13.5 GB. In addition to the increase in the actual number of computations, one must also consider that fetching data from main memory is a very slow operation compared to processor speed, so that increasing the memory requirement can significantly augment the code execution time. Thus to achieve the same level of resolution as the nonlinear mapping simulation, which took us 8 days of wall clock time, the linear mapping simulation would require approximately 6 years of wall clock time, clearly an unacceptable duration. These execution times were observed or estimated on a dual-socket Intel Xeon E5520 Nehalem (2.26 GHz) SMP machine parallelized with 16 OpenMP threads.

Consequently, not only can we increase the precision of our calculations using the nonlinear mapping for the same number of cells, but nonlinear mapping also allows a tremendous speedup in the running time over the linear mapping for the same precision, bringing the calculation from almost impossible to easily performed.

In a second set of tests, we calculated the relative error in the calculated eigenenergy of the ground state as a function of the number of grid cells, for nonlinear mapping with different minimum cell sizes and for the linear mapping with the cell size simply determined by the number of points. The box size was kept fixed at (200 Bohr)^3. In this case, the results were obtained using the imaginary time method described in Section 2.2, and are plotted in Fig. 3. The linear mapping (blue circles) gives 5% error even with 400 cells per dimension, corresponding to cell size of 0.5 Bohr. Using our nonlinear mapping, the relative error is lowered by a factor of 140 using only 100 cells per dimension for $\Delta x_{\min} = 0.01$ (cyan stars). The apparent increase in error for smaller values of $\Delta x_{\min}$ and very small number of grid points is due to a too dense cluster-

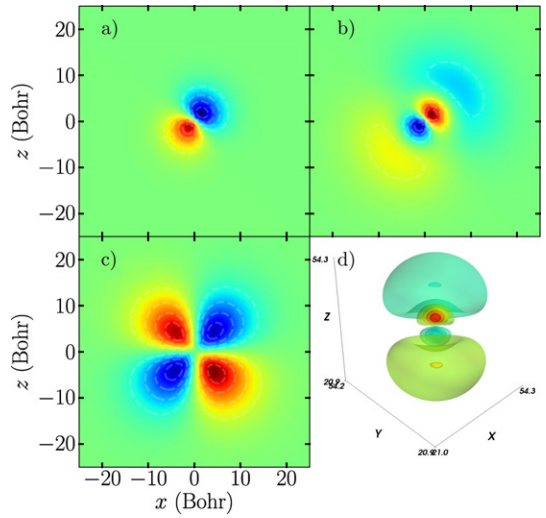

Fig. 4. (Color online.) Real part of hydrogen's (a) 2p, (b) 3p and (c) 3d eigenstates, found by our imaginary time solver with nonlinear mapping ($\Delta x_{\min} = 0.25$ Bohr). The 3p state is shown in three dimensions in (d). Green is null, red is positive and blue is negative.

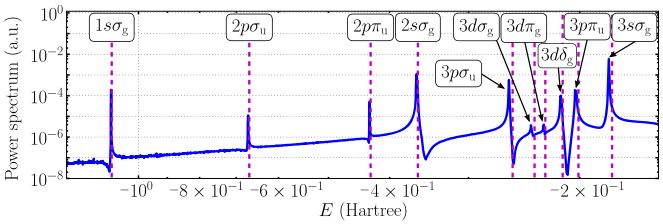

Fig. 5. (Color online.) The H_2^+ spectrum for $R = 2$ Bohr as calculated via our real time nonlinear mapping method, with $\Delta x_{\min} = 0.05$ Bohr, 100^3 grid cells, and a computational volume of 100^3 Bohr^3. The vertical magenta dotted lines are the expected values [39].

ing of these points near the ion with not enough points far from it.

Finally, we demonstrate that eigenstates can be calculated using imaginary time evolution with nonlinear mapping ($\Delta x_{\min} = 0.25$ Bohr). As an example, we plot in Fig. 4 some of the eigenstates found by our imaginary time solver with nonlinear mapping: a 2p in Fig. 4(a), a 3p in Fig. 4(b) and a 3d in Fig. 4(c) Fig. 4(d) shows the same 3p state as Fig. 4(b) but represented in three dimensions. The resulting energies have been found to match those of hydrogen with an error of 0.4–4%.

4.2. Hydrogen cation molecule

In this section we further validate our nonlinear mapping scheme by applying it to a multi-center system, the hydrogen cation molecule H_2^+, where two hydrogen nuclei share a single electron.

First, we use the real time method described in Section 2.1 to obtain the spectrum of H_2^+ for $R = 2$ Bohr, where R is the distance between the two nuclei. The results are plotted in Fig. 5. The vertical magenta dotted lines indicate the known values of the eigenenergies from reference [39] where the internuclear energy has been removed. Unlike the case of the hydrogen atom, the $n > 1$ states of H_2^+ are not degenerate. Fig. 5 shows that our method captures these states. The eigenenergies of higher excited states could be obtained by choosing a bigger computational volume and a longer running time.

Table 1 compares the values of the first five eigenenergies obtained with our code to the known values [39]. We find that the relative error is between 0.25 and 1.4%. Previous work used an FDTD-based Schrödinger equation solver with a linear mapping to calculate the first two eigenenergies of H_2^+ [3]; their eigenenergies had a relative error compared to known values of 26% for the ground state and 6% for the first excited state. Our nonlinear mapping both increases the precision of the eigenenergies and allows us to access higher excited states than was previously possible.

Table 1
The first five eigenenergies of H_2^+ from known values (first row) [39], and obtained via our real time nonlinear mapping simulation of Fig. 5 (second row). The relative error of our calculated values with respect to the known values is listed in the third row.

H_2^+ states	$\langle E \rangle_{H_2^+}$	$\langle E \rangle_{NL}$	Error
$1s\sigma_g$	−1.1026	−1.1054	0.25%
$2p\sigma_u$	−0.66753	−0.67034	0.42%
$2p\pi_u$	−0.42877	−0.43055	0.41%
$2s\sigma_g$	−0.36086	−0.36242	0.43%
$3p\sigma_u$	−0.25541	−0.25887	1.3%

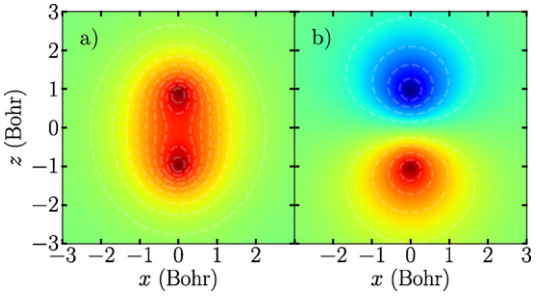

Fig. 6. (Color online.) Real part of H_2^+ ground state and first excited state: (a) shows the ground state ($1s\sigma_g$ bonding orbital) where blue is the null value and red is positive; (b) shows the first excited state ($2p\sigma_u$ antibonding orbital), where green is null, red is positive and blue is negative. Parameters are the same as those of Fig. 5.

Finally, we apply the imaginary time method to find the eigenstates of H_2^+. Figs. 6(a) and 6(b) show the real parts of the ground state ($1s\sigma_g$, bonding) and of the first excited state ($2p\sigma_u$, antibonding) of H_2^+, respectively, for an internuclear distance of $R = 2$ Bohr. These eigenstates were obtained after only 12 and 45 atomic units of imaginary time evolution. These calculated eigenstates agree well with the known solutions [40].

5. Conclusion

We have introduced a novel nonlinear mapping of spatial coordinates applicable to grid-based numerical implementations of partial differential equations. Contrary to previous work, a spatial and continuous variable is directly mapped to a discrete space suitable for computer memory storage, simplifying greatly the implementation details. Moreover, due to the cumulative sum approach, the mapping function can be sourced by any user defined function for a better grid points location control. A single free parameter allows for accurate adjustment of the mapping and thus of the calculation's precision. Furthermore, our mapping can be applied in three-dimensional and nonsymmetric systems and is not tied to any specific problem or numerical method.

We show that, in comparison to standard linear mapping, our method significantly increases accuracy while decreasing memory usage and computation time. We applied our nonlinear mapping to the time-dependent Schrödinger equation for multiple Coulomb potentials. Our solver is based on the FDTD method widely used in electrodynamics, and we have implemented wavefunction propagation in both real and imaginary time. Although we used the Coulomb potential itself as the basis for the nonlinear mapping, the technique itself is generic and can be applied to other partial differential equation solvers.

With nonlinear mapping, we were able to calculate the eigenenergies of hydrogen to within 0.2–2%. Linear mapping gave quantitatively inaccurate results for the same number of grid cells; to obtain the same accuracy as nonlinear mapping would require an increase in the computational time by almost three orders of magnitude. Eigenstates have also been found for hydrogen using nonlinear mapping. This increased efficiency and the fact that our nonlinear mapping scheme is independent of any symmetry, allows for its application to multi-center systems. In particular, we have considered the hydrogen cation molecule H_2^+, and were able to obtain eigenstates for the bonding and antibonding states. We were also able to calculate eigenenergies for the ground state and several excited states, giving good agreement with expected results, in contrast to an earlier study that employed a linear grid. Our solver thus allows quantum mechanical computations of multiple charge center systems, and could be applied, for example, to studies of atom clusters and molecules exposed to intense radiation.

References

[1] C. Lubich, From Quantum to Classical Molecular Dynamics: Reduced Models and Numerical Analysis, Zurich Lectures in Advanced Mathematics, 2000.
[2] A.M.J. Grotendorst, D. Marx (Eds.), Quantum Simulations of Complex Many-Body Systems: From Theory to Algorithms, NIC Series, vol. 10, 2002.
[3] D.M. Sullivan, D.S. Citrin, Determining quantum eigenfunctions in three-dimensional nanoscale structures, Journal of Applied Physics 97 (2005) 104305–104311.
[4] D.M. Sullivan, D.S. Citrin, Time-domain simulation of two electrons in a quantum dot, Journal of Applied Physics 89 (2001) 3841–3847.
[5] A. Soriano, Analysis of the finite difference time domain technique to solve the Schrödinger equation for quantum devices, Journal of Applied Physics 95 (2004) 8011–8019.
[6] D.M. Sullivan, D.S. Citrin, Time-domain simulation of a universal quantum gate, Journal of Applied Physics 96 (2004) 1540–15407.
[7] J. Nagel, A review and application of the finite-difference time-domain algorithm applied to the Schrödinger equation, Applied Computational Electromagnetics Society Journal 24 (2009) 1–8.
[8] A. Taflove, S. Hagness, Computational Electrodynamics: The Finite-Difference Time-Domain Method, third edition, Artech House, 2005.
[9] D.M. Sullivan, Electromagnetic Simulation Using the FDTD Method, Wiley–IEEE Press, 2000.
[10] I.W. Sudiarta, D.J.W. Geldart, Solving the Schrödinger equation using the finite difference time domain method, Journal of Physics A: Mathematical and Theoretical 40 (2007) 1885–1896.
[11] I.W. Sudiarta, D.J.W. Geldart, Solving the Schrödinger equation for a charged particle in a magnetic field using the finite difference time domain method, Physics Letters A 372 (2008) 3145–3148.
[12] R. Holland, Finite-difference solution of Maxwell's equations in generalized nonorthogonal coordinates, IEEE Transactions on Nuclear Science 30 (1983) 4589–4591.
[13] K.K. Mei, A. Cangellaris, D.J. Angelakos, Conformal time domain finite difference method, Radio Science 19 (1984) 1145–1147.
[14] M. Fusco, FDTD algorithm in curvilinear coordinates (EM scattering), IEEE Transactions on Antennas and Propagation 38 (1990) 76–89.
[15] M. Fusco, M. Smith, L. Gordon, A three-dimensional FDTD algorithm in curvilinear coordinates (EM scattering), IEEE Transactions on Antennas and Propagation 39 (1991) 1463–1471.
[16] P. Mezzanotte, L. Roselli, R. Sorrentino, A simple way to model curved metal boundaries in FDTD algorithm avoiding staircase approximation, IEEE Microwave and Guided Wave Letters 5 (1995) 267–269.
[17] A. Gordon, C. Jirauschek, F.X. Kärtner, Numerical solver of the time-dependent Schrödinger equation with Coulomb singularities, Physical Review A 73 (2006) 042505.
[18] E. Kálnay de Rivas, On the use of nonuniform grids in finite-difference equations, Journal of Computational Physics 10 (1972) 202–210.
[19] C.E. Grosch, S.A. Orszag, Numerical solution of problems in unbounded regions: Coordinate transforms, Journal of Computational Physics 25 (1977) 273–295.
[20] B. Alabi, A mapping finite difference model for infinite elastic media, Applied Mathematical Modelling 9 (1985) 6.
[21] C. Basdevanta, M. Devilleb, P. Haldenwangc, J. Lacroixd, J. Ouazzanid, R. Peyretd, O.P.A. Pateraf, Spectral and finite difference solutions of the Burgers equation, Computers & Fluids 14 (1986) 18.
[22] H. Guillard, R. Peyret, On the use of spectral methods for the numerical solution of stiff problems, Computer Methods in Applied Mechanics and Engineering 66 (1988) 17–43.
[23] J. Shen, X. Yang, An efficient moving mesh spectral method for the phase-field model of two-phase flows, Journal of Computational Physics 228 (2009) 2978–2992.
[24] H. Dwyera, B. Sandersa, Numerical modeling of unsteady flame propagation, Acta Astronautica 5 (1978) 1171–1184.
[25] M. Znojil, One-dimensional Schrödinger equation and its "exact" representation on a discrete lattice, Physics Letters A 223 (1996) 5.
[26] E. Fattal, R. Baer, R. Kosloff, Phase space approach for optimizing grid representations: The mapped Fourier method, Physical Review E 53 (1996) 1217–1227.
[27] U. Kleinekathofer, D.J. Tannor, Extension of the mapped Fourier method to time-dependent problems, Physical Review E 60 (1999) 4926.
[28] V. Kokoouline, O. Dulieu, R. Kosloff, F. Masnou-Seeuws, Mapped Fourier methods for long-range molecules: Application to perturbations in the $Rb_2(0_u^+)$ photoassociation spectrum, Journal of Chemical Physics 110 (1999) 9865.
[29] V. Meshkov, A. Stolyarov, R. Le Roy, Adaptive analytical mapping procedure for efficiently solving the radial Schrödinger equation, Physical Review A 78 (2008) 052510.
[30] J.M. Pérez-Jordá, Variational solution of the Schrödinger equation using plane waves in adaptive coordinates: The radial case, Journal of Chemical Physics 132 (2010) 024110.
[31] Z. Xiaojun, Y. Zhiyuan, L. Weigan, Characteristics of eccentric coaxial line using conformal mapping and finite-difference time-domain method, Microwave and Optical Technology Letters 16 (1997) 249–252.
[32] Y. Yang, R.S. Chen, Z. Ye, An improved formalism for the Crank–Nicolson finite-difference time-domain by conformal mapping method, Microwave and Optical Technology Letters 51 (2009) 2378–2382.
[33] P.E. Grabowski, Pseudospectral calculation of the wave function of helium and the negative hydrogen ion, Physical Review A 81 (2010) 032508.
[34] D.M. Sullivan, D.S. Citrin, Determination of the eigenfunctions of arbitrary nanostructures using time domain simulation, Journal of Applied Physics 91 (2002) 3219–3227.
[35] W. Dai, G. Li, R. Nassar, S. Su, On the stability of the FDTD method for solving a time-dependent Schrödinger equation, Numerical Methods for Partial Differential Equations 21 (2005) 1140–1154.
[36] M. Strickland, D. Yager-Elorriaga, A parallel algorithm for solving the 3d Schrödinger equation, Journal of Computational Physics 229 (2010) 6015–6026.
[37] D. Andrae, J. Hinze, Numerical electronic structure calculations for atoms. I. Generalized variable transformation and nonrelativistic calculations, International Journal of Quantum Chemistry 63 (1997) 65–91.
[38] N. Bigaouette, E. Ackad, L. Ramunno, https://github.com/nbigaouette/nonlinearmapping, 2010.
[39] M.M. Madsen, J.M. Peek, Eigenparameters for the lowest twenty electronic states of the hydrogen molecule ion, Atomic Data and Nuclear Data Tables 2 (1970) 171–204.
[40] R.F.P. Atkins, Molecular Quantum Mechanics, 4th edition, Oxford University Press, 2004.

8

Discussion

Clusters of atoms are without a doubt an extremely useful tool to study laser and matter interaction. They were in use for their optical properties even before atoms were discovered. With the advancement of both cluster creation and laser technologies, it became possible to gain a significant understanding on how light interacts with matter. Cluster studies then became an important physics research area.

At the simplest level, quantum mechanics describe the dynamics but cannot provide exact solutions for systems of more than two electrons. The process of photo-ionization of single atoms is known, but the high density of atoms inside clusters gives rise to interesting phenomena. It was a surprise to scientists ten years ago to see highly charged ions coming out of experiments using rare gas clusters with short duration (tens of femtoseconds), high intensity (10^{12} – 10^{14} W/cm^2) and small wavelength (VUV, XUV) laser pulses. More than ten years later, our understanding of the different mechanisms of energy absorption and diffusion throughout the cluster is taking shape. Even though full quantum mechanical description of clusters is not possible, some level of approximations can be assumed, allowing theoretical and numerical studies to be performed.

Our numerical tool of choice is Molecular Dynamics where we track, classically, the dynamics of electrons and ions during and after a laser pulse. MD simulations, being

classical systems, allow a larger number of particles than full quantum simulations but can still describe the large fluctuations in charge and field generated inside a cluster.

Many MD packages are freely available that could have been used for the current work. After a first attempt with one such package, it was decided to develop a new one from scratch. The MD algorithm is relatively simple; having control on the rest of the package allowed flexibility in the development that would have not been possible with a third party package. For example, existing MD codes have specific target users that do not have the same requirements as those required for this work, such as varying the number of particles during the simulation or long range interactions. By building the tools myself I was able to have more confidence in it by subjecting it to rigorous tests and validations. Additionally, even though a lot of work was put into the creation of this code base, much time was saved by not trying to understand, or worse, debug, a code from someone else. Having known beforehand the amount of time lost on an unstable code base, I would have started my MD package right away, as it proved a lot easier to move forward with it.

The $O(N^2)$ scaling of the MD algorithm prevents simulations of more than tens of thousands of particles but interesting results are still accessible. For bigger systems, some algorithm changes can be done to speed the force calculation on particles. Using a hierarchical tree can change the algorithm scaling from $O(N^2)$ to $O(N\log(N))$ and thus push the limit on cluster size upward. Having control and full understanding of the code had the added benefit of easing the process of adding new features. While the tree algorithm was implemented, it was not yet used in a publication. An interesting technology matured during the last decade; by running codes directly on GP-GPUs, the same algorithms could perform up to one hundred times faster than on conventional CPUs. The MD package was thus ported to the framework OpenCL where the MD algorithm showed a speedup of close to 80. This implementation was used in our publications since the cluster sizes that we were interested in were in the range accessible through MD (and not requiring the tree). The hierarchical tree-based algorithm is still accessible through an input parameter (not as an OpenCL implementation though), making my MD package interesting for future studies where larger clusters will be investigated.

In our first publication in 2011, the new model using excited states as a multi-step of energy transfer process from a laser pulse to rare gas clusters was introduced. This model is based on electron collisions and increases the amount of ionization in clusters. We thus dubbed this model Augmented Collisional Ionization, or ACI. With ACI, many

more electrons can participate in collisional ionization.

The first study concentrated on argon clusters in the 32.8 nm (37.8 eV) regime. At this wavelength, only the first two ionization states of (atomic) argon are accessible but experiments in 2008 saw up to Ar^{4+}. The small cluster sizes used in the experiment ($\sim$100 atoms per cluster) allowed us to quickly test and validate our model. It was found that ACI plays a crucial role in the cluster dynamics and can explain the high charge states seen in the experiment, with intensities from 5×10^{13} to 10×10^{13} W/cm^2. When ACI was enabled in the simulations, the Ar^{4+} population closely matched what was seen at FLASH. Additionally, the MD simulations allowed tracking the dynamics of each charge states. It was found that all Ar^{3+} and Ar^{4+} were created by ACI, making it a vital process in cluster dynamics where traditional ionization mechanisms cannot explain alone what is seen in laboratories.

In the second publication, the size of argon clusters was investigated. We found that as clusters get bigger and bigger – from Ar_{55} to $Ar_{2,057}$ – the importance of collisions increased. As clusters ionize progressively they become transparent to photons; ACI accelerates the rate at which Ar^{2+} are created and Ar^{2+} cannot be photo-ionized (37.8 eV photon vs. 48.7 eV IP). This process was baptized *collisionally reduced photoabsorption*. Once clusters are ionized, the larger ones will thermalize faster and the electron velocity distribution will become isotropic in contrast, with smaller clusters which keep their photo-ionization-created anisotropy.

Later on, a question presented itself; what is the influence of the cluster environment on the different states? One of the first works on the electrodynamics solver called FDTD by Sullivan contained a section on using this method to solve the Schrödinger equation. Since I was familiar with the electrodynamics FDTD that I implemented during my masters degree I decided to explore the quantum version of it. Even though the current implementation is a single electron picture, a study on the cluster states could still be possible, at least as a first step. A major problem with FDTD is the amount of memory required to resolve a three dimensional grid. Normally, FDTD is parallelized using a shared memory model so it can be distributed on many computational nodes. After the work done on implementing the MD algorithm in OpenCL to run on a GP-GPU, I decided to also port the QFDTD to OpenCL which was actually relatively quick. The video cards could run the code faster, but video cards have their own discrete memory which is a lot smaller than main memory. A novel mapping method was thus developed to reduce the number of grid cell size in the QFDTD computational domain. This new

method's innovation comes from the two spaces being mapped. Traditionally, one space is mapped to another one where some physical feature is either enhanced or reduced to ease the numerical burden. In my nonlinear mapping, one of the spaces mapped is the actual discrete memory of the computer; the physical space is mapped to the integer-referenced memory location through a cumulative sum of a source function, enforcing the monotonicity required. Due to the manner the mapping function is obtained, any source function can be used, giving great flexibility to the mapping process. It is thus possible to concentrate grid points around centres of interest, in this case ions' location. In addition to the nonlinear mapping, both real-time and imaginary-time methods were implemented, allowing comparison of the two through the same package. In the case of the imaginary method, a new way to obtain the eigenstates was described and successively used on the hydrogen atom and the simplest molecule: hydrogen cation molecule (H_2^+). Using the real-time method, it was possible to see ten excited states. This publication allowed validation of the whole technique, including the nonlinear mapping, and comparison with known values from experiments.

The ACI model, based on electron impact excitation cross-sections, is independent of the regime and does not depend on the laser parameters (pulse duration, wavelength, intensity, etc.). However, transition cross-sections are unique to each element and must be calculated and added to the simulation package before use. Argon and xenon cross-sections where generated and are accessible. It is thus interesting to apply the model to different wavelength regimes. Other models were developed to explain Wabnitz *et al.*'s 2002 VUV-xenon experiment at FLASH but when Bostedt *et al.* published in 2010 a revised intensity (to lower values) it was not clear if these models could still be able to reproduce the experimental results in light of the new, lower intensity. We decided to revisit the 2002 100 nm experiment in light of our ACI model at the revised, lower intensity.

Thanks to my OpenCL implementation (and its 80 times speedup), it was possible to acquire significant statistics over a wide range of intensities, effectively reproducing the cluster distribution in the laser focus spatial profile. The speedup gained was used to increase the number of simulations, thus increasing the statistical significance of the data, and to acquire data at different intensities to sample a non-uniform spatial distribution of the laser pulse.

We showed that ACI increased the maximum charge states observed by two states in Xe_{80} clusters at 8×10^{12} W/cm^2 and Xe_{1000} clusters at 1.5×10^{13} W/cm^2. This maximum

charge state went from Xe^{3+} to Xe^{5+} for the smaller clusters and from Xe^{5+} to Xe^{7+} for the larger clusters. For the simulation results to match the 2002 DESY experiment, ACI had to be enabled, a clear indication that ACI plays an important role in the cluster dynamics.

We then looked at the cluster size influence on the charge state spectra at 8×10^{12} W/cm^2. For the shapes to match the experimental data, a spatial averaging of the intensity in the laser profile had to be performed. ACI was vital in obtaining both the same maximum charge state (Xe^{4+}) and the same most abundant one (Xe^{1+}) for Xe_{90} clusters as the experiment.

The influence of the potential depth used in the simulations was also investigated. By increasing IBH, a deeper potential allowed an increase of the maximum charge state seen as well as the most abundant one, up to a depth of around 27.2 eV (1 Eh), when ACI was enabled.

8.1 Future direction

The largest clusters simulated were $Xe_{5,083}$ (11 icosahedral shells), much smaller than the experiment's $Xe_{90,000}$ ($\sim$30 icosahedral shells), a cluster size not possible with traditional MD simulations. The MD's $O(N^2)$ scaling makes it extremely difficult to increase the number of particles past a couple of thousands. While the OpenCL implementation is a nice addition that gives almost two orders of magnitude speedup, the algorithm's scaling is always present. Parallelizing the MD code (for shared or distributed memory machines) is also possible but a difficult task which does not free one from the algorithm's scaling. To increase cluster sizes a different algorithm will have to be used.

The tree algorithm would be the first step due to its $O(N \log N)$ scaling. The algorithm is already implemented but would require more testing before being used in production. Its advantage would be to use the ionization library developed in the present work.

Another approach could be taken instead, mainly switching from a direct particle-to-particle (PP) algorithm to a more scalable particle-mesh (PM) or even particle-particle, particle-mesh (P3M) technique. PIC for example scales as $O(N_c^3)$ for the number of grid cells and $O(N_p)$ for the number of particles.

Simulating larger clusters is essential to reach the scale of biomolecules. While experiments have already been performed on some, for example on the mimivirus or photosynthesis proteins, theoretical tools are still in their infancy.

The effects of excited states and ACI in clusters were shown to be significant in different intensity and wavelength regimes. Further investigation might reveal ACI to be present in other types of molecules or at other regimes.

The Quantum FDTD model showed interesting potential for further investigation. While still based on the one electron picture, the potential used can be arbitrary in three dimensions. By changing the Coulombic potential for a Hartree–Fock self-consistent field, a multi-electrons system could be approached. Using this atomic potential could lead to a comparison with reference [54]. Sullivan did develop a two-electron QFDTD using the Hartree-Fock formulation but his systems were mostly 2D, considerably reducing the computational burden required. My package could be used to simulate one electron in an effective potential, using the nonlinear mapping to make the calculation possible.

Additionally, the potential used in the (real time) QFDTD does not have to be time independent. Using a time dependent potential could simulate the effect of a (classical) laser field (through the vector potential). It is hypothesized that transition rates could be obtained from the output of the real time QFDTD. If rates and cross-sections could be obtained for an isolated atom, the influence of the neighbouring ions and the cluster environment could be calculated.

In the future, it will be possible to validate and study some approximations used in the MD package. For example, what is the influence of the shape of the cluster environment, approximated as a constant U_b, over the cluster dynamics? How much is an electron wavefunction affected by a neighbouring ion?

Many tools were developed for the present work. These tools still show great promise for future work.

8.2 Final words

Theoretical laser-clusters studies is an interesting amalgam of many challenging fields of physics. Clusters, being nanoscopic objects, live in a quantum world where particles are described by wavefunctions. When free inside the cluster the particles' dynamics can be treated classically through Newtonian mechanics. Unfortunately, even three hundred years after Newton, the many-body problem, also showing up in astronomy, is not solvable analytically. Computers must be used to calculate these simple trajectories using many algorithms, bringing computer science into the picture with all its quirks, problems, bugs, crashes and high expectation algorithms or new technologies. Lasers are the tool of choice to study atomic clusters. Electrodynamics, classical or quantum, describes

light, the purest form of energy. After clusters get ionized, the plasma generated can be described with the language of statistical mechanics. Additionally to all these fields, clusters can be used as a first-order model for biomolecules or can be used in biological systems. As if physics wasn't complex enough, life and biology bring so many more questions to the picture.

One is easily impressed and even overwhelmed by the wide range of fields touched by clusters studies, but how satisfying can it be to reach so many topics at once? Clusters are quite fascinating and I hope to have brought my humble contributions, through this thesis, to the height of the giants' shoulders so next generations will see even further.

9

References

[1] Reinhard, P. and Suraud, E. *Introduction to Cluster Dynamics*. Biotechnology: A Multi-Volume Comprehensive Treatise. Wiley (2004). ISBN 9783527403455. (Cited on pages 1 and 2.)

[2] Krainov, V.P. and Smirnov, M.B. *Cluster beams in the super-intense femtosecond laser pulse*. Physics Reports, **370**(3):237–331 (2002). ISSN 03701573. http://dx.doi.org/10.1016/S0370-1573(02)00272-7. (Cited on page 1.)

[3] Krainov, V.P. *et al.* *Femtosecond excitation of cluster beams*. Physics-Uspekhi, **50**(9):907—931 (2007). http://dx.doi.org/10.1070/PU2007v050n09ABEH006287. (Cited on page 2.)

[4] Haberland, H., editor. *Clusters of Atoms and Molecules: Theory, Experiment, and Clusters of Atoms*, volume 52 of *Springer Series in Chemical Physics*. Springer (1994). (Cited on page 2.)

[5] Brabec, T., editor. *Strong Field Laser Physics*, volume 134 of *Springer Series in Optical Sciences*. Springer New York, New York, NY (2009). ISBN 978-0-387-40077-8. http://dx.doi.org/10.1007/978-0-387-34755-4. (Cited on pages 2 and 3.)

[6] Levesque, J. and Corkum, P.B. *Attosecond science and technology.* Canadian Journal of Physics, **84**(1):1–18 (2006). ISSN 0008-4204. http://dx.doi.org/10.1139/p05-068. (Cited on pages 2 and 11.)

[7] Martin, T. *Shells of atoms.* Physics Reports, **273**(4):199–241 (1996). ISSN 03701573. http://dx.doi.org/10.1016/0370-1573(95)00083-6. (Cited on page 2.)

[8] Fennel, T. *et al. Laser-driven nonlinear cluster dynamics.* Reviews of Modern Physics, **82**(2):1793–1842 (2010). ISSN 0034-6861. http://dx.doi.org/10.1103/RevModPhys.82.1793. (Cited on pages 3, 9, 11, 12, 27, 28, and 47.)

[9] Varin, C. *et al. Attosecond Plasma Wave Dynamics in Laser-Driven Cluster Nanoplasmas.* Physical Review Letters, **108**(17):175007 (2012). ISSN 0031-9007. http://dx.doi.org/10.1103/PhysRevLett.108.175007. (Cited on pages 3 and 27.)

[10] Peltz, C. *et al. Fully microscopic analysis of laser-driven finite plasmas using the example of clusters.* New Journal of Physics, **14**(6):065011 (2012). ISSN 1367-2630. http://dx.doi.org/10.1088/1367-2630/14/6/065011. (Cited on page 3.)

[11] Ackermann, W. *et al. Operation of a free-electron laser from the extreme ultraviolet to the water window.* Nature Photonics, **1**(6):336–342 (2007). ISSN 1749-4885. http://dx.doi.org/10.1038/nphoton.2007.76. (Cited on page 3.)

[12] Pellegrini, C. *The history of X-ray free-electron lasers.* The European Physical Journal H, **37**(5):659–708 (2012). ISSN 2102-6459. http://dx.doi.org/10.1140/epjh/e2012-20064-5. (Cited on page 3.)

[13] Bostedt, C. *et al. Experiments at FLASH.* Nuclear Instruments and Methods in Physics Research Section A: Accelerators, Spectrometers, Detectors and Associated Equipment, **601**(1-2):108–122 (2009). ISSN 01689002. http://dx.doi.org/10.1016/j.nima.2008.12.202. (Cited on page 3.)

[14] Shintake, T. *et al. A compact free-electron laser for generating coherent radiation in the extreme ultraviolet region.* Nature Photonics, **2**(9):555–559 (2008). ISSN 1749-4885. http://dx.doi.org/10.1038/nphoton.2008.134. (Cited on page 3.)

[15] Wabnitz, H. *et al. Multiple ionization of atom clusters by intense soft X-rays from a free-electron laser.* Nature, **420**(6915):482–5 (2002). ISSN 0028-0836. http://dx.doi.org/10.1038/nature01197. (Cited on pages 3 and 16.)

[16] Bostedt, C. *et al. Multistep Ionization of Argon Clusters in Intense Femtosecond Extreme Ultraviolet Pulses.* Physical Review Letters, **100**(13) (2008). http://dx.doi.org/10.1103/PhysRevLett.100.133401. (Cited on pages 4, 20, and 22.)

[17] Chapman, H.N. *et al. Femtosecond diffractive imaging with a soft-X-ray free-electron laser.* Nature Physics, **2**(12):839–843 (2006). ISSN 1745-2473. http://dx.doi.org/10.1038/nphys461. (Cited on page 4.)

[18] Bostedt, C. *et al. Fast electrons from multi-electron dynamics in xenon clusters induced by inner-shell ionization.* New Journal of Physics, **12**(8) (2010). ISSN 1367-2630. http://dx.doi.org/10.1088/1367-2630/12/8/083004. (Cited on pages 4 and 16.)

[19] Sorokin, A. *et al. Photoelectric Effect at Ultrahigh Intensities.* Physical Review Letters, **99**(21):213002 (2007). ISSN 0031-9007. http://dx.doi.org/10.1103/PhysRevLett.99.213002. (Cited on page 4.)

[20] Richter, M. *et al. Extreme Ultraviolet Laser Excites Atomic Giant Resonance.* Physical Review Letters, **102**(16):163002 (2009). ISSN 0031-9007. http://dx.doi.org/10.1103/PhysRevLett.102.163002. (Cited on page 4.)

[21] Emma, P. *et al. First lasing and operation of an ångstrom-wavelength free-electron laser.* Nature Photonics, **4**(9):641–647 (2010). ISSN 1749-4885. http://dx.doi.org/10.1038/nphoton.2010.176. (Cited on page 4.)

[22] Schneider, J.R. *Photon Science at Accelerator-Based Light Sources.* Reviews of Accelerator Science and Technology, **03**(01):13–37 (2010). ISSN 1793-6268. http://dx.doi.org/10.1142/S1793626810000348. (Cited on page 4.)

[23] Young, L. *et al. Femtosecond electronic response of atoms to ultra-intense X-rays.* Nature, **466**(7302):56–61 (2010). ISSN 1476-4687. http://dx.doi.org/10.1038/nature09177. (Cited on page 4.)

[24] Chapman, H.N. *et al. Femtosecond X-ray protein nanocrystallography.* Nature, **470**(7332):73–7 (2011). ISSN 1476-4687. http://dx.doi.org/10.1038/nature09750. (Cited on page 4.)

[25] Kern, J. *et al.* *Simultaneous femtosecond X-ray spectroscopy and diffraction of photosystem II at room temperature.* Science (New York, N.Y.), **340**(6131):491–5 (2013). ISSN 1095-9203. http://dx.doi.org/10.1126/science.1234273. (Cited on page 4.)

[26] Seibert, M.M. *et al.* *Single mimivirus particles intercepted and imaged with an X-ray laser.* Nature, **470**(7332):78–81 (2011). ISSN 1476-4687. http://dx.doi.org/10.1038/nature09748. (Cited on page 4.)

[27] Pellegrini, C. *The challenge of 4^{th} generation light sources.* Technical Report Ipac, LCLS-SLAC (2011). http://www-public.slac.stanford.edu/scidoc/docMeta.aspx?slacPubNumber=SLAC-PUB-15289. (Cited on page 4.)

[28] Arbeiter, M. and Fennel, T. *Rare-gas clusters in intense VUV, XUV and soft x-ray pulses: signatures of the transition from nanoplasma-driven cluster expansion to Coulomb explosion in ion and electron spectra.* New Journal of Physics, **13**(5):053022 (2011). ISSN 1367-2630. http://dx.doi.org/10.1088/1367-2630/13/5/053022. (Cited on page 4.)

[29] Murphy, B. and Hoffmann, K. *Photoionization of Xe Clusters Under Intense XUV Irradiation.* Conference on Lasers . . . , pages 1–2 (2008). http://dx.doi.org/10.1109/CLEO.2008.4552186. (Cited on pages 4, 11, and 16.)

[30] Murphy, B. *et al.* *Explosion of Xenon Clusters Driven by Intense Femtosecond Pulses of Extreme Ultraviolet Light.* Physical Review Letter, **101**:203401 (2008). http://dx.doi.org/10.1103/PhysRevLett.101.203401. (Cited on pages 4, 11, 16, and 20.)

[31] Krikunova, M. *et al.* *Ionization dynamics in expanding clusters studied by XUV pump–probe spectroscopy.* Journal of Physics B: Atomic, Molecular and Optical Physics, **45**(10):105101 (2012). ISSN 0953-4075. http://dx.doi.org/10.1088/0953-4075/45/10/105101. (Cited on page 4.)

[32] Ziaja, B. *et al.* *Emission of electrons from rare gas clusters after irradiation with intense VUV pulses of wavelength 100 nm and 32 nm.* New Journal of Physics, **11**(10):103012 (2009). ISSN 1367-2630. http://dx.doi.org/10.1088/1367-2630/11/10/103012. (Cited on page 5.)

[33] Thomas, H. *et al.* *Explosions of Xenon Clusters in Ultraintense Femtosecond X-Ray Pulses from the LCLS Free Electron Laser.* Physical Review Letters, **108**(13):133401 (2012). ISSN 0031-9007. http://dx.doi.org/10.1103/PhysRevLett.108.133401. (Cited on page 5.)

[34] Tîmneanu, N. *et al.* *Fragmentation of clusters and recombination induced by intense and ultrashort x-ray laser pulses.* pages 87770J–87770J–8 (2013). http://dx.doi.org/10.1117/12.2019299. (Cited on page 5.)

[35] Long, Z.J. and Liu, W.K. *Keldysh theory of strong-field ionization.* Canadian Journal of Physics, **88**(4):227–245 (2010). ISSN 0008-4204. http://dx.doi.org/10.1139/P09-111. (Cited on page 6.)

[36] Becker, U. *et al.* *Decay channels of the discrete and continuum Xe 4d resonances.* Physical Review A, **33**(6):3891–3899 (1986). ISSN 0556-2791. http://dx.doi.org/10.1103/PhysRevA.33.3891. (Cited on pages 7 and 13.)

[37] Thomas, H. *et al.* *Shell explosion and core expansion of xenon clusters irradiated with intense femtosecond soft x-ray pulses.* Journal of Physics B: Atomic, Molecular and Optical Physics, **42**(13):134018 (2009). ISSN 0953-4075. http://dx.doi.org/10.1088/0953-4075/42/13/134018. (Cited on pages 7, 13, 24, and 47.)

[38] Ackad, E. *et al.* *Recombination effects in soft-x-ray cluster interactions at the xenon giant resonance.* New Journal of Physics, **15**(5):053047 (2013). ISSN 1367-2630. http://dx.doi.org/10.1088/1367-2630/15/5/053047. (Cited on pages 7, 15, and 47.)

[39] Kramida, A. *et al.* *NIST Atomic Spectra Database (ver. 5.0)* (2012). http://physics.nist.gov/asd. (Cited on page 8.)

[40] Ramunno, L. *et al.* *Intense Laser Interaction with Noble Gas Clusters.* In T. Brabec, editor, *Strong Field Laser Physics*, Springer Series in Optical Sciences, book part (with own title) 10, pages 225–241. Springer Berlin / Heidelberg (2008). http://dx.doi.org/10.1007/978-0-387-34755-4. (Cited on pages 9 and 12.)

[41] Agostini, P. *et al.* *Free-Free Transitions Following Six-Photon Ionization of Xenon Atoms.* Physical Review Letters, **42**(17):1127–1130 (1979). ISSN 0031-9007. http://dx.doi.org/10.1103/PhysRevLett.42.1127. (Cited on page 9.)

[42] Krainov, V.P. *et al.* *Radiative Processes in Atomic Physics*. Wiley (1997). ISBN 0471125334. (Cited on page 9.)

[43] Lewenstein, M. and L'Huillier, A. *Principles of Single Atom Physics: High-Order Harmonic Generation, Above-Threshold Ionization and Non-Sequential Ionization*. In T. Brabec, editor, *Strong Field Laser Physics*, chapter 7, pages 147——183. Springer Berlin / Heidelberg (2008). http://dx.doi.org/10.1007/978-0-387-34755-4_7. (Cited on pages 9 and 11.)

[44] Niikura, H. *et al.* *Ionization of Small Molecules by Strong Laser Fields*. In T. Brabec, editor, *Strong Field Laser Physics*, volume 134 of *Springer Series in Optical Sciences*, chapter 8, pages 185——208. Springer New York, New York, NY (2009). ISBN 978-0-387-40077-8. http://dx.doi.org/10.1007/978-0-387-34755-4. (Cited on page 9.)

[45] Corkum, P.B. *Plasma perspective on strong field multiphoton ionization*. Physical Review Letters, **71**(13):1994–1997 (1993). ISSN 0031-9007. http://dx.doi.org/10.1103/PhysRevLett.71.1994. (Cited on page 11.)

[46] Schlessinger, L. and Wright, J. *Inverse-bremsstrahlung absorption rate in an intense laser field*. Physical Review A, **20**(5):1934–1945 (1979). ISSN 0556-2791. http://dx.doi.org/10.1103/PhysRevA.20.1934. (Cited on page 11.)

[47] Georgescu, I. *et al.* *Clusters under strong vuv pulses: A quantum-classical hybrid description incorporating plasma effects*. Physical Review A, **76**(4):1–8 (2007). ISSN 1050-2947. http://dx.doi.org/10.1103/PhysRevA.76.043203. (Cited on pages 11, 12, and 47.)

[48] Laane, J., editor. *Frontiers of Molecular Spectroscopy*. Elsevier (2009). (Cited on page 12.)

[49] Eichmeier, J.A. and Thumm, M.K., editors. *Vacuum Electronics: Components and Devices*. Springer-Verlag Berlin Heidelberg (2008). (Cited on page 12.)

[50] ISO. *Space environment (natural and artificial) – Process for determining solar irradiances*. ISO 21348:2007, International Organization for Standardization, Geneva, Switzerland (2007). http://www.iso.org/iso/home/store/catalogue_tc/catalogue_detail.htm?csnumber=39911;http://www.spacewx.com/Docs/ISO_PRF_21348_e_review.pdf. (Cited on page 12.)

[51] Krainov, V.P. *Inverse stimulated bremsstrahlung of slow electrons under Coulomb scattering.* Journal of Physics B: Atomic, Molecular and Optical Physics, **33**(8):1585–1595 (2000). http://dx.doi.org/10.1088/0953-4075/33/8/309. (Cited on page 12.)

[52] Lotz, W. *An empirical formula for the electron-impact ionization cross-section.* Zeitschrift fur Physik, **206**(2):205–211 (1967). ISSN 1434-6001. http://dx.doi.org/10.1007/BF01325928. (Cited on pages 15 and 46.)

[53] Greene, C. and Santra, R. *Xenon Clusters in Intense VUV Laser Fields.* Physical Review Letters, **91**(23):1–4 (2003). ISSN 0031-9007. http://dx.doi.org/10.1103/PhysRevLett.91.233401. (Cited on page 16.)

[54] Walters, Z.B. *et al. Interaction of intense vuv radiation with large xenon clusters.* Physical Review A, **74**(4):43204 (2006). http://dx.doi.org/10.1103/PhysRevA.74.043204. (Cited on pages 16 and 120.)

[55] Herman, F. and Skillman, S. *Atomic Structure Calculations.* Prentice-Hall (1963). http://hermes.phys.uwm.edu/projects/elecstruct/hermsk/HS.TOC.html. (Cited on page 16.)

[56] Siedschlag, C. and Rost, J.M. *Small Rare-Gas Clusters in Soft X-Ray Pulses.* Physical Review Letters, **93**(4):43402 (2004). ISSN 0031-9007. http://dx.doi.org/10.1103/PhysRevLett.93.043402. (Cited on page 17.)

[57] Jungreuthmayer, C. *et al. Intense VUV laser cluster interaction in the strong coupling regime.* Journal of Physics B: Atomic, Molecular and Optical Physics, **38**(16):3029–3036 (2005). http://dx.doi.org/10.1088/0953-4075/38/16/013. (Cited on pages 17 and 41.)

[58] Ackad, E. *et al. Augmented collisional ionization via excited states in XUV cluster interactions.* Journal of Physics B: Atomic, Molecular and Optical Physics, **44**(16):165102 (2011). ISSN 0953-4075. http://dx.doi.org/10.1088/0953-4075/44/16/165102. (Cited on page 22.)

[59] Ackad, E. *et al. Clusters in intense XUV pulses: Effects of cluster size on expansion dynamics and ionization.* Physical Review A, **83**(6):063201 (2011). ISSN 1050-2947. http://dx.doi.org/10.1103/PhysRevA.83.063201. (Cited on page 22.)

[60] Uiberacker, M. *et al. Attosecond real-time observation of electron tunnelling in atoms.* Nature, **446**(7136):627–32 (2007). ISSN 1476-4687. http://dx.doi.org/10.1038/nature05648. (Cited on page 24.)

[61] Bigaouette, N. *et al. Nonlinear grid mapping applied to an FDTD-based, multi-center 3D Schrödinger equation solver.* Computer Physics Communications, **183**(1):38–45 (2012). ISSN 0010-4655. http://dx.doi.org/10.1016/j.cpc.2011.08.011. (Cited on page 25.)

[62] Nightingale, M. and Umrigar, C. *Quantum Monte Carlo methods in physics and chemistry.* Springer (1998). (Cited on page 26.)

[63] Laaksonen, L. *et al. Fully numerical hartree-fock methods for molecules.* Computer Physics reports, **4**(5):313–344 (1986). ISSN 01677977. http://dx.doi.org/10.1016/0167-7977(86)90021-3. (Cited on page 26.)

[64] Schafer, K.J. *Numerical Methods in Strong Field Physics.* In T. Brabec, editor, *Strong Field Laser Physics*, volume 134 of *Springer Series in Optical Sciences*, chapter 6, pages 111——145. Springer New York, New York, NY (2009). ISBN 978-0-387-40077-8. http://dx.doi.org/10.1007/978-0-387-34755-4. (Cited on pages 26 and 27.)

[65] Cramer, C. *Essentials of computational chemistry: theories and models.* Jonh Wiley & Sons, 2 edition (2004). (Cited on page 26.)

[66] Skeel, R.D. *Integration Schemes for Molecular Dynamics and Related Applications.* The Graduate Student's Guide to Numerical Analysis, **26**:119–176 (1998). http://dx.doi.org/10.1007/978-3-662-03972-4_4. (Cited on page 27.)

[67] Barnes, J.E. and Hut, P. *A hierarchical O(N log N) force-calculation algorithm.* Nature, **324**(6096):446–449 (1986). ISSN 0028-0836. http://dx.doi.org/10.1038/324446a0. (Cited on pages 28, 38, and 40.)

[68] Gibbon, P. and Sutmann, G. *Long-Range Interactions in Many-Particle Simulation.* In *Quantum Simulations of Complex Many-Body Systems: From Theory to Algorithms*, volume 10 of *NIC Series*, pages 467–506 (2002). http://www.fz-juelich.de/nic-series/volume10. (Cited on pages 28, 38, and 40.)

[69] Cowan, R.D. *Atomic Structure Code.* http://www.tcd.ie/Physics/people/Cormac.McGuinness/Cowan. (Cited on pages 28 and 46.)

[70] Pfalzner, S. and Gibbon, P. *Many-Body Tree Methods in Physics*. Cambridge University Press (1996). http://www.amazon.com/Many-Body-Methods-Physics-Susanne-Pfalzner/dp/0521495644. (Cited on page 40.)

[71] Bédorf, J. *et al. A sparse octree gravitational N-body code that runs entirely on the GPU processor*. Journal of Computational Physics, **231**(7):2825–2839 (2012). ISSN 00219991. http://dx.doi.org/10.1016/j.jcp.2011.12.024. (Cited on pages 40 and 41.)

[72] Greengard, L.F. *The Rapid Evaluation Of Potential Fields In Particle Systems* (1987). ISBN 9780262571920. (Cited on page 41.)

[73] Barnes, J.E. *Treecode Guide* (2001). http://www.ifa.hawaii.edu/~barnes/treecode/treeguide.html. Code available through the terms of the GPL v2. (Cited on page 41.)

[74] *Subversion*. http://subversion.apache.org. (Cited on page 42.)

[75] *Git*. http://git-scm.com. (Cited on page 42.)

[76] Fennel, T. *et al. Highly Charged Ions from Laser-Cluster Interactions: Local-Field-Enhanced Impact Ionization and Frustrated Electron-Ion Recombination*. Physical Review Letters, **99**(23):1–4 (2007). ISSN 0031-9007. http://dx.doi.org/10.1103/PhysRevLett.99.233401. (Cited on page 42.)

[77] West, J.B. and Morton, J. *Absolute photoionization cross-section tables for xenon in the VUV and the soft x-ray regions*. Atomic Data and Nuclear Data Tables, **22**(2):103–107 (1978). ISSN 0092640X. http://dx.doi.org/10.1016/0092-640X(78)90010-4. (Cited on page 46.)

[78] Marr, G. and West, J. *Absolute photoionization cross-section tables for helium, neon, argon, and krypton in the VUV spectral regions*. Atomic Data and Nuclear Data Tables, **18**(5):497–508 (1976). ISSN 0092640X. http://dx.doi.org/10.1016/0092-640X(76)90015-2. (Cited on page 46.)

[79] Lax, M. *et al. Random Processes in Physics and Finance*. Oxford Finance Series. Oxford University Press (2006). ISBN 0198567766. (Cited on page 46.)

[80] Tawara, H. and Kato, T. *Total and partial ionization cross sections of atoms and ions by electron impact.* Atomic Data and Nuclear Data Tables, **36**(2):167–353 (1987). ISSN 0092640X. http://dx.doi.org/10.1016/0092-640X(87)90014-3. (Cited on page 46.)

[81] Heidenreich, A. *et al. Electron impact ionization of atomic clusters in ultraintense laser fields.* The European Physical Journal D, **35**(3):567–577 (2005). ISSN 1434-6060. http://dx.doi.org/10.1140/epjd/e2005-00220-8. (Cited on page 46.)

[82] Lotz, W. *Electron-impact ionization cross-sections for atoms up to Z=108.* Zeitschrift fur Physik, **232**(2):101–107 (1970). ISSN 1434-6001. http://dx.doi.org/10.1007/BF01393132. (Cited on page 46.)

[83] Cowan, R.D. *The Theory of Atomic Structure and Spectra.* Los Alamos Series in Basic and Applied Sciences. University of California Press (1981). ISBN 0520038215. http://dx.doi.org/10.1038/140626a0. (Cited on page 46.)

[84] Sudiarta, I.W. and Geldart, D.J.W. *Solving the Schrödinger equation using the finite difference time domain method.* Journal of Physics A: Mathematical and Theoretical, **40**(8):1885–1896 (2007). ISSN 1751-8113. http://dx.doi.org/10.1088/1751-8113/40/8/013. (Cited on pages 48 and 49.)

[85] Yee, K. *Numerical solution of initial boundary value problems involving maxwell's equations in isotropic media.* IEEE Transactions on Antennas and Propagation, **14**(3):302–307 (1966). ISSN 0018-926X. http://dx.doi.org/10.1109/TAP.1966.1138693. (Cited on page 48.)

[86] Taflove, A. and Hagness, S. *Computational Electrodynamics: The Finite-Difference Time-Domain Method, Third Edition.* Artech House, 3 edition (2005). ISBN 1580538320. http://www.artechhouse.com/Detail.aspx?strBookId=1123. (Cited on pages 48 and 54.)

[87] Sullivan, D.M. *Electromagnetic Simulation Using the FDTD Method.* Wiley-IEEE Press (2000). ISBN 0780347471. http://www.amazon.com/Electromagnetic-Simulation-Using-FDTD-Method/dp/0780347471. (Cited on page 48.)

[88] Sullivan, D.M. and Citrin, D.S. *Time-domain simulation of two electrons in a quantum dot.* Journal of Applied Physics, **89**(7):3841 (2001). ISSN 00218979. http://dx.doi.org/10.1063/1.1352559. (Cited on page 48.)

[89] Sullivan, D.M. and Citrin, D.S. *Determination of the eigenfunctions of arbitrary nanostructures using time domain simulation.* Journal of Applied Physics, **91**(5):3219 (2002). ISSN 00218979. http://dx.doi.org/10.1063/1.1445277. (Cited on page 48.)

[90] Sullivan, D.M. and Citrin, D.S. *Time-domain simulation of quantum spin.* Journal of Applied Physics, **94**(10):6518 (2003). ISSN 00218979. http://dx.doi.org/10.1063/1.1618916. (Cited on page 48.)

[91] Sullivan, D.M. and Citrin, D.S. *Time-domain simulation of a universal quantum gate.* Journal of Applied Physics, **96**(3):1540 (2004). ISSN 00218979. http://dx.doi.org/10.1063/1.1766409. (Cited on page 48.)

[92] Sullivan, D.M. and Citrin, D.S. *Determining quantum eigenfunctions in three-dimensional nanoscale structures.* Journal of Applied Physics, **97**(10):104305 (2005). ISSN 00218979. http://dx.doi.org/10.1063/1.1896437. (Cited on page 49.)

[93] Sullivan, D.M. *Determining a complete three-dimensional set of eigenfunctions for nanoscale structure analysis.* Journal of Applied Physics, **98**(8):084311 (2005). ISSN 00218979. http://dx.doi.org/10.1063/1.2108157. (Cited on page 49.)

[94] Sudiarta, I.W. and Geldart, D.J.W. *Solving the Schrödinger equation for a charged particle in a magnetic field using the finite difference time domain method.* Physics Letters A, **372**(18):3145–3148 (2008). ISSN 03759601. http://dx.doi.org/10.1016/j.physleta.2008.01.078. (Cited on page 49.)

[95] Sudiarta, I.W. and Geldart, D.J.W. *The finite difference time domain method for computing the single-particle density matrix.* Journal of Physics A: Mathematical and Theoretical, **42**(28):285002 (2009). ISSN 1751-8113. http://dx.doi.org/10.1088/1751-8113/42/28/285002. (Cited on page 49.)

[96] Strickland, M. and Yager-Elorriaga, D. *A parallel algorithm for solving the 3d Schrödinger equation.* Journal of Computational Physics (2010). ISSN 00219991. http://dx.doi.org/10.1016/j.jcp.2010.04.032. (Cited on page 49.)

[97] Dai, W. *et al. On the stability of the FDTD method for solving a time-dependent Schrödinger equation.* Numerical Methods for Partial Differential Equations, **21**(6):1140–1154 (2005). ISSN 0749159X. http://dx.doi.org/10.1002/num.20082. (Cited on page 53.)

[98] Saito, M. and Matsumoto, M. *A PRNG Specialized in Double Precision Floating Point Numbers Using an Affine Transition.* In *Monte Carlo and Quasi-Monte Carlo Methods 2008*, pages 589–602 (2009). ISBN 978-3-642-04107-5. http://dx.doi.org/10.1007/978-3-642-04107-5_38. (Cited on page 59.)

[99] Thomason, L. *TinyXML.* http://www.grinninglizard.com/tinyxml/index.html. (Cited on page 60.)

[100] *NetCDF.* http://www.unidata.ucar.edu/software/netcdf. (Cited on page 60.)

[101] Hunter, J.D. *Matplotlib: A 2D graphics environment.* Computing In Science & Engineering, **9**(3):90–95 (2007). (Cited on page 135.)

10

Appendix: Open-Source Packages

Many different open-source packages were used throughout this work. While not related to physics *per se*, their value is huge. During the years, I often found myself recommending some to my colleagues. I thus propose listing some of the most useful ones that, in my opinion, should be used more often by scientists.

All the specified packages are available on all platforms (Windows, Linux, Mac and even BSD) except stated otherwise.

Python

Python is an extremely versatile programming language. Being *interpreted* (as opposed to *compiled*), it allows fast development with its high level design. Many programming languages are praised by their user but deeper investigation sometimes reveals them to be complicated and hard to learn.

Python has code readability as its design philosophy. A program written in Python can have a single line and can scale extremely large projects like web sites or video games.

Documentation is of high quality and the community is always helpful. It is available here: http://docs.python.org/3

Python is the ideal tool for almost every coding project. The most important drawback is the fact that it is interpreted. As all interpreted languages, it is slower than compiled languages because of the overhead of the interpreter. This only prevents the most performance critical algorithms to be implemented directly in Python, and different wrappers allow calling compiled routines (C, C++ or Fortran for example).

The recommended way to install Python on Windows is to use Python(x,y) described later. On other platforms, package managers make the installation a breeze.

NumPy and SciPy

Fortran and C/C++ users will surely want to work with arrays of data. The closest to arrays Python can offer is a *list* which is not suited for fast loops over them.

A fast array implementation for Python is *NumPy*. It includes support for multi-dimensional arrays, matrices and some high level mathematical functions that act on these arrays. NumPy allows fast execution of arrays operation by using, under the hood, compiled routines.

Additionally to NumPy, *SciPy* is the scientific library for Python that adds support for more specific scientific mathematical functions and algorithms. It includes for example linear algebra algorithms, discrete Fourier transforms (FFT), optimization algorithms, statistical routines, integration functions, etc.

NumPy's homepage can be found at `http://www.numpy.org` and SciPy at `http://www.scipy.org`.

Matplotlib

Matplotlib [101] is the plotting library for Python. It is extremely powerful and supports a large range of different figure types (see the gallery at `http://matplotlib.org/gallery.html` for many examples). Almost all figures in this thesis were generated by Python and Matplotlib.

It is an easy to library. It's syntax is close to the (proprietary and expensive) Matlab and thus makes a great replacement for it. The quality of the generated figures is also, in my opinion, highly superior to Matlab's. More information on Matplotlib can be found on its homepage at `http://matplotlib.org`.

Python(x,y)

On Linux, it is extremely easy to install and use Python, NumPy, SciPy and Matplotlib. On Windows though, their homepage gives link to download their source code which can then be compiled. This is something Windows users are probably not willing to do.

Instead, I recommend *Python(x,y)* which is a complete distribution of Python and *close to one hundred* libraries, including NumPy, SciPy, Matplotlib and many others. It also includes a great Integrated Development Environment (IDE) called *Spyder*.

With Python(x,y) one can replace fully Matlab on Windows as it includes everything required for scientific programming.

More information on Python(x,y), including download links, can be found on its homepage at https://code.google.com/p/pythonxy/wiki/Welcome.

NetCDF

NetCDF (Network Common Data Form) is both a set of libraries and a file formats. It basically allows storing architecture and machine independent data in a self-describing and array-oriented way.

The self-describing nature means that all information required to interpret the data is included in the actual file. For example, saving an array representing particle velocities might contain not only the data, but also vital metadata like the array size and optional information like data units. This gives great flexibility to analyze the data as one does not need to worry about incorrectly interpreting it. NetCDF can also compress the data when saving it, allowing significant size reduction files output.

NetCDF files are portable and thus can be accessed (read and write) on all platforms and from many different languages. Wrappers exist for C, C++, Fortran, Python and others.

NetCDF was created (and is still developed) by the University Corporation for Atmospheric Research (UCAR) and can be downloaded at
http://www.unidata.ucar.edu/software/netcdf/.

PyMOL

PyMOL is a molecular visualization system written in Python. It is used here to visualize and animate clusters after simulations. It was selected over others (like VMD) since it was

faster and allowed changing the number of particles during the simulations, an important requirement. Figure 9 was created with PyMOL.

PyMOL can be downloaded for all platforms at http://www.pymol.org. The wiki, located at http://pymolwiki.org contains a great deal of information, documentation and examples.

Valgrind

As described in section 2.6.2, *Valgrind* is an extremely useful tool for development of (compiled) programs. It allows analyzing the memory access of a program and can reveal many subtle programming errors. For example, arrays' out-of-range access or using uninitialized variables are problems that can be quite hard to diagnose but still have significant consequences.

One piece of advise I can give to someone writing any kind of software is to run the program through Valgrind. In all but trivial programs Valgrind *will* detect problems, even for experienced programmers. It must be noted that while the MD, QFDTD and all other libraries developed for this work had errors, Valgrind detected them and I am proud to say that the packages are now free of *all* of these errors, raising confidence in the simulations results.

Valgrind is available on Linux and Mac only (unfortunately not on Windows). It's homepage can be found here: http://www.valgrind.org.

Git

Git is a version control system (VCS). A VCS allows keeping a history of some work, for example a program's source code or even a full thesis. Git has many advantages over other VCS (like *cvs* or *subversion*). It is *distributed*, meaning it does not depend on a centralized server. Branches and tags can be created easily, specially compared to subversion, to explore new ideas.

Git has, unfortunately, a relatively steep learning curve. New users are often overwhelmed by the vast amount of options or even by its flexibility; Git can be used in many different workflow.

Keeping a history of one's work is invaluable. Not only is it a good way to keep track of the development, it can also help debugging. Often, one realizes something has broken in the program; what modification introduced the bug? These can be extremely hard

problems to debug. Using a revision control system, it is possible to pinpoint the exact modification that created the problem.

Git's homepage http://git-scm.com host its documentation. For Windows integration, many options exist. SourceTree (http://www.sourcetreeapp.com/), TortoiseGit (https://code.google.com/p/tortoisegit), GitExtensions (http://code.google.com/p/gitextensions or Git-Cola
(http://git-cola.github.io) are all great tools.

LaTeX

This thesis was written with LaTeX, a powerful document writing and typesetting.

New users often found it hard to learn, or at least to format their document to their exact requirements. After having written this thesis with University of Ottawa's formatting requirements, I decided to share my configuration.

My LaTeXclass for the University of Ottawa is thus freely accessible on GitHub at https://github.com/nbigaouette/uottawa_thesis. I hope it will be useful to other students and help them use this high quality software.